ITER Fast Ion Collective Thomson Scattering

Feasibility study

Bindslev, Henrik; Meo, Fernando; Korsholm, Søren Bang

Publication date:
2003

Document Version
Publisher's PDF, also known as Version of record

Annex 1

ITER Fast Ion Collective Thomson Scattering

Feasibility study[*]

Henrik Bindslev, Fernando Meo, Søren Korsholm

Association EURATOM-Risø
Risø National Laboratory
Denmark
20 November 2003

[*] This work was performed as part of EFDA Contract 01.654

Executive Summary

We recall the measurement requirements for the confined fusion alphas in ITER, set out in the ITER Final Design Report. They require a time resolution of 100 ms, a spatial resolution of $a/10$ and that the full fusion alpha distribution from 100 keV to 3.5 MeV should be resolved. The requirements on energy or velocity space resolution are not given in the design report.

Collective Thomson scattering (CTS) can provide spatially and temporally resolved measurements of the 1-D fast ion velocity distribution along a direction which depends on the scattering geometry. In particular the scattering geometry may be arranged to measure the distribution as a function of velocity parallel to the magnetic field, or as a function of velocity perpendicular to the magnetic field. The parallel distribution would bring out the dynamics of alphas with large parallel velocities with a large fraction on passing orbits, one sign of the velocity corresponding to the co direction and the other sign to the counter direction. CTS cannot distinguish an alpha particle from four deuterons moving with the same velocity. Measured distributions are thus a sum of the alpha and other fast ion distributions, each weighted by the square of the specie charge. Fast deuterons from NBI move in the co direction and spread out in the perpendicular velocity space. Their energies reach 1 MeV and thus superimpose with the alpha distribution up to alpha energies of 2 MeV in the co-direction (the direction of the plasma current) and to a slightly lesser extent in the perpendicular direction. The phase space densities of the beam deuterons are comparable to the alphas. Measurements in the co and perpendicular directions will thus generally have a significant beam contribution. Measurements in the counter direction would essentially be free of beam contributions, and thus give essentially clear access to measuring part of the alpha distribution. If the alpha distribution were isotropic this measurement would suffice to define the velocity distribution. The fusion alpha distribution and its dynamics are in fact expected to be anisotropic, making measurements in the perpendicular and in the co directions valuable despite the overlaid beam distribution. Here it is fortuitous that the interaction between a fast ion population, with a given velocity distribution, and the rest of the plasma, in particular wave particle interactions, is largely the same irrespective of whether the fast ions are alpha particles or deuterons. Thus, the dynamics observed in the perpendicular and co directions will be common to beam deuterons and alphas.

On this background we augment the measurement requirements with the need to resolve the parallel direction, co and counter, as well as the perpendicular direction. Further we require that the velocity space resolution permits at least 8 velocity bins to be resolved either side of zero, i.e. for the parallel measurements we require at least 8 velocity bins be resolved in the counter direction and 8 bins in the co-direction.

The requirements on the relative accuracy of the measurements of the distribution stated in the design report, we translate into a requirement that the uncertainty in the measured 1-D velocity distributions be less than $6\times10^{9}\mathrm{s/m}^{4}$ for an alpha density of $8\times10^{17}\mathrm{m}^{-3}$. At other densities the requirements on the uncertainty limit scale proportionally.

We introduce a measure of the information content in the resolved fast ion distribution, which we call the *resolving power, L,* one significance of which is that the uncertainty in the measured 1-D velocity distribution, σ, is essentially given by

$$\sigma \approx \frac{6\times10^{9}\mathrm{s/m}^{4}\ \sqrt{N}}{L}$$

where N is the number of velocity bins into which the distribution is resolved. Thus to meet the ITER measurements requirement at an alpha density of $8\times10^{17}m^{-3}$ with 8 velocity bins either side of zero requires a resolving power, L, greater than 4. At the lower density of $4\times10^{17}m^{-3}$ the demand on resolving power would be 8. This resolving power would also meet the ITER requirements on alpha density measurement at the required lower density limit of $1\times10^{17}m^{-3}$.
CTS, in a scattering geometry which resolves perpendicular fluctuations, has the potential to provide temporally and spatially resolved measurements of the fuel ion ratio, n_D/n_T. This capability can in some case be integrated into the CTS for fast ion diagnosis.
On the basis of simple considerations of spatial resolution, plasma access, scattering cross section and current or potential availability of sources we restrict the investigations to systems with probe frequencies in the ranges of 60 GHz, 170 GHz, 3 THz and 28 THz.

With a probe frequency in the 60 GHz range we find resolving powers above 10 for measurements across the plasma for both the scattering geometries resolving the parallel velocity distributions (i.e. including the counter direction with no beam ions overlaied), and those resolving the perpendicular distributions. This with a temporal resolution of 40 ms, a spatial resolution of a/10, and near full radial coverage[1]. Thus this system more than satisfies all the ITER design requirements. The system design is based on existing or near term technologies, including the probe source assumed to be a long pulse gyrotron delivering 1 MW.
The upper electron densities at which the 60 GHz systems can meet the full set of diagnostic requirements are $1.3\times10^{20}m^{-3}$ for the parallel measurements and $1.2\times10^{20}m^{-3}$ for the perpendicular measurements, both at an electron temperature of 25 keV. These densities are at the Greenwald limit. At 35 keV the density limits reduce to $1.0\times10^{20}m^{-3}$.
The 60 GHz system is the only system which can meet all the measurement requirements with existing or near term technology. The system requires one probe for measuring the full profile of parallel distributions and one probe for the profile of perpendicular measurements. Profile measurements of the deuterium to tritium ratio can be integrated into the system, which resolves the perpendicular fast ion distributions. This would require no additional openings in the plasma facing components and no additional front end mirrors.

Systems with probe frequencies in the 170 GHz range fall far short of the measuring requirements, essentially because the presence of the fundamental electron cyclotron resonance in the plasma gives rise to intense background radiation, even with attempts to use the edge region of the electron cyclotron resonance as a viewing dump. The system can only provide one measuring volume. With an optimistic estimate of the plasma emission background (3 keV) we find that the probe power would need to

[1] By a spatial resolution of $a/10$ we imply that the system is capable of having non-overlapping measuring volumes spaced by 1/10 of the minor radius. Since the centres of the measuring volumes can be shifted to give dense coverage, the spatial resolution is set by the spatial extent of each scattering volume or measurement volume, over which each measurement point in a radial profile is spatially averaged. The spatial extents of the scattering volumes are thus also 1/10 of the minor radius. With near full radial coverage we imply that the system can take measurements from a set of densely spaced non-overlapping measuring volumes which collectively cover most of the plasma cross section.

exceed 7 MW to achieve a temporal resolution of 100 ms (integration time of 50 ms and 50% probe modulation duty cycle) and a resolving power of 4. Meeting the accuracy requirements at the lower fast ion density would require a probe in excess of 15 MW in one focussed beam. Achieving even the lower of these power levels in one beam is unrealistic.

The only other system that is close to meeting all the ITER design requirements is the 3 THz system, but his system requires a non-trivial development of a probe source. A resolving power of 4 can be achieved with a probe having a pulse energy of 6 Joules and 600 ns pulse duration. Reaching the resolving power of the 60 GHz system and fulfilling the ITER requirements on accuracy at the lower alpha density would require a pulse energy of 15 Joules in 600 ns. At this frequency we are limited to using a far forward scattering geometry with a scattering angle around 4°. To measure the parallel velocity distribution (which includes the counter direction that is free from beam ions), the beam lines must pass vertically through the plasma. This geometry will also permit measurement of the perpendicular velocity distribution. The length of the scattering volume is around 50 cm giving a spatial resolution normalised by the plasma radius of a/6 (50 cm resolution compared with a plasma half height of 3 metres) which is a little short of the ITER measurement requirements. This system can provide full coverage of the vertical plasma cross section with a single probe line. Measurement of the fuel ion density ratio could also be integrated into this system and use the same probe line as the fast ion diagnostic. A separate viewing line would be required. Such a system could have the same spatial resolution as the fast ion diagnostic.
This system has no upper operational density limit of significance. The performance presented here assumes a maximum electron temperature of 25 keV and that the electron distribution remains Maxwellian far into the tail. Small deviations from this can significantly increase the ECE emission above the 2 eV receiver noise temperature at the antenna, augmenting the probe power requirements. Higher electron temperatures would also readily lead to increased probe power requirements. The performance is limited by the achievable receiver noise temperature. Our calculations assume use of low noise detectors used in astrophysics. They are fragile and would need further development for use in this CTS. Sources to deliver a probe pulse energy of 6 to 15 Joules in 600 ns at a repetition rate of 10 Hz (to meet the requirement on time resolution) are not currently available. While it may be possible to reach these specifications with a free electron laser run as an amplifier, this solution appears prohibitively expensive. An alternative route is an optically pumped molecular gas laser, such as a D_2O laser pumped by a CO_2 laser. Achieving 6 to 15 Joules from the molecular laser would require on the order of 200 to 500 Joules in the CO_2 laser, at 10 Hz. The line width requirements on the CO_2 laser would be the same as those required at the probe frequency. Designing such a source is a formidable engineering task.

A CTS at 28 THz would use a CO_2 laser as the source for the probe. At this frequency the geometry is limited to far forward scattering with a scattering angle around 0.5°. This implies that to measure the parallel velocity distribution and hence the counter direction, where the beam ion population is negligible, the beam lines must pass vertically through the plasma. The small scattering angle gives rise to scattering (measuring) volumes which are much longer than in the other systems considered. To reduce the extent of the scattering volume and hence improver the spatial resolution,

and to increase the signal strength, one seeks to reduce the widths of the probe and receiver beams. To achieve a scattering volume length of 50 cm corresponding to a relative resolution of a/6 (the ITER measuring requirement is a/10) a Gaussian beam radius of 1.3 mm is required. With such narrow beams the velocity space resolution only permits 1 velocity bin to be resolved either side of zero velocity, i.e. far short of the 8 bins we set as target and achieved with other systems. With only one bin resolved the measurement would not constitute a measurement of the distribution but merely a weighted average over the counter travelling part of the fusion alpha distribution[2].
With a Gaussian beam radius of 2 mm the spatial resolution is a/4 and the velocity space resolution permits 2 independent velocity bins to be resolved in the counter direction. Resolving 3 bins results in a spatial resolution of a/2.5. Achieving the target of resolving 8 velocity bins in the counter direction requires a Gaussian beam radius of 1 cm (scattering angle reduced to 0.4° to compensate the reduced signal with wider beams) leading to a scattering volume length of 5 metres, i.e. resulting in no spatial resolution for the vertical beam line required to measure the parallel velocity distribution and hence the counter direction. The conclusion is that a CO_2 laser based CTS cannot resolve the fusion alpha velocity distribution in the counter direction where NBI ions are negligible, with a spatial resolution which meets the ITER measurement requirements. The measurements which can be achieved in the counter direction with a CO_2 system fall far short of what can be achieved with the 60 GHz system.
To combine reasonable velocity space resolution with reasonable spatial resolution it is necessary to use a geometry where the probe and receiver beams are tangential to the toroidal direction. In this geometry a spatial resolution of a/4 can be achieved together with a velocity space resolution providing 8 velocity bins either side of zero. In this geometry the parallel velocity distribution cannot be measured, only the perpendicular distribution. While still short of the measurement requirements, it does represent an interesting diagnostic potential. Each spatial measurement will require its own source, and probe and receiver beam lines. A CO_2 laser based CTS in the toroidal geometry can also be considered for diagnosing the fuel ion ratio.
For the fast ion measurements a resolving power of 4 can be achieved with a probe pulse energy of 100 Joules and a pulse length of 1 μs. To increase the resolving power to 10 to reach the required accuracy at the lower fusion alpha density and to reach the resolving power achieved with the 60 GHz system, the pulse length must be increased to above 6 μs and the pulse energy to above 600 Joules. This at a pulse rate of 10 Hz to meet the ITER requirements or 25 Hz to reach the time resolution achieved with the 60 GHz system. For N spatial points, N such sources would be required. The CO_2 system benefits from not having any practical operational limits in density or temperature.

In conclusion, the only system which can fully meet the ITER measurement requirements for confined fusion alphas is the 60 GHz system. This includes measuring the fusion alphas in the counter direction where there are essentially no beam ions. This is achievable with existing or near term technologies, the most demanding of which is the development of a 1 MW long pulse gyrotron at 60 GHz.

[2] Note that this limitation is due purely to the beam width and geometry and cannot be helped by increasing the probe power or pulse length. Insufficient probe power or pulse length would lead to poor resolving power, which would introduce a separate limitation on the achievable velocity space resolution.

Such gyrotrons already exist for the more challenging higher frequency of 140 GHz. The technologies have been tested successfully on current machines. The system can meet the full set of measurement requirements for electron densities up to the Greenwald limit for the reference electron temperature of 25 keV. At higher temperatures the density limit is reduced in such a way that the limit effectively is a beta limit, which is close to the plasma operational beta limits. Thus it is not expected that this limit will be of practical consequence. The 60 GHz fast ion diagnostic can be combined with a fuel ratio diagnostic at 60 GHz which uses the same front ends as the 60 GHz fast ion diagnostic.

The only other system which is close to meeting all the ITER measurement requirements for confined fusion alphas is the 3 THz system. This system does, however, require significant source and detector developments.

The CO_2 laser system cannot meet the ITER measurement requirements for confined fusion alphas. In particular, the system cannot measure the velocity distribution of the fusion alphas in the counter direction with the required spatial resolution. Resolving 8 velocity bins leads to no spatial resolution, while resolving 3 velocity bins leads to a resolution of a/2.5. The CO_2 laser based system can measure the perpendicular distribution with a spatial resolution of a/4. A CO_2 laser based CTS does require significant source developments.

Contents

1 Outline of the ITER CTS feasibility study

In this report we investigate the feasibility of diagnosing the fast ions in ITER by collective Thomson scattering (CTS), exploring and comparing the diagnostic potentials of CTS systems base on a range of different probe frequencies.
In this section we first recall the requirements for measurements of the confined fusion alpha particles in ITER set by the ITER team. Then we outline the considerations, which enter into the selection and evaluation of CTS systems. System definition includes choice of probe frequency, geometry of probe and receiver beam patterns and probe power, but ultimately covers many more details. Here we introduce terms and methods used in the more detailed system evaluations later in the report.
In Sections 2 through 5 we consider four different types of CTS systems, which differ by the ranges in which their probe frequencies lie. In Section 6 we summarize and compare the diagnostic potentials uncovered in the preceding four sections. A number of more detailed discussions are placed in appendices along with supporting material.

1.1 Requirements on measurements of confined alphas

The ITER team set out the requirements for diagnosing confined fusion alphas in ITER as a set of target values for resolution and accuracies in the document *Design Requirements and Guidelines Level* 1 in the ITER Final Design Report [1]. Essentially the same information was published in Reference [2]. The requirements state that the energy spectrum and the density profile are to be measured and this with the following accuracies, ranges and resolutions:

Time resolution	100 ms
Spatial resolution	a/10 ≈ 20 cm
Energy resolution	To be defined
Energy range	0.1 MeV to 3.5 MeV
Density range*	10^{17}m^{-3} to 2×10^{18}m^{-3}
Accuracy	20%

Table 1. Accuracies, ranges and resolutions with which the fusion alpha energy spectrum and density profile should be resolved, according to the document *Design Requirements and Guidelines Level* 1 in the ITER Final Design Report [1]. *In the *Design Requirements* the density range is only indicated to apply to the density profile measurements, not to the energy spectrum.

These specifications need to be extended to provide a basis for assessing the adequacy of a fast ion diagnostic. The energy resolution needs to be defined. There is no mention of a need to resolve the fast ion pitch angle (or ratio between velocity parallel and perpendicular to the magnetic field). Despite the isotropic birth rate distribution of fusion alphas resulting from thermonuclear fusion, as opposed to fusion involving beam ions, the finite drift orbits combined with the plasma inhomogeneity lead to anisotropic fusion alpha distributions. Furthermore, the dynamics of trapped and passing fast ions can be quite different, and there are differences between co (current) and counter travelling fast ions. It appears therefore that it is desirable to have some information on the two-dimensional fast ion distribution as a function of parallel and perpendicular velocity, $f(v_{||},v_{\perp})$. We suggest that a reasonable requirement is the resolution of the parallel velocity distribution, $f_{||}(v_{||}) = \int f(v_{||},v_{\perp})\, d\, v_{\perp}$, and the perpendicular velocity distribution, $f_{\perp}(v_{\perp}) = \int f(v_{||},v_{\perp})\, d\, v_{||}$, which will give access to a

significant part of the anisotropy in the distribution and in its dynamics. For both the parallel and perpendicular distributions we should define the required velocity space resolution, or equivalently, given the defined velocity range (corresponding to the defined energy range), we may set the number of bins into which the velocity distributions should be resolved. We suggest that a reasonable number of velocity bins is 8 either side of zero velocity, i.e. 16 bins in total for the parallel velocity distribution. We suggest the same number of velocity bins for the perpendicular velocity distribution. To give meaning to the accuracy, defined as a relative quantity, we need to define the lowest velocity space density this accuracy should be meet at. We note that for the fast ion density measurement the lower limit on the density range is $10^{17}\mathrm{m}^{-3}$. Resolving the details of a distribution is clearly more demanding than measuring the integral over the distribution. To retain an approximately comparable demand on the measurement of the distribution in 16 bins we propose that the 20% accuracy be required down to a density of $4\times10^{17}\mathrm{m}^{-3}$. The density measurement can be considered as the result of collecting the contents of the $N = 16$ velocity space bins into one bin. Neglecting the generally modest level of correlations between the uncertainties in different bins, the relative accuracy of the density measurements can be expected to be on the order of $N^{1/2} = 4$ times better than the relative accuracies of the densities in each of the 16 velocity space bins. A fusion alpha density of $4\times10^{17}\mathrm{m}^{-3}$ corresponds to an average velocity space density of $15\times10^{9}\mathrm{s/m}^{4}$. An accuracy of better than 20% on this figure gives us an upper limit on the uncertainty (defined as one standard deviation) of $3\times10^{9}\mathrm{s/m}^{4}$ for the resolution of the velocity distribution.

The measurement requirements for one-dimensional fast ion velocity distributions, derived from the requirements published in Reference [1] and repeated in Table 1 with the addition of requirements on the velocity space resolution and the lower density limit, are summarised in Table 2.

Time resolution	100 ms
Spatial resolution	a/10 ≈ 20 cm
Velocity resolution	16 velocity bins, 8 either side of 0 velocity.
Velocity range	-13×10^{6}m/s to -2×10^{6}m/s and 2×10^{6}m/s to 13×10^{6}m/s
Uncertainty (STD) at lowest density of $4\times10^{17}\mathrm{m}^{-3}$	$\sigma < 3\times10^{9}\mathrm{s/m}^{4}$
Uncertainty (STD) at an alpha density of $8\times10^{17}\mathrm{m}^{-3}$	$\sigma < 6\times10^{9}\mathrm{s/m}^{4}$

Table 2. Measurement requirements for 1-D fast ion velocity distributions, derived from the requirements in Table 1 with the addition of requirements on the velocity space resolution and translation of the relative accuracy into a limit on absolute error bars.

Collective Thomson scattering (CTS) can measure the one-dimensional velocity distribution defined as the projection of the full 3-D distribution onto a direction in velocity space which can be varied. In particular the parallel and perpendicular velocity distributions discussed above can be resolved. CTS cannot distinguish alpha particles from other ion species. The spectral power density is proportional to the square of the ion charge. Thus four beam deuterons travelling in the co direction with

a velocity of 10^7m/s (corresponding to an energy of 1 MeV per deuteron) would give the same signal as one alpha particle travelling in the same direction with the same velocity. The consequence is that for velocities below 10^7m/s (corresponding to alpha energies below 2 MeV) in the co direction, and to some extent in the perpendicular directions, CTS would measure a combination of the alpha and neutral beam deuteron distributions, $f = xf_\alpha + (1-x)f_D/4$, where the ratio, defined by the factor x, would not be resolved by the CTS measurement. In the counter direction the beam ions would not obscure the fusion alpha measurements. For this reason it is of particular interest to identify CTS systems that can be operated in a geometry which resolves the parallel velocity distribution, thus giving the distribution in the counter direction with one velocity sign and the co direction with the opposite sign.
Deuterons and alphas with identical velocities have identical drift orbits and gyro radii, and have identical interactions with waves and turbulence. Thus two populations of fast ions with identical distributions, only one being alphas and the other deuterons with twice the density, will influence the rest of the plasma (drive waves etc.) and be influenced by the plasma in largely the same way. Only difference is that alphas slow down by electron drag at twice the rate compared with the deuterons. Thus the fast ion physics phenomena we observe with CTS will apply to alphas as well as to the deuterons. We therefore find that it is important to resolve the perpendicular velocity distribution despite the fact that deuterons will make up part of the measured population at velocities below 10^7m/s.

1.2 Probe frequencies

Considerations of availability of sources, conditions for the scattered radiation to carry information on the fast ions, and accessibility of the plasma to electromagnetic radiation, leads to 4 frequency ranges for the probe radiation, worthy of further consideration (we elaborate on this in subsection 1.9). Characteristic frequencies for the four ranges are indicated in Table 3. These are the systems, which are investigated in some detail in this report.

Probe frequency (approximate)	**Relation to electron cyclotron emission (ECE) spectrum**	**Likely Source**	**Main concern**	**Discussed in Section**
60 GHz	X-mode radiation below the ECE spectrum	Gyrotron	Refraction and ECE	2
170 GHz	0-mode between the fundamental and the second harmonic of the ECE spectrum	Gyrotron	ECE	3
3 THz	In upper tail of the ECE spectrum	Optically pumped FIR laser	Source availability and ECE	4
28 THz	Far above the ECE spectrum	CO_2 laser	Small scattering angle and source	5

Table 3. List of approximate probe frequencies of the CTS systems being considered for diagnosing fast ions in ITER.

1.3 Equation of transfer

The diagnosis of the fast ion phase space density by CTS is based on detecting the spectrum of radiation scattered from an injected beam of probe radiation by microscopic fluctuations in the plasma driven by the fast ions (for a review of theory and a broad range of references see [3]). The *equation of transfer* for a CTS system, describing the spectral power density of the received scattered radiation, $\partial P^s / \partial \nu^s$, in terms of incident probe beam power, P^i, and the characteristics of the plasma and scattering geometry, can be cast in the form [3,4]:

$$\frac{\partial P^s}{\partial \nu^s} = P^i O_b \left(\lambda_0^i\right)^2 r_e^2 n_e \frac{1}{2\pi} \Sigma \,. \tag{1.1}$$

Here $\nu^s = \omega^s / 2\pi$ is the frequency of the scattered radiation, O_b, is the *beam overlap*, which accounts for the overlap of the probe and receiver beam patterns (discussed further in Subsection 1.5), λ_0^i is the vacuum wave length of the incident probe radiation, r_e the classical electron radius, n_e the electron density, and Σ the *scattering function*, which accounts for the spectral variations in the microscopic fluctuations that give rise to scattering, and the spectral variations in the coupling of the incident probe field via the bilinear interaction with the fluctuations into the received scattered field. The scattering function gives rise to most of the spectral variation in the received scattered power density and accounts the fast ion information contained in this scattered radiation. The scattering function is discussed further in Subsection 1.4 and in Appendix B.

1.4 Scattering function and collective fluctuations

Scattering of incident radiation at the electron plasma frequency or higher is principally due to microscopic fluctuations in the electron density, electron flux (first two moments of the electron velocity distribution), magnetic field and electric field. In many situations scattering off electron density fluctuations dominates. The received scattered radiation emanates from the region where the probe and receiver beam patterns overlap (the *scattering volume*). The received scattered radiation with frequency ν^s has the wave vector $\mathbf{k}^s$ in the scattering volume. Received scattered radiation at this frequency is due to scattering of the probe radiation by the Fourier component of the microscopic fluctuations characterized by the frequency

$$\nu^\delta = \nu^s - \nu^i \tag{1.2}$$

and wave vector

$$\mathbf{k}^\delta = \mathbf{k}^s - \mathbf{k}^i \,, \tag{1.3}$$

where $\nu^i = \omega^i / 2\pi$ is the frequency of the incident probe radiation and $\mathbf{k}^i$ is its wave vector in the scattering volume.

The discrete natures of ions and electrons both give rise to microscopic fluctuations in the electron distribution and in the electric and magnetic fields. When considering the frequency spectra of scattered radiation, the scattering resulting from the fluctuations driven by ions and by electrons are referred to as the *ion feature* and *electron feature* respectively. The ion feature is further split into the *bulk ion feature* and *fast ion*

feature. The electron feature extends throughout the frequency window where the fast ion feature exists, but the fast ion feature dominates when the wave length of the resolved Fourier component of the fluctuations is much longer than the Debye length, λ_D ; that is when

$$k^{\delta}\lambda_D << 1, \tag{1.4}$$

where $k^{\delta} = \left|\mathbf{k}^{\delta}\right|$. In this regime the microscopic fluctuations can be described as *collective fluctuations* induced by the motion of discrete charges. Condition (1.4), the condition that the detected fluctuations be collective, sets an upper limit on the scattering angle, θ ,

$$\theta = \angle\left(\mathbf{k}^{\mathrm{i}}, \mathbf{k}^{\mathrm{s}}\right), \tag{1.5}$$

which becomes more severe as the probe frequency increases. Examples of the relative contributions of electrons, bulk ions and fast ions to the CTS scattering functions [4], Σ , are shown in Figure 1 through Figure 3. Figure 1 is for a probe frequency of 60 GHz and forward scattering; Figure 2 is for the same frequency but now in a back scattering geometry. At this probe frequency there is no limitation on the usable scattering angles in ITER due to condition (1.4).

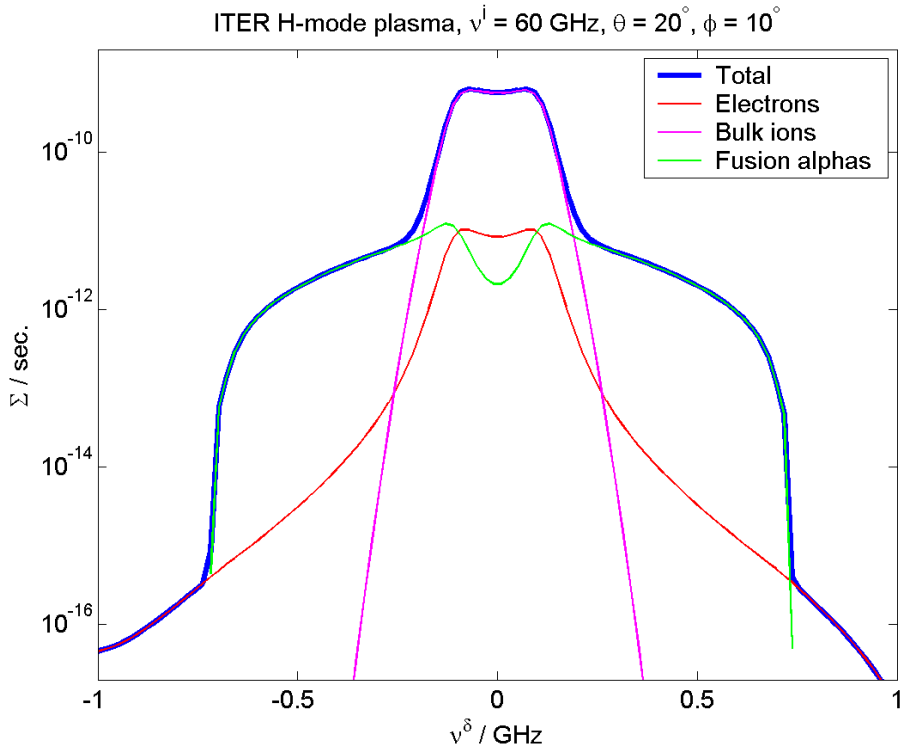

Figure 1. CTS scattering function, Σ , as a function of resolved fluctuation frequency, $\nu^{\delta} = \nu^{s} - \nu^{i}$. Here the probe frequency is $\nu^{i} = 60$ GHz, scattering angle $\theta = \angle(\mathbf{k}^{i},\mathbf{k}^{s}) = 20^{\circ}$, and fluctuation angle $\phi = \angle(\mathbf{k}^{\delta},\mathbf{B}) = 10^{\circ}$. The incident and received scattered radiations are both in X-mode. The plasma is a reference H-mode ITER equilibrium with, $B = 5.3\ \mathrm{T}$, $n_e = 1\times10^{20}\ \mathrm{m}^{-3}$ and $T_e = T_i = 25$ keV (see Appendix A). The fusion alpha density is $n_{\alpha} = 5\times10^{17}\ \mathrm{m}^{-3}$. The fusion alphas are assumed to have a classical slowdown distribution. The figure shows the total scattering function (fat blue curve), the

electron contribution (thin red curve), bulk ion (thin magenta curve) and fusion alpha (thin green curve) contributions.

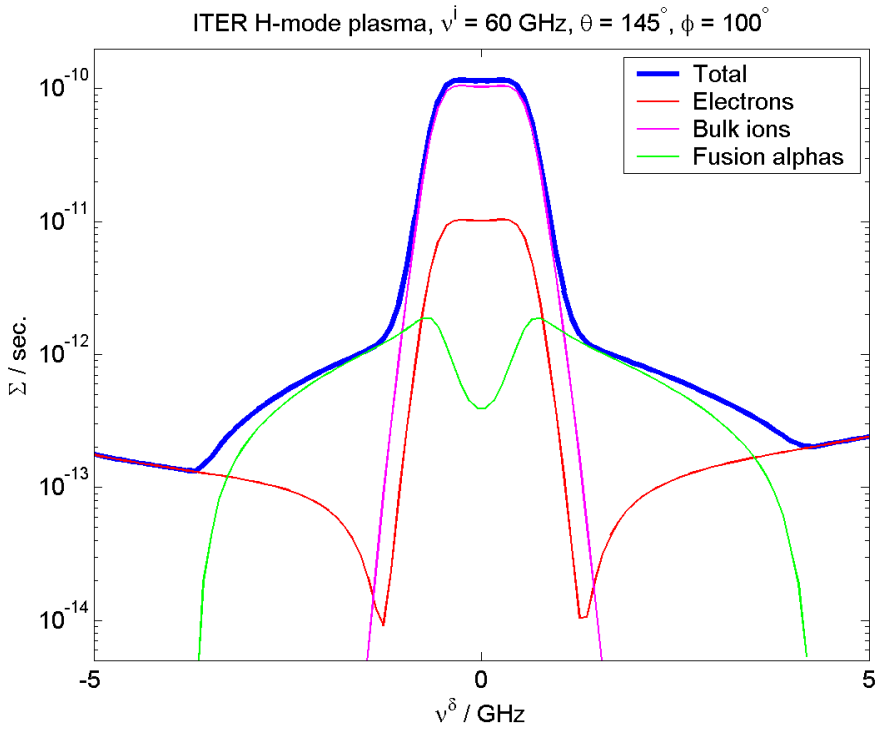

Figure 2. CTS scattering function, Σ, for the same plasma as in Figure 1. Here the probe frequency is again $\nu^i = 60$ GHz, but $\theta = 145°$, $\phi = 100°$.

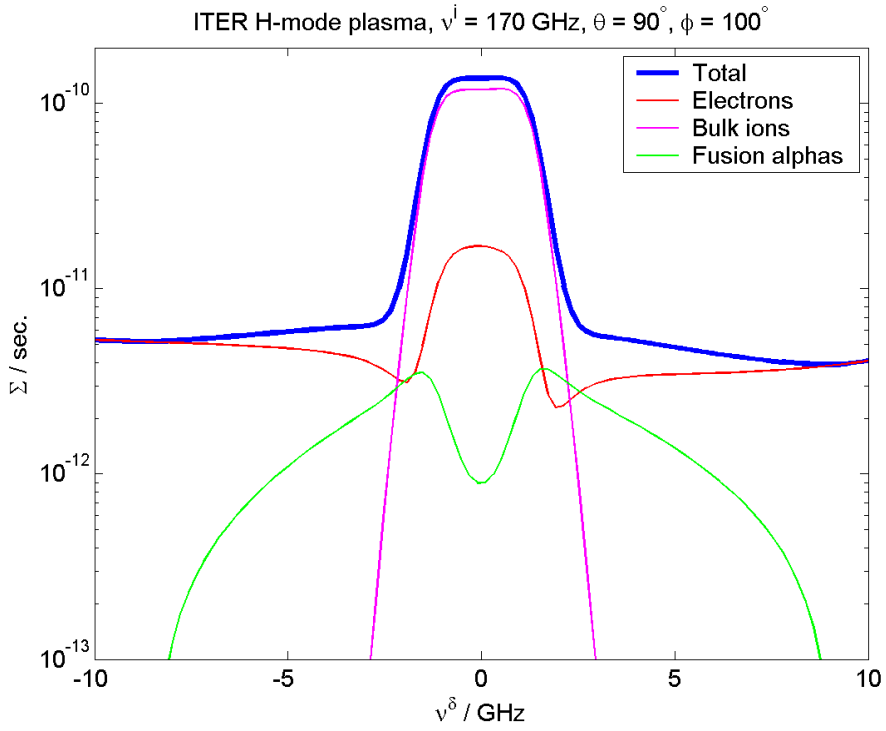

Figure 3. CTS scattering function, Σ, for the same plasma as in Figure 1. Here the probe frequency is $\nu^i = 170$ GHz, $\theta = 90°$, $\phi = 100°$.

At the higher probe frequency of 170 GHz the fast ion feature is at or below the electron feature for a scattering angle of 90 degrees, as shown in Figure 3. This makes it more difficult to extract information about the fast ion distribution from the spectra. At 170 GHz a scattering angle in the range of 30 degrees would bring the fast ion feature well above the electron feature, providing a more suitable geometry for CTS at 170 GHz. At 3 THz and 28 THz scattering angles of the order of 3 to 4 degrees and 0.3 to 0.4 degrees would be appropriate (see Appendix B).

A CTS spectrum carries information about the distribution of ion velocity components along $\mathbf{k}^{\delta}$; that is it resolves the one-dimensional velocity distribution

$$f^{(1)}(u) = \int \delta\left(u - \mathbf{v}\cdot\mathbf{k}^{\delta}/k^{\delta}\right) f(\mathbf{v}) d\mathbf{v}\,. \tag{1.6}$$

To resolve anisotropy in the fast ion distribution it is necessary to resolve the 1-D distribution along a number of different directions relative to the static magnetic field, which implies recording CTS spectra for different values of the *fluctuation angle* $\phi = \angle\left(\mathbf{k}^{\delta}, \mathbf{B}\right)$. As a general design objective we would seek to resolve the fast ion velocity components near parallel and near perpendicular to the magnetic field, corresponding to ϕ near 0° (or 180°) and near 80° or 100°. We avoid choosing ϕ in the range close to 90° for several reasons; principal among them is that in this range the fast magneto-sonic wave (FMS) enters the spectrum, giving rise to a near singular spectral response at the fluctuation frequency satisfying the FMS wave's dispersion relation [4]. The frequency of the FMS is very sensitive to the component of the wave vector parallel to the magnetic field. With finite beam width the resolved fluctuations necessarily contain a distribution of wave vector components parallel to B. The received spectrum is thus the convolution of a peaked function with the distribution of resolved wave vectors. Spectral features could thus be accounted for by details in the beam patterns of probe and receivers, making it impossible to make inference about the fast ion distribution without detailed and reliable modelling of the beam distributions after propagation through the plasma. Such modelling is not currently available.

For more details on the scattering function, the electron and fast ion features, and their dependencies on probe frequency, scattering angle and resolved direction, please refer to Appendix B.

1.5 Beam overlap and scattering volume

Radiation is scattered all along the probing beam. The intensity of the scattered radiation emanating from a spatial region is proportional to the intensity of the probe in that region. The receiver only collects scattered radiation from the region, which falls within the receiver beam pattern. The received signal resulting from radiation emanated from a given region is weighted by the intensity of the receiver beam in that region. The net result is that the contribution to the received CTS signal from the fluctuations in a given spatial region is weighted by the product of the intensity of the probe and receiver beams in that region [5,6]. It is convenient here to introduce a *normalized beam intensity*, *I*, which is normalized such that its integral over the beam cross section is one. In transmitting mode the normalized beam intensity is defined as

$$I = P \Big/ \int_A P da, \tag{1.7}$$

where P is the power per unit cross sectional area in the beam and the integral is over the beam cross section. The CTS system thus measures the plasma fluctuations spatially weighted by the product of normalized beam intensities, $I^{\mathrm{i}}I^{\mathrm{s}}$. It is this weighting that ensures that the measurement is spatially localized. The received CTS signal is proportional to the spatial integral of $I^{\mathrm{i}}I^{\mathrm{s}}$. This integral is called the *beam overlap* [7], O_b,

$$O_b = \int_V I^{\mathrm{i}} I^{\mathrm{s}} d\mathbf{r}. \tag{1.8}$$

O_b accounts for the effects of the widths of the probe and receiver beam patterns and the extent to which they overlap in the plasma. As a measure of the spatial localisation of the measurement we define the *scattering volume*, V_{scat}, as the spatial region from which 90% of the received scattered radiation comes and which has the smallest volume,

$$V_{\mathrm{scat}} = V' \text{ for which } \int_{V'} I^{\mathrm{i}} I^{\mathrm{s}} d\mathbf{r} = 0.9 \times O_b \text{ and } \int_{V'} d\mathbf{r} \text{ is smallest.} \tag{1.9}$$

The smallest volume implies that the limit of the scattering volume follows a surface on which the weighting function, $I^{\mathrm{i}}I^{\mathrm{s}}$, is constant (an iso-surface). The finite extent of the spatial weighting function implies a finite resolution of the wave vector $\mathbf{k}^{\delta}$ of the fluctuations. The measurement is a convolution of the Fourier components of the fluctuations with the distribution, $f_{\mathbf{k}}$, of resolved wave vectors, $\mathbf{k}^{\delta}$. The distribution $f_{\mathbf{k}}$ is the Fourier transform of the weighting function $I^{\mathrm{i}}I^{\mathrm{s}}$.

We now consider the case of Gaussian beams uniform in the scattering region, which is discussed in some detail in Appendix C. The beam intensities can be approximated as normal distributions with infinite variance along the beams. The beam characteristics (orientation and widths) can be summed up in their inverse covariance matrices, α^{i} and α^{s}. The weighting function is a normal distribution with inverse covariance $\alpha = \alpha^{\mathrm{i}} + \alpha^{\mathrm{s}}$. Iso-surfaces of the weighting function, $I^{\mathrm{i}}I^{\mathrm{s}}$, identified by the parameter s, are given by

$$r_i \alpha_{ij} r_j = 4s^2 \tag{1.10}$$

where $\mathbf{r}$ is the spatial coordinate relative to the peak of the weighting function, which is also the centre of the scattering volume. The iso-surface, corresponding to $s = 1$, is tangent to the Gaussian half widths[3] of the probe and receiver beams when viewed in the beam plane[4] projection (see Figure 4), and encloses the volume from which 75% of the scattering comes. The iso-surface corresponding to $s = 1.23$ encloses the volume from which 90% of the scattering comes, and thus defines the scattering volume.

For Gaussian beams, uniform in the scattering region, the expression for beam overlap, O_b, simplifies to

[3] The Gaussian half width is defined as the distance from the beam centre to the point where the beam intensity is down to $1/e^2$ of the peak value. We refer to half widths rather than radii because we consider non-circular beam cross sections.

[4] The *beam plane* is the plane that includes the centre of the scattering volume and is spanned by the direction vectors of the incident probe beam and the receiver beam in the region where the two beams intersect.

$$O_b = \frac{1}{\left|\sin(\theta)\right|} \frac{2}{\sqrt{2\pi\left(\left(w_{\mathrm{n}}^{\mathrm{i}}\right)^2 + \left(w_{\mathrm{n}}^{\mathrm{s}}\right)^2\right)}} \exp\left(-\frac{2\Delta n^2}{\left(w_{\mathrm{n}}^{\mathrm{i}}\right)^2 + \left(w_{\mathrm{n}}^{\mathrm{s}}\right)^2}\right). \qquad (1.11)$$

Here θ is the scattering angle, w_n^{i} and w_n^{s} are the Gaussian half widths of the probe and receiver beams in the direction orthogonal to the beam plane, while Δn is the shortest distance between the beam centre lines. The distribution of resolved wave vectors, $f_{\mathbf{k}}$, is a normal distribution with inverse covariance matrix, $\alpha^k = \alpha^{-1}$. Two examples of the weighting functions, scattering volumes and resolved wave vector distributions are given in Figure 4.

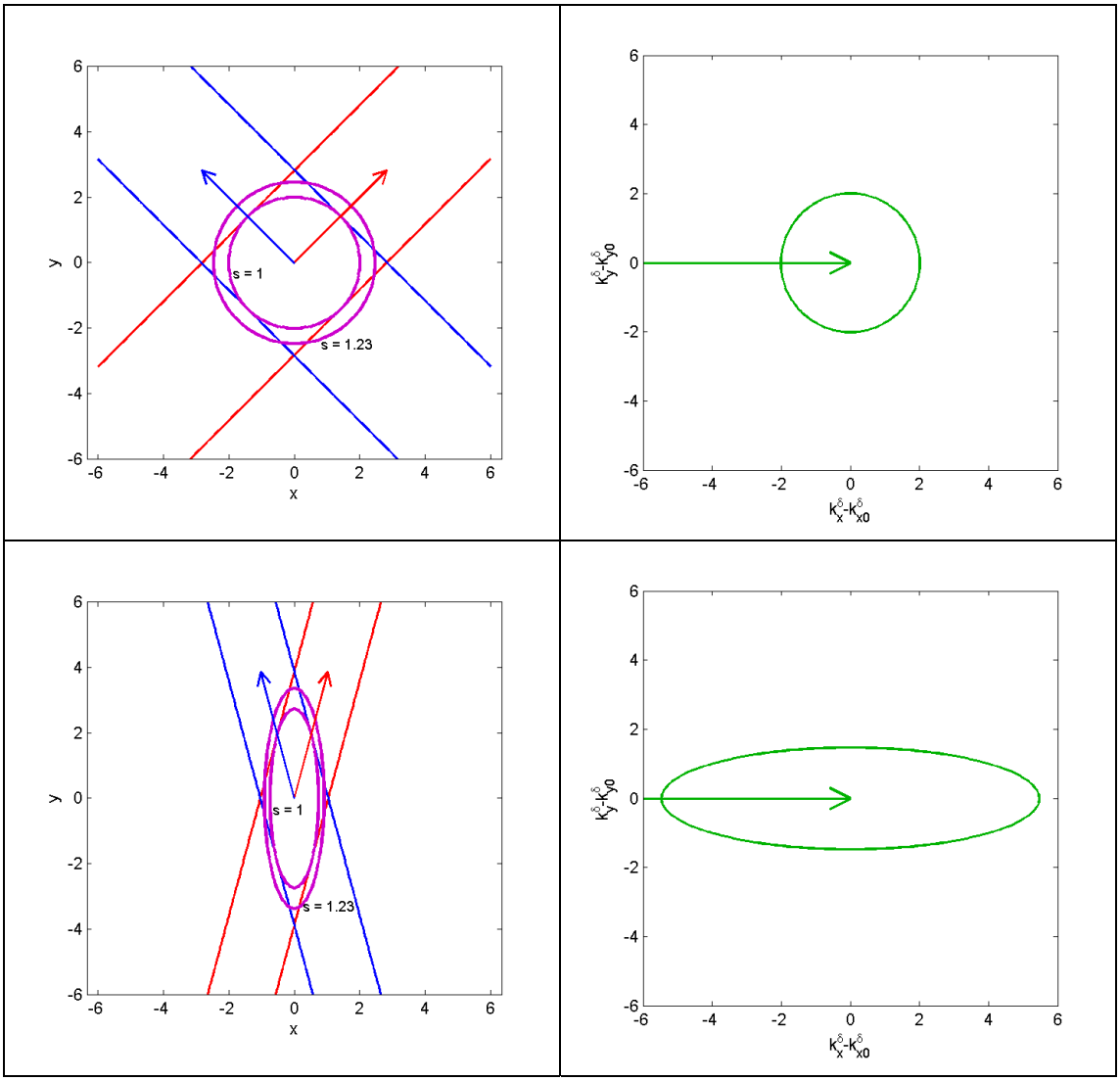

Figure 4. Left plots show the Gaussian widths of probe and receiver beams (red and blue lines) and contours of the CTS weighting function at $s = 1$ and s = 1.23, where s refers to Equation (1.10). The latter contour encloses the region from which 90% of the CTS signal comes and thus is a useful definition of the *scattering volume*. The right plots show a contour of the corresponding distribution of resolved fluctuation wave vectors, $f_{\mathbf{k}}$. At the contour the value of $f_{\mathbf{k}}$ has dropped to $1/e^2$ of its peak value, i.e. 2 standard deviations off the

location of the peak. The scattering angle is 90° in the upper plots and 30° in the lower plots.

From expression (1.11) it is clear that the beam overlap, and hence the CTS signal, is maximized by having the beam centres intersect, i.e. $\Delta n = 0$, by minimising the beam widths in the direction orthogonal to the beam plane and by minimising $\sin(\theta)$. Minimising $\sin(\theta)$ results in a long scattering volume and hence reduces the spatial resolution. It is noteworthy that the beam overlap does not depend on the beam distributions in the beam plane. Distributions in these directions do affect the spatial resolution. Reducing the beam widths in the plasma may require focussed beams with their waists in the plasma. The smaller the waist in the plasma is the larger the required aperture at the reactor vessel wall becomes. For a given aperture and frequency there is a lower limit to beam size that can be projected a given distance from the aperture. Figure 5 shows a set of 60 GHz beams which could be produced through an aperture of 30 cm.

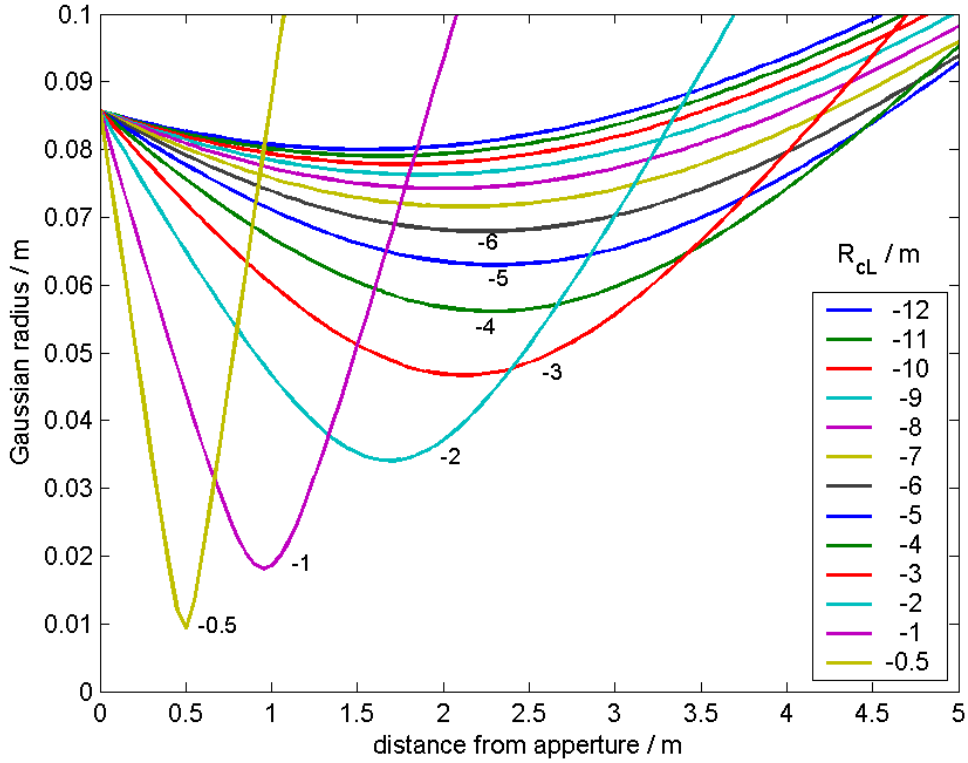

Figure 5. Gaussian half widths (where the field is 1/e of the peak value, in the plot labelled Gaussian radius) of Gaussian beams at 60 GHz emanating from a common aperture, but with different phase front radii of curvature, R_{cL}. For a Gaussian half width of 8.5 cm the required aperture would be just under 30 cm.

In particular it shows that a Gaussian half width on the order of 6 cm could be achieved over a wide range of the plasma cross section.
We need to ensure robustness of the beam overlap against alignment uncertainties and variable refraction. This may increase the optimum beam widths orthogonal to the beam plane above the minimum widths achievable with the maximum permissible aperture. Assume that despite alignment uncertainties, perfect intersection was

achieved for a given plasma and a given receiver frequency. The receiver needs to maintain overlap over the full frequency range of the CTS spectrum. Refraction varies with frequency; that is we have finite *dispersion*. The beams need to be wide enough that overlap is maintained at both frequency ends of the fast ion CTS spectrum.
To ensure a finite scattering volume, the probe and receiver beams would not generally follow the same trajectories. As a consequence their trajectories would be refracted differently by changes in the plasma refractive index, principally caused by changes in electron density. Again the beam widths need to be wide enough that density variations do not cause loss of overlap. Even if the CTS system has beam steering, there are density variations on time scales that are too short to be compensated for by steering.
Another lower limit on the beam widths comes from the need to achieve a certain resolution in velocity space. To first order the relative resolution in velocity space equals that in wave vector space, that is $\delta v / v = \delta k^{\delta} / k^{\delta}$. As a practical measure we will use 2 standard deviations in the distribution of wave vectors, $f_{\mathbf{k}}$, as an indication of the resolution of k^{δ}. The narrower the beams the wider $f_{\mathbf{k}}$ becomes and hence the coarser the velocity space resolution. The finite width of $f_{\mathbf{k}}$ also results in a finite distribution of $\phi = \angle\left(\mathbf{k}^{\delta}, \mathbf{B}\right)$, the consequences of which were discussed in Subsection 1.4 for geometries where ϕ is near 90°.
To illustrate the preceding considerations of beam size, beam overlap, scattering volume and wave vector resolution, we trace Gaussian beams in a reference ITER H-mode plasma (see Appendix A) and compute these quantities. In Figure 6 we plot the results for a 60 GHz CTS in back scattering geometry, corresponding to having both probe and receiver antennae in a mid-plane port. In the scattering region the beam Gaussian half widths in the beam plane are both 8 cm. These widths are kept close to the minimum of 6 cm to minimize the radial extent of the scattering volume, which is 43 cm. The Gaussian half widths orthogonal to the beam plane are 15 cm, well above the achievable minimum, to increase robustness. The resulting beam overlap at negligible distance between beam centres is O_b = 6.7 m^{-1}. Dispersion reduces the overlap at the spectral limits of the fast ion feature to respectively 4.2 m^{-1} and 5.7 m^{-1} at 55 GHz and 65 GHz. From the distribution of resolved wave vectors we find that two standard deviations in the modulus of the fluctuation wave vector, normalized by the mean modulus of the wave vector, is $2\sigma\left(k^{\delta}\right)\big/k^{\delta} = 1.2\times10^{-2}$, implying that the wave vector resolution is not of consequence to the velocity resolution in this system. The resolution of fluctuation direction is on the order of $2\sigma\left(\phi\right) = 1.1°$, which would be of consequence if ϕ were near 90°. Here ϕ = 100˚, which is sufficiently far from 90˚ to keep the CTS spectrum free of the fast magneto-sonic wave discussed in Subsection 1.4.

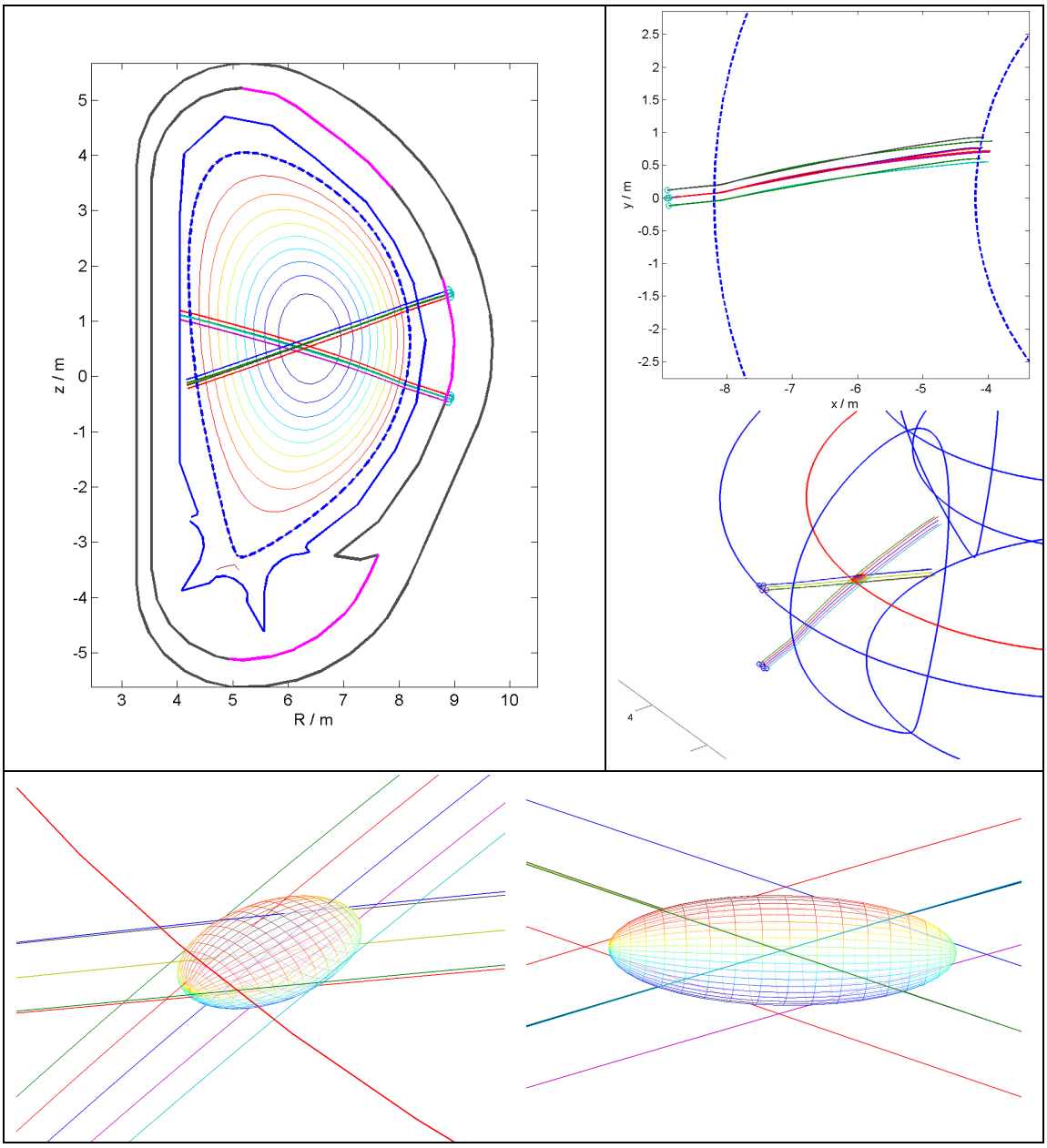

Figure 6. Beam traces for the reference ITER equilibrium (see Figure 1). $\nu^i = \nu^s = 60$ GHz. Both probe and receiver antennae are on the low field side. The Gaussian beams are represented in the plots by 5 rays; the beam centre and 4 beams displaced 1 Gaussian half width from the centre. The top left plot shows the poloidal map of the beams, the normalized flux surface contours of the plasma and outlines of the first wall and vacuum cessel. Top right shows a top view of the beams and plasma limits. In the middle right plot and in the two lower plots the ellipsoidal outlines of the scattering volume are shown as semi-transparent nets. The bottom right plot shows the beams and scattering volume in the beam plane projection. In the scattering region the beam Gaussian half widths in - and orthogonal to the beam plane are respectively 8 cm and 15 cm, $\theta = 145°$, $\phi = 100°$. The radial extent of the scattering volume is 43 cm. $\sigma\left(k^\delta\right)/k^\delta = 6\times10^{-3}$, $\sigma(\phi) = 0.6°$, $O_b = 6.7$ m^{-1}.

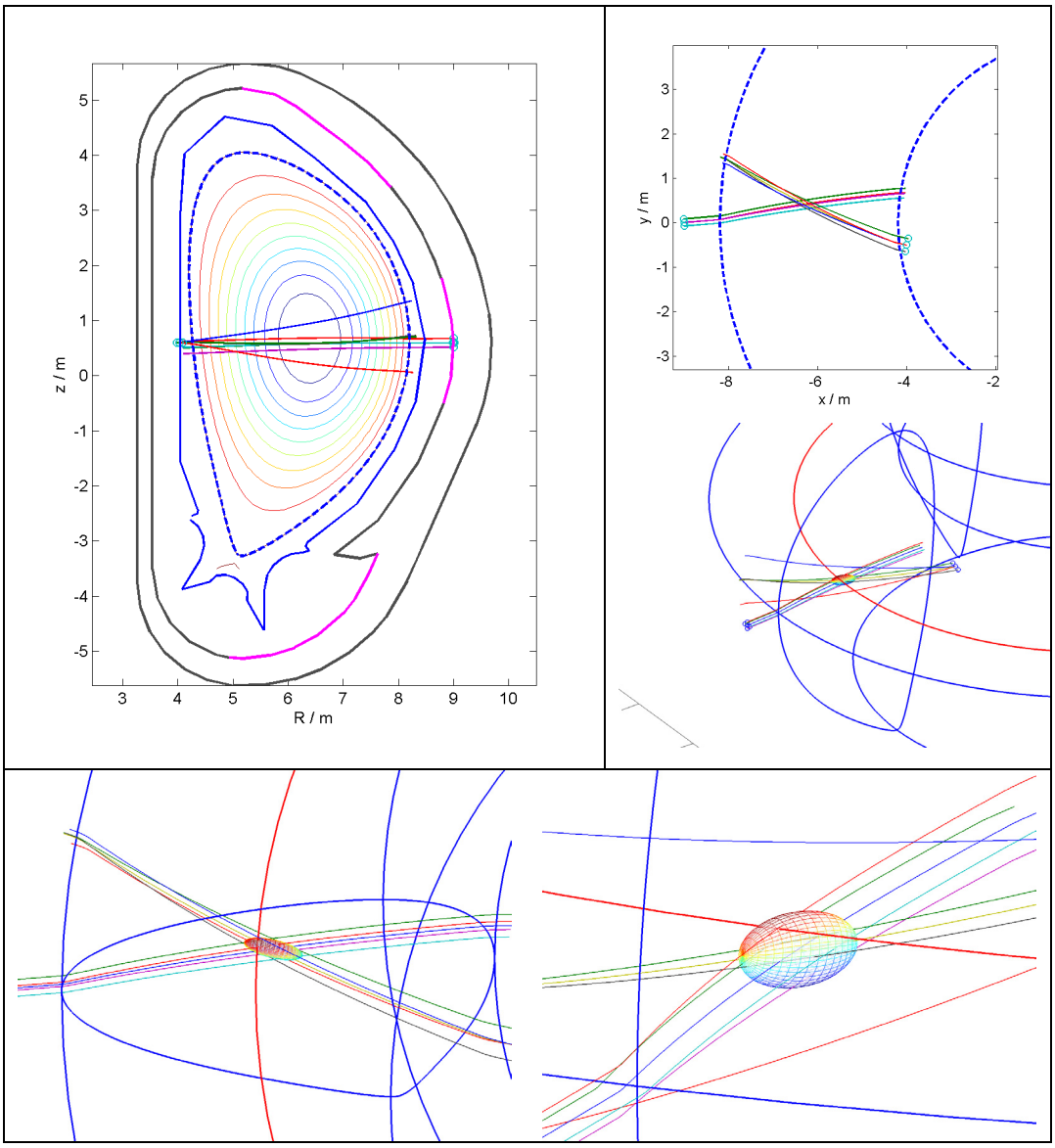

Figure 7. As in Figure 6, only here for a forward scattering geometry with the receiver on the high field side. The receiver beam is diverging in the vertical direction to reflect the limited vertical aperture permitted on the high field side. The Gaussian half widths orthogonal to the beam plane are 10 cm for the probe and 34 cm for the receiver in the scattering region. In the beam plane the beam half widths are 9.5 cm and 8.4 cm for probe and receiver respectively. Here $\theta = 25.5°$, $\phi = 174°$. The radial extent of the scattering volume is 55 cm. $\sigma\left(k^{\delta}\right)/k^{\delta} = 0.067$, $O_b = 3.94$ m^{-1}.

In Figure 7 we show an example of the scattering geometry achievable with 60 GHz in a forward scattering geometry with the receiver on the high field side. The receiver beam pattern has a Gaussian half width opening angle of 7° in the vertical direction due to the limited vertical aperture available on the high field side. This widens the receiver beam pattern in the direction orthogonal to the beam plane, reducing the beam overlap but improving the robustness. The beam overlap is nearly constant at $O_b = 3.94$ m^{-1} throughout the spectral range of the fast ion feature which for this

forward scattering geometry extends only 800 MHz on either side of the probe (see Figure 1). The radial extent of the scattering volume is 55 cm. The relative resolution of the wave vector is $2\sigma\left(k^{\delta}\right)/k^{\delta} = 0.13$, which represents a lower limit on the relative velocity resolution. Unlike in the back scattering case, this limit is of practical consequence here. The number of velocity space points (or bins), N_v, which can be resolved each side of zero velocity is given by

$$N_v = \frac{k^{\delta}}{2\sigma\left(k^{\delta}\right)} \log\left(\frac{\nu^{\delta}_{\alpha\max}}{\nu^{\delta}_{\alpha\min}}\right). \tag{1.12}$$

Here $\nu^{\delta}_{\alpha\max}/\nu^{\delta}_{\alpha\min}$ is the ratio between the upper and lower frequencies where the fast ion feature dominates the spectrum on either side of the probe. From Figure 1 we find that this ratio is 0.8 GHz / 0.2 GHz = 4, so in the forward scattering geometry we can typically resolve N_v= 10 points logarithmically spaced in the counter direction and 10 points in the co direction.

In Figure 8 we consider a scattering geometry for 170 GHz and right angle scattering, with the beams focussed as tightly as possible with a 30 cm aperture to maximize the beam overlap. For this geometry we find a beam overlap of 18.6 m^{-1}. Dispersion is small, but with these narrow beams accurate beam alignment is required.

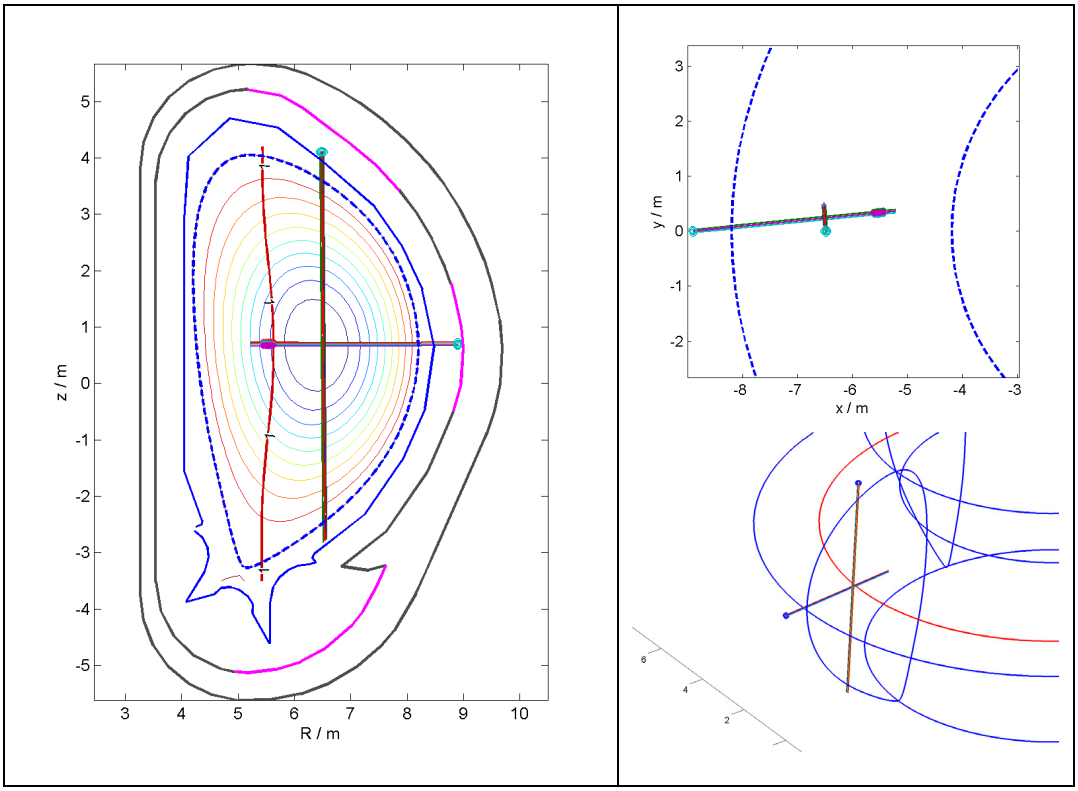

Figure 8. As in Figure 6, only here for 170 GHz and right angle scattering. The probe is injected from a mid-plane port while the receiver is in an upper port. The Gaussian radii of the beams in the scattering region are all 3 cm. Here $\theta = 90°$, $\phi = 97.6°$. The radial extent of the scattering volume is 7.4 cm. $\sigma\left(k^{\delta}\right)/k^{\delta} = 0.013$, $O_b = 18.6$ m^{-1}.

In Table 4 we sum up the relations between probe frequency, scattering geometry, beam overlap, spatial resolution and wave vector resolution, including also

considerations for 3 THz and 28.28 THz. For the latter two frequencies the Gaussian beam width has been reduced to 1 cm. Though even smaller beam widths could be achieved with reasonable apertures, the need to have a finite wave vector resolution and hence velocity space resolution, makes significant further reduction in the beam widths undesirable.

ν^{i}	60 GHz	60 GHz	170 GHz	170 GHz	3 THz	28 THz
θ	25.5°	145°	90°	90°	4°	0.4°
$w_b^{\mathrm{i}}/\mathrm{cm}$	9.5	8	3	6	1	1
w_b^{s}/cm	8.4	8	3	6	1	1
$w_n^{\mathrm{i}}/\mathrm{cm}$	10	15	3	6	1	1
w_n^{s}/cm	34	15	3	6	1	1
O_b / m^{-1}	3.9	4.2	18.6	9.4	809	8082
ΔR /cm	55	43	7.4	14.8	n/a	n/a
$\Delta_{\max}$ /cm	55	43	7.4	14.8	50	500
$k^{\delta}/2\sigma_y^k$	7.8	83	37.8	75.6	7.8	7.3

Table 4. Set of scattering geometries and associated linear extents of the scattering volume and standard deviations of the distribution of resolved wave vectors. Here w_b^{i} and w_b^{s} are the beam Gaussian half widths in the beam plane while w_n^{i} and w_n^{s} are the widths orthogonal to the beam plane. ΔR is the radial extent of the scattering volume (where n/a is entered for this quantity several orientations of the scattering volume can be considered, implying ΔR can take a range of values). $\Delta_{\max}$ is the largest extent of the scattering volume. The remaining parameters have been defined in the preceding text.

1.6 Spectral power density

By means of the equation of transfer for a CTS system, Equation (1.1), we compute the spectral power densities of the received CTS signals for the considered systems. In the computations we use the reference ITER plasma (see Appendix A) with a fast ion density up to 5×10^{17} m^{-3}. We cover the range of probe frequencies and geometries discussed in the previous subsection. Figure 9 and Figure 10 show the CTS spectra for a 60 GHz probe and, respectively, forward and back scattering geometries. Figure 11 to Figure 13 cover the systems with probes at 170 GHz, 3 THz and 28 THz.
The spectral sensitivity to the fast ion population is brought out by plotting the spectra corresponding to different fast ion densities. The spectral power densities are in units of received power per unit frequency interval (eV) and thus assume a specified incident power in the probe and specified value for the beam overlap. For the 60 GHz and 170 GHz systems we assume 1 MW incident power. Long pulse sources at this power can safely be assumed to be available. In the far infra red (FIR) range of 3 THz the sources we consider are optically pumped lasers, for instance a D_2O laser pumped by a CO_2 laser. We will assume 600 ns pulses at energies of 6 Joules, requiring 200 Joules in the CO_2, giving a FIR power of 10 MW. We will assume a repetition rate of 10 Hz. This is probably achievable but will require significant engineering development. At infra red (IR) frequency of 28 THz we assume a CO_2 laser with pulse energies of 100 Joules in 1 μs corresponding to 100 MW, with a 10 Hz

repetition rate. This too is a source at the edge of technology. For all the systems we assume the beam overlap values given in Table 4. With increasing frequency the beam overlap increases, due to increasing focussing of the beams and reduction in scattering angle. Despite this the spectral sensitivity to fast ions, per unit incident power decreases with frequency, in other words the scattering cross section drops significantly with increasing frequency.

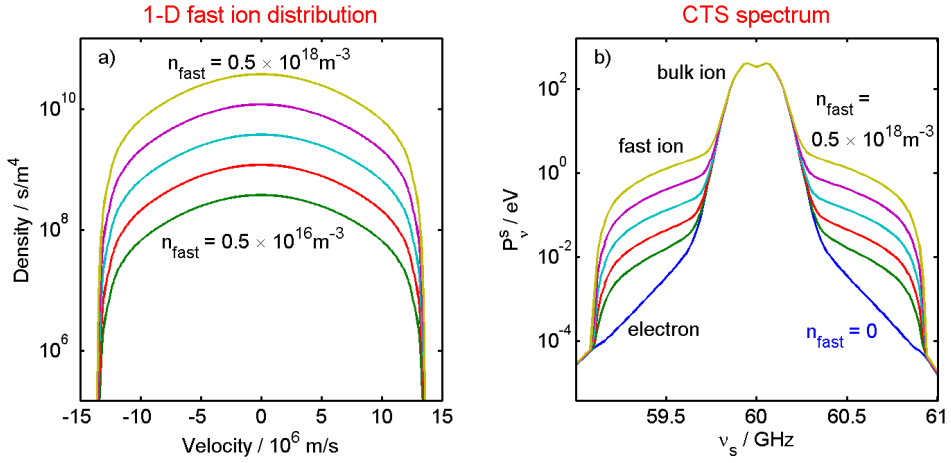

Figure 9. CTS spectral power densities (right) for a range of fast ion densities (left) (Note here we consider both densities and phase space densities, where the latter is the number of particles per unit volume and per unit 1-D velocity, and hence has units of s/m^4). The plasma is the reference ITER plasma (Appendix A). Here $\nu^i = 60$ GHz, $\theta = 25°$, $\phi = 10°$, $P^i = 1$ MW, $O_b = 3.9$ m^{-1}. The fast ion density is varied in the range 5×10^{17}m^{-3} to 0 m^{-3} (5×10^{17}m^{-3} to 5×10^{15}m^{-3} in equally spaced logarithmic steps). The spectral variation due to the fast ion population is on the order of 2 eV.

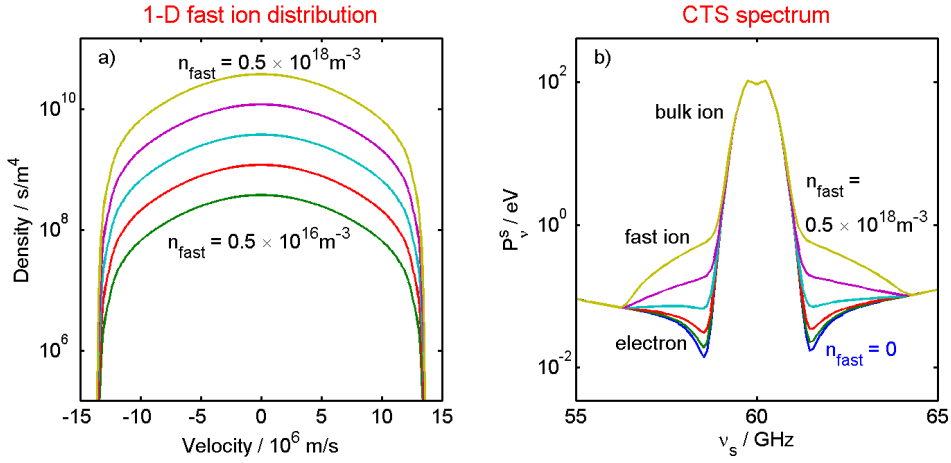

Figure 10. As Figure 9 only here, $\theta = 145°$, $\phi = 100°$, $O_b = 4.2$ m^{-1}. The spectral variation due to the fast ion population is on the order of 0.5 eV.

For the 60 GHz systems we find a spectral fast ion sensitivity on the order of 1 eV. This drops to 0.2 eV for the 170 GHz system. While the fast ion feature is several orders of magnitude greater than the electron feature for 60 GHz systems, this is not the case for the 170 GHz system where the electron feature is on the order of 1 eV, which makes extracting the fast ion information more delicate. The spectral power density of the fast ion feature is to be seen against the noise background. At 60 GHz we are below the ECE spectrum, so background emission (ECE) from the plasma will generally be well below 200 eV. In the 60 GHz range the receiver noise temperature at the antenna can generally be assumed to be around 10 eV.
In contrast to the situation at 60 GHz, at 170 GHz the fundamental electron cyclotron resonance will be in the plasma causing an ECE background of anywhere from 3 or 4 keV up to the peak electron temperature in the plasma (25 keV in the reference plasma). As a first figure of merit, with which to compare systems, we might consider the fast ion signal to noise ratio in a channel covering the entire fast ion feature on one side of the probe frequency, and integrated for a *probe on time* of $\tau = 20$ ms. An actual system will of course resolve the spectrum into many channels. For the 60 GHz systems, where the fast ion feature covers 0.7 GHz (forward scattering) and 3 GHz (back scattering) the signal to noise ratios of such a single channel would be on the order of 37 (forward scattering) and 19 (back scattering). For the 170 GHz system, where the fast ion feature covers 6 GHz, the signal to noise ratio would be on the order of 0.7 with the most optimistic noise temperature of 3 keV.

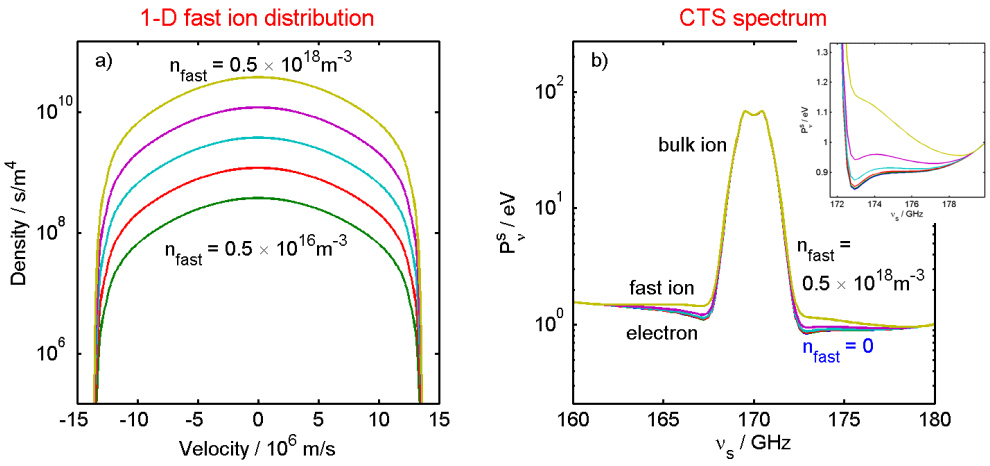

Figure 11. As Figure 9 only here, $\nu^i = 170$ GHz , $\theta = 90°$, $\phi = 100°$, $O_b = 18.6$ m^{-1} . The inset zoomed plot of the spectrum on a linear scale shows that the spectral variation due to the fast ion population is on the order of 0.2 eV.

At 3 THz, considered in Section 4, we are in the upper tail of the ECE spectrum. The background plasma emission is in the range 0.1 to 10 eV. Assuming cooled receiver and great attention to minimising transmission losses, the antenna noise temperature may be brought down to on the order of 2 eV, which is to be compared with the fast ion feature spectral power density on the order of 0.4 eV. Here the fast ion feature has a spectral bandwidth of 5 GHz on either side of the probe giving a signal to noise ratio of 11 in a channel covering the entire feature and being integrated for 600 ns.

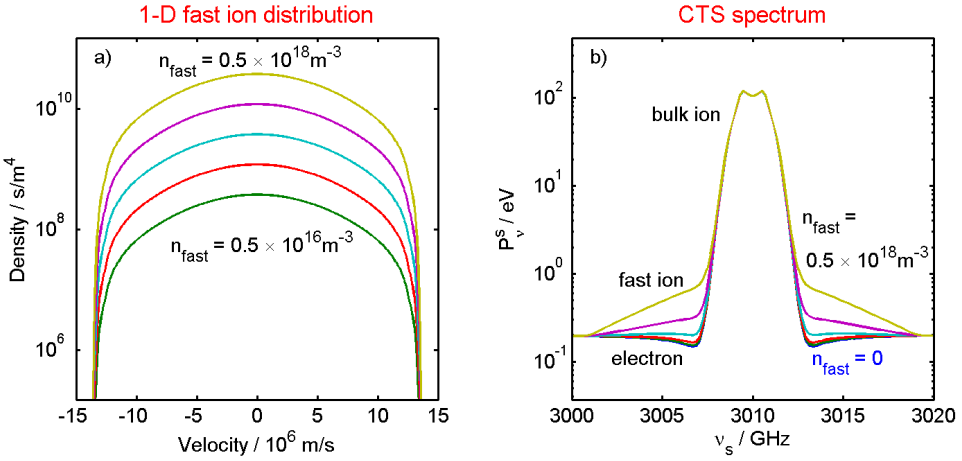

Figure 12. As Figure 9 only here, $\nu^{\mathrm{i}} = 3$ THz, $\theta = 4°$, $\phi = 10°$, $P^{\mathrm{i}} = 10$ MW, $\tau = 600$ ns, $E^{\mathrm{i}} = 6$ Joule, $O_b = 800$ m^{-1}. The spectral variation due to the fast ion population is on the order of 0.4 eV.

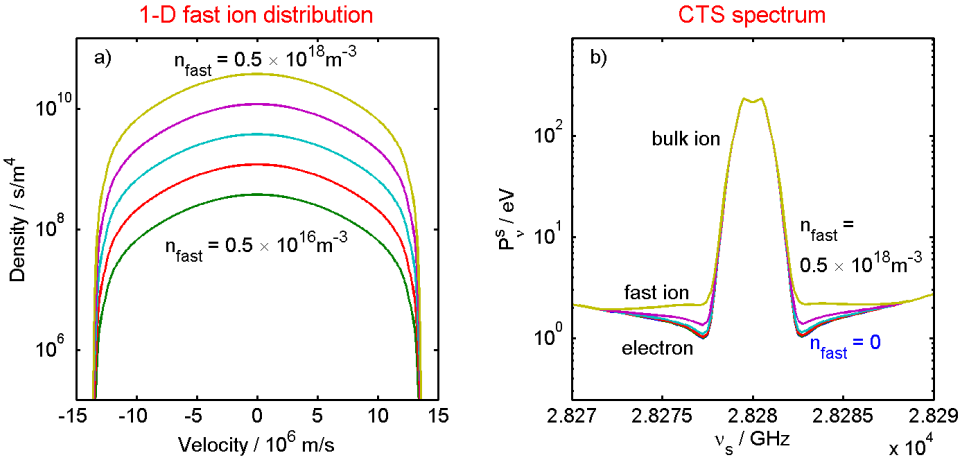

Figure 13. As Figure 9 only here, $\nu^{\mathrm{i}} = 28.28$ THz, $\theta = 0.4°$, $\phi = 100°$, $P^{\mathrm{i}} = 100$ MW, $\tau = 1$ μs, $E^{\mathrm{i}} = 100$ Joule, $O_b = 8000$ m^{-1}. The spectral variation due to the fast ion population is on the order of 1 eV.

The IR CO_2-laser based system, considered in Figure 13, benefits from negligible plasma emissions, so we can assume a noise of 5 eV stemming from the receiver. The best signal to noise ratio is achieved by operating this probe at a pulse power where the spectral power density of the signal is approaching the noise level. We assumed a pulse length of 1 μs. It is not realistic to expect pulse rates above 10 Hz at pulse energies of 100 Joules so when comparing with the other systems we cannot benefit here from averaging over several pulses. As a consequence the integration time is that of a single pulse, set here to $\tau = 1$ μs, without yielding a better time between measurements than in the other systems. The same holds for the 3 THz system. With a fast ion bandwidth of approximately 7 GHz the fast ion signal to noise ratio for the IR

system comes out at approximately 17. It should be emphasised that this single channel signal to noise ratio is just a crude means of comparing the diagnostic capabilities of the different systems. A more refine measure of the fast ion information, which can be extracted from the different systems, follows in the next subsection.

1.7 Accuracy of inferred fast ion distribution

From the CTS spectra estimates of the fast ion distribution can be inferred. The distribution is conceptually a continuous function. On the basis of the measurements, we can estimate the value of this function at a finite set of nodes. Effectively the value at each node is the average value of the continuous function over an interval centered on the node and with a width corresponding to the distance between nodes. We will refer to such intervals as *velocity bins.* We will assume that the spectra are resolved in a sufficient number of channels that the discreteness of the spectral channels does not significantly reduce the information content of the spectrum. The number of nodes, with which we resolve the velocity distribution, cannot exceed the number of channels the spectrum is resolved in. By resolving the spectrum in a sufficient number of channels, the number of nodes is not determined by the number of channels, but rather by the required accuracy of distribution estimates at nodes and the information content of the spectra. If we increase the number of nodes we reduce the accuracy of each node estimate. If the uncertainties at all nodes are independent, then the standard deviation in each node estimate is proportional to the square root of the number of nodes and inversely proportional to the square root of the inter node distance.
In the following figures we present the uncertainties in the function estimates with 6.8×10^5 m/s between nodes. Figure 14 to Figure 18 show the uncertainties in estimated node values as error bars. The magnitudes of the error bars are also plotted as separate dashed curves. The solid red curve in each figure is the model classical slowdown fast ion distribution used to generate the CTS spectra. The cyan error bars indicate the uncertainties due to the spectral noise only. The magenta error bars include the effect of uncertainties in nuisance parameters[5] such as scattering angle, and electron density and temperature. Estimates of nuisance parameter values are obtained from other diagnostics or the system definition. Uncertainties in these estimates increase the uncertainties in the inferred fast ion distribution. Uncertainties in nuisance parameters are given in the figure captions and in Table 5.
From Figure 14 and Figure 15 we note that a considerable number of nodes can be resolved with a satisfactory accuracy with the 60 GHz system. Though nodes are assumed right out to the birth velocity, only those nodes, where the error bars are smaller than the model function value, are plotted. Figure 16 shows the uncertainties in the fast ion function estimates for the 170 GHz system. Here the uncertainties exceed the model function values, so no nodes are plotted. Even when averaging over all nodes the uncertainty remains larger than the model mean. This is for a noise temperature of 3 keV. The noise temperature may well be higher.
Figure 17 and Figure 18 show the situation for the 3 THz and 28.28 THz options. In both cases the probe power has been chosen sufficiently high to give a good resolution of the fast ion distribution. Developing sources at those power levels at these frequencies are demanding tasks.

[5] Nuisance parameters are quantities which the measured data, here the CTS spectra, depend on but which are not of direct interest themselves.

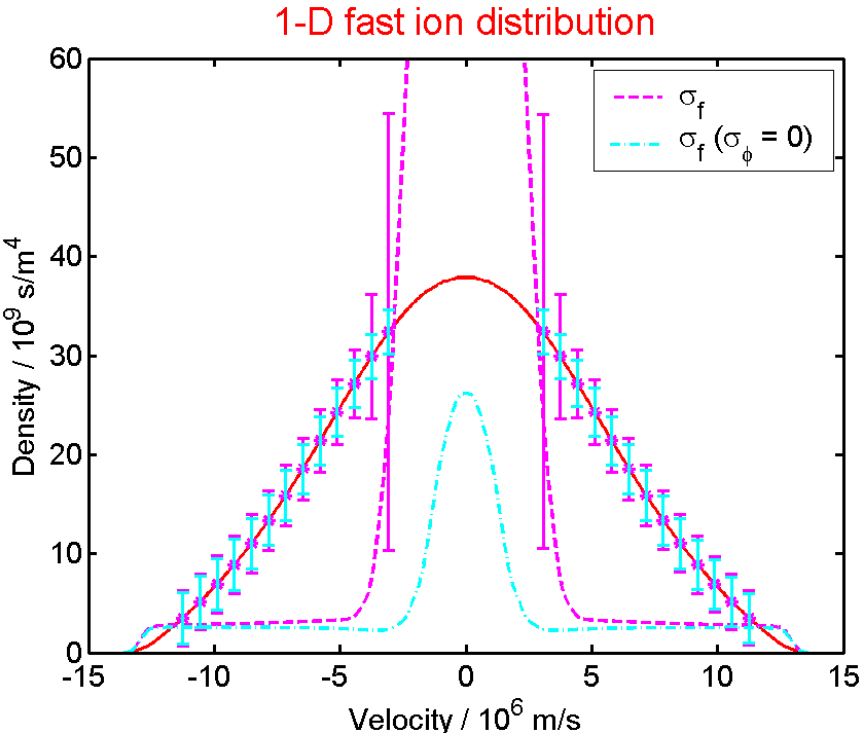

Figure 14. Resolution of the fast ion distribution. The red curve is the model fast ion distribution (classical slowdown) used in generating the CTS spectra. The error bars show one standard deviation in the posterior distribution for each resolved node in the fast ion distribution. The cyan bars show the contribution from the spectral noise while the magenta bars include also the effects of uncertainties in nuisance parameters. Here $\nu^{\mathrm{i}} = 60$ GHz, $\theta = 25°$, $\phi = 10°$, $P^{\mathrm{i}} = 1$ MW, $O_b = 3.9$ m^{-1}, $T_N = 200$ eV, $\tau = 20$ ms, $n_\alpha = 5\times10^{17}$ m^{-3}. The remaining plasma parameters are those of the ITER reference plasma. Uncertainties in nuisance parameters are: $\sigma_\theta = 1°$, $\sigma_\phi = 1°$, $\sigma_\psi = 1°$, with the remaining given in Table 5. Resolving power (see subsection 1.8) L = 13.

Nuisance parameter		**Uncertainty (1STD)**
θ	Scattering angle, $\angle(\mathbf{k}^{\mathrm{i}},\mathbf{k}^{\mathrm{s}})$	Depending on system
ϕ	Resolved fluctuation angle, $\angle(\mathbf{k}^{\delta},\mathbf{B})$	Depending on system
ψ	Asymmetry angle, $\angle(\mathbf{k}^{\delta}\times\mathbf{B}\times\mathbf{k}^{\delta},\mathbf{k}^{\mathrm{i}}\times\mathbf{k}^{\mathrm{s}})$	Depending on system
B	Magnetic field strength	$\sigma_B = 0.1\times B$
n_e	Electron density	$\sigma_{n_e} = 0.2\times n_e$
T_e	Electron temperature	$\sigma_{T_e} = 0.1\times T_e$
n_i	Impurity ion density	$\sigma_{n_i} = 0.5\times n_i$
R_i	Ratio of fuel ions	$\sigma_{R_i} = 0.3\times R_i$
T_i	Bulk ion temperature	$\sigma_{T_i} = 0.3\times T_i$
O_b	Beam overlap	$\sigma_{O_b} = 0.3\times O_b$

Table 5. Nuisance parameters and their assumed uncertainties.

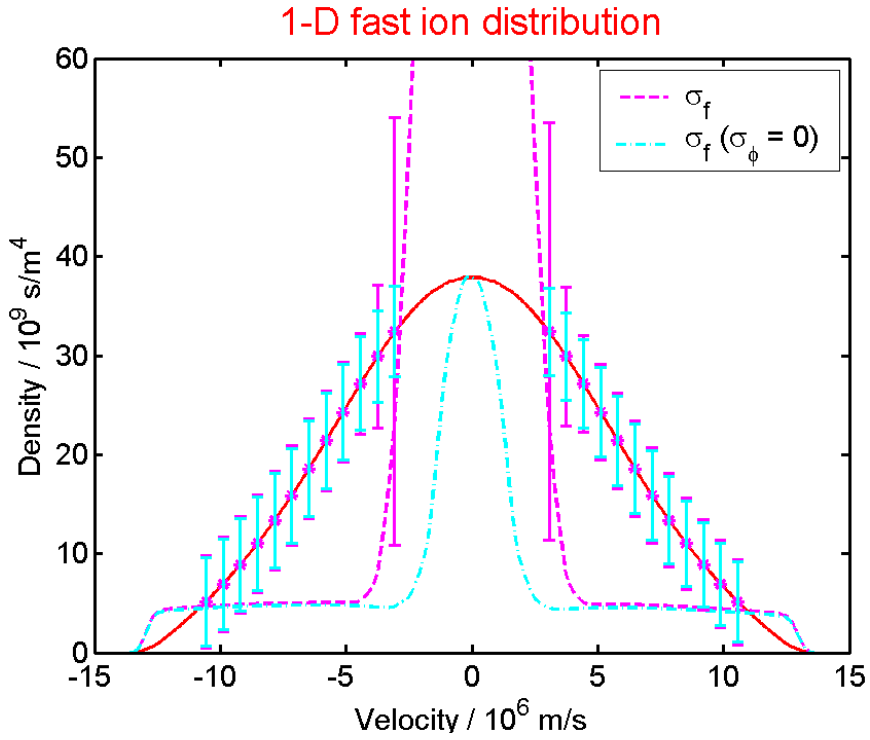

Figure 15. As Figure 14 only here, $\theta = 145°$, $\phi = 100°$, $O_b = 4.2\ \mathrm{m}^{-1}$, $L = 7.2$.

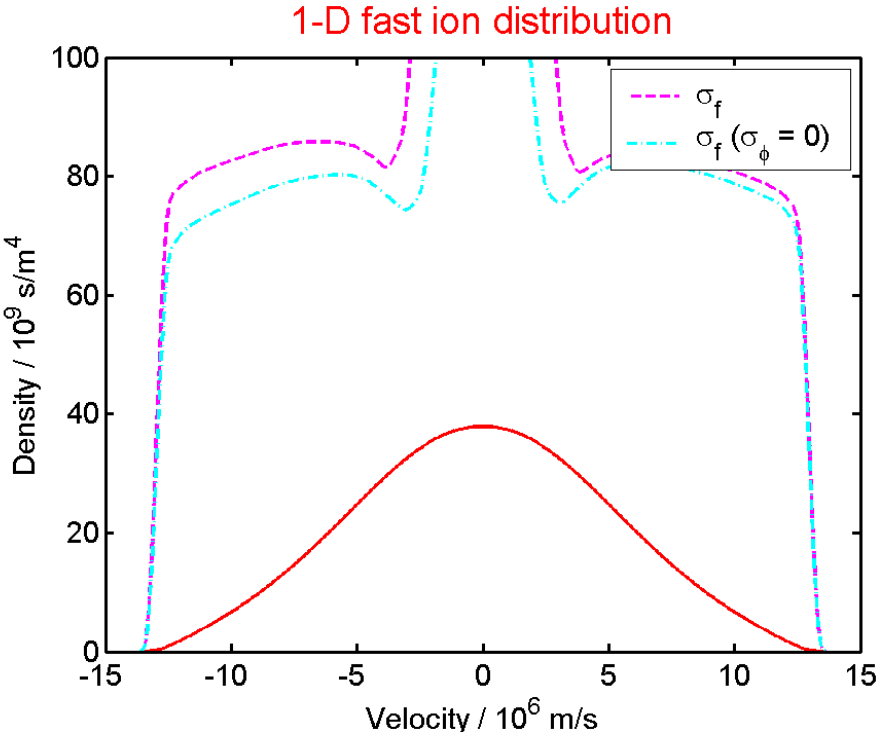

Figure 16. As Figure 14 only here, $\nu^{\mathrm{i}} = 170\ \mathrm{GHz}$, $\theta = 90°$, $\phi = 100°$, $O_b = 18.6\ \mathrm{m}^{-1}$ $T_N = 3\ \mathrm{keV}$. No resolved nodes are indicated because the uncertainties on all are larger than the model density at each node. As in the previous figures the velocity space resolution is set at 6.8×10^5m/s. $L = 0.4$.

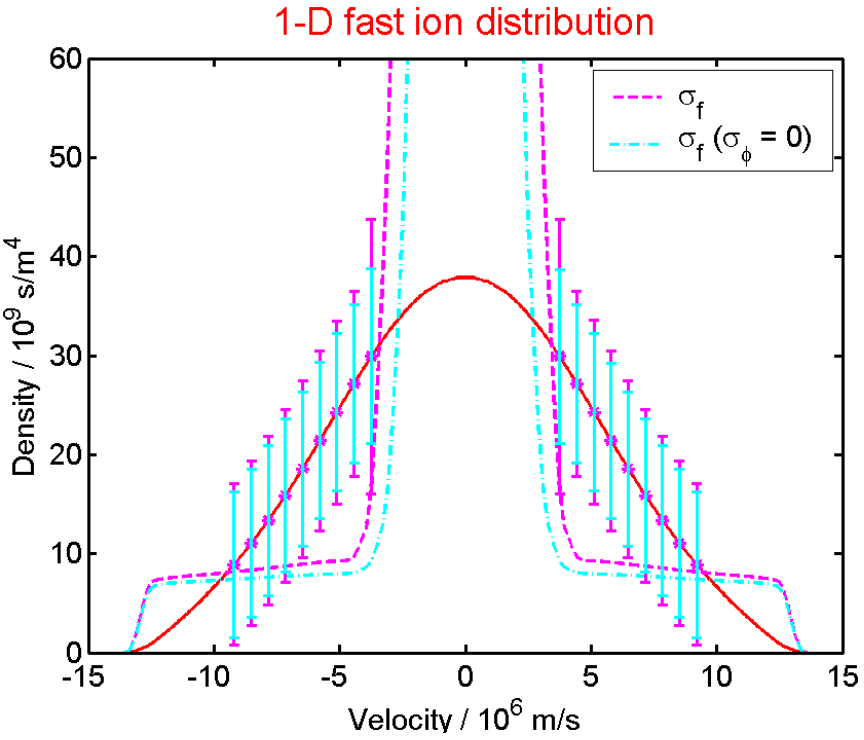

Figure 17. As Figure 14 only here, $\nu^{i} = 3$ THz, $\theta = 4°$, $\phi = 10°$, $P^{i} = 10$ MW, $\tau = 600$ ns, $O_b = 800$ m^{-1}, $T_N = 2$ eV, $\sigma_\theta = 0.1°$, $\sigma_\phi = 0.1°$, $\sigma_\psi = 0.1°$. $L = 4.2$.

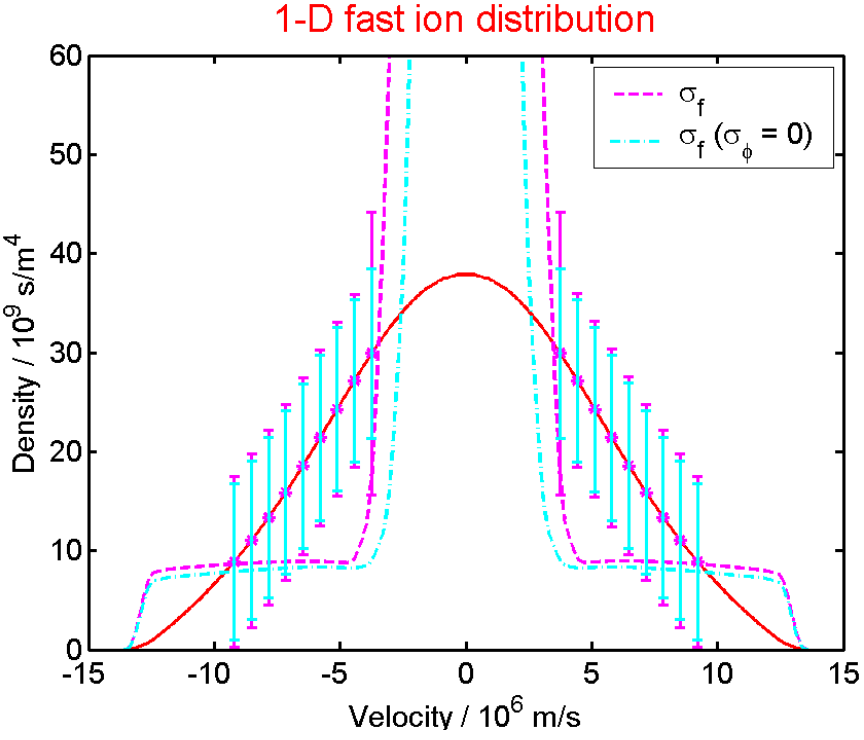

Figure 18. As Figure 14 only here, $\nu^{i} = 28.28$ THz, $\theta = 0.4°$, $\phi = 100°$, $P^{i} = 100$ MW, $\tau = 1$ μs, $O_b = 8000$ m^{-1}, $T_N = 5$ eV, $\sigma_\theta = 0.1°$, $\sigma_\phi = 0.1°$, $\sigma_\psi = 0.1°$. $L = 4$.

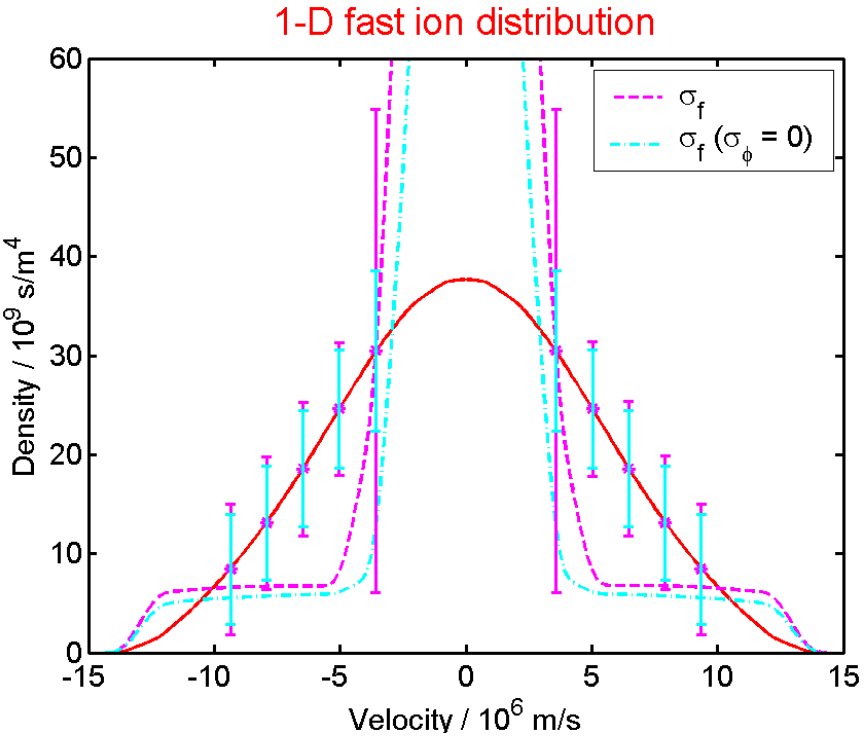

Figure 19. As Figure 18 only here with the distance between nodes doubled. The uncertainties (error bars) are reduced approximately by root 2. $L = 4$.

Figure 19 demonstrates the reduction in node uncertainties which result from increasing the distance between resolved nodes.

1.8 Resolving power

To compare the diagnostic capabilities of different diagnostic designs it is useful to have a common measure of the information each design yields on the fast ion velocity distribution. In the previous subsection we saw that when resolving a continuous function in a finite set of nodes, the accuracy of each node is roughly inversely proportional to the square root of the number of nodes. We want an information measure which is independent of the choice of number of nodes. Such a measure is provided by the *resolving power* [8,9], L, defined as

$$L^2 = \mathrm{trace}\left(\alpha^{(\theta)}\right) \tag{1.13}$$

where $\alpha^{(\theta)}$ is the *Fisher information matrix* of the *posterior distribution* for the estimated *parameters of interest*; here the fast ion velocity distribution density, f_n, at the nodes. By representing the continuous fast ion velocity distribution by its values at a finite set of nodes we represent the distribution by a vector, f_n, in an $N^{(\theta)}$ dimensional vector space. The posterior is the probability density that a certain discretised fast ion distribution, f_n, is the true distribution given the measured data and any *prior information* we may have. The maximum of the posterior, $\widehat{f}_n$, is the *maximum likelihood estimate* in the absence of prior information being used. In the vicinity of the maximum, the posterior can be approximated by a multivariate normal distribution under very general conditions. It takes the form

$$P(\mathbf{f}) \propto \exp\left\{-\frac{1}{2}\left(f_i - \widehat{f}_i\right)\alpha_{ij}^{(\theta)}\left(f_j - \widehat{f}_j\right)\right\}. \tag{1.14}$$

The Fisher information matrix, $\alpha^{(\theta)}$, appearing in the expression, is the inverse of the covariance

$$\alpha^{(\theta)} = \left(\mathbf{C}^{(\theta)}\right)^{-1} \tag{1.15}$$

which in turn is related to the posterior as

$$C_{ij}^{(\theta)} = \int \left(f_i - \widehat{f}_i\right)\left(f_j - \widehat{f}_j\right) P(\mathbf{f})\, d\mathbf{f}\,. \tag{1.16}$$

The posterior defines fully the information we have on the fast ion distribution. The resolving power, *L*, is a scalar which quantifies the information, and has the useful property that (within limits) it does not depend on the number of nodes $N^{(\theta)}$ we chose to resolve the distribution in (compare Figure 18 and Figure 19). The greater the accuracy of the measurement the smaller the spread in the posterior, which is reflected in smaller values for the covariance matrix, $C_{ij}^{(\theta)}$, and larger values for its inverse, the Fisher information matrix, $\alpha^{(\theta)}$. If $\alpha^{(\theta)}$ were a diagonal matrix

$$\alpha^{(\theta)} = \mathrm{diag}\left(\frac{1}{\sigma_1^2}, \frac{1}{\sigma_2^2}, \ldots, \frac{1}{\sigma_{N^{(\theta)}}^2}\right) \tag{1.17}$$

(if not, consider the vector f_n in the base spanned by the eigenvectors of $\alpha^{(\theta)}$, which would diagonalise $\alpha^{(\theta)}$) then the uncertainties in the population density at each node (each element in f_n) would be independent. The accuracy of the i'th node, defined as the inverse standard deviation for that node, $l_i = 1/\sigma_i$, is the square root of the i'th eigenvalue of $\alpha^{(\theta)}$. From the definition of the resolving power in equation (1.13) it follows that

$$L^2 = \sum_{i=1}^{N^{(\theta)}} l_i^2\,. \tag{1.18}$$

When the uncertainties in the estimate of the fast ion distribution is dominated by the broad band spectral noise then the variance, σ_i^2, of the estimate of the fast ion velocity space density at a node, i, is proportional to the number of nodes covering a given velocity space interval. If we double the number of nodes we double the variances and halve the square accuracies, l_i^2, leaving the resolving power, *L*, largely unchanged. The insensitivity of the resolving power, *L*, to the number of nodes, $N^{(\theta)}$, holds also when uncertainties in nuisance parameters play a dominant role.
To make the resolving power a unit-less quantity we normalize the fast ion velocity distribution density by the *target accuracy*, Δ. We chose the *target accuracy* to be the maximum uncertainty in a resolved node that makes it useful to resolve that node. (If the target accuracy cannot be reached we should reduce the number of nodes.)

If the uncertainties at all nodes are independent then L^2 is the number of nodes which we can resolve with the *target accuracy*. Conversely, if we chose to resolve only one node, then the accuracy of the estimate of that node would be *L* times better than the target accuracy.
With the lower estimate of phase space density at $f_\alpha = 6.6\times10^9\,\mathrm{s/m^4}$ (see Appendix A) we chose a target accuracy of

$$\Delta = 6\times10^9\,\mathrm{s/m^4} \tag{1.19}$$

as a suitable target. In our evaluation of diagnostic designs in subsequent sections we require that the diagnostic should be able to resolve at least 16 components of the distribution with the target accuracy (8 on each side of zero), corresponding to a

resolving power $L > 4$. The target accuracy, we have chosen as a normalising factor, corresponds to the ITER measurements requirements at alpha densities above $8\times10^{17}\text{m}^{-3}$ as set out in the measurement requirements summarised in Table 2, and is in fact twice the maximum STD uncertainty ($\sigma < 3\times10^{9}\text{s/m}^{4}$) at the minimum density. To achieve this more demanding accuracy we would need a resolving power $L > 8$.
In Figure 14 to Figure 19, showing the error-bars on resolved nodes in the inferred fast ion distributions for different CTS systems, the corresponding resolving powers, L, are given in the captions.
Generally the uncertainties in the node estimates are correlated. A principal component analysis of the posterior brings out these correlations, identifying which features of the fast ion distribution are resolved well and which are poorly resolved. It may, for instance, be that the estimate is uncertain with respect to a scaling factor but that the relative shape is well resolved. Such information is not revealed by error bars, but is brought out in the principal component analysis. For a detailed discussion of the concepts briefly sketched here please refer to [8,9].
The accuracies of principal components and the two most poorly resolved principal components are presented along with the figure for the resolving power in Figure 20 to Figure 24 for the diagnostic systems we consider in this section. Figure 20 and Figure 21 show that the 60 GHz systems have a satisfactory diagnostic capability with only a couple of poorly resolved components corresponding to uncertainty in a common scaling factor and uncertainty near the transition to the bulk ion feature. The resolving power at 13 and 7 is comfortably above our minimum requirement of 4. The 170 GHz option has a resolving power of 0.4, well below the minimum requirement.

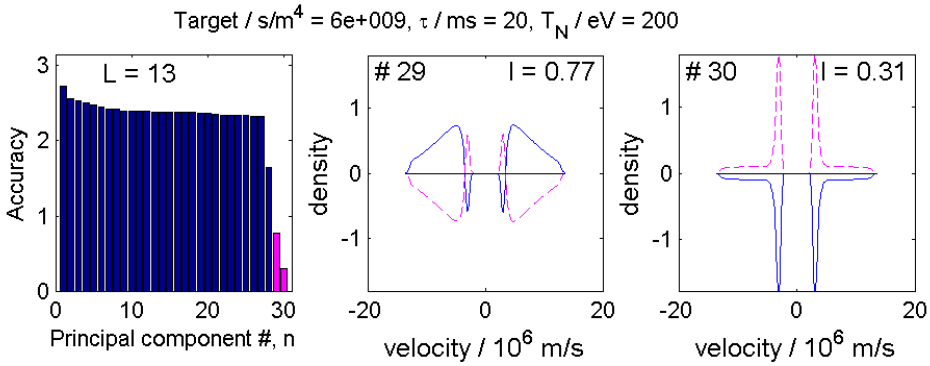

Figure 20. Accuracies (right) of the principal components of the posterior for the resolved nodes of the fast ion distribution. Centre and left are the functional shapes of the most poorly resolved principal components. Here $\nu^{\text{i}} = 60\ \text{GHz}$, $\theta = 25°$, $\phi = 10°$, $P^{\text{i}} = 1\ \text{MW}$, $O_b = 3.9\ \text{m}^{-1}$, $T_N = 200\ \text{eV}$, $\tau = 20\ \text{ms}$, $n_\alpha = 5\times10^{17}\ \text{m}^{-3}$. The remaining plasma parameters are those of the ITER reference plasma. Uncertainties in nuisance parameters are: $\sigma_\theta = 1°$, $\sigma_\phi = 1°$, $\sigma_\psi = 1°$, with the remaining given in Table 5. Same system as in Figure 14.

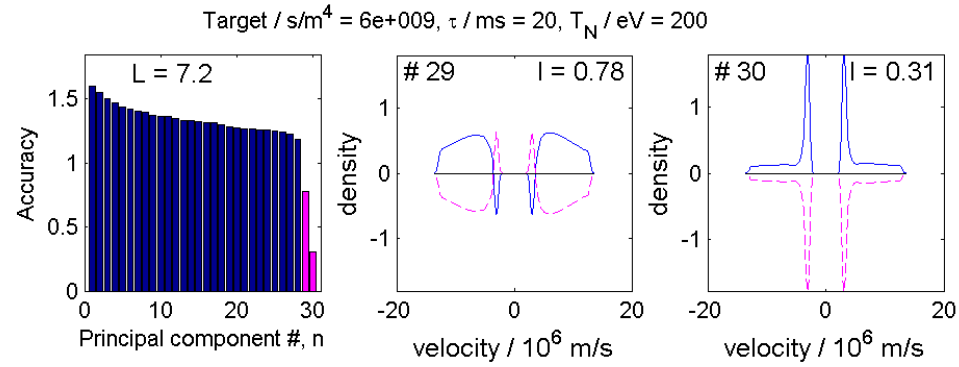

Figure 21. As Figure 20 only here, $\theta = 145°$, $\phi = 100°$, $O_b = 4.2$ m^{-1}. Same system as in Figure 15.

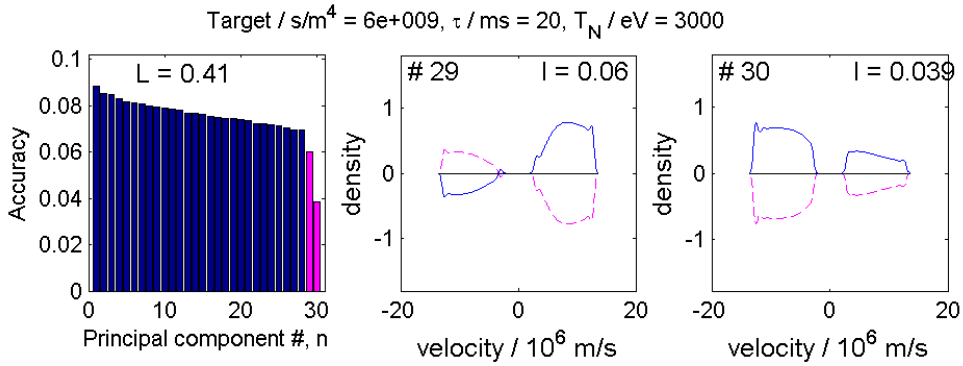

Figure 22. As Figure 20 only here, $\nu^{\mathrm{i}} = 170$ GHz, $\theta = 90°$, $\phi = 100°$, $O_b = 18.6$ m^{-1}. Same system as in Figure 16.

Figure 23 and Figure 24 show the accuracies of principal components for the 3 THz and 28 THz systems. Both systems have two poorly resolved components similar to the 60 GHz case, and resolving powers which meet the minimum requirement. The uncertainties in scattering geometry have been assumed to be smaller here than in the microwave systems. This is because these systems need the increased accuracy here to avoid adverse effects on the resolving power. It does not imply that these accuracies in geometry are readily achievable.

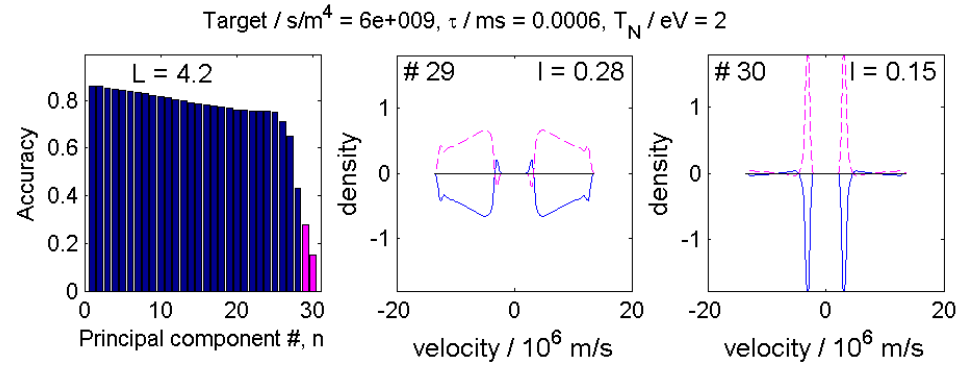

Figure 23. As Figure 20 only here $\nu^{\mathrm{i}} = 3$ THz, $\theta = 4°$, $\phi = 10°$, $P^{\mathrm{i}} = 10$ MW, $\tau = 600$ ns, $O_b = 800$ m^{-1}, $T_N = 2$ eV, $\sigma_\theta = 0.1°$, $\sigma_\phi = 0.1°$, $\sigma_\psi = 0.1°$. Same system as in Figure 17.

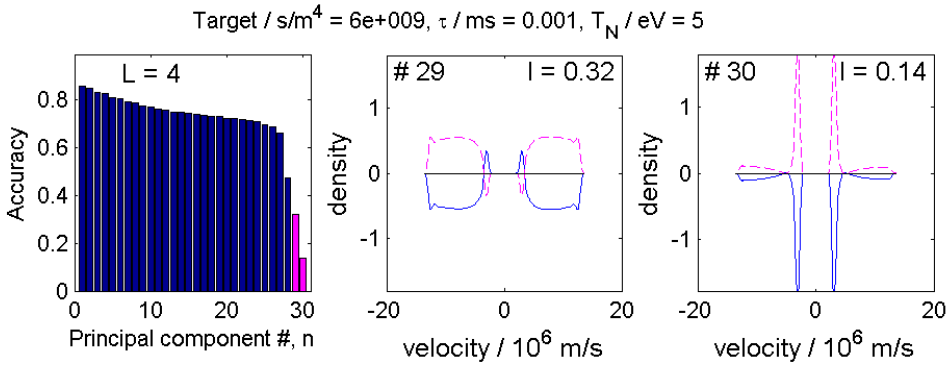

Figure 24. As Figure 20 only here $\nu^{\mathrm{i}} = 28.28$ THz, $\theta = 0.4°$, $\phi = 100°$, $P^{\mathrm{i}} = 100$ MW, $\tau = 1$ µs, $O_b = 8000$ m^{-1}, $T_N = 5$ eV, $\sigma_\theta = 0.1°$, $\sigma_\phi = 0.1°$, $\sigma_\psi = 0.1°$. Same system as in Figure 18.

We summarise the results on resolving power in Table 6.

ν^{i}	θ	ϕ	P^{i}	O_b	T_N	τ	L
60 GHz	25°	10°	1 MW	3.9 m^{-1}	200 eV	20 ms	13
60 GHz	145°	100°	1 MW	4.2 m^{-1}	200 eV	20 ms	7.2
170 GHz	90°	100°	1 MW	18.6 m^{-1}	3 keV	20 ms	0.4
3 THz	4°	10°	10 MW	800 m^{-1}	2 eV	0.6 µs	4.2
28.28 THz	0.4°	100°	100 MW	8000 m^{-1}	5 eV	1 µs	4.0

Table 6. Summary of system and resulting resolving power.

The resolving power is a function of beam overlap, probe power, integration time, scattering angle and noise temperature. For the reference plasma the relationships are summarized in equations (1.20) to (1.24), for the diagnostics indicated.

60 GHz, forward scattering:

$$\frac{L}{4} = \frac{P^{\mathrm{i}}}{1\mathrm{MW}} \sqrt{\frac{\tau}{20\,\mathrm{ms}}} \frac{O_b}{1.2/\mathrm{m}} \sqrt{\frac{25°}{\theta}} \frac{200\,\mathrm{eV}}{\mathrm{T_N}} \frac{\Delta}{6\times10^9\,\mathrm{s/m^4}} > 1. \qquad (1.20)$$

60 GHz, back scattering:

$$\frac{L}{4} = \frac{P^{\mathrm{i}}}{1\mathrm{MW}} \sqrt{\frac{\tau}{20\,\mathrm{ms}}} \frac{O_b}{2.3/\mathrm{m}} F(\theta,\varphi) \frac{200\,\mathrm{eV}}{\mathrm{T_N}} \frac{\Delta}{6\times10^9\,\mathrm{s/m^4}} > 1. \qquad (1.21)$$

The expression includes the function $F(\theta,\varphi)$ shown in Figure 25.

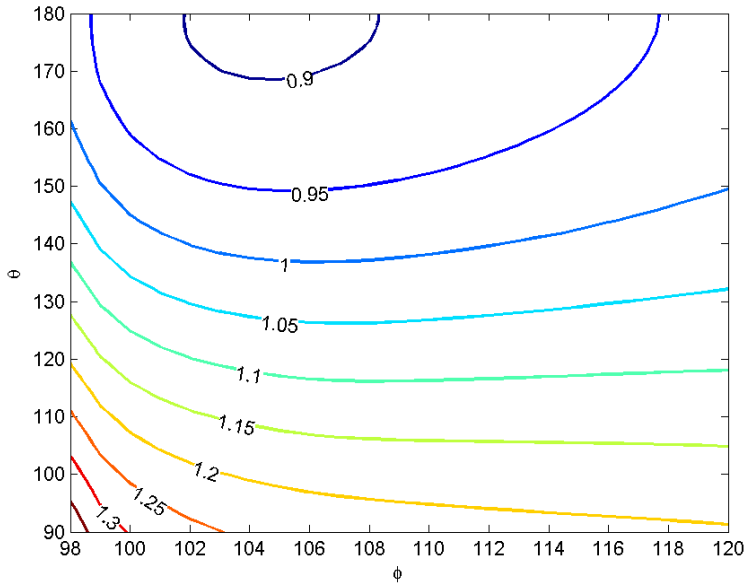

Figure 25. Plot of the scaling factor, $F(\theta,\varphi)$, which accounts for the dependence of the resolving power, L, on scattering angle, θ, and the angle, ϕ, between the resolved fluctuation wave vector and the magnetic field.

170 GHz, $\theta = 90°$, $\phi = 100°$:

$$\frac{L}{4} = \frac{P^{\mathrm{i}}}{5\,\mathrm{MW}} \sqrt{\frac{\tau}{100\ \mathrm{ms}}} \frac{O_b}{18/\mathrm{m}} \frac{3\ \mathrm{keV}}{\mathrm{T_N}} \frac{\Delta}{6\times10^9\,\mathrm{s/m^4}} > 1. \qquad (1.22)$$

3 THz, $\theta = 4°$, $\phi = 10°$:

$$\frac{L}{4} = \frac{P^{\mathrm{i}}}{10\ \mathrm{MW}} \sqrt{\frac{\tau}{550\ \mathrm{ns}}} \frac{O_b}{800/\mathrm{m}} \frac{2\ \mathrm{eV}}{\mathrm{T_N}} \frac{\Delta}{6\times10^9\,\mathrm{s/m^4}} > 1. \qquad (1.23)$$

28.28 THz, $\theta = 0.4°$, $\phi = 100°$:

$$\frac{L}{4} = \frac{P^{\mathrm{i}}}{100\,\mathrm{MW}} \sqrt{\frac{\tau}{1\ \mu\mathrm{s}}} \frac{O_b}{8000/\mathrm{m}} \frac{5\ \mathrm{eV}}{\mathrm{T_N}} \frac{\Delta}{6\times10^9\,\mathrm{s/m^4}} > 1. \qquad (1.24)$$

1.9 Selection of systems for further consideration

In the preceding subsections we have discussed most of the considerations which limit the choices of probe frequency. The need for spatial localisation of the measurements rules out the use of probe frequencies below the millimetre wave range. In the millimetre wave range, gyrotrons provide powerful probe sources. In this frequency range the left hand X-mode cutoff (L-cutoff) sets a lower frequency limit. For the ITER reference plasma the L-cutoff is approximately 49 GHz on the low field side of the plasma, 42 GHz in the centre and 33 GHz on the high field side. An X-mode frequency window exists between the L-cutoff and the lower limit of the ECE emission spectrum. Relativistically downshifted fundamental electron cyclotron emission sets in around 65 GHz. It is this window which is exploited in the 60 GHz

systems discussed in this section. The preliminary investigations presented in this section indicated that CTS systems based on probe frequencies in the 60 GHz range could be viable. These systems will be explored in greater detail in Section 2.
With increasing frequency, the fundamental electron cyclotron absorption enters the plasma. For the reference ITER plasma complete absorption due to relativistically down-shifted EC resonance takes place at 100 GHz for horizontal rays propagating orthogonal to the magnetic field. Between 100 GHz and 150 GHz there is no access to the plasma centre because of fundamental EC absorption. Between 150 GHz and 200 GHz there is access to the centre from the low field side and top port. This is exploited in the 170 GHz system discussed. In this range the fundamental EC resonance in the plasma is giving rise to high noise background. The preliminary investigations in this section showed difficulties in achieving adequate resolution of the fast ions with a 170 GHz system. It is investigated further in Section 3.
At frequencies between 200 GHz and 700 GHz there is no access to the centre of the plasma because of EC absorption. Above 700 GHz higher harmonic gyrotrons may provide a source, but their power will be much lower than the fundamental gyrotrons operating in the 100 GHz range. Optically thin EC emission gives too strong a noise background for the currently foreseen high harmonic gyrotrons. Free electron lasers in the THz range provide high power but their line widths are currently too wide to be considered as sources for the probe radiation. This could be addressed by using the FEL purely as an amplifier. Cost would be an issue though. Other lasers in the THz range are generally weaker, so for these to be considered we must chose frequencies sufficiently high that the ECE emission is reduced to below 10 eV. To guarantee this we consider probe frequencies in the 3 THz range. In this section we have made a preliminary identification of the source and receiver performance required for CTS at 3 THz. This option is discussed further in Section 4.
Between 3 THz and 28 THz we have not been able to identify powerful sources with narrow line widths, which, given the decreasing scattering cross section, can compete with the 3 THz option. Thus next frequency we consider is that of the CO_2 laser at 28.28 THz. The CO_2 laser is a powerful source. Though the preliminary investigations in this section show that a CTS based on a CO_2 laser as probe source would be technologically demanding, it will be discussed in further detail in Section 5.
The requirement that the fast ion feature be significant compared with the electron feature, combined with the decreasing scattering cross section with increasing frequency, effectively sets an upper limit to the probe frequency at the CO_2 laser frequency of 28.28 THz, so probes with higher frequencies are not considered.

2 Probe frequency below electron cyclotron spectrum (≈ 60 GHz)

2.1 Introduction

The first frequency range we assess is that below the electron cyclotron frequency. One of the main concerns of this range of frequencies is refraction. However, proper design optimisations, such as minimisations of the angle between the launch direction and the density gradient, minimize this effect. The collective scattering condition (1.4) places no limitation on which scattering geometries can be used for measuring the fast ion feature in ITER. Limits on usable geometry are set by antenna position and refraction.

The choice of scattering geometry determines to a large extent the spatial resolution, robustness and resolving power, L, of the CTS diagnostic system. The resolving power was defined and discussed in subsection 1.8. It is a measure of the accuracy with which the system can estimate the fast ion velocity distribution for a given velocity space resolution. For all systems discussed in this report we selected a minimum requirement of $L = 4$ corresponding to requiring that the systems resolve at least $L^2 = 16$ orthogonal components of the fast ion distribution (essentially 16 point in the distribution) with an STD uncertainty, σ, smaller than the target accuracy, $\Delta = 6\times10^9 \mathrm{s/m^4}$. In this section, various scattering geometries are analysed for a range of plasma parameters.

To measure both the parallel and perpendicular component of the fast ion velocity distribution, two separate systems are proposed. For the perpendicular component, the proposed design consists of a radially launched probe and a large quasi-optical mirror coupled to a set of receivers, both located in the midplane port of the low field side (LFS), as illustrated in Figure 6 and Figure 30. For the parallel component measurements, we find that LFS toroidally launching probes and viewing detectors suffer too much refraction. Hence a forward scattering system with detectors on the high field side (HFS) measuring scattered radiation from a probe launching from the LFS, as illustrated in Figure 7 and Figure 53, is proposed in this report. Similar to the proposed reflectometry system for ITER, the HFS receivers will be viewing the plasma between blanket modules in the equatorial midplane. The detectors will consist of quasi-optical mirrors located behind the blanket modules using the horizontal gap between blanket modules as an antenna.

The standard plasma used in this study is the H-mode for ITER with $n_e(0) = 1.0\times10^{20}\mathrm{m^3}$, $T_e(0) = 25$ keV, $B_o = -5.3$ T, $I_p = -15$ MA (see Appendix A). It is important to analyse the CTS diagnostic potential for a range of plasma parameters. To this end, the electron density and temperature will be scaled by factors DS and TS respectively.

This section is divided into six subsections. The first discusses ECE background radiation studies and its implication on plasma operating scenarios and possible frequencies between 50 and 90 GHz. Even with very strict criteria, frequencies below 65 GHz have acceptable ECE noise levels. In the second subsection, an analysis of Gaussian beam traces in vacuum is presented to identify the range of achievable beam diameters. These influence the achievable radial resolution and beam overlap. The third subsection defines beam parameters used in this study. The following two

subsections analyse performances of both the LFS back-scattering and HFS forward-scattering system at different densities. The optimisations, for each scattering geometry, consist essentially of a compromise between the beam overlap, the scattering volume size that determines the radial resolution, and the robustness. The criteria in order of importance for both systems are:

1) Measurement of the central region with good spatial resolution at different plasma parameters
2) Sufficient overlap in the spectral range (Dispersion effects).
3) Robustness of the overlap and localization of the measurement against variations of density such as sawteeth.
4) All the above criteria at other radial positions.

The final subsection discusses concerns about the impact the probe radiation may have on other diagnostics.

2.2 ECE noise

The chosen spectral range is at the low frequency limit of the electron cyclotron emission (ECE) spectrum. The fundamental cyclotron resonance is outside the plasma on the low field side. The residual emission is due to the high energy tail of the thermal distribution emitting into the spectral range via relativistic Doppler shift. Ray-trace calculations, assuming Maxwellian velocity distributions, have been done for a range of frequencies and launch geometries at different plasma parameters. For each ray-trace the single pass ECE radiation temperature is calculated. Figure 26 shows contours of ECE radiation temperature for a scan of frequencies and toroidal angles at the density and temperature scaling factors of DS = TS = 1.

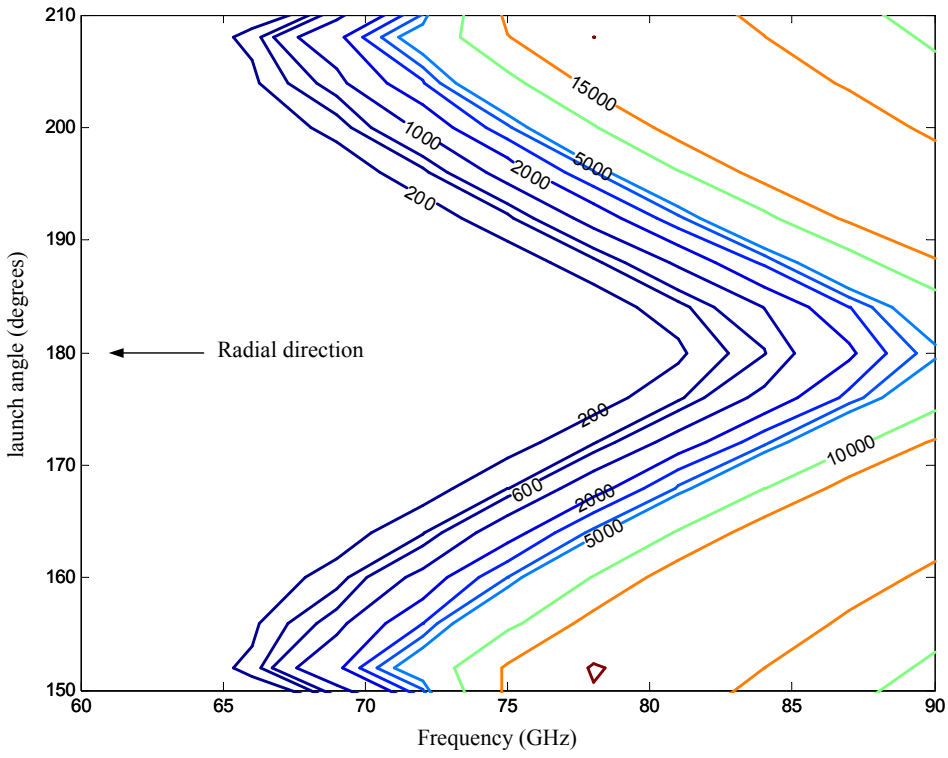

Figure 26. Ray-trace calculations showing the contours of the single pass radiation temperatures over ranges of frequencies and viewing angles. The contour labels are in units of eV. The viewing position is located at the

equatorial LFS port viewing horizontally and scanning over the toroidal direction DS=TS=1.0.

In Figure 26 the rays are launched horizontally from the mid-plane on the LFS, with a toroidal scan, the maximum of which yields the highest ECE level of any viewing position and direction. We note that at this density and temperature 65 GHz is the upper frequency limit below which first pass radiation temperatures are below 200 eV for all viewing directions. To account for indirect radiation, we do a number of scans of viewing angles (both toroidally and poloidally) at different positions around the plasma at and then take the maximum ECE radiation temperature as the representative value for each frequency at a certain plasma DS and TS scaling factor. Figure 27 shows the contours of the upper frequency limit of the ECE threshold of 200 eV versus the plasma density and temperature scaling factor.

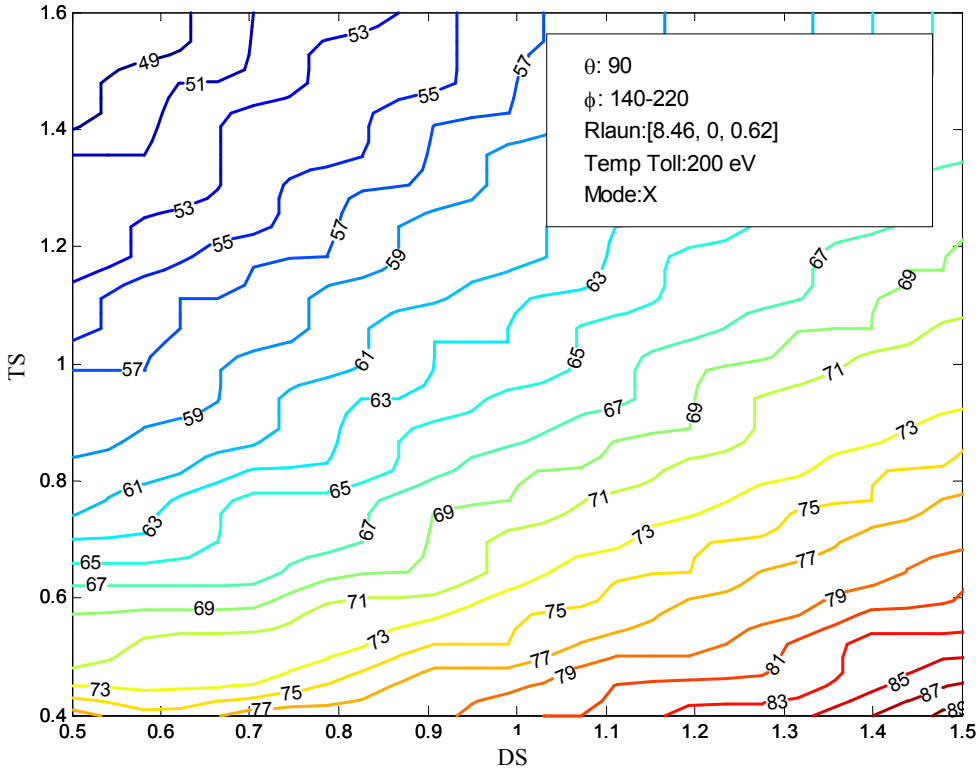

Figure 27. Contours of the upper frequency limit as a function of density scaling, DS, and temperature scaling, TS. The frequency limit is the upper frequency at which the single pass ECE radiation temperature is below 200 eV for any viewing direction. The contour labels are in units of GHz.

This scan was not confined to stay within the beta limit. At DS = TS = 1.0, we have an upper limit of 65 GHz. At higher electron temperatures, the upper frequency limit is reduced. However, it is important to note that the resolving power calculations throughout this report assume a background noise temperature of 200 eV. From Equation (1.20), the resolving power is inversely proportional to the noise temperature, T_N, which we assume is equal to T_{ECE}, since the expected detector noise temperature will be in the range of 10 eV assuming a transmission line loss of 10 dB. Hence, at a given density, we can scale the resolving power to re-evaluate the

minimum requirement at a less stringent noise level. A central frequency of 60 GHz is a good compromise between acceptable refraction and low ECE noise levels for the ITER reference plasma. At higher temperatures, such as TS = 1.4 (~35 keV), the upper frequency limit becomes 57 GHz. For this reason, we also analyse the feasibility of operating at 55 GHz in this report.

2.3 Gaussian beam and beam ray traces

As mentioned in subsection 1.5, there is a lower limit to the beam size that can be projected a given distance from a given aperture. Figure 28 shows Gaussian beam parameters from an aperture diameter of 200 mm for different radii of curvature at the aperture. The Gaussian half-width w on the ordinate of the graph is multiplied by 2×1.6 to represent the beam diameter ($D_b = w \times 2 \times 1.6$) which includes 99.4 % of the total power. The black curve (right ordinate) in the graph is the mapping of the flux surface to the distance from the aperture from a LFS launch. The figure clearly shows for an aperture of 200 mm, the minimum D_b that can be achieved at the centre ($\psi = 0$) of the plasma is 200 mm.

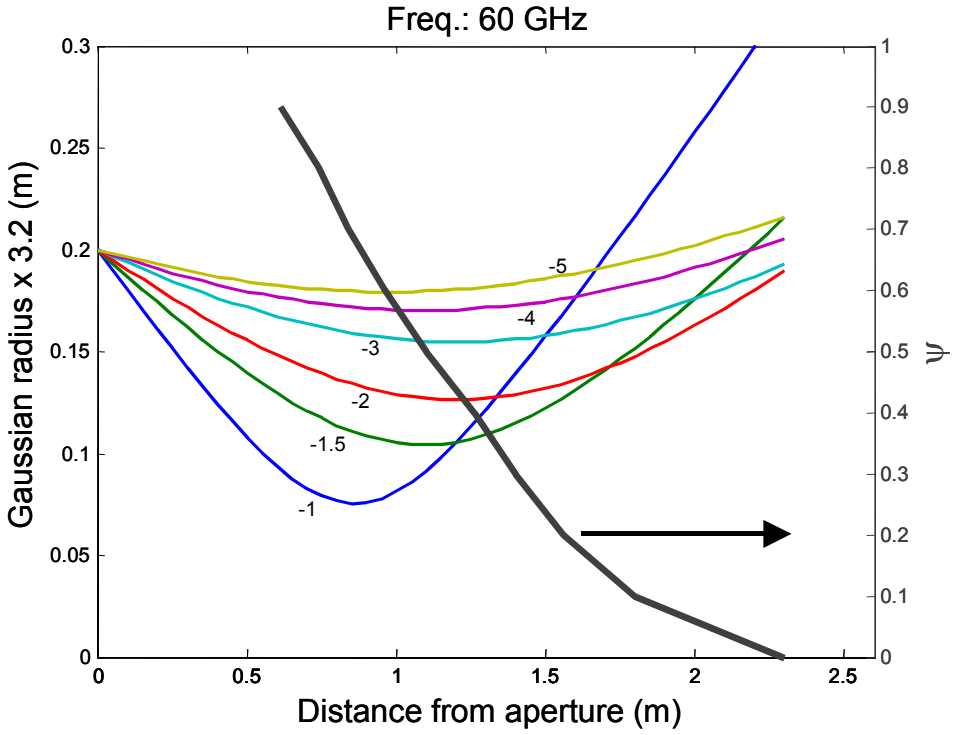

Figure 28. Beam diameter (Gaussian radius × 3.2) for different radii of curvature (in meters) for an aperture diameter of 200 mm. The black curve represents the flux coordinates as a function of distance from a LFS launcher aperture. ν^i = 60 GHz.

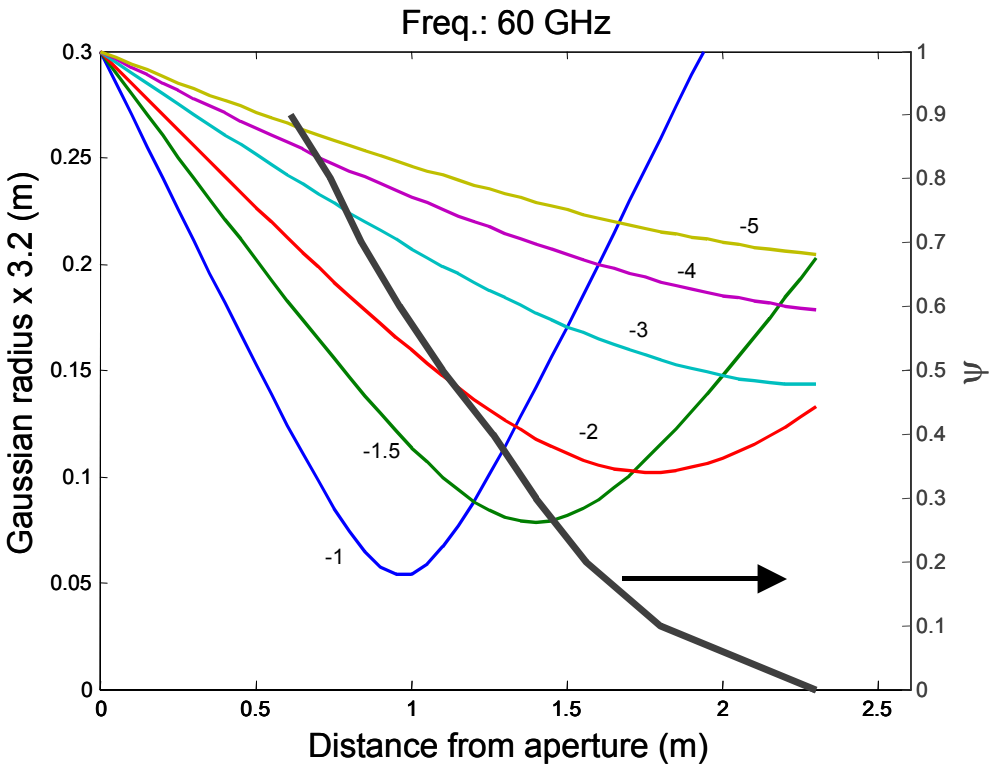

Figure 29. Beam diameter (Gaussian radius × 3.2) for different radii of curvature (in meters) for an aperture diameter of 300 mm. The black curve represents the flux coordinates as a function of distance from a LFS launcher aperture. At ν^i = 60 GHz.

Figure 29 shows the same curves as Figure 28, but for an aperture diameter of 300 mm. We clearly see the advantage and flexibility in increasing the aperture size to this value. These graphs will be important in this study since beam size will influence the beam overlap, its robustness and the radial resolution as mentioned in subsection 1.5. The Gaussian beams in the beam overlap calculations are represented by a bundle of rays consisting of 5 independent rays; the beam centre and 4 rays, each at one Gaussian half width from the centre. With these 5 rays the refraction of a Gaussian beam is modelled, but not the diffraction. To account to some extent for the diffraction, we choose the bundle of rays, which is tangent to the real Gaussian beam in vacuum at the distance from the aperture that is of interest. We use this ray bundle as an approximation to the Gaussian beam locally in the plasma. It, of course, does not account for the plasma modification of the diffraction, which we assume is of modest importance in our studies.

2.4 Nomenclature of beam parameters

In this section, we define some nomenclature and variables that describe the beam properties. As described in subsection 1.5, the beam plane is spanned by the probe and receiver beams. Varying the beam widths in the beam plane influences the radial resolution. Varying the beam width orthogonal to the beam plane changes the beam overlap. It is important to note, that the beam plane is near vertical for the LFS backscattering system and near horizontal for the HFS forward-scattering systems.

The directions orthogonal to the beam are denoted κ for the horizontal direction and θ for the direction orthogonal to that. Thus we introduce the following variables:

$D_{b\kappa}$ and $D_{b\theta}$:	Beam diameters at the launch position
Ω_κ and Ω_θ :	Opening angles at launch
κ :	Toroidal angle between launch direction and density gradient. $\kappa = 0^o$ is a purely radial launch. $\kappa > 0$ is a launch in the same direction as plasma current.
θ_L :	Poloidal angle of launch from the vertical direction.

LFS system:

In the beam plane: $D_{b\theta}$, Ω_θ
Orthogonal to the beam plane: $D_{b\kappa}$, Ω_κ

HFS system:

In the beam plane: $D_{b\kappa}$, Ω_κ
Orthogonal to the beam plane: $D_{b\theta}$, Ω_θ

2.5 LFS backscattering system

2.5.1 Set-up

For the measurement of the fluctuation wave vector, $\mathbf{k}^{\delta}$, near perpendicular to the magnetic field, a backscattering system as sketched in Figure 30 is proposed. The system is designed with no movable parts to sweep launch and viewing directions. The receivers shown consist of a common relaying mirror in the port plug serving several viewing lines. The different receiver beams measure at different radial positions. The ***k*** vectors of the fluctuations, the received scattered radiation, and the probe radiation are shown in Figure 31.
Several designs have been considered, including the two shown in Figure 30. The system sketched in the upper drawing seeks to minimise the first wall aperture. The lengths of the beams in the port in this schematic have been exaggerated for illustrative purposes. The simpler system sketched in the lower drawing requires a larger first wall aperture, but yields a better cross profile performance. The optimisation studies presented here, assume the type of systems, which minimise the required apertures.

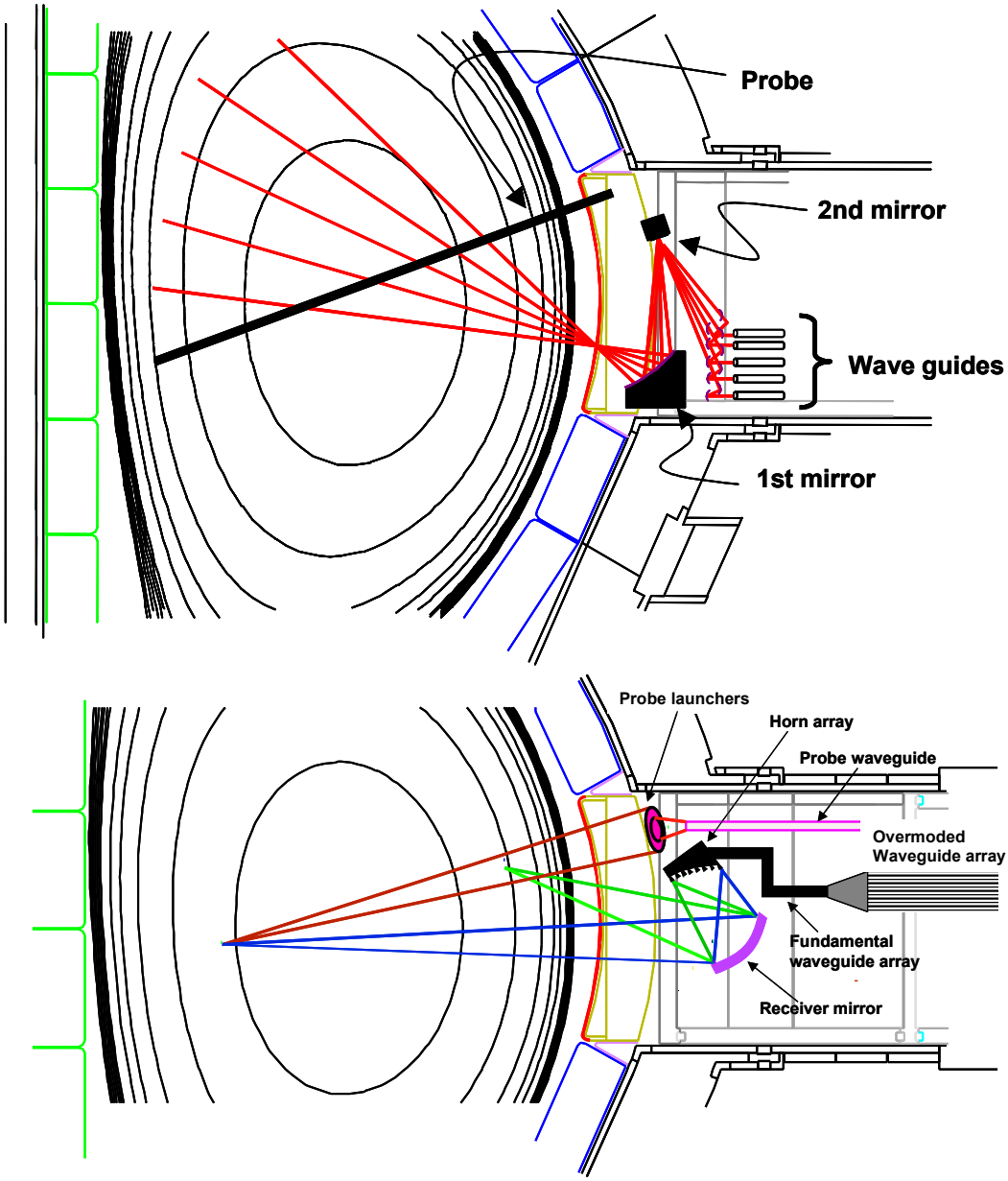

Figure 30. Poloidal view of the LFS back scattering CTS system. The top drawing sketches a system layout which minimises the aperture in the first wall. Here the probe is sblack and the receiver beams red. This layout is the basis of most of the optimisations presented here. The bottom drawing sketches a system with simpler front end quasi optics. This system is the result of further optimisations. Here the probe is red. In blue and green are shown the two extremes of the receiver beams.

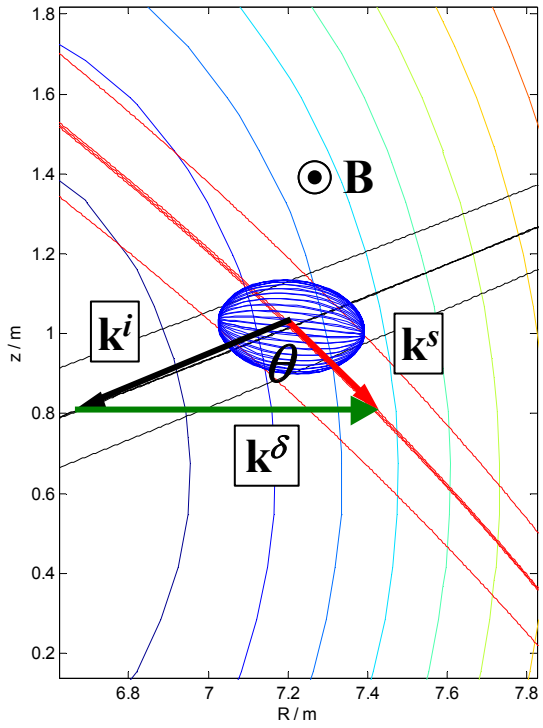

Figure 31. LFS scenario: A poloidal map of the probe beam (black), the receiver beam (red), the scattering volume (blue) with the k vectors of the received scattered radiation, the probe radiation, and the fluctuation wave vector. $\mathbf{k}^{\delta} = \mathbf{k}^{s} - \mathbf{k}^{i}$.

2.5.2 Diagnostic performance

In this study of diagnostic performance we include two possible receiver positions, as shown in Figure 32. Receiver position *1* in red is at the lower most part of the port, whereas receiver position *2* in blue is located at the equatorial position. Each viewing angle is considered as a separate receiver. The probe launch angles are $\kappa^{i} = 10°$ and $\theta_L{}^{i} = 110°$. For both receiver positions *1* and *2*, each of the receiver beams at the different viewing angles, θ_L, shown in Figure 32, exhibits different refraction patterns. Hence, different κ values for each receiver have been found to maximize the beam overlaps at the standard density, DS = 1. Changing the density either way will of course change the refraction and thus degrade the overlap. A more refined optimisation of κ^{s} for each receiver has been done to ensure the minimum requirement of the resolving power ($L > 4$) at all density scalings in the range 0.7 to 1.2. Figure 120 and Figure 121 of Appendix D show the same configurations at DS = 0.7 and 1.1 respectively.

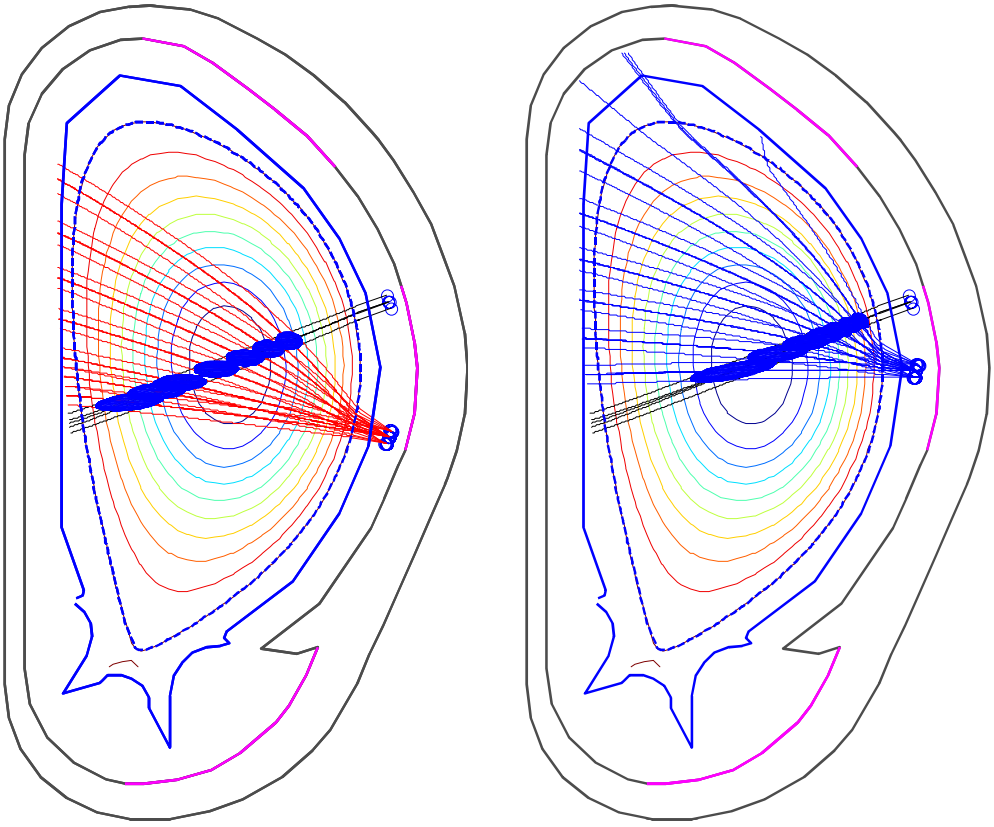

Figure 32. Poloidal cross-sections of beam traces in a DS = 1 plasma for two possible receiver positions with the scattering volumes in blue. (a) Receiver position *1* in red for θ_L = 80-55°, and (b) receiver position *2* in blue for θ_L = 90-60°. The smallest θ_L shown, for each receiver, is the limiting angle before reflection occurs.

2.5.2.1 Optimisation of beam properties

The beam parameters in this study are defined as follows:

LFS system:

In the beam plane: $D_{b\theta}{}^{i} = 200$ mm, $\Omega_{\theta}{}^{i} = 0^{o}$, $D_{b\theta}{}^{s} = 200$ mm, $\Omega_{\theta}{}^{s} = 0^{o}$

$\perp$ to the beam plane: $D_{b\kappa}{}^{i} = 200$ mm, $\Omega_{\kappa}{}^{i} = 2^{o}$, $D_{b\kappa}{}^{s} = 200$ mm, $\Omega_{\kappa}{}^{s} = 0^{o}$

Figure 33 shows the top view of a beam trace of the probe in black and two receivers in blue. We can clearly see the receiver beams suffer refraction in the toroidal direction, which pose a problem in getting a sufficiently good overlap over a range of radial positions. To ensure sufficient overlap over the range of radial positions, the probe beam opening angle $\Omega_{\kappa}{}^{i}$ is set to 2° as shown in Figure 33. Recall that widening the beam in the toroidal direction increases the robustness at the expense of the beam overlap. The value of $\Omega_{\kappa}{}^{i} = 2^{o}$ is an optimised value for density scalings between 0.7 and 1.2. This opening angle is approximately equivalent to the divergence angle of the

Gaussian beam depicted in Figure 34. The aperture in the toroidal direction is 70 mm for these Gaussian beams.

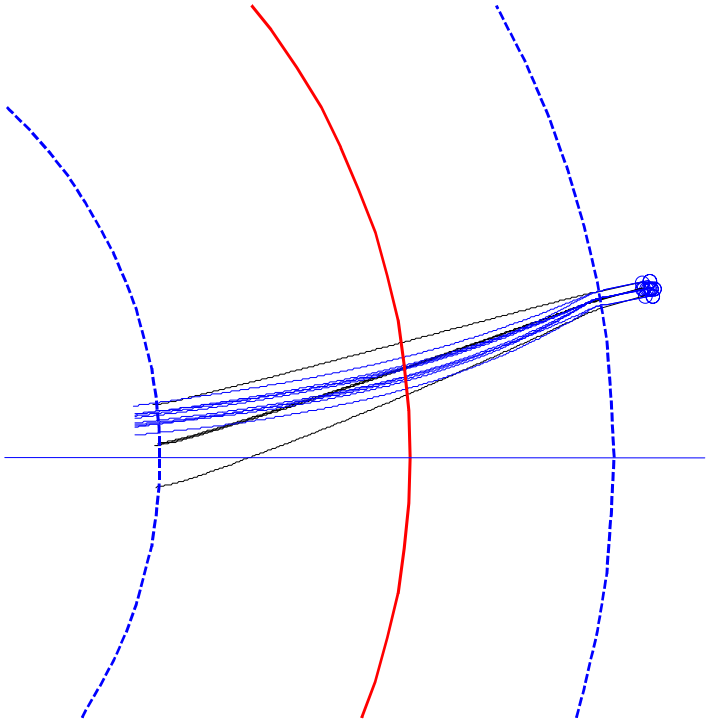

Figure 33. Top view of the probe in black and two receiver beams in blue. The toroidal divergence angle of the probe is $\Omega_\kappa = 2^\circ$.

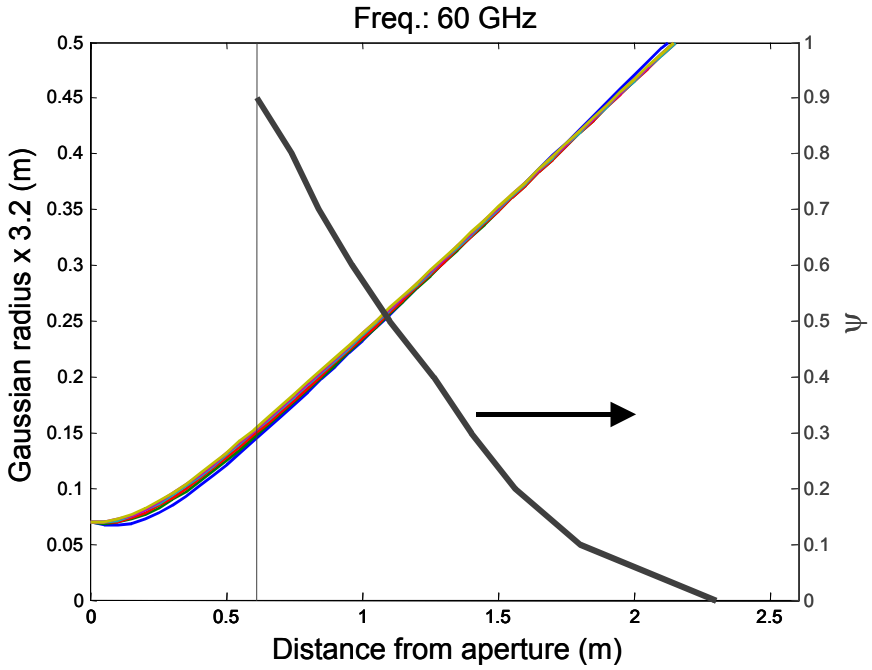

Figure 34. Gaussian beam diameters as functions of distance for an aperture of 70 mm and different radii of curvature at the aperture. On the right ordinate is the flux mapping versus the distance from the aperture for a LFS launch. These configurations are approximately equivalent to a beam bundle with $\Omega = 2^\circ$.

As a reference, all receivers beams are straight ($\Omega_\kappa^s = \Omega_\theta^s = 0^o$) with diameters of $D_{b\kappa}$ = $D_{b\theta}$ = 200 mm. Changing the $D_{b\theta}$ of the probe and receivers does not significantly affect the beam overlap since it changes the beam width in the beam plane. However, it does affect the radial resolution.

2.5.2.2 Resolving power and robustness to variations in density

Figure 35 shows the resolving power, L, versus the flux coordinate, ψ, where the scattering volume is located. The red points and curves are for the lower receiver (position 1) shown in Figure 32 a, while the blue points and curves are for the upper receiver (location 2) shown in Figure 32 b. This colour scheme is used in Figure 36 to Figure 42. The flux coordinates of the points in Figure 35 correspond to the spatial locations of the scattering volumes shown in Figure 32. Figure 36 shows the corresponding values for the beam overlap. Both graphs are at DS = 1.0 and show the effect of changing the density ±10%. The negative flux coordinate values represent the HFS measurements. In general, receivers in position *1* (in red) have lower resolving power and beam overlap than receiver in position *2* (in blue). This is due to the larger scattering angles for receiver position *2*, and the corresponding larger beam overlap values. In position *2* the scattering volumes are larger than those obtained with position *1*, resulting in poorer radial resolution for the same beam diameters. For example, for the measurement in the centre of the plasma, the two receiver positions have approximately the same angle, ϕ, between the resolved fluctuations and the magnetic field with ϕ=98.6˚ and ϕ=99.0˚ respectively. The scattering angle θ for receiver position *1* is 140.3˚ and for receiver position *2* it is 160.4˚. Consequently, for the same beam overlap, the resolving power, as found with the simple parameterization given in equation (1.21), is 10 % higher for receiver position *1* than for position *2*. However, the beam overlap (and scattering volume) for receiver position *2* is about twice that of receiver position *1*. This demonstrates the compromise between beam overlap and resolving power on the one hand, and radial resolution on the other.

Another issue to compare between the two receiver positions is the access of the LFS plasma. Receiver position *1* requires larger angles from the horizontal plane compared to receiver position *2*. For example, to access the plasma on the LFS at ψ = 0.25, receiver position *1* requires an angle of 35˚ from the horizontal (θ_L^s = 55˚) compared to about 15˚ (θ_L^s = 75˚) for receiver position *2*. Viewing directions with smaller θ_L^s are more susceptible to refraction. Measuring the HFS plasma with the LFS backscattering system generally results in poorer radial resolution and smaller resolving powers than LFS measurements.

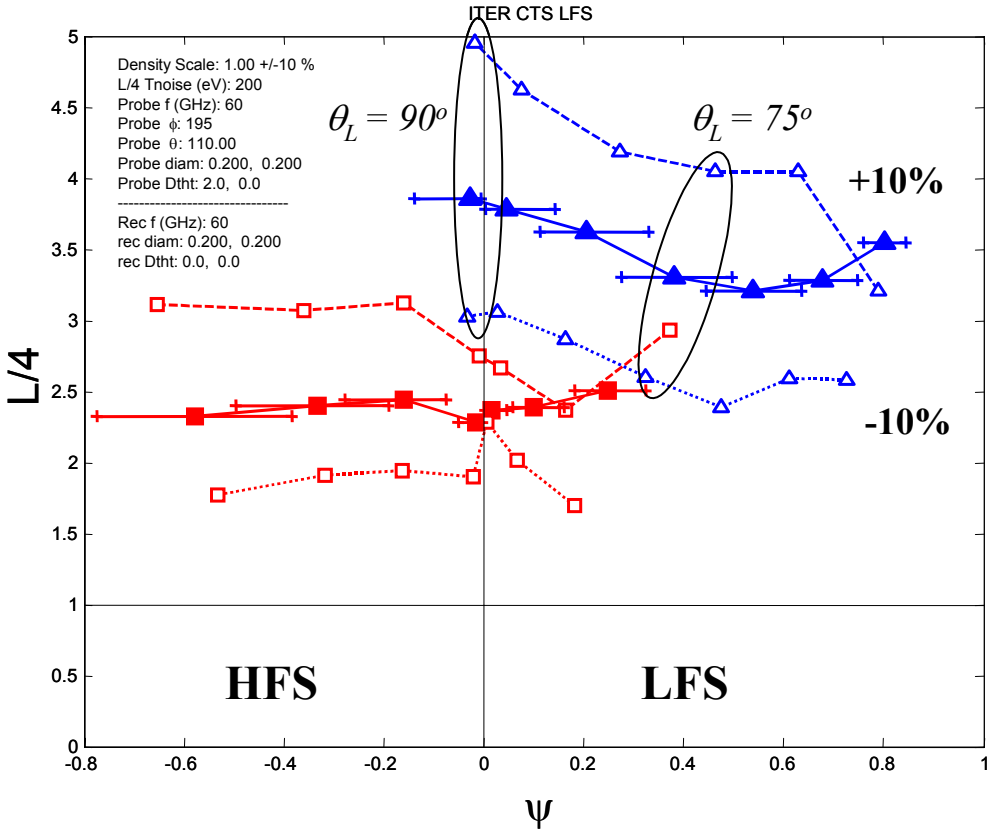

Figure 35. L / 4 of the two receivers for the angles shown in Figure 32 versus the magnetic surfaces, where the centre of the scattering volume is located. Data for receiver position 1 are shown in red and for receiver position 2 in blue. DS = 1.0 ±10% variation. $D_{b\theta}{}^{i} = D_{b\kappa}{}^{i} = D_{b\theta}{}^{s} = D_{b\kappa}{}^{s} = 200$ mm, $\Omega_{\kappa}^{s} = \Omega_{\theta}^{s} = 0°$ for the receivers and $\Omega_{\kappa}^{i} = 2°$, $\Omega_{\theta}^{i} = 0°$, $\kappa^{j} = 10°$ for the probe. The dashed lines correspond to +10% and the dotted lines correspond to −10%. Note, the negative flux coordinate values represent the HFS measurements.

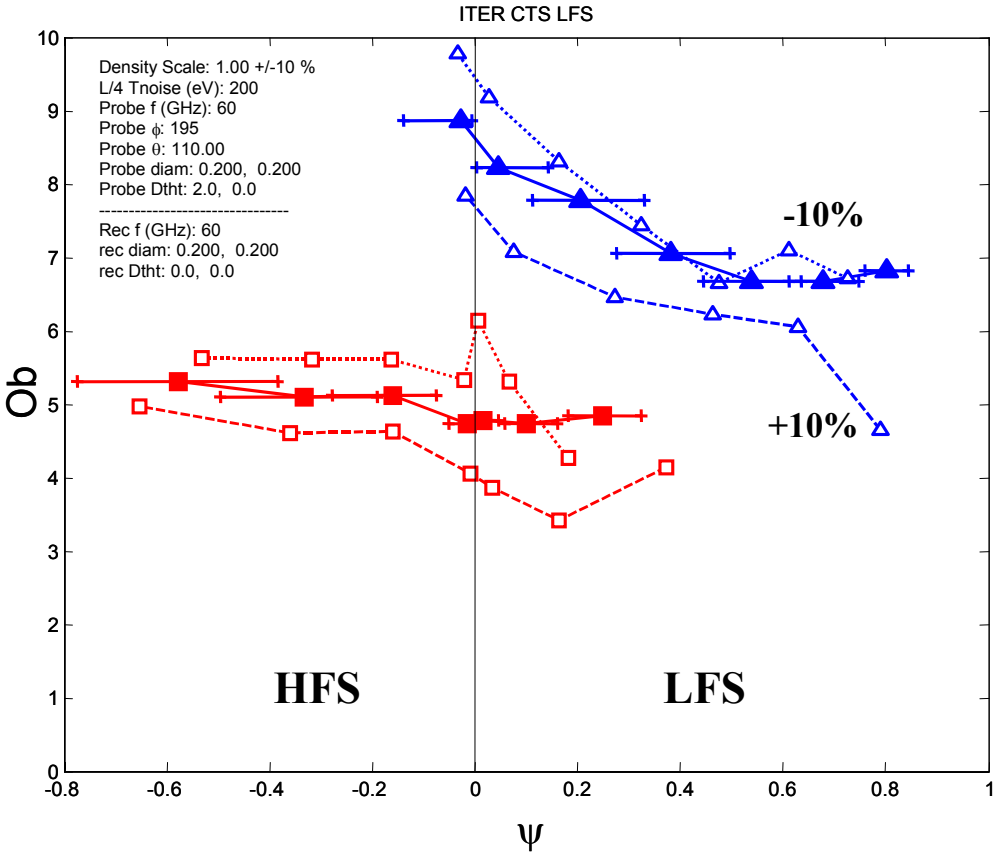

Figure 36. Beam overlap at different radial position for receiver position 1 in red and receiver position 2 in blue. Same beam configuration as in Figure 35.

Recall that the graphs assume beam diameters of $D_{b\theta}$ = 20 cm. Appendix D shows L/4 radial profiles at two values of $D_{b\theta}$. The flux surface extents of the scattering volumes in the centre are $\Delta\Psi$ = 0.23 and 0.08 for $D_{b\theta}$ = 200 mm and 100 mm respectively. To focus the beam in the beam plane (reducing $D_{b\theta}$) down to diameters < 200 mm in the centre requires aperture diameters in the vessel wall > 200 mm as shown in section 2.3. For example, if we were to use the Gaussian beam properties from Figure 28 with the aperture diameter of 200 mm, the radial resolution can only be improved in the region between ψ = 0.4 and 0.6. On the other hand, an aperture diameter of 300 mm in the poloidal direction will enable improvement of the radial resolution in the centre. Figure 35 shows that the system is robust against 10% fluctuations in density at the reference density. Figure 37 and Figure 38 show the radial profile of the resolving power at DS = 0.7 and DS = 1.1 respectively. The minimum requirement of L/4 > 1 is satisfied at these densities including the density variations. The robustness of radial positioning against density fluctuations at DS=0.7 and DS = 1.0 is satisfactory with a maximum $\Delta\psi$ = 0.13. At a higher density of DS=1.1, the central measurement is robust in radial positioning especially for receiver position *2*. However, at larger radii it is less satisfactory. This is not surprising since at higher densities and smaller θ_L the beams are more sensitive to refraction. The optimisation to improve robustness of radial positioning at higher densities such as using a smaller value of κ^j for the probe is still ongoing.

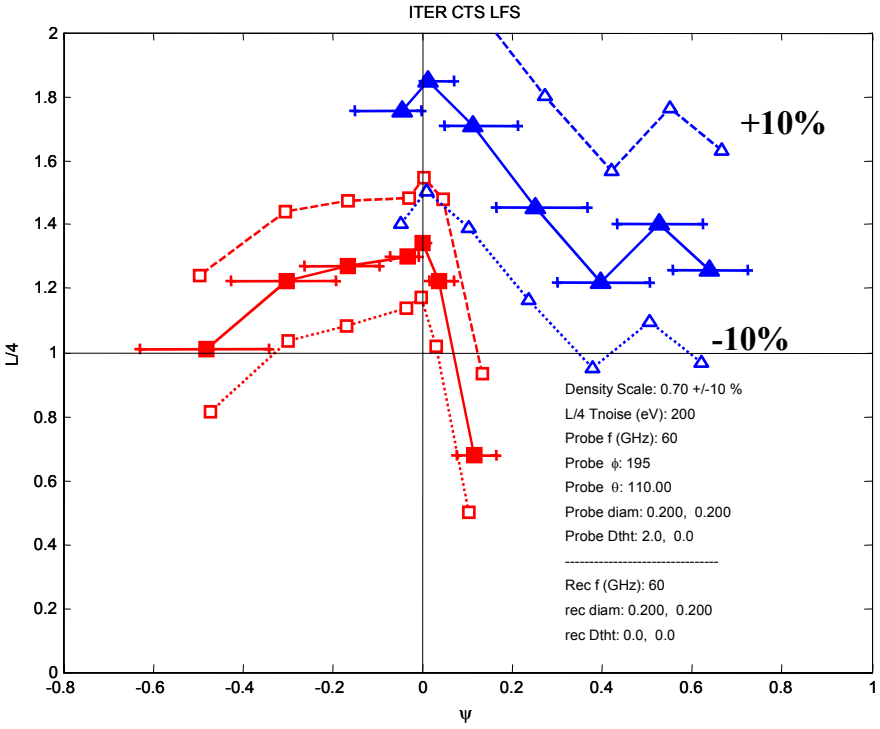

Figure 37. *L* /4 of the two receivers for the angles shown in Figure 32 versus the magnetic surfaces where the centre of the scattering volume is located. DS = 0.7 ±10% variation. $D_{b\theta}$ = 20 cm. The dashed lines correspond to +10% and the dotted lines correspond to –10%.

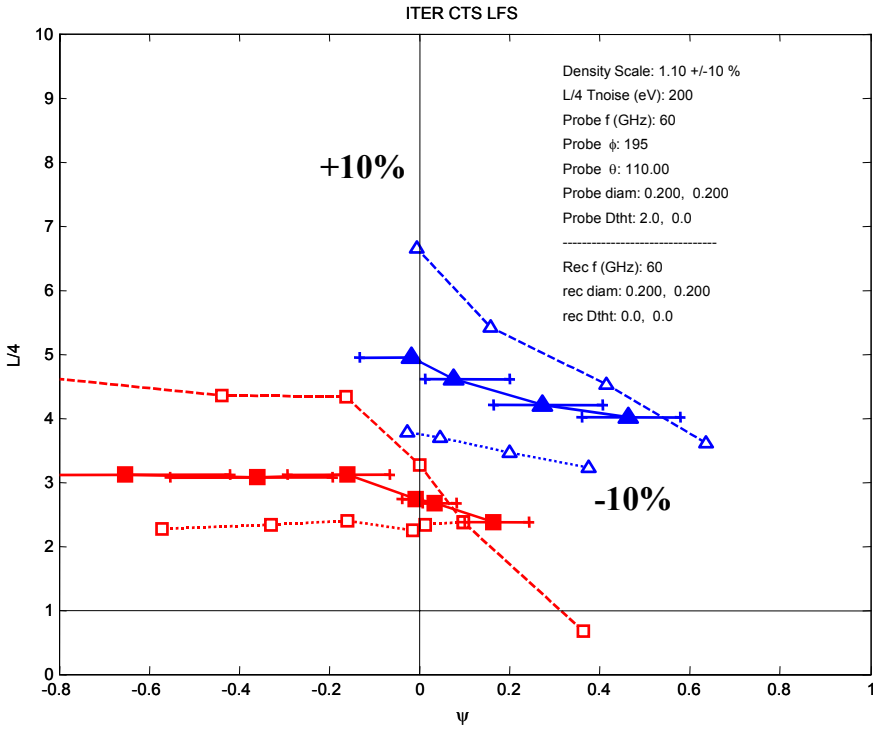

Figure 38. *L* /4 of the two receivers for the angles shown in Figure 32 versus the magnetic surfaces where the centre of the scattering volume is located. DS = 1.1 ±10% variation. $D_{b\theta}$ = 20 cm. The dashed lines correspond to +10% and the dotted lines correspond to –10%.

2.5.2.3 Dispersion effects

Dispersion reduces the beam overlap at the spectral limits of the fast ion feature. The spectral half width is $\delta\upsilon^s = v_\alpha k^\delta / 2\pi$ where v_α is the particle velocity. Using the fusion alpha birth velocity of 12.9×10^6 m/s at 3.5 MeV, the spectral half width of the LFS system ranges from 2.5 to 4.5 GHz as shown in Figure 39. The calculation of the resolving power in the previous section assumes that the overlap is constant over the spectral range. This, of course, is not the case; the overlap may degrade at higher and lower frequencies within the spectral width. Hence a *minimum* resolving power (L^*) is plotted in Figure 40, which is the *L* calculated with the lowest overlap value within the frequency range. The same has been done for density factors of DS = 0.7 (Figure 41) and DS = 1.1 (Figure 42). Not surprising, DS = 0.7 has a relatively weak sensitivity to dispersion in contrast to higher densities, where the beam overlap is more sensitive to frequency. All graphs show that the minimum requirement on the beam overlap, derived from the requirement on the resolved power, is satisfied over the whole spectral range for receiver position *2*.

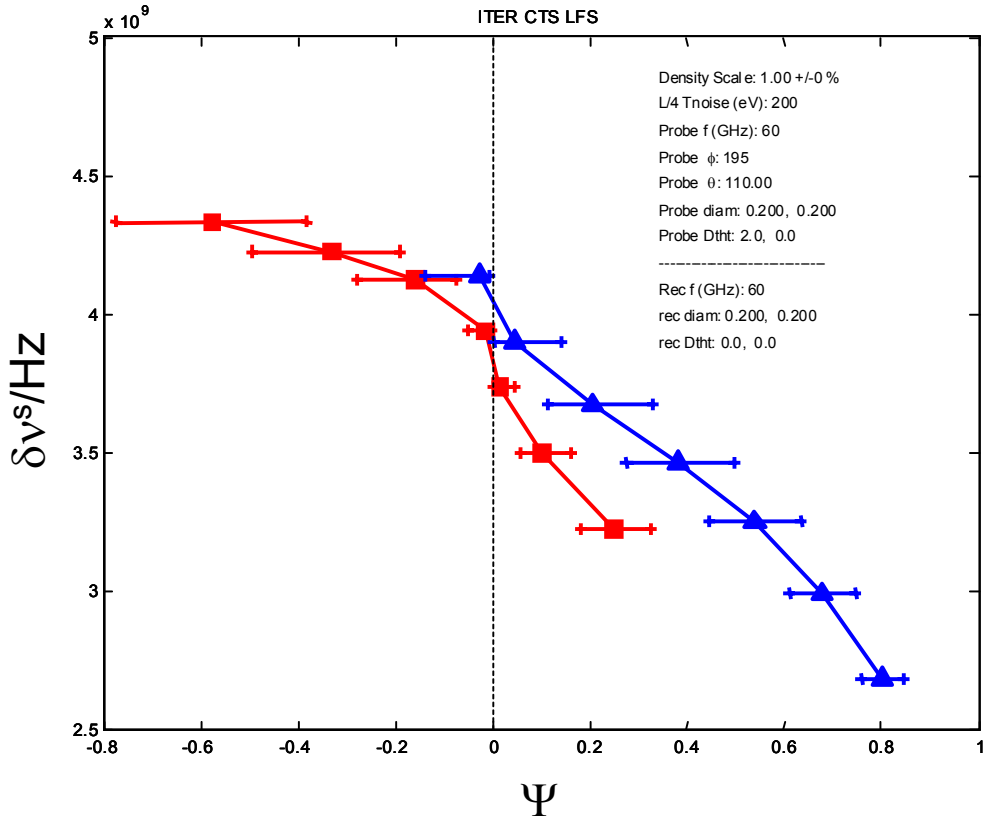

Figure 39. The spectral half-width for the LFS detectors. Data for receiver position 1 are shown in red and for receiver position 2 in blue.

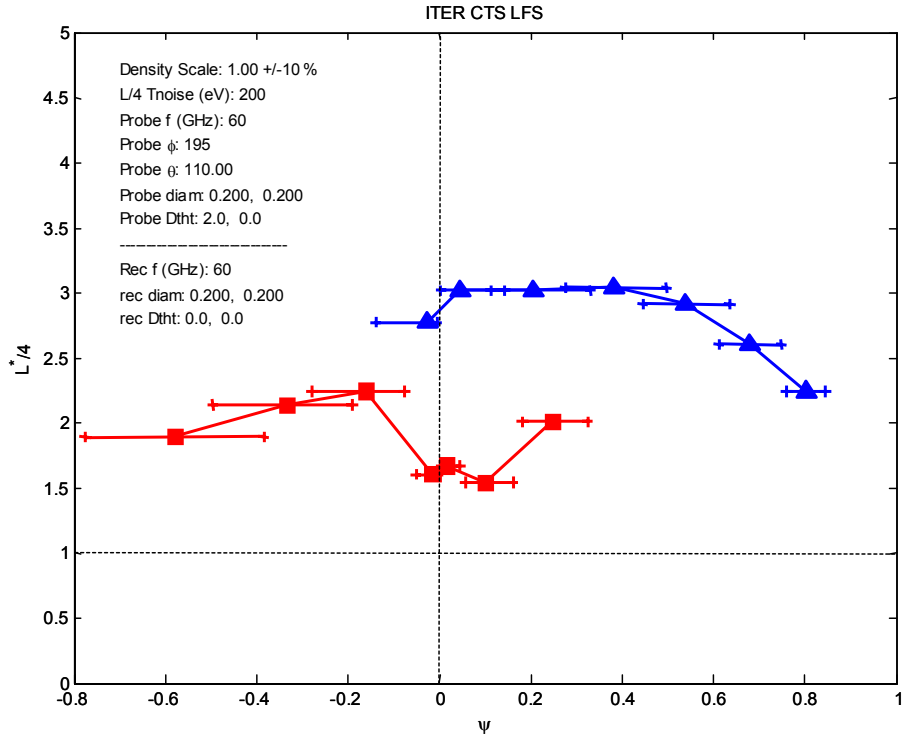

Figure 40. The resolving power divided by 4, $L^*/4$, obtained assuming the lowest beam overlap within the frequency range, plotted as a function of Ψ for both detector positions for a plasma density of DS = 1.0.

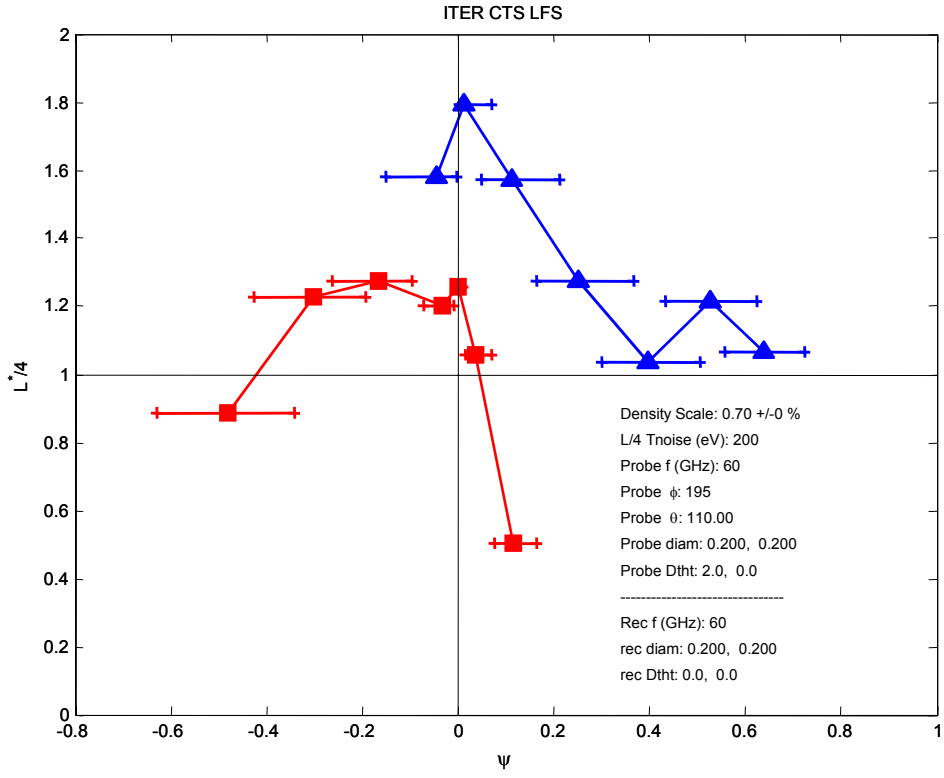

Figure 41. As Figure 40, only here with DS = 0.7.

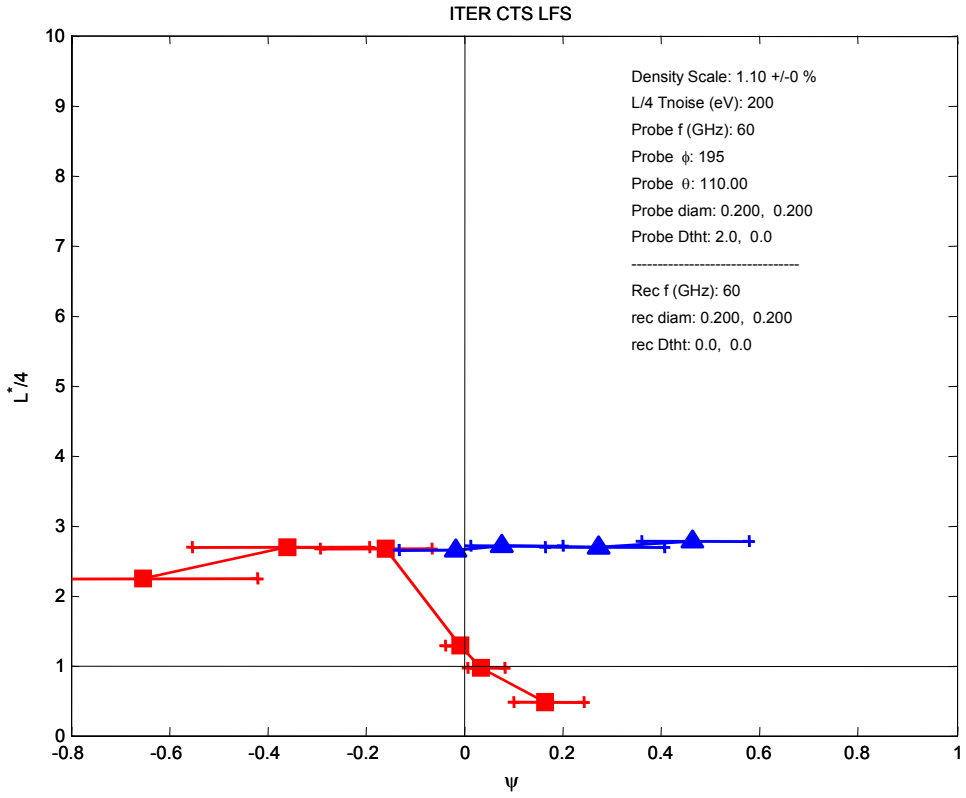

Figure 42 As Figure 40, only here with DS = 1.1.

2.5.2.4 Spectral information for the LFS system

The issue of spectral information was already discussed at some length in section 1 both in general and for the individual frequency options. Hence, in this subsection we just briefly present the key figures showing the principal component analysis and spectral power density of the central measurement point of Figure 35 (receiver position *2*) at DS = 1.0 for the LFS system. Recall that in all the calculations of resolving power of the LFS system we use a gyrotron power of 1 MW, an integration time of 20 ms, and the noise temperature level of 200 eV. The results are presented in Figure 43 to Figure 45. It is worth noting that in the spectra the fast ion feature is clearly distinguishable above the electron feature. Further we note the smallness of the uncertainties in the determination of the fast ion distribution despite the many resolved nodes, and the high resolving power of $L=15$, which implies that 28 orthogonal components of the fast ion distribution can be resolved with an STD uncertainty which is typically $L/28^{1/2} = 2.8$ times smaller than the target of 6×10^9s/m^4, i.e. typically close to 2×10^9s/m^4. If the uncertainties in nodes were equal and uncorrelated then this would be the magnitude of the magenta error bars shown in Figure 44. The finite correlations, brought out in the principal component analysis presented in Figure 45, cause the slight increase of the error bars to the level of 3×10^9s/m^4 found in Figure 44. If we chose to reduce the number of nodes to 16 then the STD uncertainty in resolved components would typically be $\Delta/(L/4) = 1.6\times10^9$s/m^4. With an mean fast ion phase space density in the range of 20×10^9s/m^4 , as may be expected (see Appendix A), this implies a typical relative uncertainty of less than 10 % with 16 components resolved, and less than 15 % with 28 components resolved.

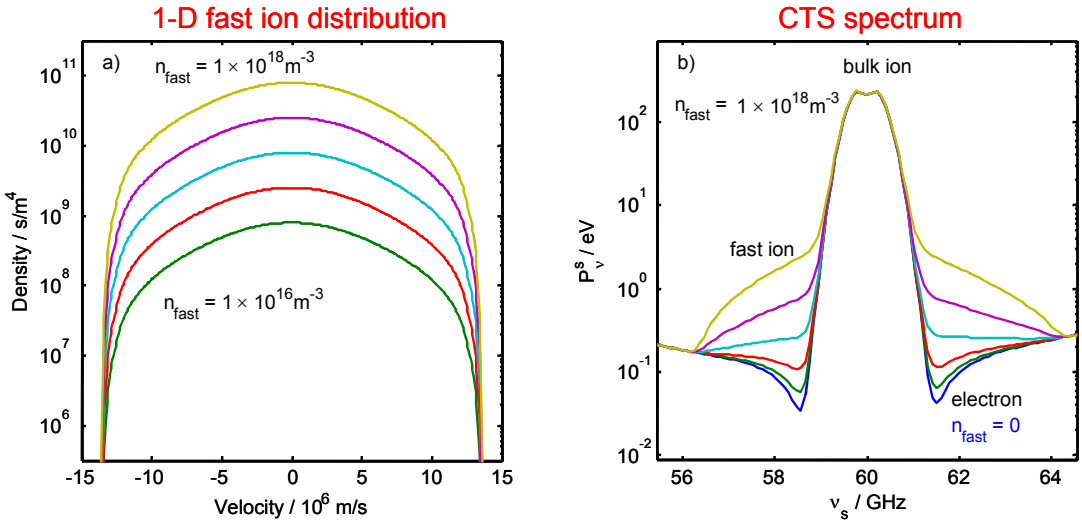

Figure 43. CTS spectral power densities (right) for a range of fast ion densities (left) for the central measurement point of Figure 35 (receiver position *2*) at a density scaling of DS = 1.0 for the LFS system and a gyrotron power of 1 MW.

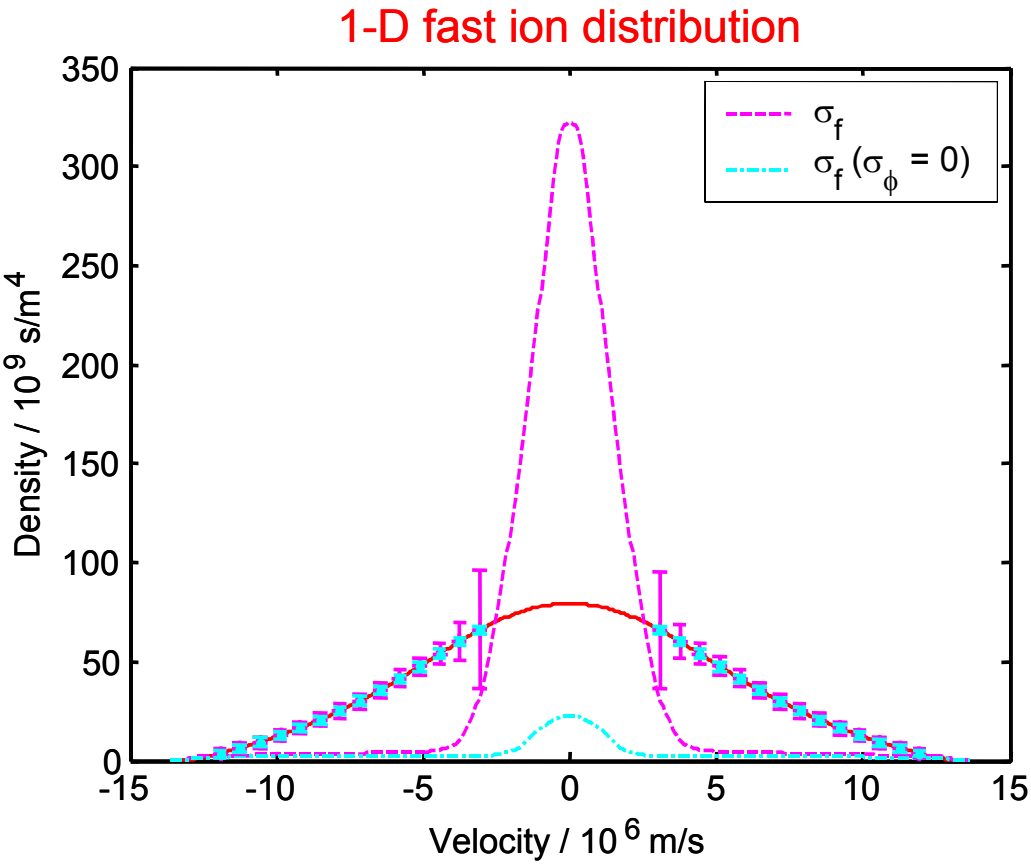

Figure 44. Resolution of the fast ion distribution for the central measurement point of Figure 35 (receiver position *2*) at DS = 1.0 for the LFS system, with a noise temperature, T_N, of 200 eV, a gyrotron power of 1 MW and an integration time of 20 ms. The corresponding resolving power, L, is 15.

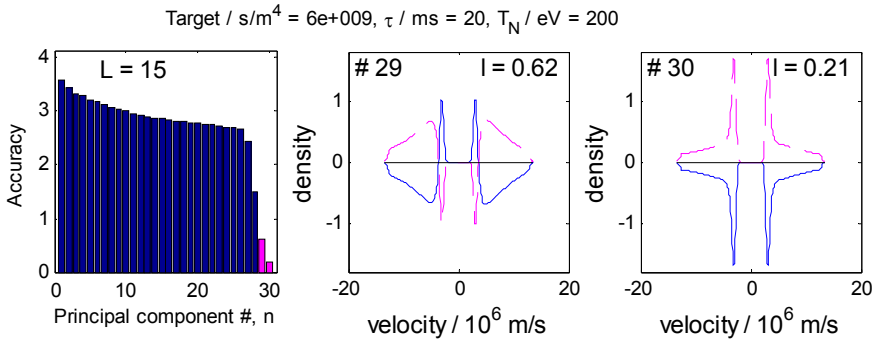

Figure 45. Principle components analysis of the central measurement point of Figure 35 (receiver position *2*) at DS = 1.0 for the LFS system, with a T_N of 200 eV, a gyrotron power of 1 MW and an integration time of 20 ms. Right, accuracies of the principal components of the posterior for the resolved nodes of the fast ion distribution. Centre and left are the functional shapes of the most poorly resolved principal components.

2.5.3 55 GHz option

This section investigates the feasibility of using a probe frequency of 55 GHz. Since this frequency is considered for operation at higher plasma temperature, the analysis is made at DS = 1.0 and TS = 1.4. The beam parameters are identical to the optimised case for 60 GHz in the previous subsections. At this lower frequency we are approaching the low field side L-cutoff of 49 GHz hence there is more concern about refraction. The receivers measuring at smaller θ_L (more extreme angles from the horizontal) are reflected as illustrated in Figure 46. This figure shows the beam traces at ν^i = 55 GHz for the same launch angles of receiver position *2* as in the previous section. We include only receiver position *2* in this study due to the less favourable results from receiver position *1*. Figure 47 shows the comparison of beam overlap between ν^i = 55 GHz and 60 GHz for the same beam configurations. Surprisingly, the degradation is constant over the radial profile.

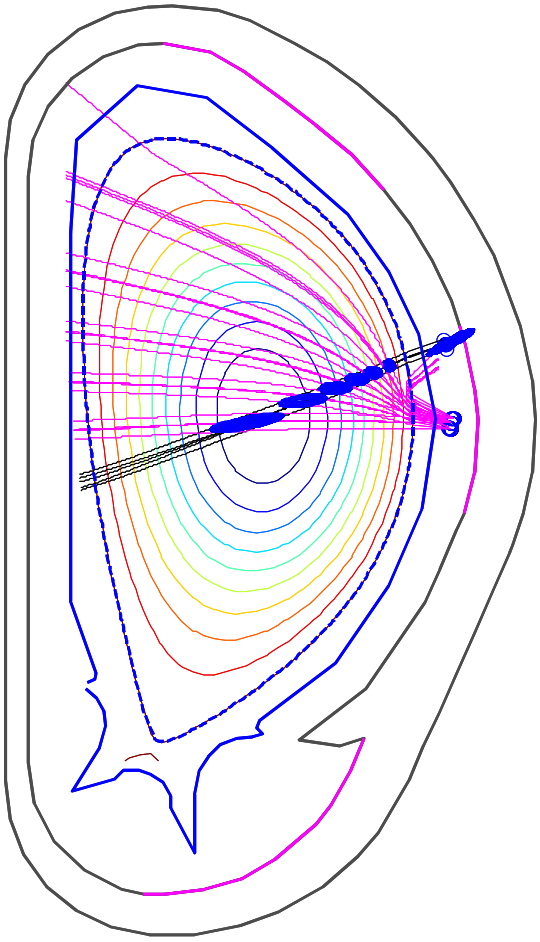

Figure 46. Poloidal projection of the beam traces at ν = 55 GHz for the same θ_L scan as in Figure 32.

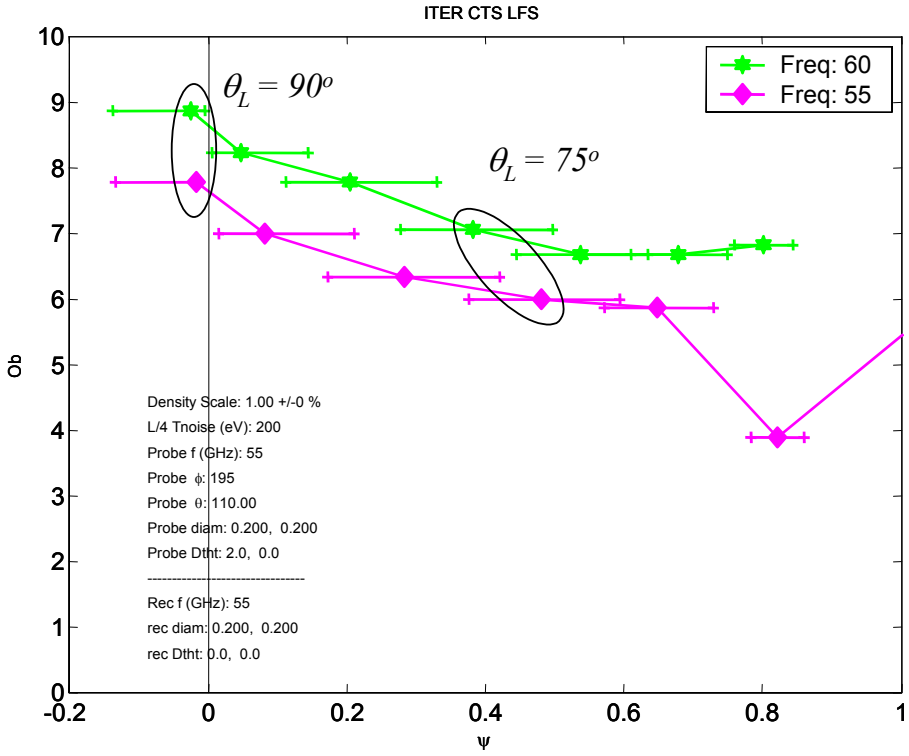

Figure 47. Comparison of the overlap between 60 and 55 GHz for receiver position *2* at the same θ_L angles as used for Figure 35. The plasma density scaling factor for both is DS = 1.0. The temperature scaling for the 60 GHz and 55 GHz case is 1.0 and 1.4 respectively.

The radial positions change significantly between the two frequencies. However, the central measurement remains unchanged. With lower frequency we approach the L-cutoff and thus, the beams are more susceptible to density variations. This is confirmed in Figure 48 and Figure 49 which show the behaviour of the beam overlap and L /4 with a 10% variation in density at DS = 1.0. The radial robustness is relatively poor. For example, for the measurement at $\theta_L = 75°$, the radial position shifts over the range of $\psi = 0.4 – 0.7$. However, the figures also show that the only measurement which is very robust is the central measurement, obtained with $\theta_L = 90°$.

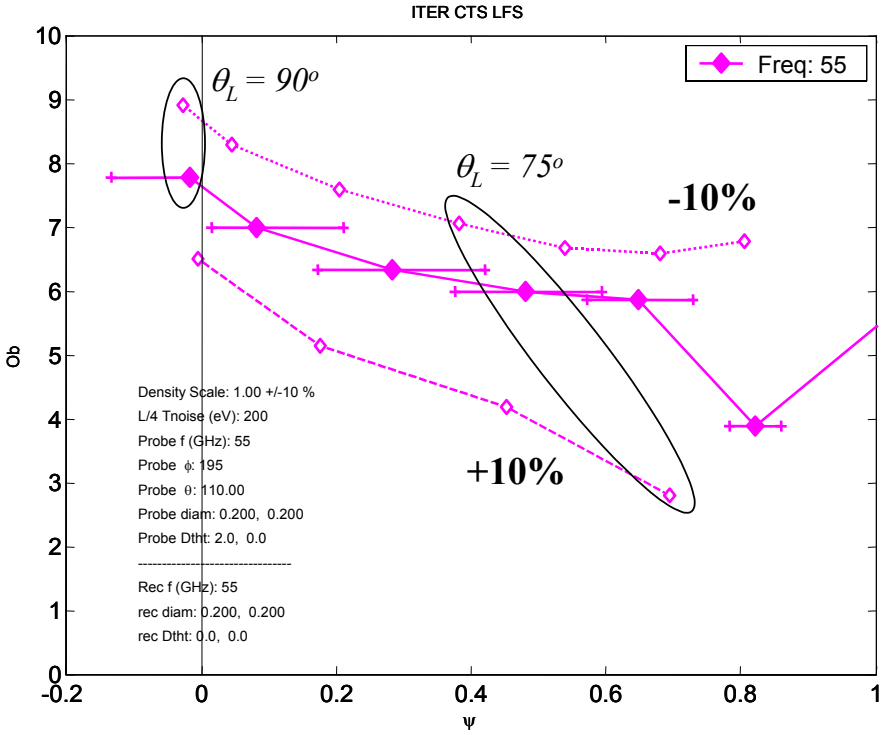

Figure 48. Radial profile of beam overlap at ν^i = 55 GHz for receiver position 2 at DS = 1.0, TS = 1.4, with a 10% density variation (dashed: +10%, dotted: -10%).

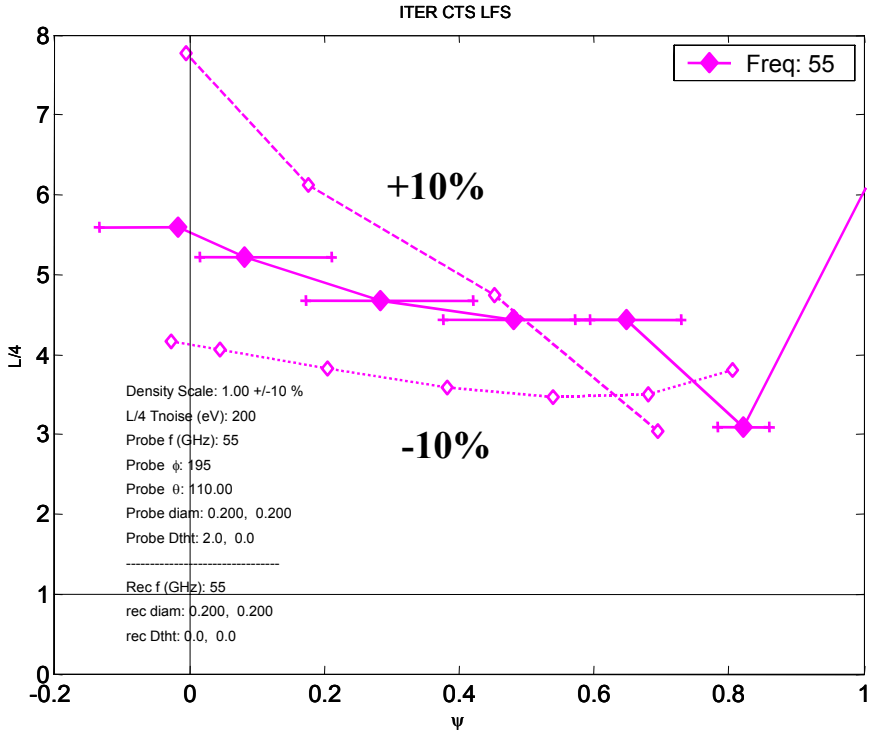

Figure 49. L / 4 at ν^i = 55 GHz for receiver position *2* at DS = 1.0, TS = 1.4, with a 10% density variation (dashed: +10%, dotted: -10%).

Analysing the effects of dispersion at this frequency, Figure 50 illustrates the non-symmetrical effect on beam overlap over the spectral width. Frequencies below

55 GHz suffer increasing degradation of the beam overlap because of the approach to the L-cutoff. To demonstrate this effect, Figure 51 shows the poloidal and top view of beam traces at one launch angle measuring at $\psi = 0.31$ at the central frequency. The plots also show beam traces at the frequencies at the two ends of the spectral range. Figure 52 shows the resolving power assuming the minimum beam overlap within the spectral range for both 60 and 55 GHz, which is still above the required limit, except near the plasma edge with the 55 GHz probe.

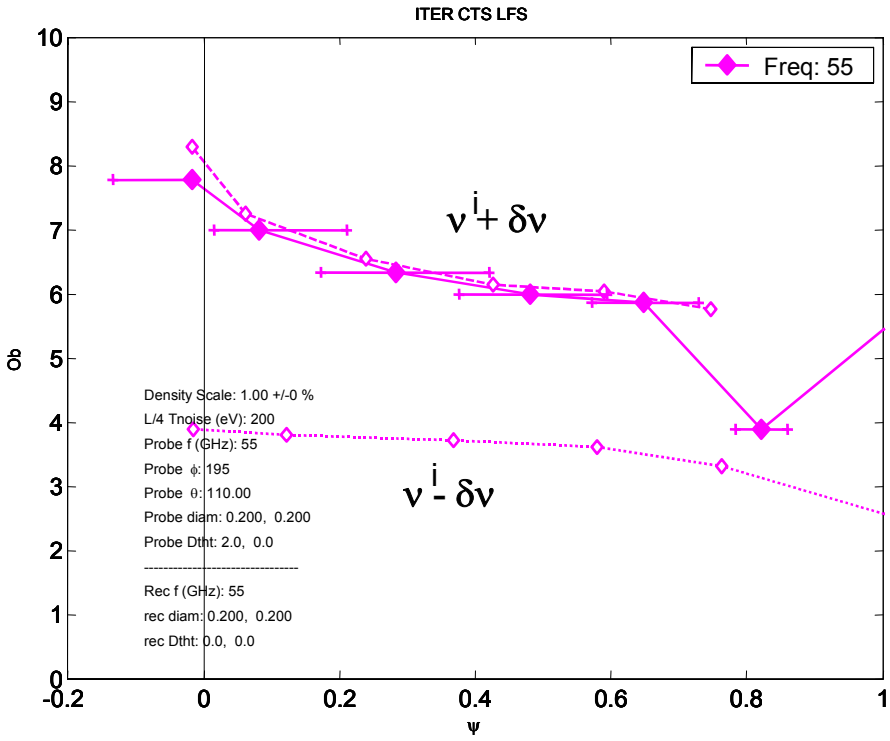

Figure 50. Radial profile of the beam overlap at $\nu^i = 55$ GHz and at $\nu^i \pm \delta\nu$ for receiver position 2 at DS = 1.0 and TS = 1.4. The spectral width depends on the scattering angle and is computed separately for each point on the graph.

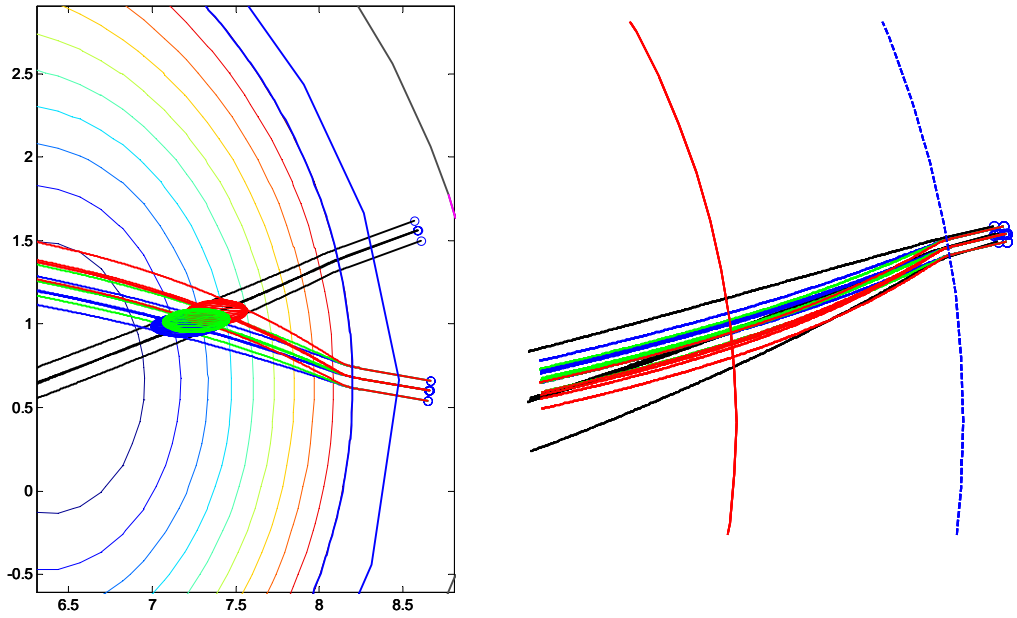

(a) **(b)**

Figure 51. a) Poloidal map and b) top view of probe and receiver beams. In a) is also plotted the associated scattering volumes. The receiver beams are for the three frequencies of $\nu^i = 55$ GHz (green), $\nu^i + \delta\nu = 57.86$ GHz (blue), and $\nu^i + \delta\nu = 52.14$ GHz (red).

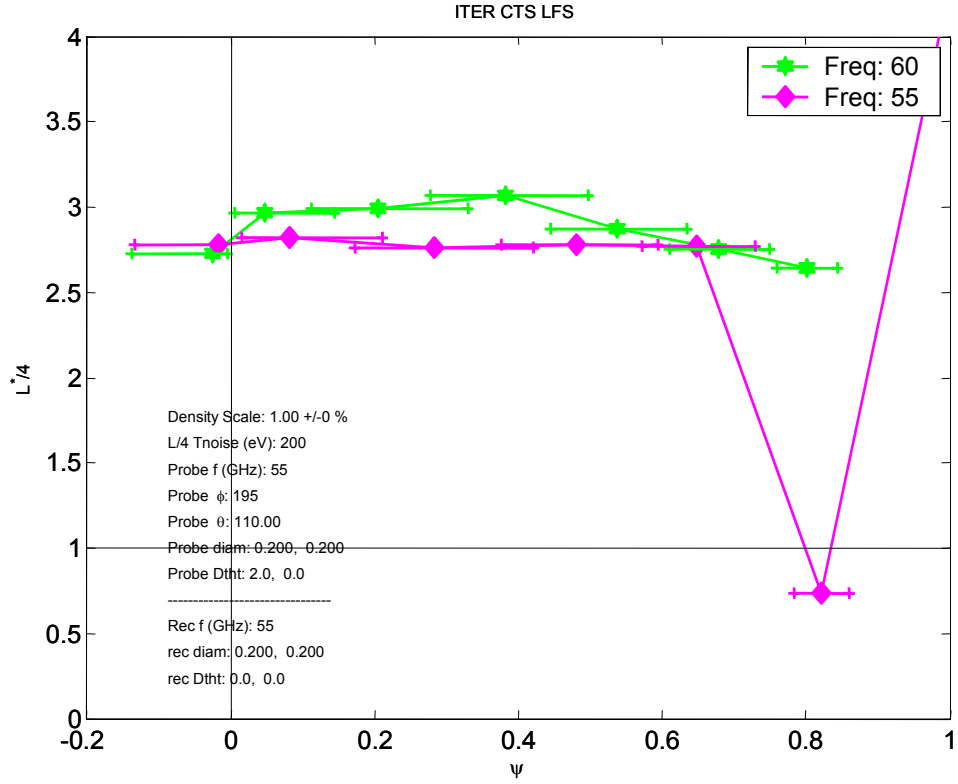

Figure 52. Comparison of L*/4 between 60 and 55 GHz for receiver 2 at the same θ_L angles as in Figure 35. The plasma density scaling factor for both is DS = 1.0. Temperature scaling for the 60 GHz and 55 GHz cases are 1.0 and 1.4 respectively.

2.5.4 Conclusion

In subsection 2.5 we considered a back scattering system with receivers on the low field side, which resolves the perpendicular velocity distribution. For the reference plasma this system can achieve a radial resolution of better than $a/10$ (the ITER requirement) and a radial coverage from half radius on the high field side to ¾ radius on the low field side. The achieved resolving power was above 10 across the profile, corresponding to for instance the ability to resolve 16 points on the fast ion velocity distribution (8 either side of zero velocity), with an accuracy which is $L/4 = 2.5$ times better than the target accuracy of $\Delta = 6\times10^9 s/m^4$, i.e. with error bars smaller than $3\times10^9 s/m^4$, thus fully meeting the ITER measurement requirements discussed in subsection 1.1. With a mean fast ion phase space density in the range of $20\times10^9 s/m^4$, as may be expected (see Appendix A), this implies a typical relative uncertainty of less than 15% with 16 components resolved. This with a time resolution of 40 ms (20 ms integration time and probe modulated on-off with a duty cycle of 50%).
Since we are closer to the L-cutoff on the LFS than on the HFS, the receiver beams of this system are more susceptible to refraction than those of the HFS system. The general trend in beam refraction at these frequencies is that the smaller the angle (toroidally and poloidally) between launch direction and density gradient, the less sensitive the beam trajectory is to changes in density and frequency. Using receiver position *2* rather than *1*, which reduces the radial resolution and increases the resolving power, gives a more robust system and results in a very satisfactory resolving power from the plasma centre to the LFS edge. The most important measurement is the centre of the plasma. Receiver position 2 is viewing this region at $\theta_L = 90°$, which makes this view the most robust one. A 70 × 300 mm opening in the vessel for the probe gives the system added flexibility to focus the beam in the beam plane to ensure good resolution and widen the beam orthogonal to the beam plane to ensure robustness. The radial coverage would be $\psi = 0$ to 0.7 for DS = 1.0, and $\psi = 0$ to 0.5 for both DS = 0.7 and 1.1. To operate at higher temperatures, a dual frequency system is envisaged: one at 60 GHz and the other at 55 GHz. The 55 GHz option, intended to operate at higher temperatures of TS = 1.4 (35 keV), uses the configuration which was optimised for 60 GHz. The minimum requirement of the resolving power is satisfied for the 55 GHz frequency range. However, the robustness of radial positioning against density changes and dispersion is rather poor except for the central measurement.

2.6 HFS forward scattering system

2.6.1 Set-up

For measurement of the parallel component of the fast ion velocity distribution, a HFS forward scattering system is proposed. Analyses on ITER plasma scenarios have shown that LFS back scattering system with toroidally launched probes and viewing detectors to measure the parallel velocity distribution are susceptible to significant refraction resulting in a fragile system, especially at higher densities. The top view of the HFS system is illustrated in Figure 53. A top view of the *k* vectors in Figure 54 shows the fluctuation vector $\mathbf{k}^{\delta}$, and hence the resolved velocity direction, is mainly parallel to the magnetic field.

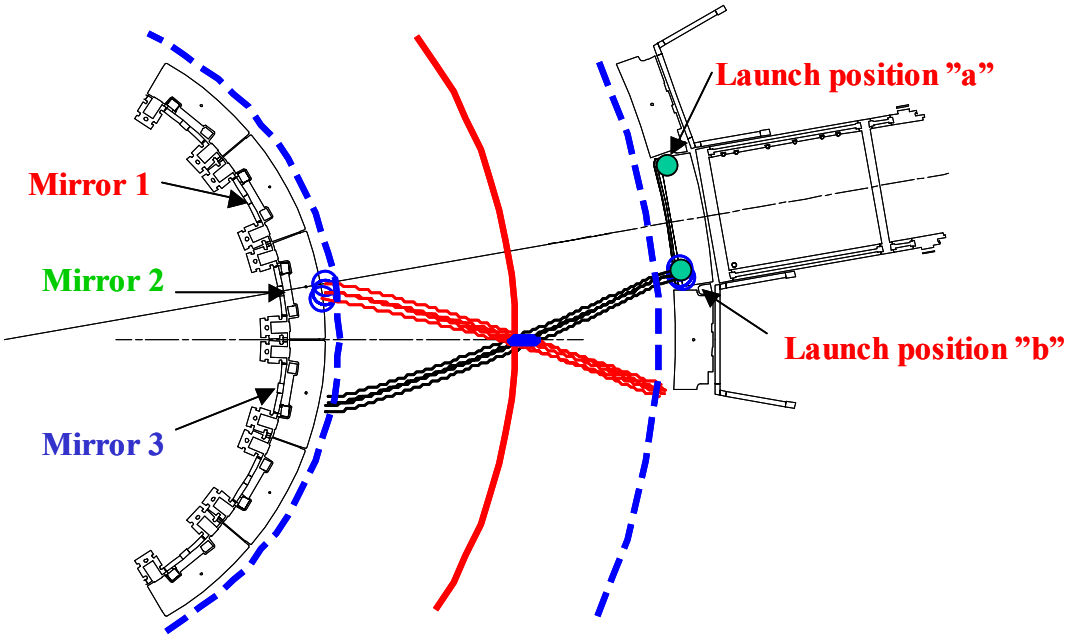

Figure 53. Top view of the HFS system. In the analysis, probes are launched from positions "a" and "b" and receiver mirror positions 1, 2, and 3 are considered.

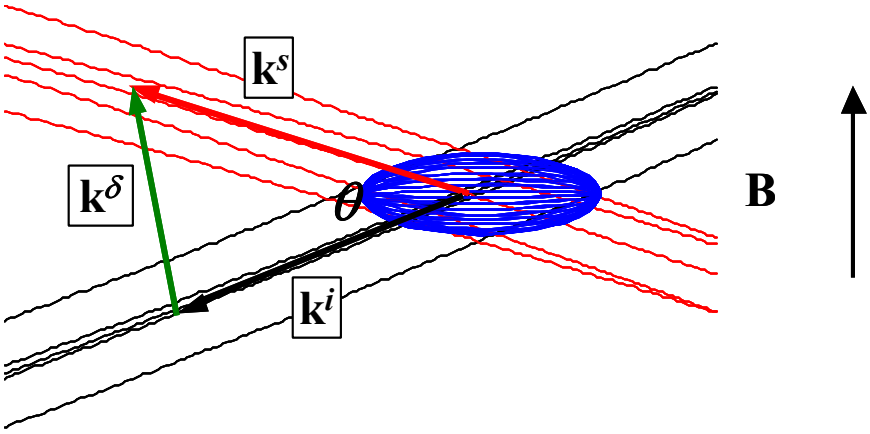

Figure 54. HFS scenario: A top view projection of the probe beam (black), receiver beam (red), the scattering volume (blue) with the wave vectors of the received scattered radiation, $\mathbf{k}^s$, and the incident probe radiation, $\mathbf{k}^i$, and the resolved fluctuations, $\mathbf{k}^\delta = \mathbf{k}^s - \mathbf{k}^i$.

Figure 53 shows the LFS port position with respect to the HFS blanket modules. The possible probe launch locations are labelled position "a" and "b", while the three possible mirror positions for the receivers are labelled 1, 2, 3. The HFS receivers consist of a quasi-optical mirror located behind the blanket modules and use the gap between the modules as an antenna as sketched in Figure 55. The blanket modules to be used are labelled 3 and 4. The gap between the two modules views the plasma near the equatorial midplane. The mirror behind the blanket module couples to a number of waveguides each positioned to view different angles. Similar to the reflectometry system, the signals are brought out in waveguides which run up along the vacuum vessel wall behind the blanket modules toward the upper port. The waveguides will be

located toroidally between the cooling manifold and the blanket module central anchor point as illustrated in Figure 55 (b). The width of the mirror is 35 mm and the vertical gap is assumed to be 30 mm.

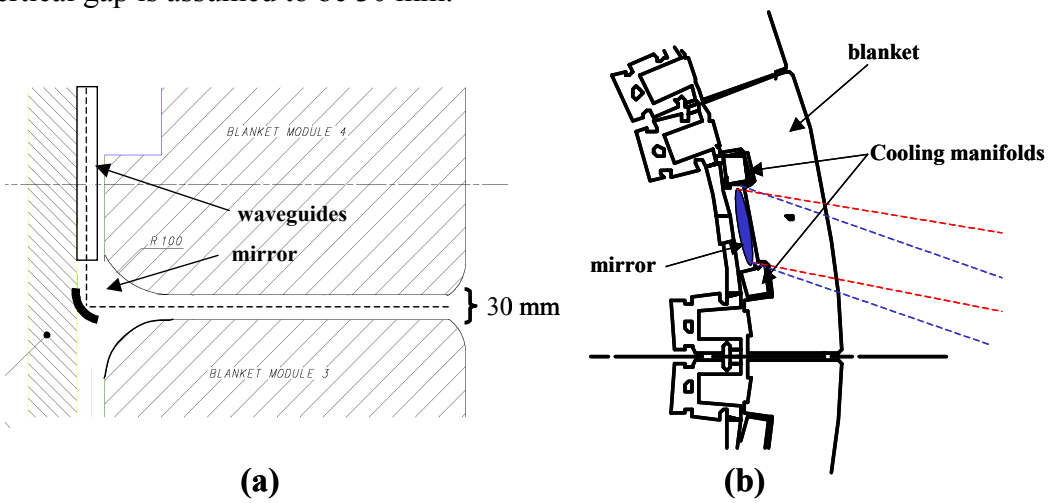

Figure 55. (a) Cross section of blanket modules 3 and 4 with mirror coupled to wave guides assuming modification to the blanket modules gap diameter to 30 mm. (b) Top view of mirror position behind the blanket modules.

2.6.2 Antenna pattern between blankets

The width of the antenna pattern of the slot between the blankets impacts on the performance of the diagnostic. A simple 2 dimensional full wave modelling of the emission from a slot aperture antenna is used to calculate the field structure. We assume:

- No variation in the the horizontal direction, y, i.e. $\partial_y = 0$.
- The aperture is in the plane $x = 0$ and centred on $z = 0$.
- The domain is finite in z and semi-infinite in x.
- At $x = 0$ the field is 0 outside the aperture. It can be constant or have a variation inside the aperture.

Here we investigate the radiation pattern from a uniform field distribution over an aperture, which is 6 wavelengths high (30 mm for a frequency of 60 GHz). This might be considered the fundamental slot mode. Figure 56 shows the power pattern near the aperture. Cross sections at different position are fitted by a Gaussian and the half-width w is plotted versus position in Figure 57.

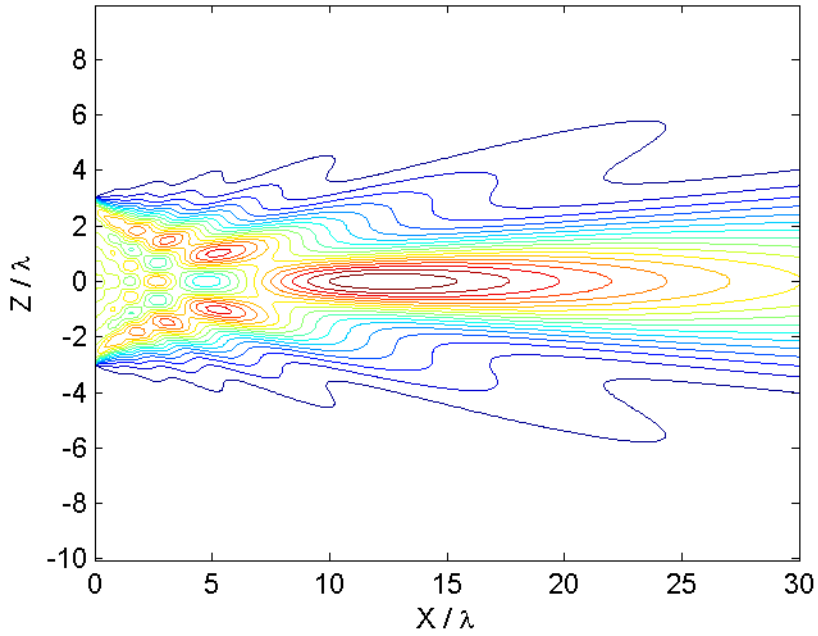

Figure 56. Contour plot of the power pattern near the aperture. The contours are equidistant. The dimensions on the axis have been normalized to the wavelengths.

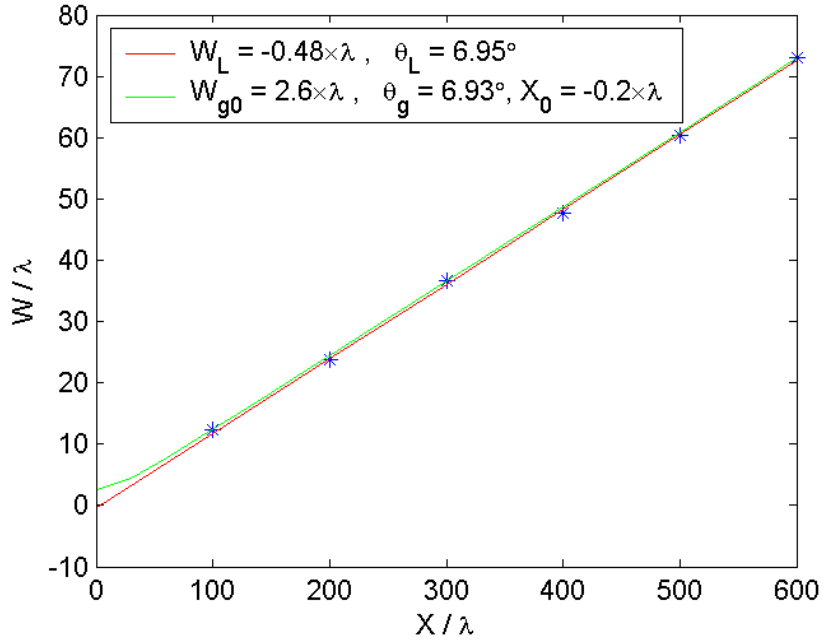

Figure 57 Gaussian half widths, *w*, at a number of distances, x, from the aperture plotted as blue markers. The red line is a straight-line fit. The green curve is a Gaussian beam profile computed from the widths at x = 300λ and 600λ.

In the far field, the central lobe, which has most of the power, is close to a Gaussian power distribution, implying that in the far field the antenna pattern can be

approximated as a Gaussian beam, characterized by its divergence angle, α_θ, (the angle from the beam centre line where the power is reduced to $1/e^2$ of the power at the beam centre) in the vertical direction, which is the Z direction in the present modelling. To good approximation the divergence angle is given by

$$\alpha_\theta = \frac{7^\circ \times 6c}{\nu D_{b\theta}}, \tag{2.1}$$

where c is the velocity of light in vacuum, ν is the frequency, and $D_{b\theta}$ is the receiver poloidal slot width, which is equal to the vertical gap of the blanket modules. Hence at 60 GHz and a vertical gap of 3 cm, the vertical receiver beam divergence angle is $\alpha_\theta = 7^\circ$. This widens the receiver beam pattern in the direction orthogonal to the beam plane, reducing the beam overlap but improving the robustness.

To verify the full wave code, its results are compared with an approximation from Reference [10] for the far-field radiation pattern launched in the E-plane by a rectangular aperture. The rectangular TE_{10} mode uniformly fills the aperture along the direction of the E-field, (30 mm wide). The field expression in the E plane does not depend on the width of the slot or field distribution in the orthogonal direction. It is given by

$$E \propto \frac{\sin Y}{Y} \tag{2.2}$$

$$Y = \frac{kb}{2}\sin\theta. \tag{2.3}$$

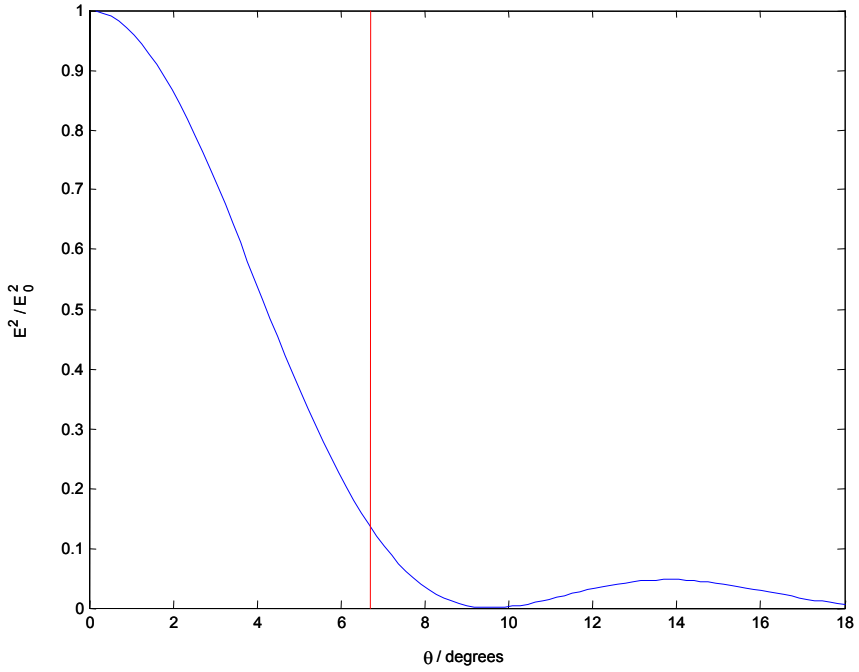

Figure 58. Far field calculation from equations (2.2) and (2.3) as a function of angle. The vertical line represents the Gaussian radius where the power is $1/e^2$ of the maximum.

We see from Figure 58 that the Gaussian radius, indicated by the vertical red line corresponds to an angle of 6.7º, which is in good agreement with the value calculated by the full wave code and the simple parameterization (2.1).

2.6.3 Simulations results

We analysed the options sketched in Figure 53 with probe launch positions "a" and "b", and receivers at positions 1, 2, and 3. This section only shows results for receiver position 2 and launch position b, which give the best results. Analyses of some of the other combinations are given in Appendix E.

2.6.3.1 Optimisation of beam properties

The following summarizes the beam parameters used in the study of the forward scattering system with HFS detectors:

HFS system:

In the beam plane: $D_{b\kappa}{}^{i} = 200$ mm, $\Omega_{\kappa}{}^{i} = 0$, $D_{b\kappa}{}^{s} = 350$ mm, $\Omega_{\kappa}{}^{s} = 0$.

$\perp$ to the beam plane: $D_{b\theta}{}^{i} = 200$ mm, $\Omega_{\theta}{}^{i} = 0$, $D_{b\theta}{}^{s} = 300$ mm, $\Omega_{\theta}{}^{s} = 7$º.

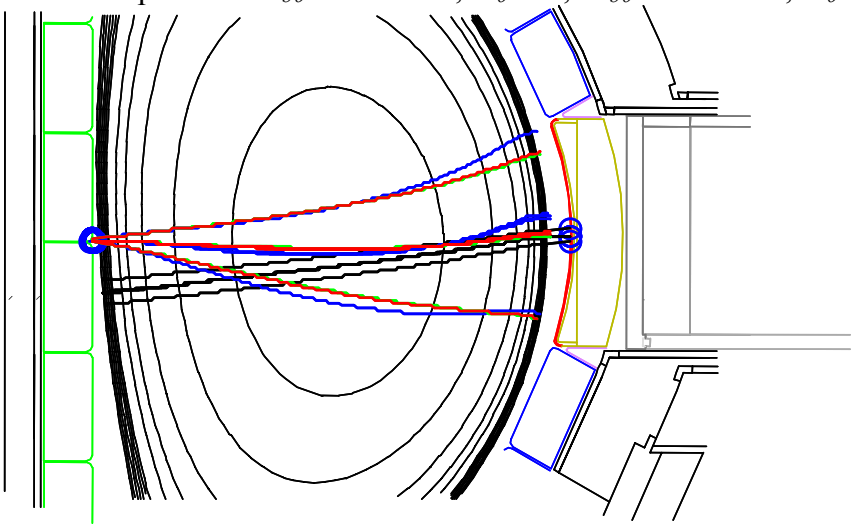

Figure 59. Poloidal view of the probe and receiver beams for the HFS system.

Beam traces of the probe and of two receivers at different κ values are shown in Figure 59. The probe will be launched at $\theta_L > 90^{o}$ to avoid striking the edges of the blanket modules. Therefore the probe poloidal launch position is strategically chosen to cover the central plasma and to avoid the blanket edges at all density values. A series of ray traces shown in Figure 122 in Appendix E illustrates that the vertical refraction of rays launched with positive κ (same direction as plasma current) is lower than for rays launched in the negative κ. This difference is larger at higher densities, at larger κ, and at lower frequencies.

Beam overlap and resolving power studies have been done for different probe configurations (launch angle κ^{i} and launch position at "*a*" or "*b*") for each receiver mirror position at different κ^{s}. The configurations with the best results are shown in Figure 60, which shows κ^{s} scans at different density scalings. It is remarkable the extent to which the refractions of probe and receiver beams compensate each other to

keep the radial locations of the scattering volumes near constant over a broad range of densities. This is also brought out in Figure 61 discussed in the next subsection.

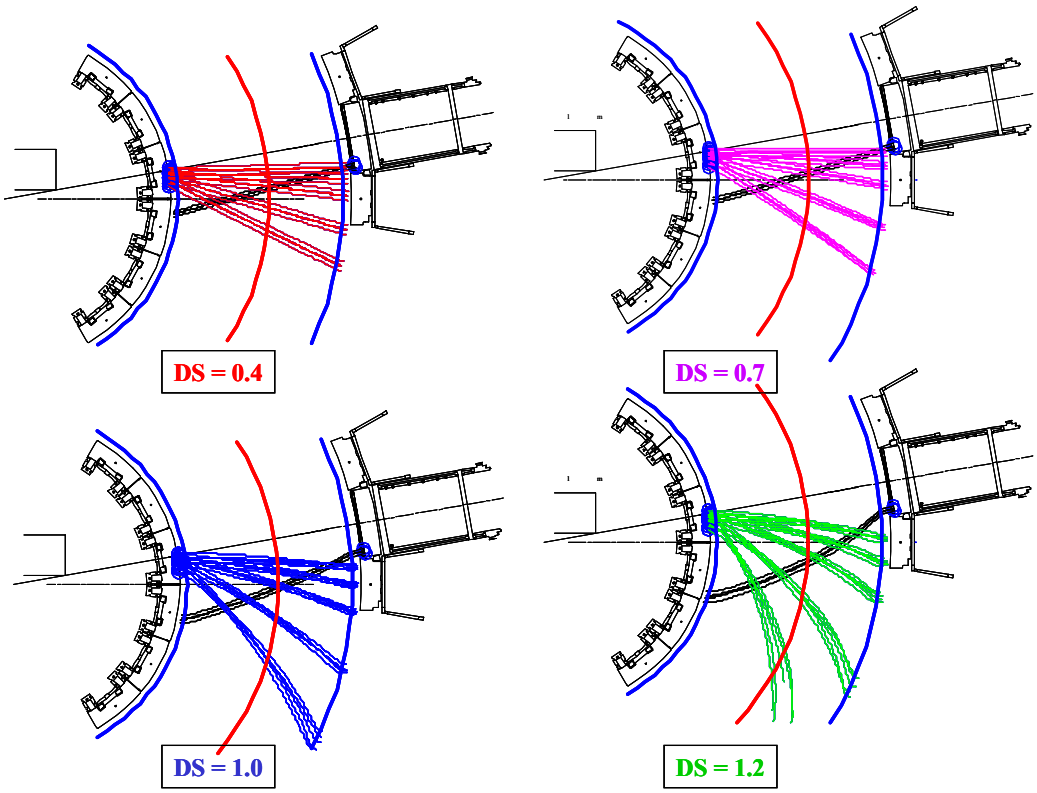

Figure 60. Beam traces at four values of the density scaling.All for the same launch and viewing directions.

2.6.3.2 Resolving power and robustness to variations in density

Shown in Figure 61 is the resolving power divided by 4 for different viewing angles of receiver mirror 2, plotted against the radial location of the scattering volume for four different plasma density scaling factors. Also shown as dashed and dotted lines for each density value are the effects of ± 10% variation in the density. This graph represents the best geometry for the HFS system: mirror 2 as receiver, probe launch at position "*b*" (see Figure 53) and probe launch angle $\kappa^j = 10^o$. The figure shows an excellent robustness in the resolving power L and in spatial localisation against density fluctuations of 10%, for the plasma density range DS = 0.4 – 1.2. This configuration also enables measurements on both the HFS and LFS.
Figure 62 shows the beam overlap for the same configuration at different plasma densities. It is important to note that the beam overlap improves with *decreasing* density due to the fact that there is less refraction in the toroidal direction resulting in a lower scattering angle, which increases the beam overlap. Despite the lower beam overlap at higher density, the resolving power increases strongly with density as can be seen in Figure 61. We see that at a density of DS = 0.4, the resolving power is below the minimum requirement.

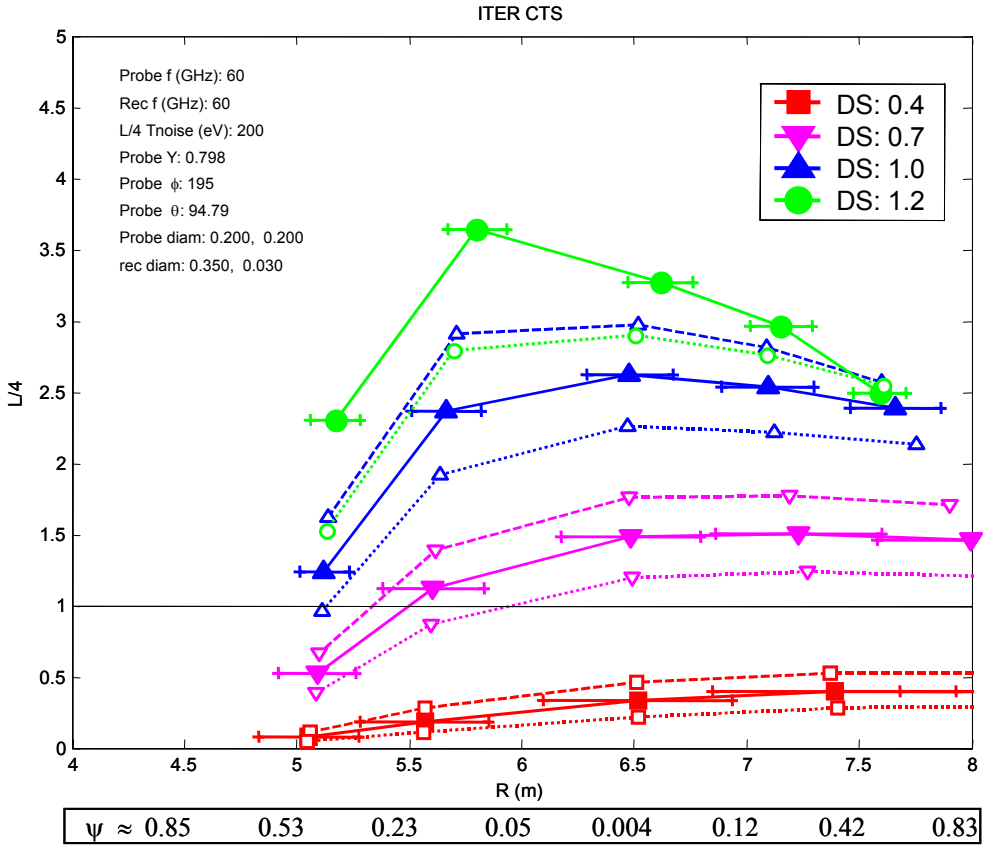

Figure 61. Resolving power, L/4, for different κ^s plotted against the radial location of the scattering volume. Probe launch from position "*b*", Mirror 2, κ^j = 10°. The flux coordinate corresponding to the abscissa values are displayed. Each colour and symbol represents a plasma density, the dashed and dotted lines are respectively the results of +10% and -10% changes in the density.

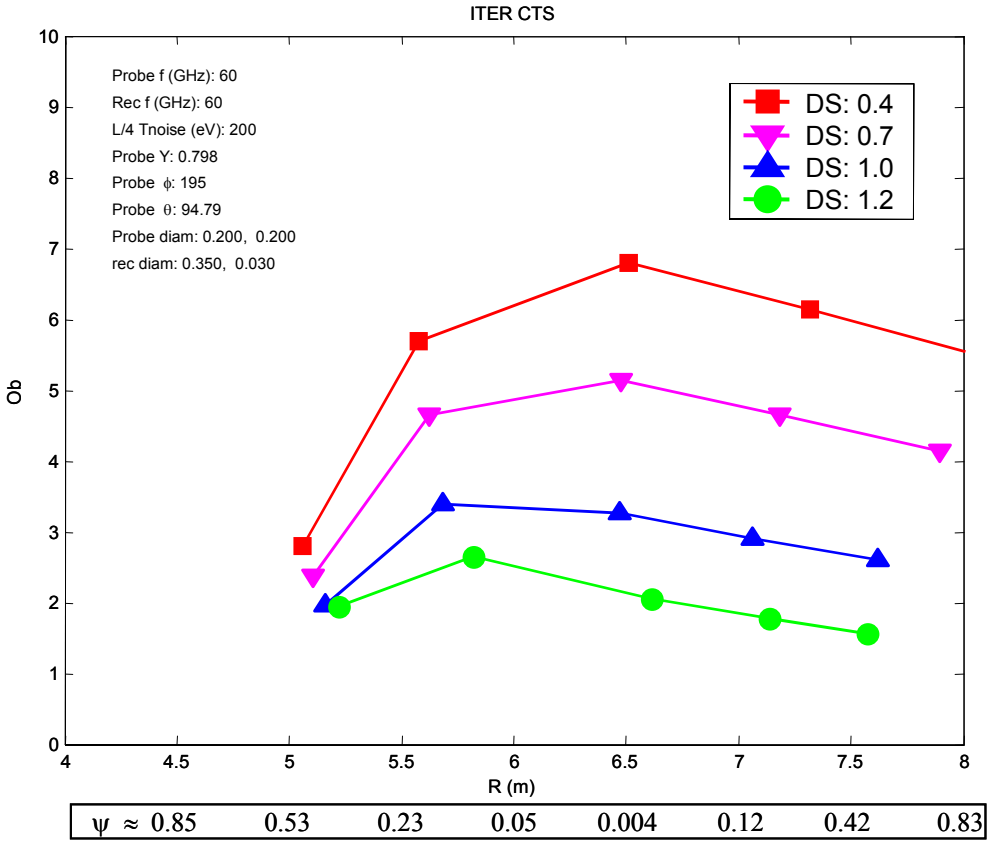

Figure 62. The beam overlap for the same configuration as Figure 61 at different plasma densities.

It is important that the probe launch is off perpendicular. Increasing the toroidal launch angle to $\kappa^j = 15°$ improves the radial resolution, but at the expense of the overlap and resolving power as can be seen in Figure 123 in Appendix E. A probe launched from position "*a*" and using mirror 2 decreases the scattering angle and hence the overlap. Figure 124 shows the resolving power achieved with mirror 2 and the probe launch at position "*a*" at the same $\kappa^j = 10°$. We see a sufficient resolving power, but a poor radial resolution.
The measurements with mirror 1 at either probe launch location do not have sufficient resolving power due to the larger scattering angles for both probe launch positions "a" and "b (see Figure 125).
Due to the restriction on κ^j , because of refraction, scattering angles using measurements from mirror 3 are too small, leading to poor spatial resolution. This configuration is also not sufficiently robust against density variations.

2.6.3.3 Dispersion effects

The spectral width of the fast ion feature, for this HFS forward scattering geometry, is between 0.5 and 1.5 GHz, depending on the radial location of the scattering volume, as shown in Figure 63. As a result, the beam overlap in this spectral range varies very little, making the HFS system virtually unaffected by dispersion.

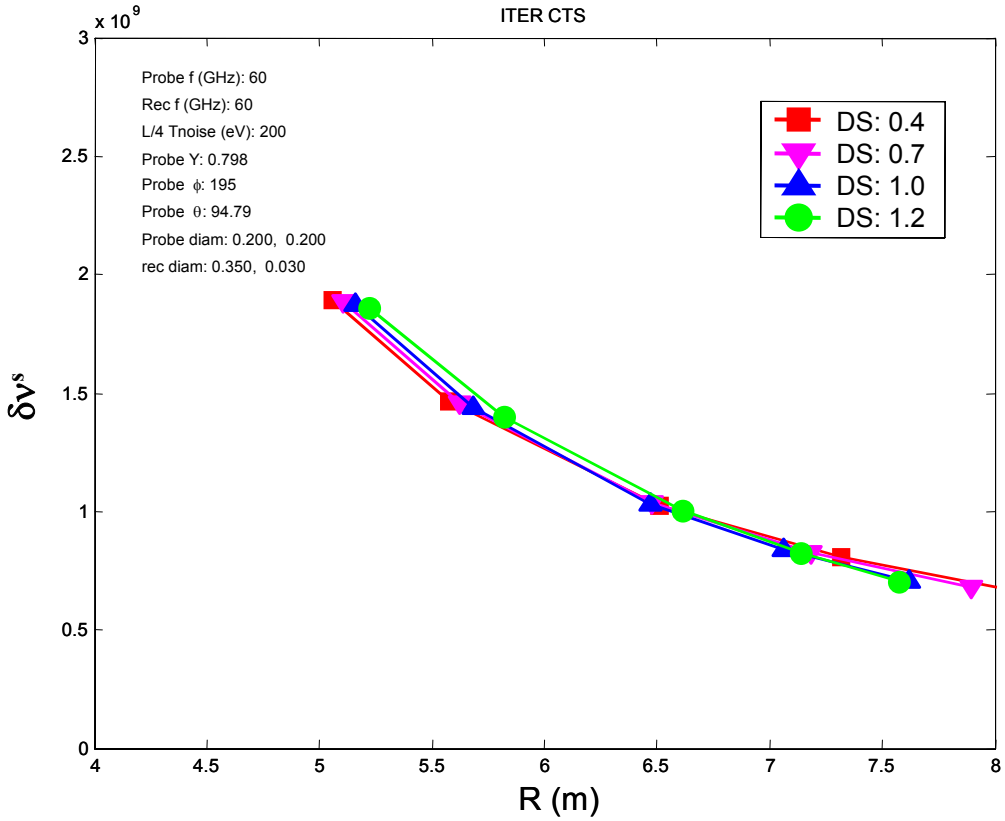

Figure 63. Spectral half-width of the same measurements as in Figure 61 for each radial measurement at each plasma density.

2.6.3.4 Spectral information for the HFS system

Here we return to a closer look at the achievable spectral information, now for the forward scattering system in the geometry that takes measurements in the centre. We assume DS = 1. Recall that in all the calculations of resolving power of the HFS system we assume a 1 MW probe, an integration time of 20 ms, and the noise temperature level of 200 eV. The results are presented in Figure 64 to Figure 66. One should note that the fast ion feature is clearly distinguishable above the electron feature. Furthermore we note the smallness of the uncertainties in the determination of the fast ion distribution, and the high resolving power of 10.

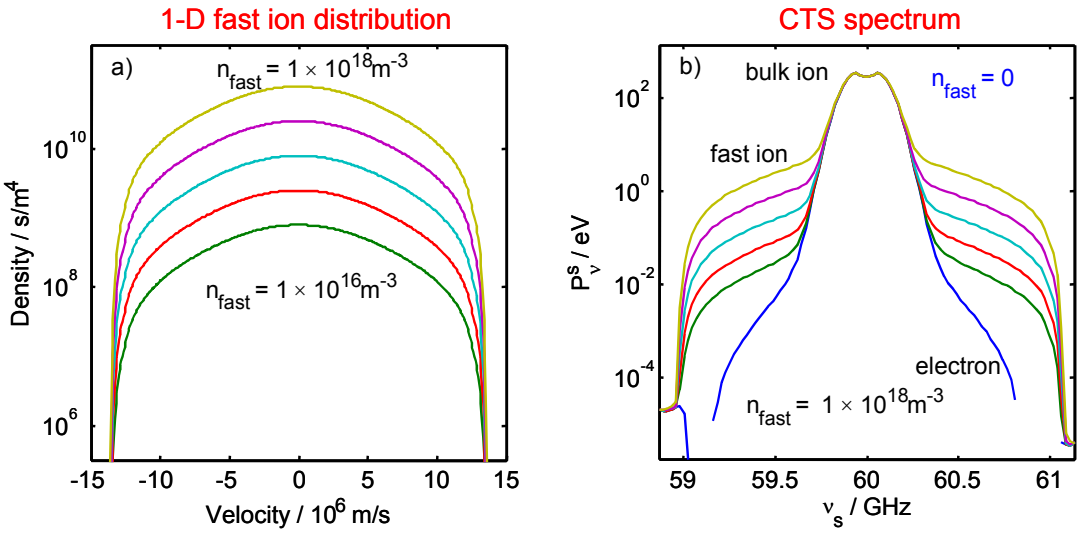

Figure 64. CTS spectral power densities (right) for a range of fast ion densities (left) for the central measurement point of Figure 61 at a density scaling of DS = 1.0 for the HFS system and a gyrotron power of 1 MW.

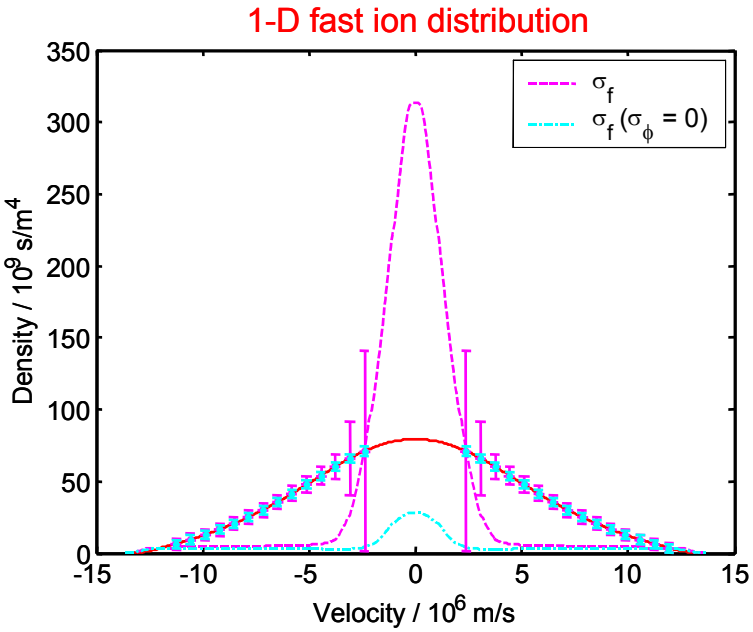

Figure 65. Resolution of the fast ion distribution for the central measurement point of Figure 61 at DS = 1.0 for the HFS system with a noise temperature, T_N, of 200 eV, a gyrotron power of 1 MW and an integration time of 20 ms. Resolving power L = 10.

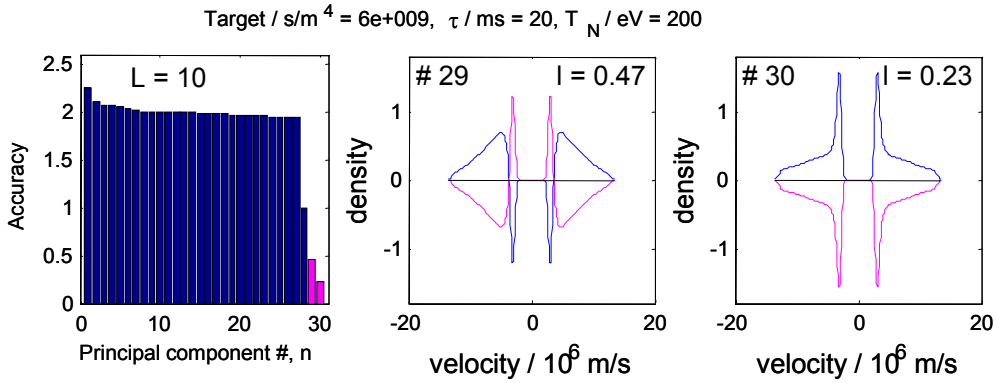

Figure 66. Principle components analysis of the central measurement point of Figure 61 at DS = 1.0 for the HFS system, with a T_N of 200 eV, a gyrotron power of 1 MW and an integration time of 20 ms. Resolving power L = 10.

2.6.4 55 GHz option

As with the LFS system, we also include studies of the 55 GHz probe option for the HFS system. Since the L-cutoff frequency is lower on the HFS, refraction is not as big a problem even for 55 GHz. We can see clearly from Figure 67, the minimum requirement on L is satisfied and the robustness of the radial position against 10% variation of the density is excellent.

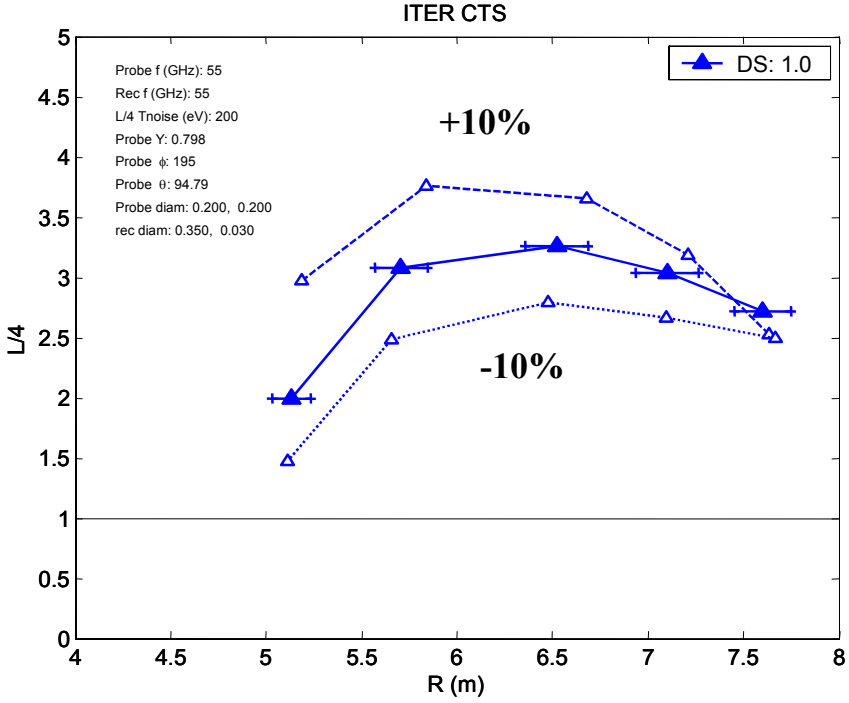

Figure 67 Radial profile of the resolving power divided by 4 for ν^j = 55 GHz at DS = 1.0, TS = 1.4, with a 10% density variation (dashed: +10%, dotted: -10%).

As with the 60 GHz frequency, the spectral width is narrow and thus dispersion effects pose no problems.

2.6.5 Conclusion

As mentioned in section 1.9, the L-cutoff on the HFS is 33 GHz. Hence refraction is not as large a problem as on the LFS. The HFS system considered with receiver mirror 2 located behind the blanket and the probe at position "b" (see Figure 53) has resolving powers above 10, implying for instance the ability to resolve 16 points on the fast ion velocity distribution (8 either side of zero velocity), with an accuracy which is $L/4 = 2.5$ times better than the target accuracy of $\Delta = 6\times10^9$s/m^4, i.e. with error bars smaller than 3×10^9s/m^4. With a mean fast ion density in the range of 20×10^9s/m^4, as may be expected (see Appendix A), this implies a typical relative uncertainty of less than 15 % with 16 components resolved. This with a time resolution of 40 ms (20 ms integration time and probe modulated on-off with a duty cycle of 50%). The radial resolution is approximately 20 cm corresponding to a/10. The mirror will be coupled to several waveguides hence having the possibility of measuring multiple positions simultaneously from $\psi = 0.5$ on the low field side till $\psi = 0.35$ on the high field side of the plasma. The system is robust and can operate at densities from 0.7 to 1.2×10^{20}m^{-3} (actually 1.3×10^{20}m^{-3} if we exclude the need to tolerate further 10% increases in density). This system satisfies all the diagnostic requirements set out for a fast ion diagnostic for ITER.
Similar performance up to densities of 1×10^{20}m^{-3} is found with the 55 GHz option which entails the possibility to operation at temperatures of at least 35 keV.

2.7 Unabsorbed probe power and potential effects on other diagnostics

At the 60 GHz the absorption in the plasma is very weak, implying that the probe is essentially only absorbed by the first walls of the vessel. The highest probe radiation intensity hitting the wall is on the high field side at the first reflection. The probe beams have a sufficient size at the first wall reflection that the power density presents an acceptable load on the wall. The first reflection foot print does not cross the gaps between blanket modules to avoid sending intense probe radiation in behind the modules. At the second reflection the beam will have spread out very considerably and thus present a much reduced power density. After multiple reflections the radiation will have spread out over the vacuum vessel cavity. The average power per unit area hitting the first wall can be estimated as

$$P_{wall} = \frac{P^{\mathrm{i}}}{A\eta}, \tag{2.4}$$

where P^{i} is the probe power, A is the surface area of the first wall and η is the absorption coefficient, typically assumed to be around 30 %. With a total probe power of 2 MW (two units of 1 MW) and a surface area of 1000 m^2 the average power per unit area hitting the walls in ITER under all angles is estimated at 7 kW/m^2. While this is very small compared with the total power density of electromagnetic radiation from the plasma hitting the walls the question has nonetheless arisen as to whether this probe power would adversely affect diagnostics and if so, what can be done. It appears unlikely that optical diagnostics would be affected due to the great difference in frequency. Microwave diagnostics operating at higher frequencies such as the ECE diagnostics can insert an effective high pass filter, for instance in the form of a section of fundamental waveguide. The position reflectometers operating in the same frequency range may need notch filters. Bolometers need not be affected, but could be

protected by letting them view the plasma through a honey comb mesh with a hole diameter of 2 mm.
The discontinued JET CTS system and the current TEXTOR CTS system also had and have probes which were and are not absorbed by the plasma. In both the JET and TEXTOR systems this resulted in an average probe power on the walls at the same level as at that expected for ITER. The bolometers in JET were not affected by the CTS probe. These same bolometers were affected by Lower Hybrid heating. In TEXTOR no damage to any diagnostics has been reported. Adverse effects on bolometers have not been noted, but will be investigated. For FTU adverse effects of the CTS probe on the bolometers have been reported [U. Tartari, private communication]. The new CTS at ASDEX upgrade wile present a probe wall power up to 7 times greater that that expected for ITER so this will offer an excellent opportunity to check for adverse effects.

3 Probe frequency between electron cyclotron harmonics (≈ 170 GHz)

3.1 Introduction

One of the options considered for collective Thomson scattering (CTS) at ITER uses a probe frequency between the fundamental and second harmonic of the electron cyclotron resonance. In this frequency range refraction is less significant than at frequencies below the fundamental EC resonance, considered in the previous section. To diagnose the plasma centre, the probe frequency must be chosen such that at this frequency the fundamental cyclotron resonance layer is in the plasma on the high field side (HFS) of the centre, while the second harmonic remains outside the plasma. Having the EC resonance layer in the plasma permits the use of the resonance layer as a dump for the gyrotron probe beam, preventing multiply reflected stray light from disturbing other diagnostics.

On the other hand, having the electron cyclotron resonance inside the plasma provides an extended source of radiation with a spectral power density approaching the maximum electron temperature in the plasma, i.e. on the order of 25 keV. Minimising the level at which this radiation enters the receiver is of paramount concern for a CTS system operating in this frequency range. To this end the colder but still optically thick part of the cyclotron resonance can be employed as a viewing dump. If viewed directly by the receiver the viewing dump gives rise to a spectral power density in the receiver equal to the temperature of the dump section of the resonance layer.

The need to limit the scattering angle in order to suppress the electron feature favours the use of the upper port for the receiver, with the probe in the equatorial port. This implies that direct view of the lower cold part of the cyclotron resonance layer is under a shallow angle which makes the beam dump temperature low over too narrow a frequency range.

In the mid 1990's Bindslev *et al.* considered this geometry in studies of this, $\omega_C < \omega < 2\omega_C$, frequency option for the ITER-FDR project [11]. The set-up was dismissed due to too high ECE background noise and a too high sensitivity to parameter changes.

To overcome the problem of high sensitivity to plasma parameters the less hot region of the resonance layer can be viewed indirectly via reflection in the first wall as illustrated in Figure 68. With specular reflection in the low field side first wall just above the divertor, the receiver can effectively view the less hot region of the resonance layer at near right angles, making the setup more broad band, as the radial frequency shift of the resonance layer keeps the dump region at nearly the same vertical location.

In 1996 Bindslev *et al.* proposed essentially this approach for the JET system [13]. The considerations for the JET system were tested experimentally and finally dismissed, due to too high sensitivity to changes in the refraction due to plasma parameter variations. Recently, Tartari *et al*. [12] considered this option with a probe frequency of 170 GHz for a fast ion CTS for ITER.

Viewing the less hot part of the resonance layer via wall reflection permits some of the much hotter radiation emitted from the central region of the resonance layer, to enter the receiver via diffraction in irregularities in the section of wall viewed by the receiver. We will neglect this contribution in the subsequent discussion. At the highest electron temperatures an additional background radiation problem is

introduced, which is not ameliorated by specularly reflecting walls: At temperatures of 30 keV and above significant relativistically downshifted second harmonic EC emission will be present in direct view of the receiver at a frequency of 170 GHz. At higher frequencies the same effect occurs at lower temperatures.

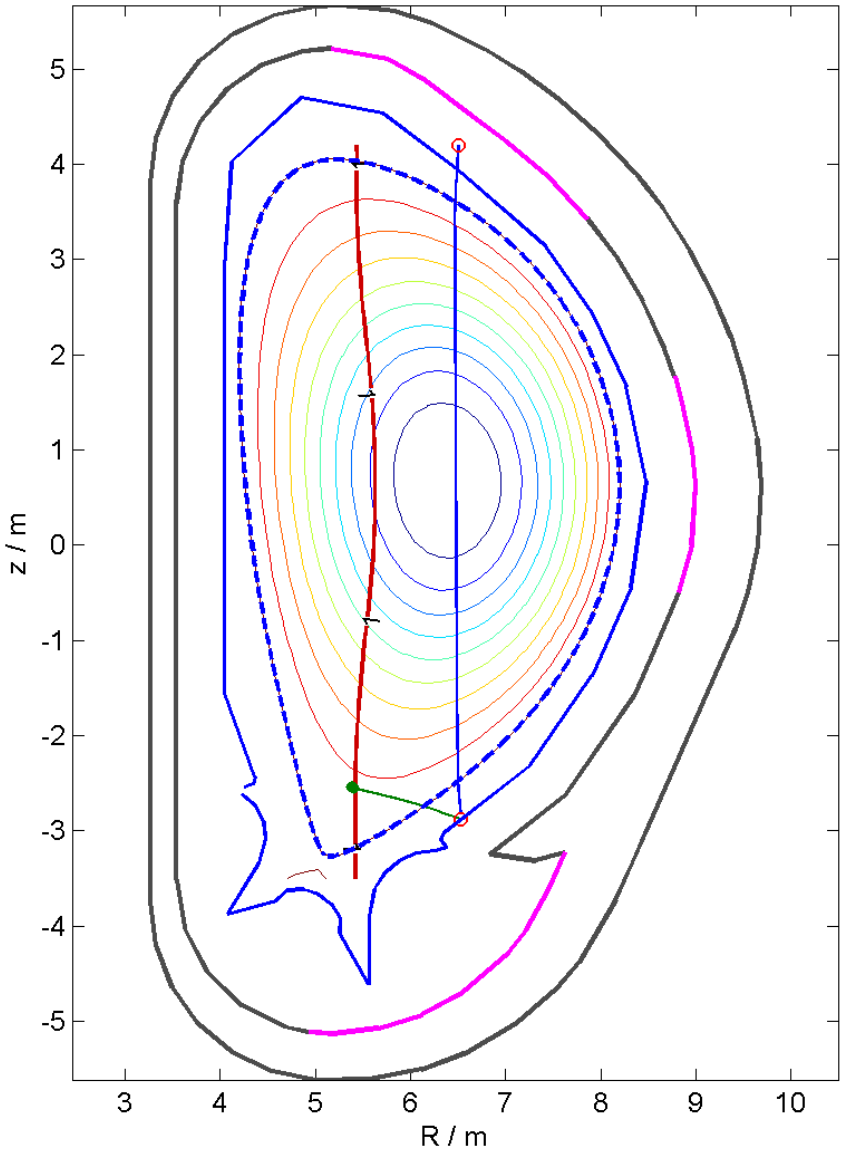

Figure 68. Poloidal map of a ray trace at 170 GHz illustrating the use of the low temperature region of the electron cyclotron resonance as a viewing dump via reflection in the first wall at (R, z) = (6.53 m, -2.88 m). The receiver antenna is at (R, z) = (6..5 m, 4.2 m). The rays are essentially in the poloidal plane. The plasma is the reference plasma with a central electron density of 10^{20}m^{-3} and central electron temperature of 25 keV. The first pass (blue ray) is launched 10° from vertical towards the machine centre. The spectral power density of radiation collected from the plasma in direct view of the receiver (the blue ray segment) is 0.12 keV while the spectral power density collected from the segment after reflection (the green ray segment) is 3.95 keV.

In Table 7 we present the results of calculations intended to give a first indication of the spectral power density collected from the reference plasma with the receiver in the upper port viewing the plasma centre and using the low temperature region of the electron cyclotron resonance as a viewing dump via a wall reflection as illustrated in Figure 68. The collected radiation consist both relativistically down shifted second harmonic radiation emitted from the plasma in direct view of the plasma, and radiation emitted from the part of the resonance used as a viewing dump. Increasing the frequency from 170 GHz the cyclotron resonance moves towards the high field side of the plasma and eventually reached the plasma edge for a frequency around 195 GHz. This results in a decreasing spectral power density of the radiation emitted from the dump. At the same time the increasing frequency increases the intensity of the relativistically down shifted second harmonic radiation in direct view of the receiver. The result is that the total spectral power density seen by the receiver, which is estimated at 4.1 keV at 170 GHz, increases monotonically to 8.5 keV at 200 GHz. Decreasing the frequency results in a minor reduction in the total spectral power density seen by the receiver down to 3.5 keV at 155 GHz. At 150 GHz the spectral power density is estimated at 1.9 keV, but here operation of the receiver beam is affected by anomalous dispersion associated with the proximity of the cyclotron resonance layer to the vertical leg of the viewing path. At lower frequencies the centre of the plasma is obscured by the cyclotron resonance. Since we need a free spectral range of approximately 10 GHz either side of the probe frequency it appears that 170 GHz is the optimum choice for the probe frequency for this frequency interval and viewing geometry. The noise temperature is then estimated to be around 4 keV.

Frequency / GHz	Direct view radiation temperature	Dump radiation temperature	Total radiation temperature
≤ 145	Not usable; resonance in direct view of receiver		
150	0.0 keV	1.9 keV	1.9 keV
155	0.0 keV	3.5 keV	3.5 keV
160	0.0 keV	3.9 keV	3.9 keV
165	0.0 keV	4.0 keV	4.0 keV
170	0.1 keV	4.0 keV	4.1 keV
175	0.3 keV	3.9 keV	4.1 keV
180	0.6 keV	3.6 keV	4.2 keV
185	1.4 keV	3.1 keV	4.4 keV
190	2.7 keV	2.3 keV	5.0 keV
195	5.0 keV	1.6 keV	6.6 keV
200	8.5 keV	Uncertain	8.5 keV
≥ 205	≥ 13 keV	Uncertain	≥ 13 keV

Table 7. Spectral power density of radiation collected from the plasma in direct view of the receiver and from the segment after reflection which is essentially the beam dump temperature. The calculations assume the ray geometry shown in Figure 68 and the reference plasma with a central electron density of $10^{20}m^{-3}$ and central electron temperature of 25 keV. The ray launch points and directions are kept constant for all frequencies. This in fact under estimates slightly the radiation temperatures at both the upper and the lower frequencies of this investigation. The dump radiation temperature has been indicated as uncertain for frequencies of 200 GHz and above because the dump is well into the scrape of layer.

3.2 Orthogonal geometry

The geometry advocated by Tartari *et al*. has the probe beam entering horizontally through the equatorial port with vertical signal collection through the upper port, as presented in Figure 69 below [12].

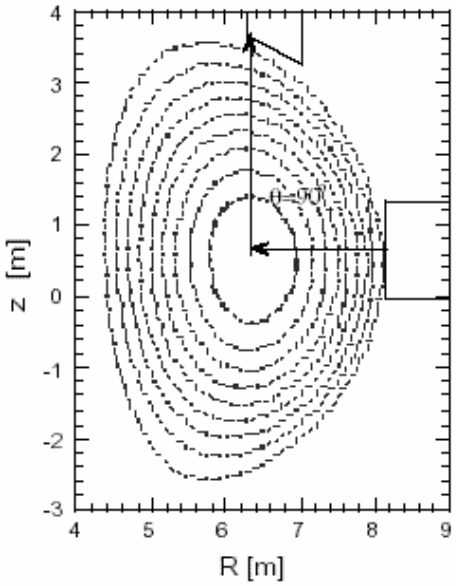

Figure 69. Directions of injection and collection in the orthogonal geometry. [From [12] (Figure 3.9)].

As discussed in the introduction above, Tartari *et al*. seek to solve the problem of ECE noise entering the receiver by letting the receiver beam be reflected in the first wall near the bottom of the vessel to view the resonance layer near the plasma edge where the temperature is reduced compared with the centre.
In the following sections we first present ray traces for the receiver for a few scenarios, and then the probe and receiver system is evaluated by pseudo-beam traces, where, among others, the beam overlap is calculated. Following this we look closer into the matter of beam dump, and then the spectral information is discussed before we conclude on the diagnostic capability achievable with this geometry. In these calculations we assume a probe frequency of 170 GHz found in the discussion in the introduction in Section 3.1 to be optimum for reducing the intensity of the ECE emission collected by the receiver, while staying clear of anomalous dispersion at the lowest frequencies.

3.2.1 Receiver ray tracing

Tartari *et al.* use ITER equilibrium parameters similar to the parameters of the reference ITER equilibrium used here (see Appendix A), except that $T_e = 27.4$ keV and the central magnetic field is 5.16 T in Tatari's equilibrium [12], while the corresponding values are 25 keV and 5.3 T for the reference ITER equilibrium we use. In the "parameters scan studies" presented in the Tartari report electron temperatures up to 30 keV were considered. With appropriate scaling of the electron temperature and magnetic field of the reference ITER equilibrium to the Tartari nominal case, the receiver behaves as presented in Figure 70. The receiver beam ECE

noise temperature is seen to be as low as 30 eV for one of the rays, while it is 130 eV to 240 eV for rays going closer to the centre. This represents one contribution to EC radiation entering the receiver, which is due to the down shifted radiation in direct view of the receiver. Except at the highest temperatures, a much more significant contribution comes from the EC radiation reflected into the receiver beam pattern via the wall. To minimise this contribution the wall must be perfectly reflecting and reflect the receiver beam into a less hot yet still perfectly absorbing part of the EC resonance layer near the plasma edge. Form a scan of rays, from the lower part of the vessel wall towards the cold part of the resonance layer, presented in Figure 71, we see that the total noise temperature cannot be lower than 2200 eV.

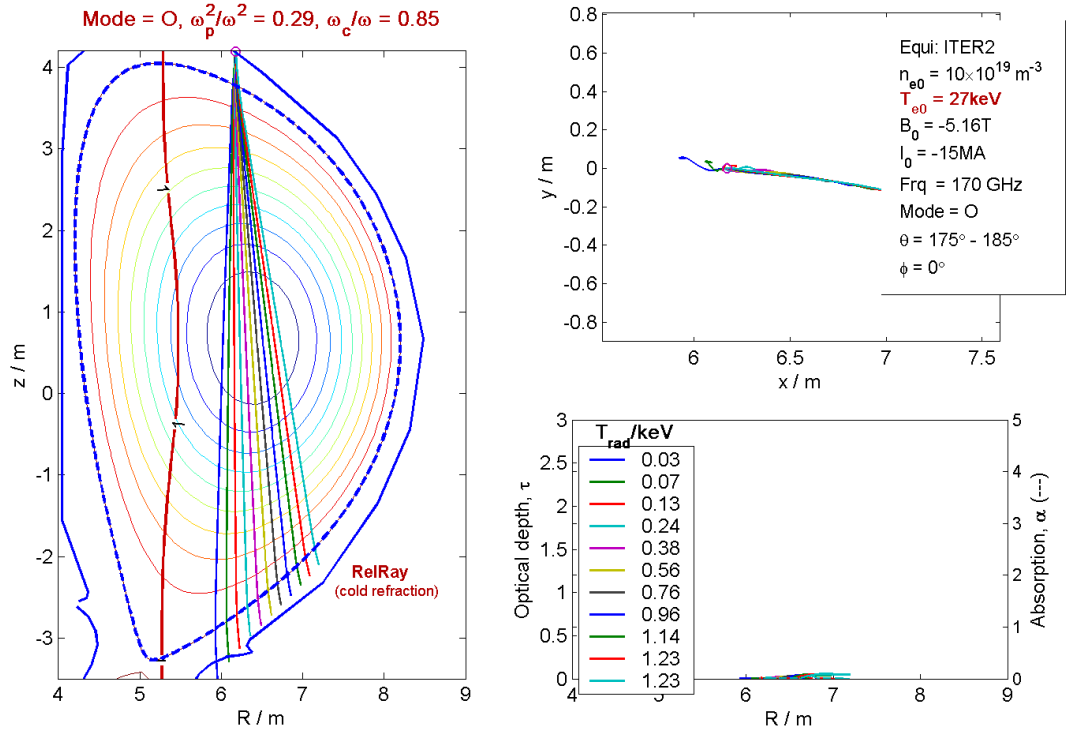

Figure 70. Scan of possible receiver directions for O-mode at 170 GHz with parameters as shown in the top right corner of the figure (nominal Tartari case).

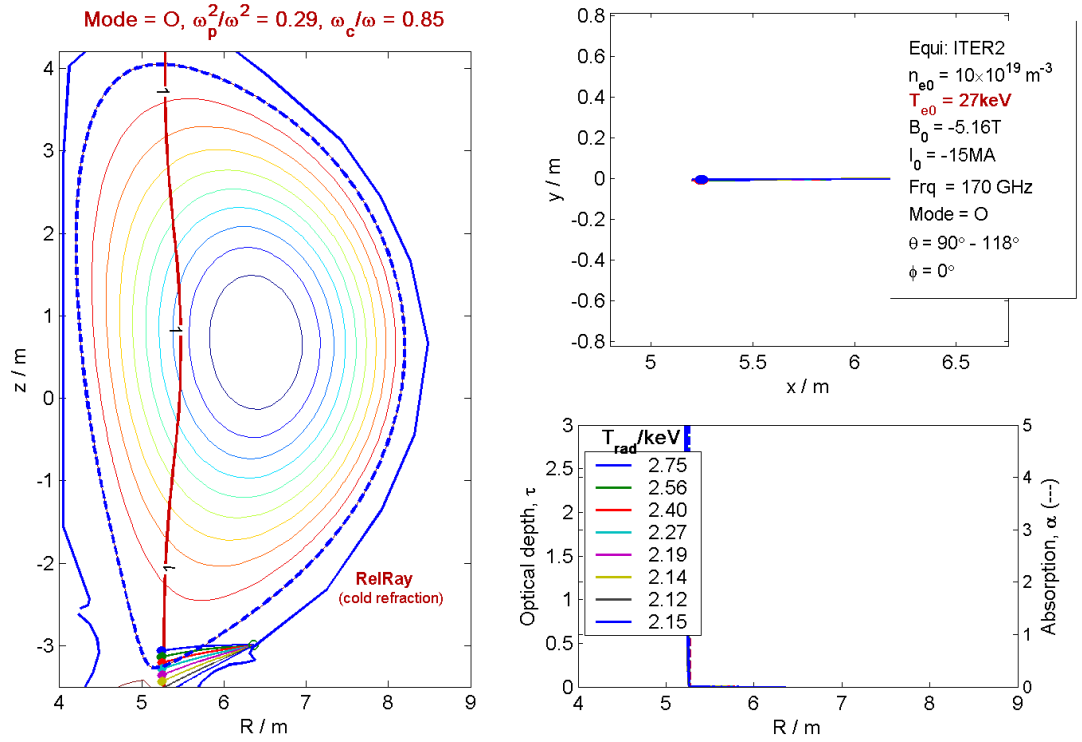

Figure 71. Scan of possible beam dump directions for O-mode at 170 GHz with parameters as shown in the top right corner of the figure (nominal Tartari case).

Here we did not make any assumptions on how and in which direction the beam is reflected, since this will be treated more thoroughly in Section 3.2.3, where a more realistic noise figure is given.

Additionally, we test the orthogonal scattering geometry for the nominal parameters of the reference ITER equilibrium. The results of the ray traces are shown in Figure 72 and Figure 73. In this case the total ECE noise temperature for the receiver, including the beam dump, may be reduced to 1700 eV. This is due to a slightly lower T_e and a slightly higher central magnetic field, B. The latter causes the second harmonic resonance to move further out of the plasma, meaning that less ECE noise is Doppler shifted into the plasma from the LFS.

Seeing now that the reference ITER equilibrium parameters yield the best result (lowest ECE noise temperature), we perform the rest of the studies with those parameters. Once more, we should mention that the beam dump will be discussed more thoroughly in Section 3.2.3, while the numbers presented here for the ECE noise are the best case scenario, without considering whether the walls can in fact reflect the receiver beam in the optimum direction.

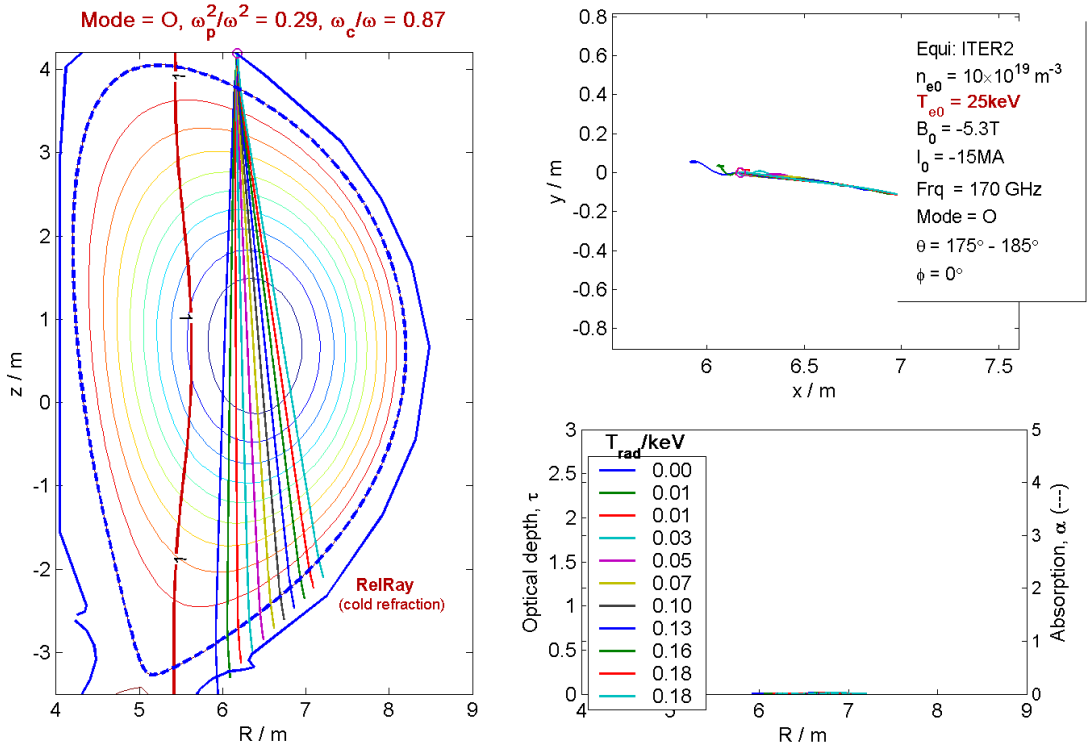

Figure 72. Scan of possible receiver directions for O-mode at 170 GHz with the reference ITER parameters as shown in the top right corner of the figure.

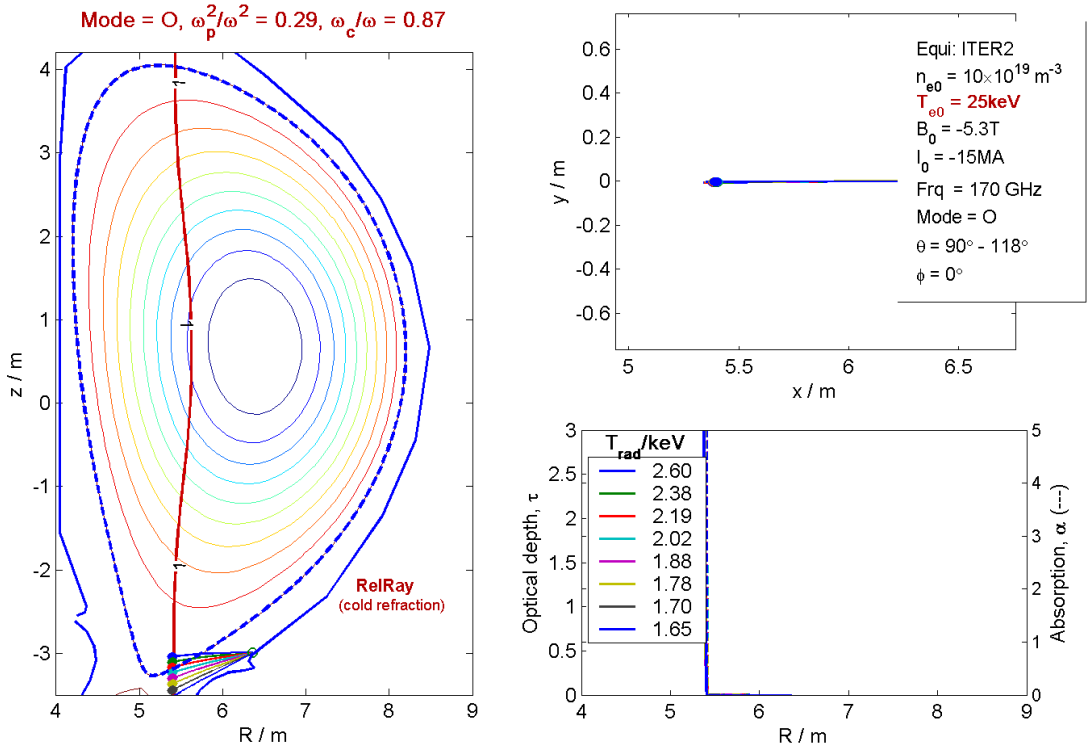

Figure 73 Scan of possible beam dump directions for O-mode at 170 GHz with the nominal ITER2 parameters as shown in the top right corner of the figure.

3.2.2 Beam tracing

We evaluate the system of receiver and probe for the orthogonal scattering geometry by doing a pseudo-beam tracing, by which the beam overlap and scattering volume location, scattering angle, and much more is calculated. For the central frequency of 170 GHz and the reference ITER equilibrium parameters the result is presented in Figure 74 and in Section F.1. We have assumed a Gaussian radius, w, of 3 cm at the plasma centre, which will be discussed in Section 3.2.3. We find that for this beam tracing, the beam overlap is: $O_b = 16.0$ m^{-1}, which is slightly less than the achievable maximum of 18.8 m^{-1}. The scattering angle is 87.5º, while the angle between the magnetic field and the scattered wave number is 90.8º. The scattering volume is at a major radius of 6.30 m and a vertical position of 0.62 m, which is very close to the plasma centre. We also see that the linear extents of the scattering volume along the major axis of the scattering volume are 8.3 cm, 5.2 cm and 7.7 cm, in roughly the x-, y-, and z-directions (radial, poloidal, vertical), meaning that the scattering volume is well localised.

The scattering angle of 87.5° corresponds to a spectral width of ± 8.75 GHz. Thus the beam traces are repeated for the same geometry and parameters with the frequency of the receiving beam being changed to 170 GHz ± 8.75 GHz, and the results are presented in Sections F.2 and F.3, respectively. Here we find that the beam overlap is $O_b = 17.5$ m^{-1} and 13.6 m^{-1}, respectively, while the scattering angle changes to 87.9º and 87.0º, respectively, reflecting the slightly changed beam trajectories. The angle between the magnetic field and the wave number of the received scattered radiation is changed to 91.0º and 90.5º, respectively, and the ECE noise temperature is not changed significantly, while changes in refraction shift the radial location of the scattering volume center by 5 cm when the frequency changes from 161.25 GHz to 178.75 GHz. From this beam tracing investigation it may be concluded that the geometry is pretty robust with regards to obtaining the full frequency width without major changes in the scattering volume and ECE noise.

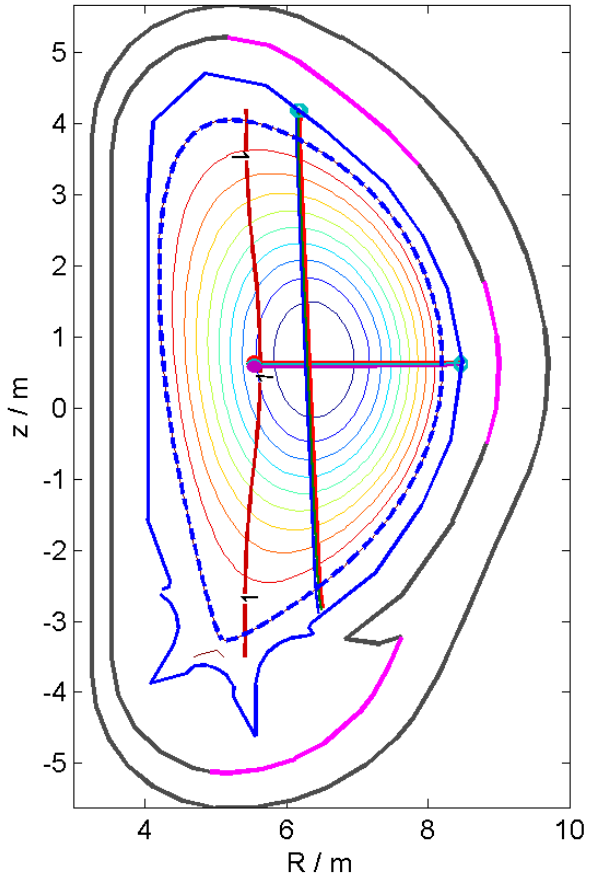

Figure 74. Beam traces for the 170 GHz scattering geometry with the probe in the horizontal plane (nominal reference ITER parameters). The exact parameters used for the beams are presented in Appendix F.1.

3.2.3 Beam dump study

In order to assess more closely the idea of using the low temperature part of the resonance layer as a beam dump, we look at the beam diameter at the strike point at the bottom of the vessel, and see where the beam is reflected from there, and which ECE temperature the reflected beam is looking at. In this section we only consider receiver beams, which are perpendicular to the toroidal magnetic field, since this geometry minimises the down shifted radiation in direct view of the receiver.
With an aperture of 30 cm for the top port receiver, one can obtain a focussed beam pattern with a Gaussian radius, w, of down to 3 cm at the plasma centre, 4.5 m from the aperture, as seen from the green curve in Figure 75. Narrowing the Gaussian radius at the centre increases the beam overlap and in turn the signal strength, but increases the width of the beam at the bottom of the vessel. Thus we assume $w = 3$ cm at the plasma centre, and a Gaussian radius just above 8 cm at the reflection area at the bottom of the vessel, which is just over 7 m from the upper port aperture. By defining the beam width as $2\times1.6\times w$, 99.4% of the power is contained in the beam, and the beam width at the reflection point is 26 cm.

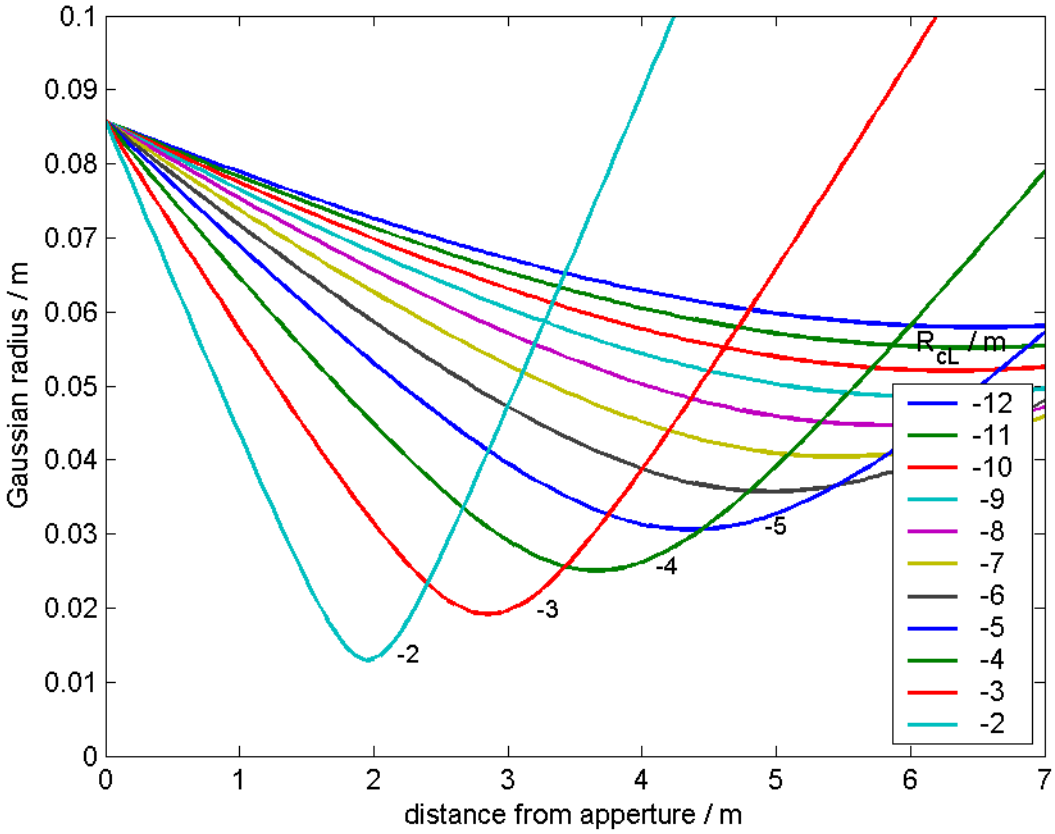

Figure 75. The Gaussian radius of the receiver beam as a function of distance from the aperture. The plasma centre is approximately 3.5 m from the aperture.

With Gaussian beam traces (in vacuum) we investigate in which direction the receiving beam will be reflected, assuming specular reflection at the bottom part of the vessel wall. Such a beam trace is presented in Figure 76. We see that the beam will intersect the cyclotron resonance layer in the normalized poloidal flux surface interval of $0.90 < \Psi < 0.95$.

In Figure 77 and Figure 78 we present ray traces from two positions on the wall at the bottom of the vessel within the area of the reflected beam. These rays cover the range between $0.9 < \Psi < 1.0$, and it is seen that the ECE noise temperatures are in a range from 3.5 to 4.1 keV for those rays which are representative of the receiver beam. It is further noted that the ECE noise temperature does not change much by moving the reflection point. We also consider the ECE noise temperature for the lower and upper part of the spectrum, i.e., for 170 GHz ± 8.75 GHz. The same launch point and angles (as in Figure 77) have been used, and the results are presented in Figure 79 and Figure 80. From the figures we see that the ECE noise temperatures only vary slightly, i.e. ± 0.1 keV, from what was found for 170 GHz.

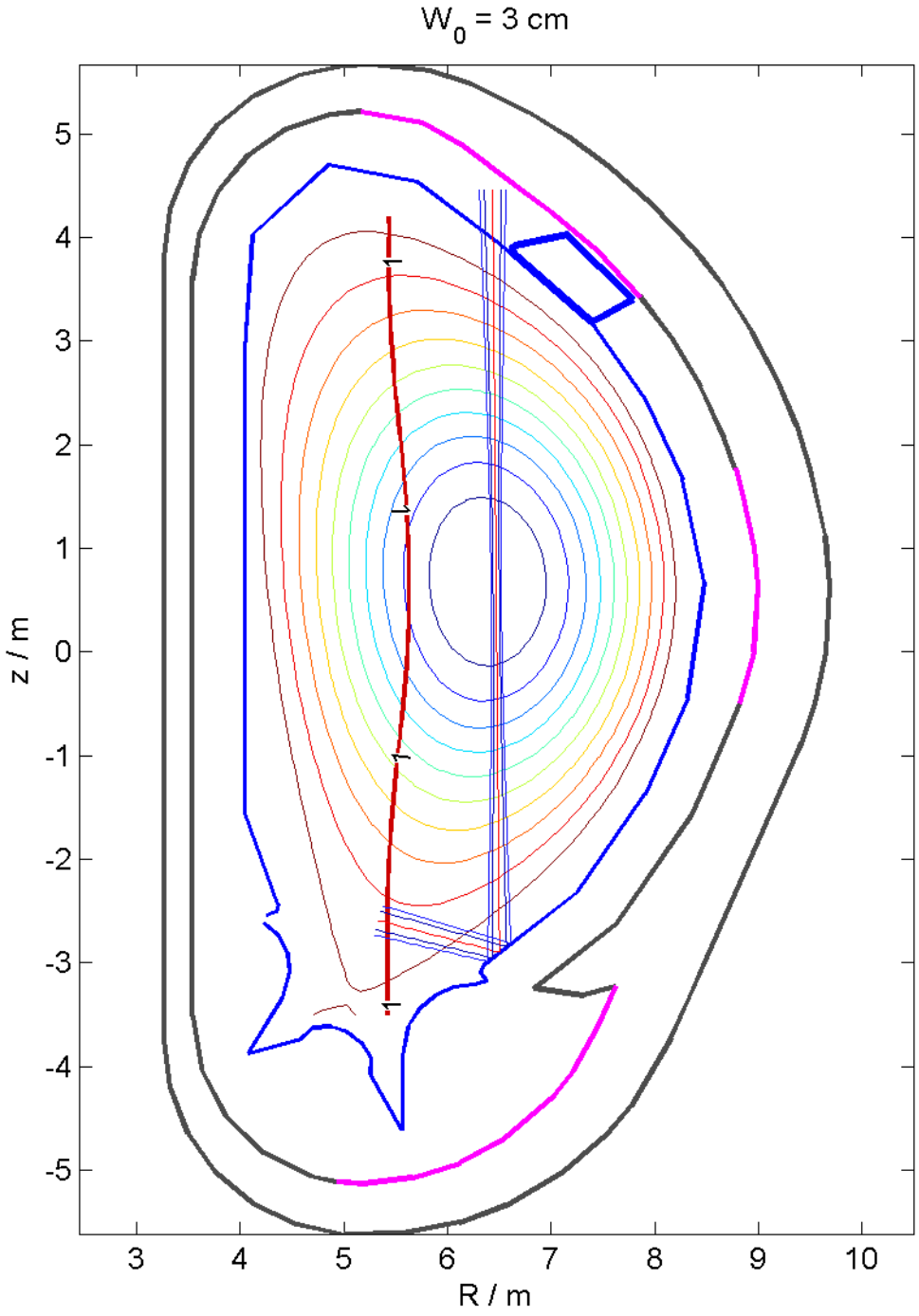

Figure 76. Gaussian beam trace in vacuum for a beam with a Gaussian radius of 3 cm at the plasma centre. Specular reflection of the vessel wall is assumed. The red line is the beam centre, the inner set of blue lines is the Gaussian radius and the outer set is 1.6 × Gaussian radius, within which 99.4% of the power is contained. The flux contours are in steps of 0.1 from 0.1 to 1, the latter being the seperatrix.

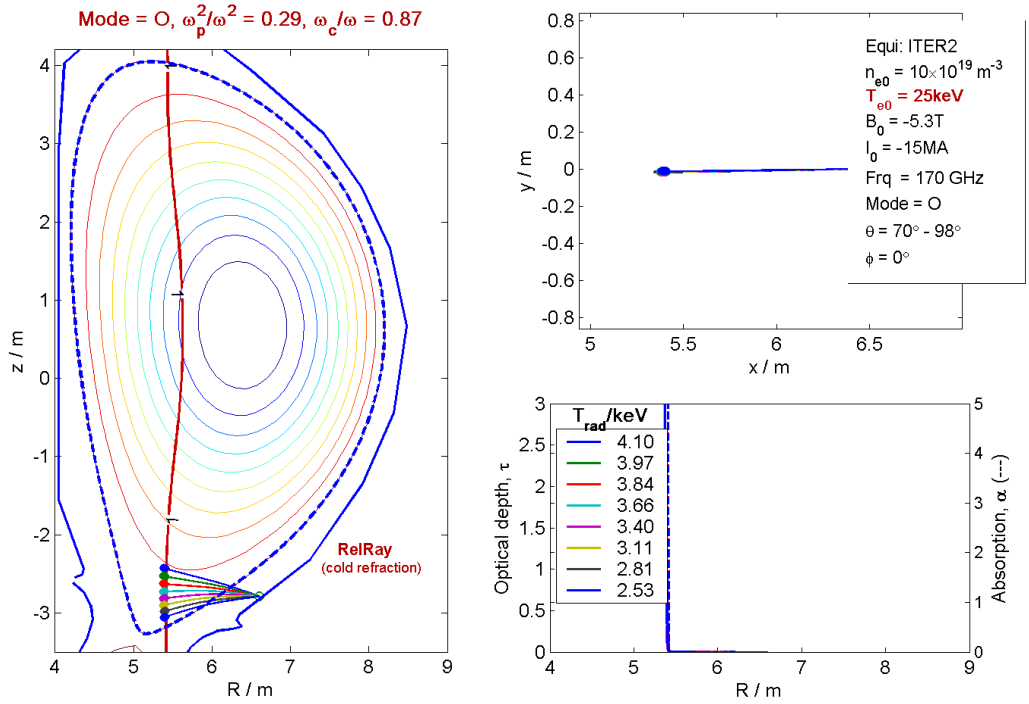

Figure 77. Ray traces of possible beam dump directions for O-mode at 170 GHz with the reference ITER parameters as shown in the top right corner of the figure. Launch from upper part of beam area.

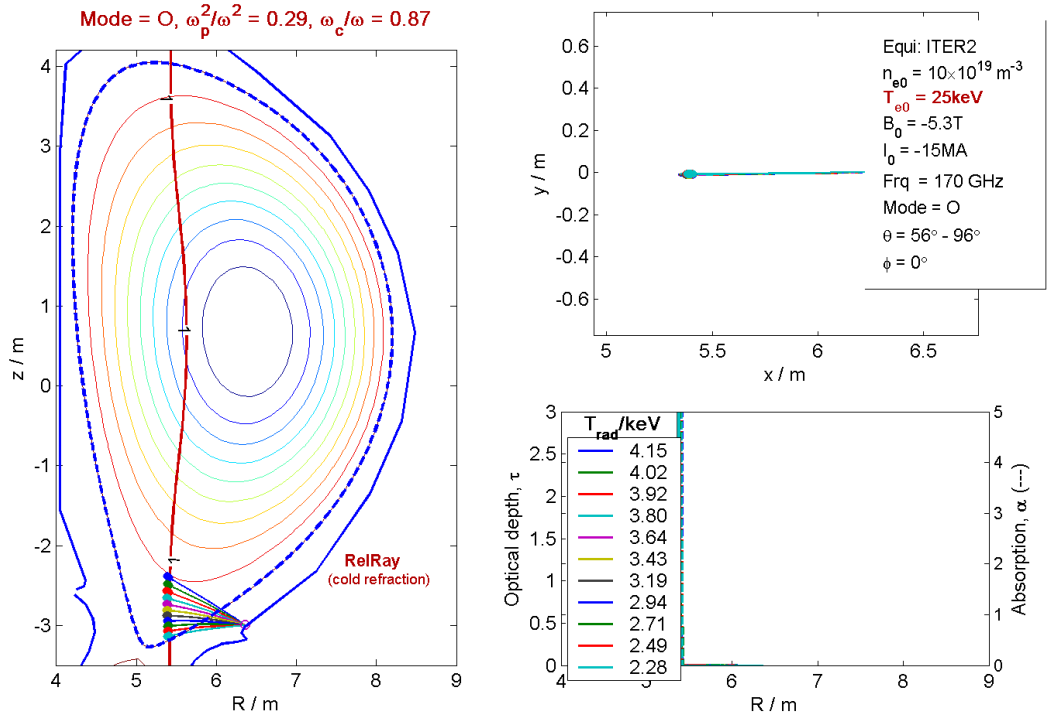

Figure 78. Ray traces of possible beam dump directions for O-mode at 170 GHz with the reference ITER parameters as shown in the top right corner of the figure. Launch from lower part of beam area.

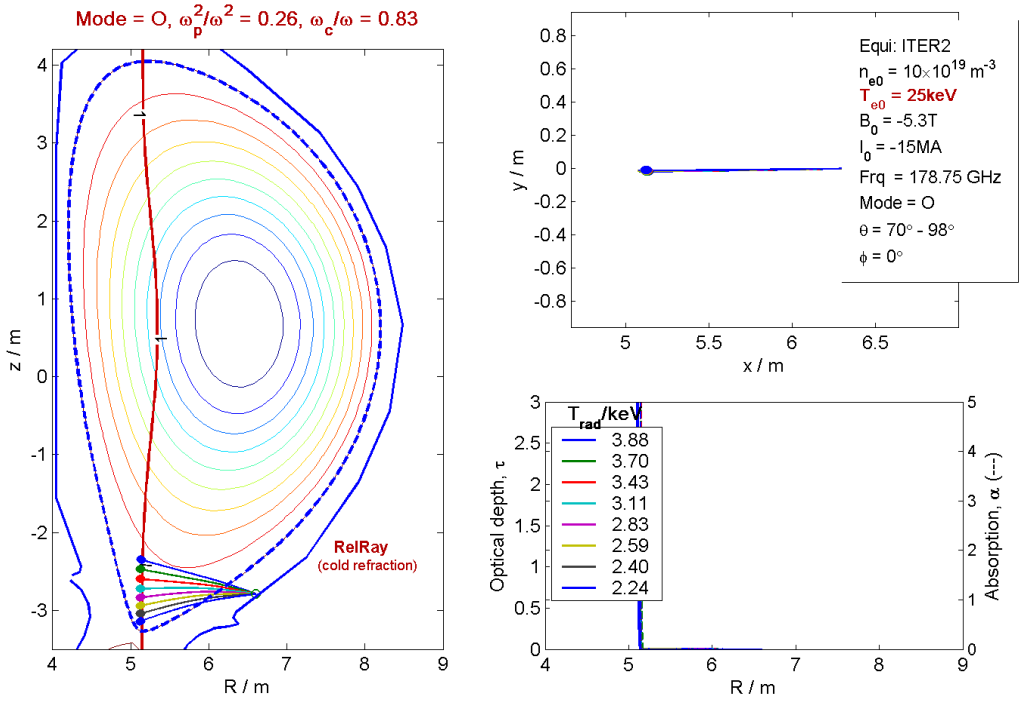

Figure 79. Ray traces of possible beam dump directions for O-mode at 178.75 GHz with the reference ITER parameters as shown in the top right corner of the figure. Launch from lower part of beam area.

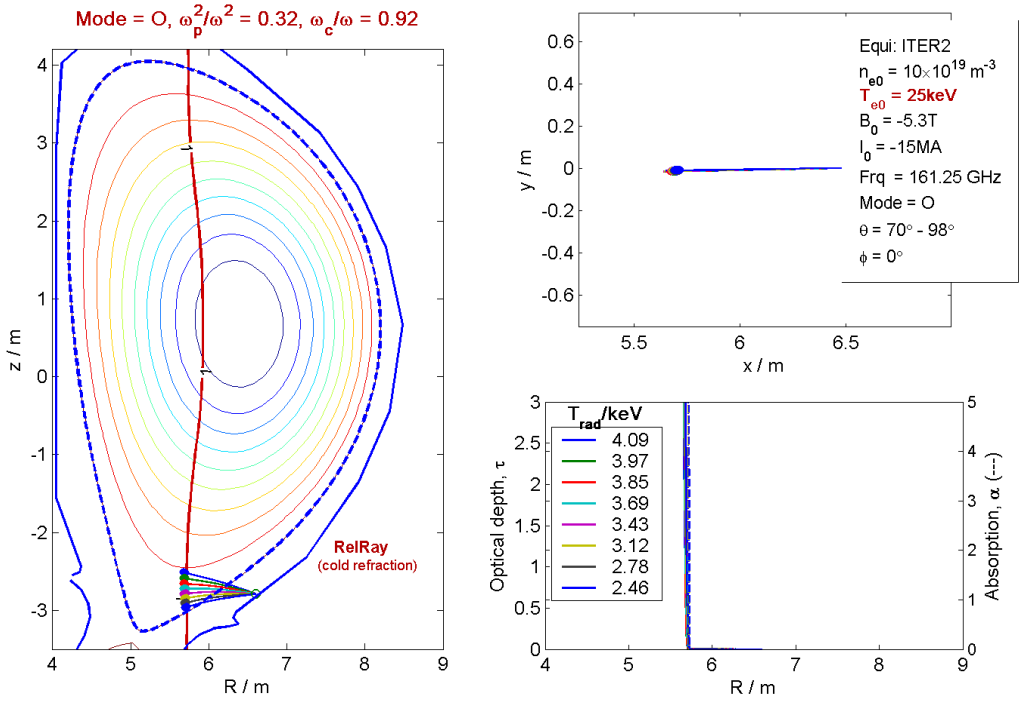

Figure 80. Ray traces of possible beam dump directions for O-mode at 161.25 GHz with the reference ITER parameters as shown in the top right corner of the figure. Launch from lower part of beam area.

3.2.3.1 Conclusion on the beam dump

For the studies of the beam dump we have optimised the Gaussian beam properties so that the Gaussian radius is 3 cm at the plasma centre, and this causes the diameter of the beam at the wall at the bottom of the vessel to be approximately 26 cm. Increasing the beam Gaussian radius at the centre will decrease the diameter of the beam at the wall, but that would also lead to a reduction in the beam overlap and the signal strength, and it would not significantly change the ECE noise temperature seen by the receiver in the EC beam dump.

In order to make use of the EC resonance layer beam dump, as efficiently as presented above, specular reflection at the bottom part of the vessel wall is required. If this is not achieved, diffuse reflection will cause the ECE noise temperature to be larger for the rays hitting the resonance layer within the $\Psi = 0.9$ surface. For this frequency, geometry and assuming specular reflection the reflected beams will look at the resonance layer within $0.90 < \Psi < 0.95$, where the ECE noise temperature varies from 3.5 to 4.1 keV.

One may consider directing the reflected beam further down the resonance layer, i.e., outside the last closed flux surface, $\Psi > 1.0$, but this would require changing the blanket module to tilt the reflecting surface.

3.2.4 Spectral resolution

A final test in assessing the performance of the orthogonal geometry 170 GHz CTS system is to look at the spectral information that can be determined from measurements by the system. An equivalent study for the optimised 170 GHz geometry described in Section 3.3 is presented in Section 3.3.2. It is also possible to perform the study for the present orthogonal geometry. However, we will not proceed with this analysis here, because the angle of the resolved direction to the magnetic field, $\phi = \angle\left(\mathbf{B}_0, \mathbf{k}^{\delta}\right)$, is close to 90º. This will cause the fast-magnetosonic wave to enter the spectrum, and it becomes impossible to distinguish the fast-ion features [4]. The CTS system installed at TFTR at Princeton suffered from this [4]. After detailed studies of perpendicular scattering for the TFTR system it was concluded that it would be impossible reliably to extract fast ion information when the wave vector of the resolved fluctuations are near perpendicular to the magnetic field because of spectral sensitivity to details in the probe and receiver beam intensity distributions.

3.2.5 Conclusion on the performance of the orthogonal option

An immediate disadvantage of this scattering geometry is that the resolved direction in velocity space is confined to a narrow range near perpendicular to the magnetic field, preventing alpha anisotropy studies. The 90° scattering angle gives problems in discriminating the alpha feature from the electron feature. With $\phi = \angle\left(\mathbf{B}_0, \mathbf{k}^{\delta}\right)$ close to 90º the fast-magneto-sonic wave enters the spectrum, which has disabled previous CTS systems as discussed in Section 3.2.4 above.

3.3 Optimised scattering geometry

To avoid the problem with the fast-magneto-sonic wave we change the geometry to take ϕ approximately 10° away from perpendicular. In order to avoid possible

increases in the ECE noise temperature by giving the receiver a toroidal component, we change ϕ by shifting the horizontal position of the probe aperture and thus its toroidal launch component. The widths of the equatorial ports are about 1.4 m. Since we assume the aperture for the beam to have a radius of 15 cm, we can move the centre of the probe aperture by 55 cm horizontally. We give the horizontal probing beam a toroidal orientation in order to intersect with the unaltered near vertical receiving beam. This also means that the previous ray traces of the receiving beam are still valid, including naturally the ECE noise temperature and beam dump study.

3.3.1 Beam tracing

In Figure 81 beam traces for the optimised geometry are presented, and we find that the angle of the resolved direction to the magnetic field is, $\angle\left(B_0, k^{\delta}\right) = 104°$, the scattering angle is 86.8º, and the beam overlap is 18.0 m^{-1}. The resulting spectral resolution is discussed in the next section.

One matter of concern with any scattering geometry is the robustness against sawtooth crashes. This is tested by decreasing the density by 10%, and observing the differences in beam overlap and beam displacement. The resulting figure is presented in Appendix F.5 in the Appendix, and we find that the scattering angle is slightly changed while the beam overlap is decreased by nearly 25% to 13.8 m^{-1}. The angle of the resolved direction to the magnetic field is maintained at 104°. These are modest changes.

It is also important to test the beam overlap for the outer edges of the scattered spectrum. Results of such a test are presented in the table in Appendix F.6. It is found that the beam overlap is reduced to 15.8 m^{-1} and 16.3 m^{-1} and the beam centroids are displaced by about 1 cm for the central frequency. Altogether, these changes are of no significance.

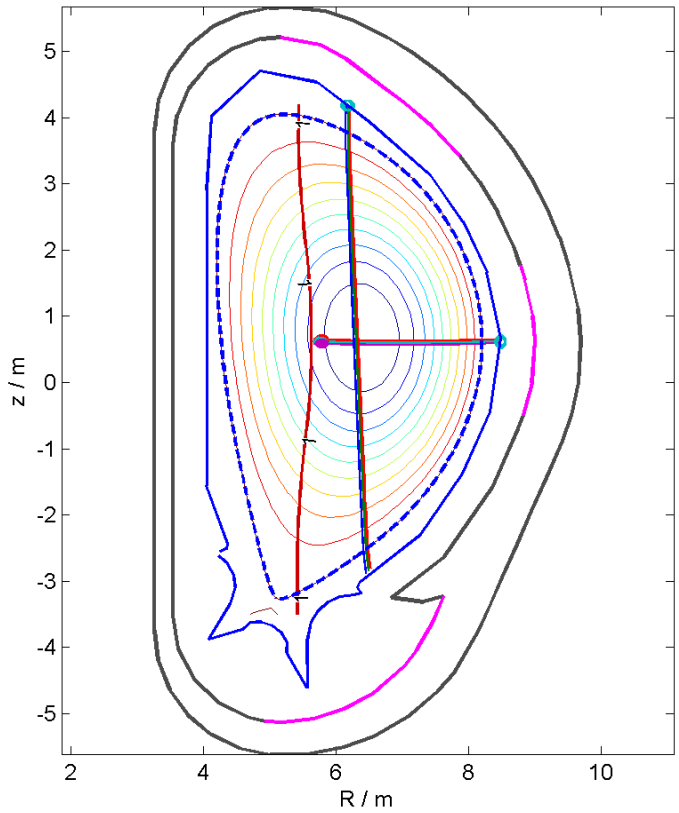

Figure 81. Beam traces for the optimised 170 GHz scattering geometry with the probe displaced in the horizontal plane (reference ITER parameters). The exact parameters used for the beams are presented in Appendix F.4.

3.3.2 Spectral resolution

For the final test of the optimised geometry for the 170 GHz option we investigate the resolving power through a principle components analysis of the posterior for the inferred fast ion distribution. The input parameters are a noise temperature of 3.5 keV (which was the minimal noise temperature seen by the receiving beam in the beam dump according to Section 3.2.3), a gyrotron power of 1 MW, an integration time of 20 ms, and a Gaussian beam radius of 3 cm at the scattering volume. Furthermore, we use the standard parameter uncertainties and the target of $6\times10^{9}\,\mathrm{s/m^4}$ as those used to evaluate the sub cyclotron resonance frequency options.

The results of the analysis are presented in Figure 82 to Figure 84. We see that for 1 MW of gyrotron power the resolving power L is only 0.33, implying that no components of the spectrum are resolved with the target accuracy. It is also seen in the CTS spectrum of Figure 83 that the fast ions only give rise to a modes spectral variation.

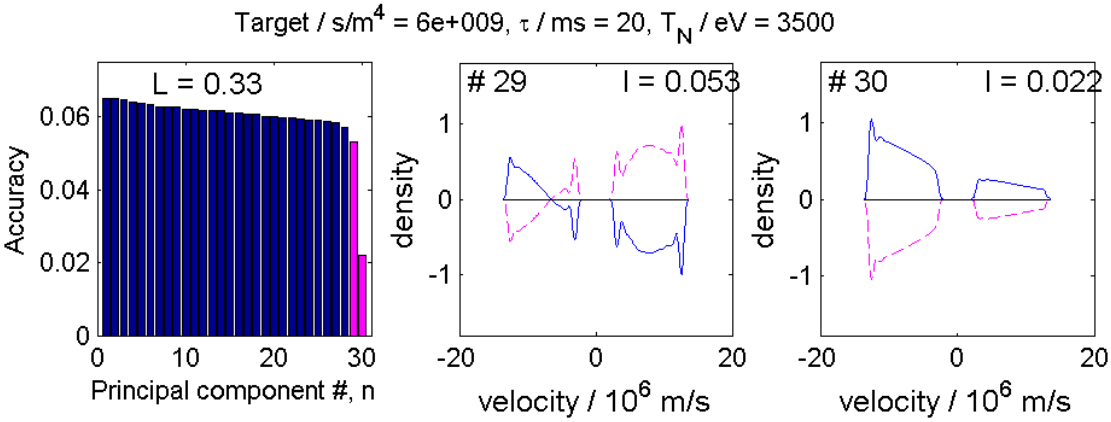

Figure 82. Principle components analysis of the optimised 170 GHz option with a TN of 3500 eV, a gyrotron power of 1 MW and an integration time of 20 ms.

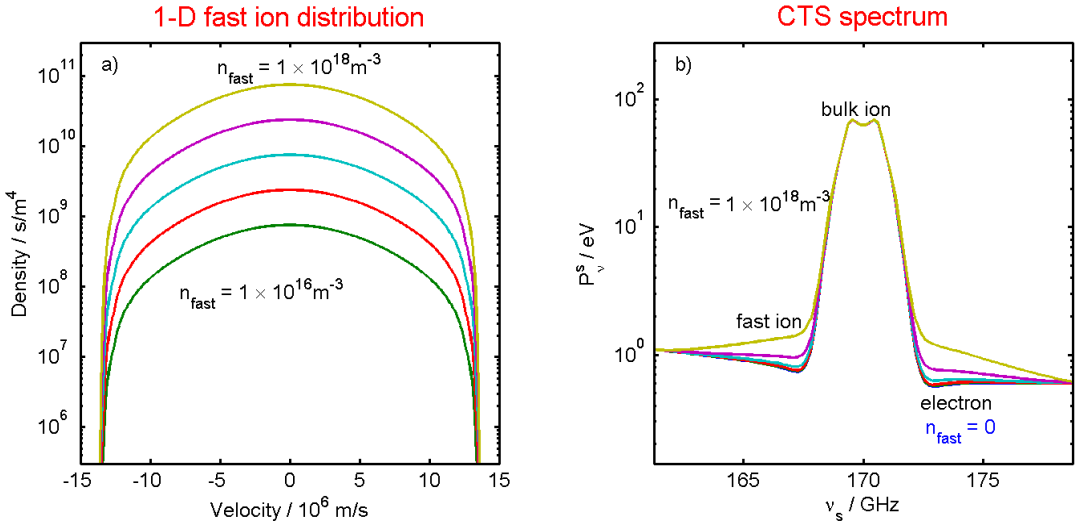

Figure 83. The CTS spectrum of the optimised 170 GHz option with a gyrotron power of 1 MW.

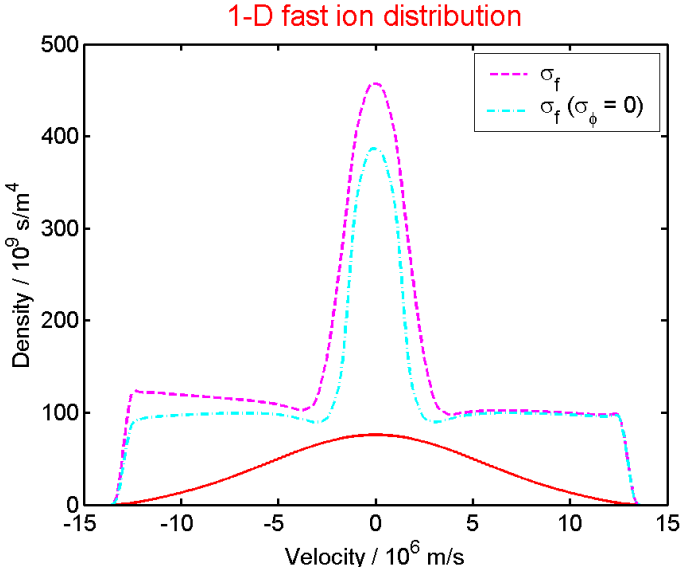

Figure 84. The 1-D fast ion distribution of the optimised 170 GHz option with a TN of 3500 eV, a gyrotron power of 1 MW and an integration time of 20 ms.

In order to improve the signal to noise ratio we increased the gyrotron power to 2 MW while keeping the remaining parameters fixed. The results are presented in Figure 85 to Figure 87, where we see the expected doubling in the resolving power.

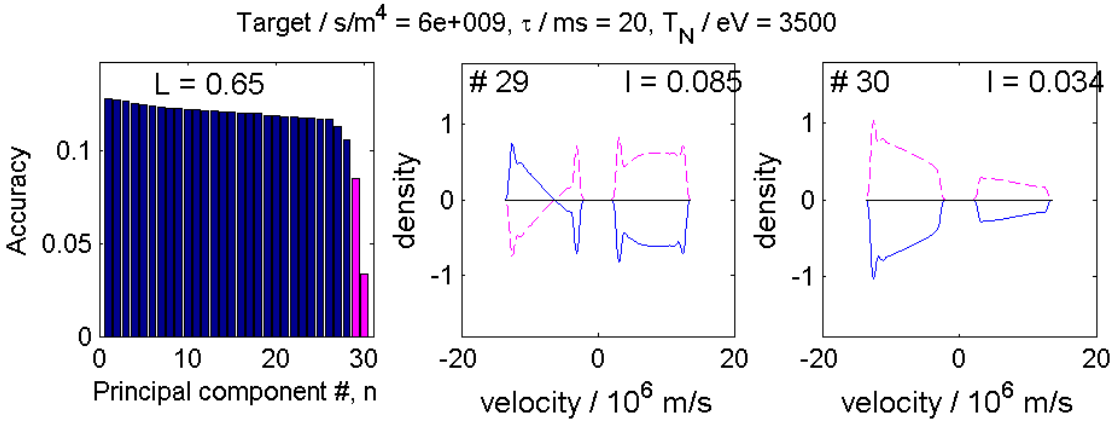

Figure 85. Principle components analysis of the optimised 170 GHz option with a TN of 3500 eV, a gyrotron power of 2 MW and an integration time of 20 ms.

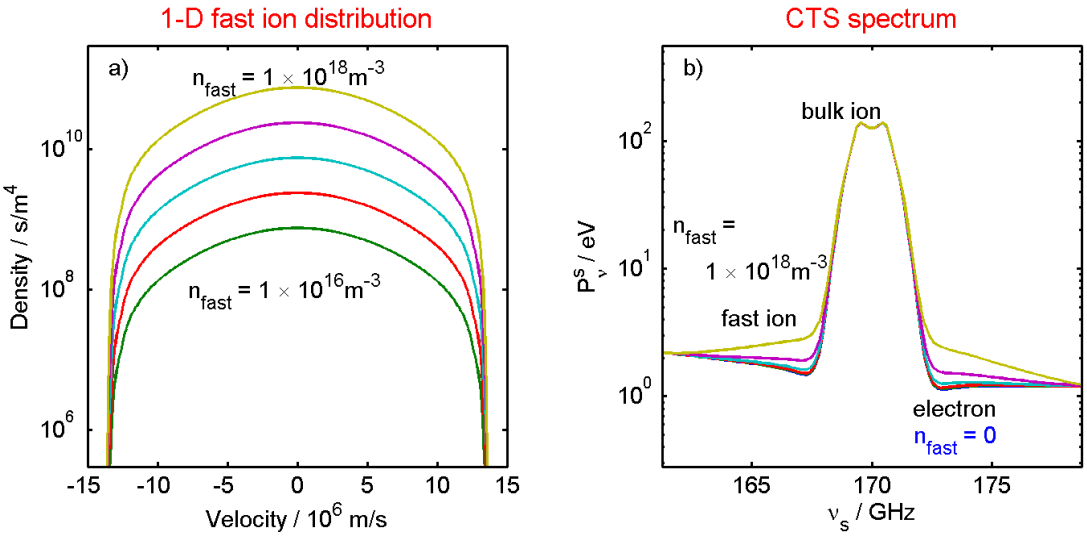

Figure 86. The CTS spectrum of the optimised 170 GHz option with a TN of 3500 eV, a gyrotron power of 2 MW and an integration time of 20 ms.

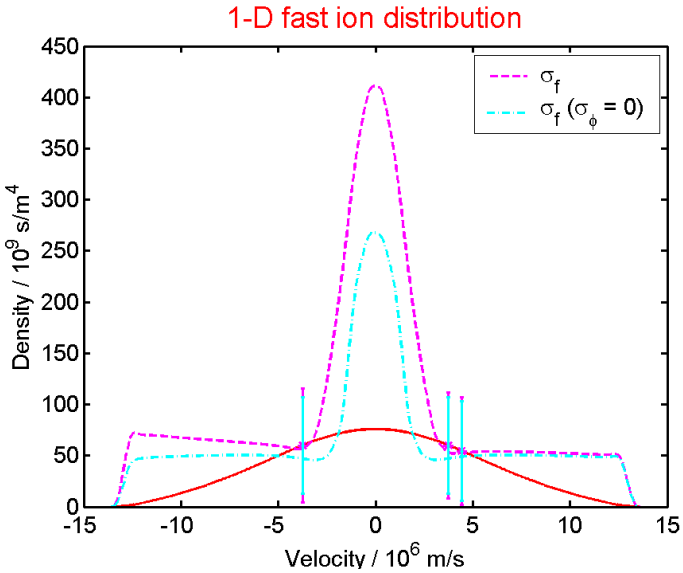

Figure 87. The 1-D fast ion distribution of the optimised 170 GHz option with a TN of 3500 eV, a gyrotron power of 2 MW and an integration time of 20 ms.

Another way to see the difficulty in resolving the fast ion features, even with the optimised 170 GHz geometry, is by comparing the contributions to the scattering function Σ of the different species. From the plots in Figure 88 it is evident that the fast ion contribution is small compared with the electron contribution over most of the fast ion spectral range.

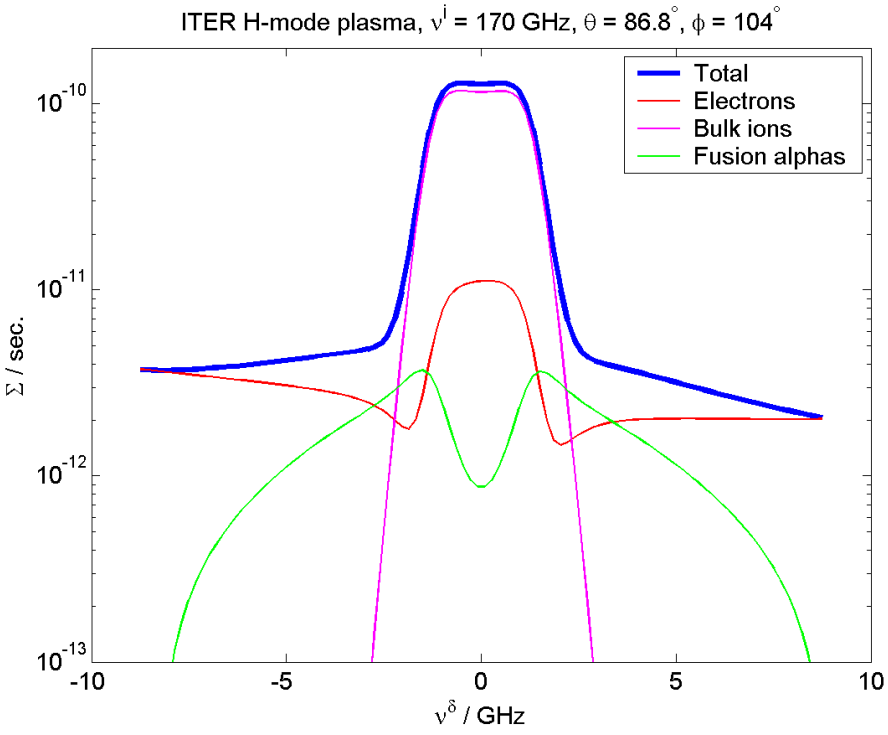

Figure 88. The scattering function, Σ, for the optimised geometry of the 170 GHz option.

3.4 Robustness to changes in plasma parameters

In order to test the robustness of the system against varying plasma parameters we calculate the direct radiation for central electron temperatures of 30 and 35 keV, and make a scan of the density from 0.4 to 1.2 times the nominal density.

3.4.1 Changes of the electron temperature

The results of the ray traces for the higher central electron temperatures are presented in Figure 90 and Figure 91. For convenience we plot the reference case, i.e. 25 keV, in Figure 89.

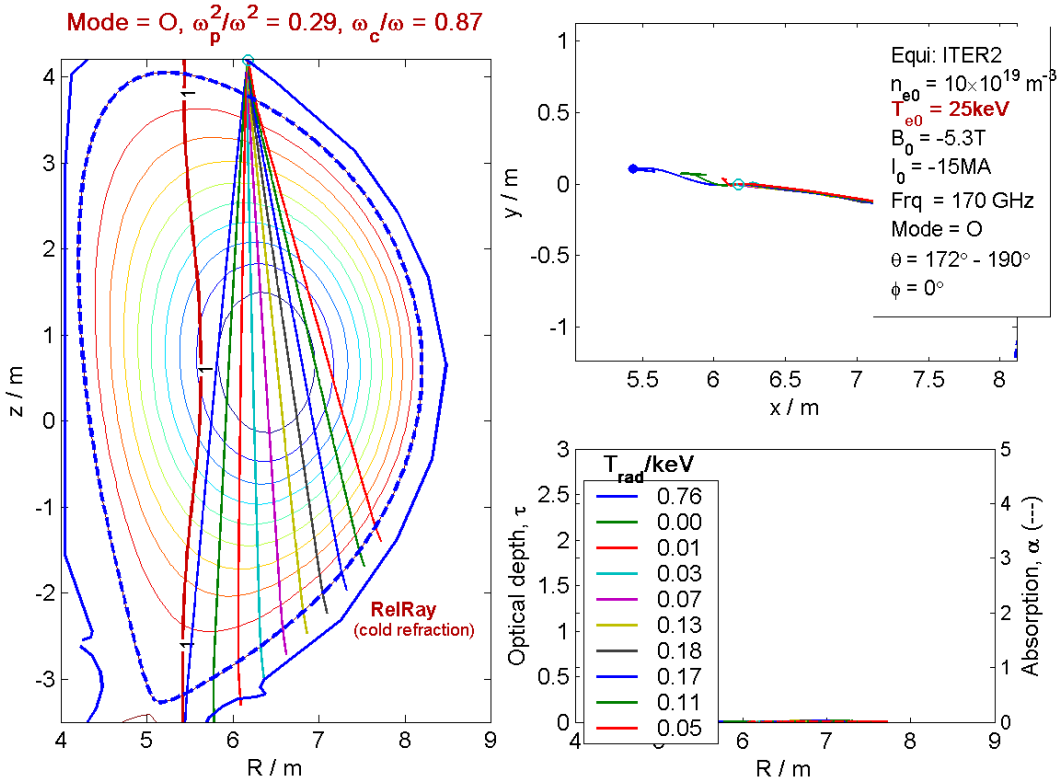

Figure 89. Scan of receiver directions for O-mode at 170 GHz with the reference ITER parameters as shown in the top right corner of the figure, and T_e=25 keV.

By comparing the figures we see that the spectral power density of the ECE in direct view of the receiver rises from 0.03-0.07 keV for T_{e0} = 25 keV to 0.4-0.8 keV for T_{e0} = 30 keV, while at T_{e0} = 35 keV the ECE noise temperature rises to 2-5 keV. To these values one should also add the ECE noise temperatures of the beam dump, which for the nominal case is 3.5 to 4.0 keV. This value increases when the central electron temperature rises. This is demonstrated in Figure 92 and Figure 93, where one sees that for 30 keV the ECE noise temperature for rays in the receiver beam dump is 4.1 to 4.9 keV, while for the 35 keV case the temperature is 4.7 to 5.7 keV. For the 35 keV case the total ECE noise temperature is thus in the range of 7 to 10 keV, while for the 30 keV case it is 4.5 to 5.7 keV.

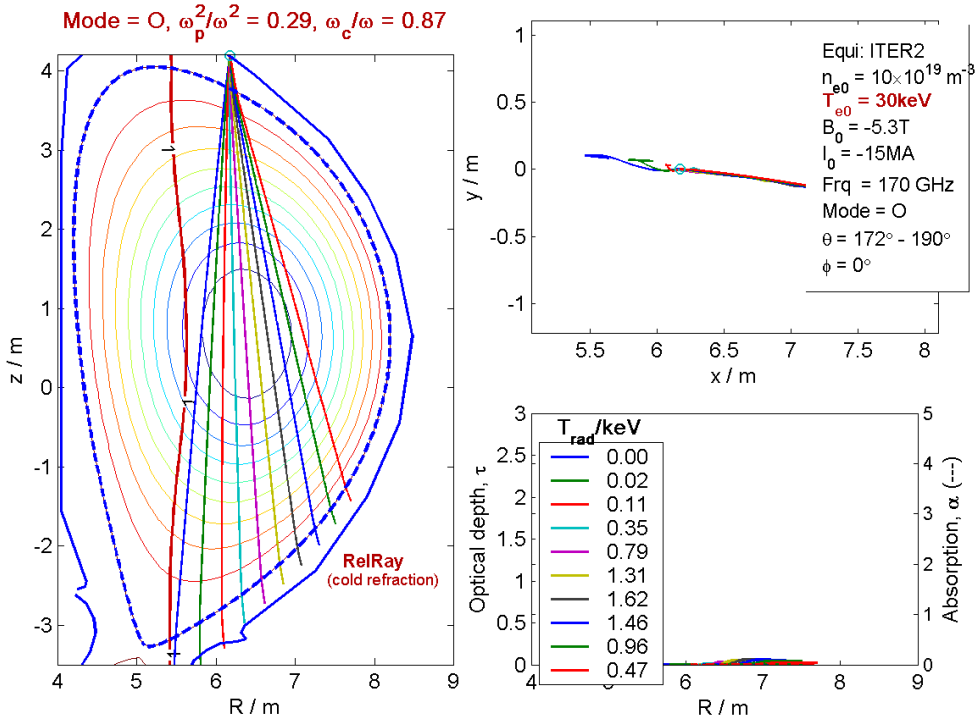

Figure 90. Scan of receiver directions for O-mode at 170 GHz with the reference ITER parameters, except for T_e=30 keV, as shown in the top right corner of the figure.

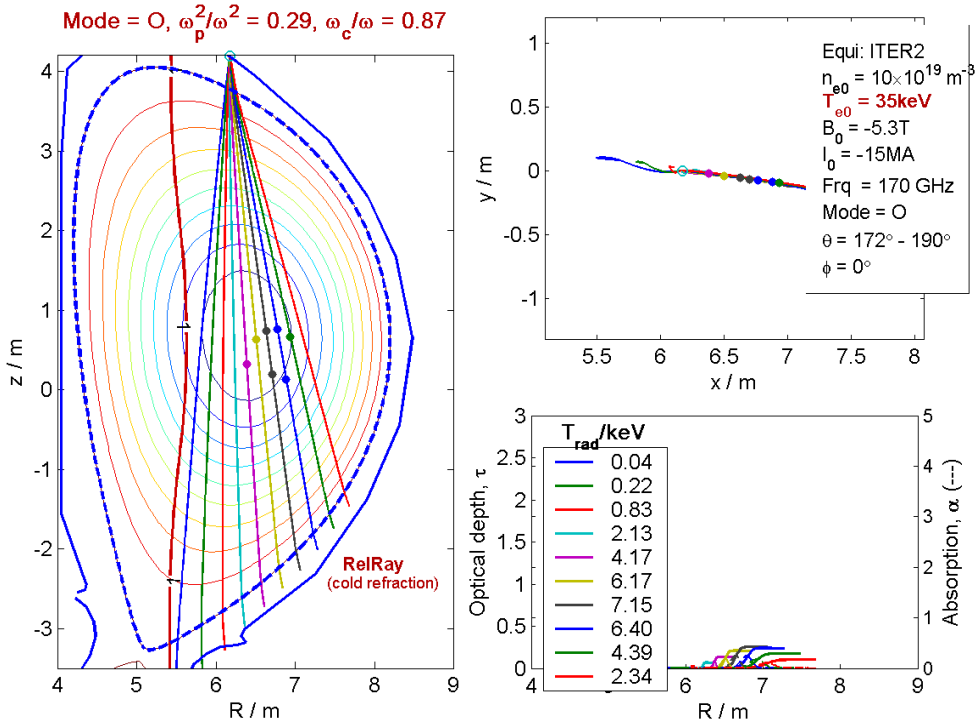

Figure 91. Scan of receiver directions for O-mode at 170 GHz with the reference ITER parameters, except for T_e=35 keV, as shown in the top right corner of the figure.

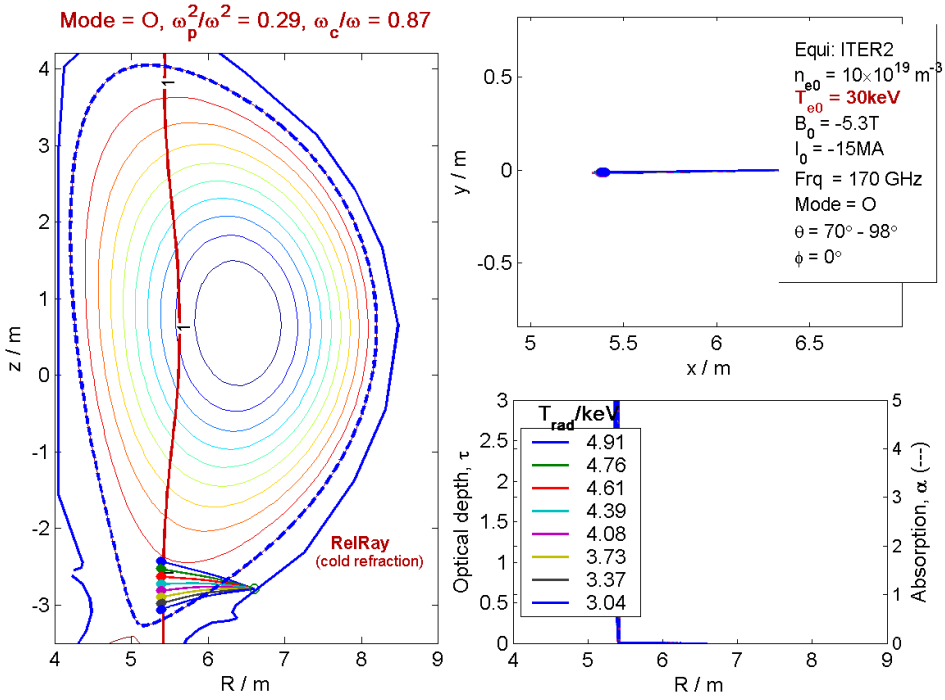

Figure 92. Ray traces of possible beam dump directions for O-mode at 170 GHz with the reference ITER parameters, except for T_e=30 keV, as shown in the top right corner of the figure.

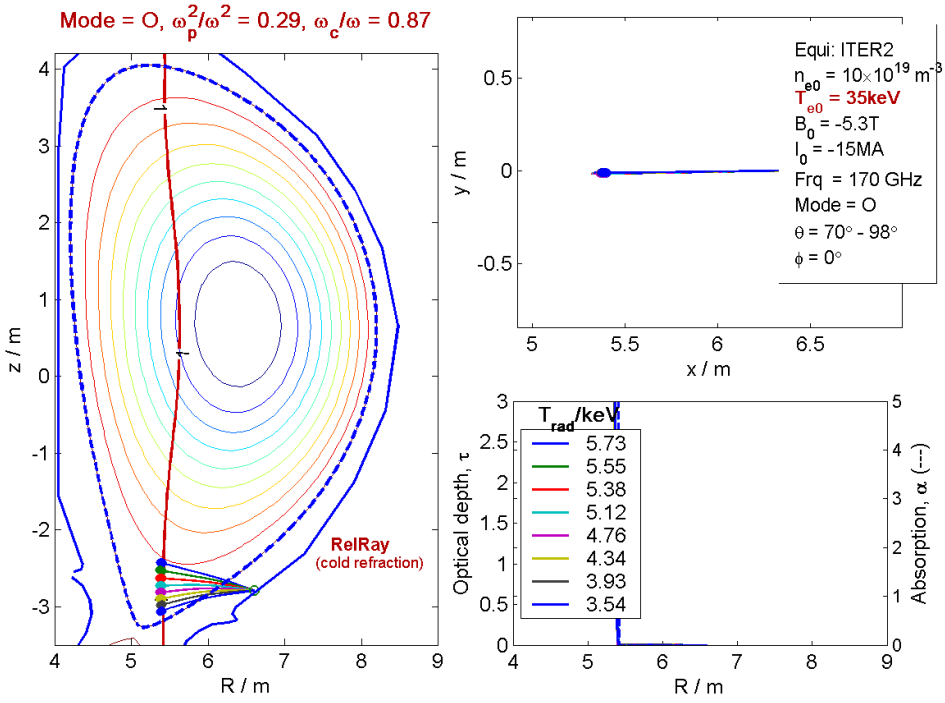

Figure 93. Ray traces of possible beam dump directions for O-mode at 170 GHz with the reference ITER parameters, except for T_e=35 keV, as shown in the top right corner of the figure.

3.4.2 Changes of the plasma density

Variations in density particularly affect the refraction. We elucidate the density effect on the strike point of the receiver by a scan of the density from a factor of 0.4 to 1.2 of the nominal density (1.2 corresponds to the Greenwald density for I_p=15 MA). These scans are presented in Figure 94, and it is apparent that the strike point at the bottom of the vessel changes with density. The strike point moves by nearly 40 cm along the vessel wall when the density is changed from the nominal to 40% of the nominal density, while it moves by 16 cm when the density is changed to 80% of the nominal. When the density is changed to 120% of the nominal value the strike point moves by 13 cm in the opposite direction. In order to use the resonance layer as a beam dump in a low temperature area, as described in Section 3.2.3, one needs the vessel surface to be specularly reflecting in the whole area where the beam strikes. Since the beam moves by up to 40 cm (to one side only), the reflecting area has to be rather large, or the receiving antenna has to be moveable in order to steer the receiving beam onto the reflecting surface. The receiving antenna has to be broadband, which precludes the use of the remote steering considered for the ECRH system on ITER. Thus the broadband antennae require movable mirrors close to the plasma.

3.5 Conclusion

In the assessment of possible CTS systems for ITER we have looked at the option of using a frequency in the window of $\omega_C < \omega < 2\omega_C$. Constraints on scattering angle and the need to use a plasma edge section of the electron cyclotron resonance as a viewing dump implies that we must place the receiver in the upper port. Making this work over a sufficiently wide frequency range to accommodate the full CTS spectrum requires that the dump is viewed orthogonally via a wall reflection. Noting that with this receiver geometry there is a marked increase in the intensity of the relativistically down shifted second harmonic ECE in direct view of the receiver as the frequency is increased above 180 GHz, noting that the collected ECE is essentially constant below 170 GHz down to the frequency where the cyclotron resonance interferes with access to the plasma centre, and noting that the free spectral range required either side of the probe is 10 GHz we concluded that 170 GHz is the optimum probe frequency in this frequency range. The bulk of the investigations in this section thus focus an O-mode system with the receiving antenna located in the upper port looking vertically down through the plasma centre, while the 170 GHz probing beam is injected via the equatorial port. In order to limit the ECE noise picked up by the receiver due to the fundamental cyclotron resonance layer present in the HFS of the plasma, the receiving beam is reflected on the wall at the bottom of the vessel, and directed towards a less hot part of the resonance layer. In this way the ECE radiation temperature seen by the receiver corresponds roughly to that of the resonance layer where it is intersected by the reflected receiver beam. The reflection has to be specular. Any diffraction of the beam by irregularities on the wall will cause the ECE noise temperature to rise because parts of a diffracted receiver beam will intersect hotter parts of the resonance layer. The area that has to be specularly reflecting at the bottom of the vessel should have a diameter of at least 28 cm. In order to use the setup for plasma parameters other than the nominal ones, one would need to increase the specularly reflecting surface significantly, since the centre of the beam moves by up to 40 cm along the vessel wall with varying densities. Alternatively, one would need to steer the receiving antenna, which would require moving components close to the plasma to

allow the antenna to be broadband. The ECE noise temperature seen by the CTS receiving antenna is at best in the range of 3.5 keV for the nominal parameters of the reference ITER equilibrium.

Two geometries have been investigated with the difference being the location of the launch point of the probe. The idea of having an orthogonal geometry with the probe and receiver in the same poloidal cross section has to be abandoned, since effects from the fast magneto-sonic wave will obscure the fast ion information in the CTS signal, when the resolved direction is perpendicular to the magnetic field. By moving the launch point of the probe to one side of the equatorial port one can obtain an angle of 104º to the magnetic field, but studies of the spectral resolution (see Section 3.3.2) show that even with a gyrotron power of 2 MW and an optimistic assumption on noise power, the resolving power, L, is less than one ($L = 0.65$).

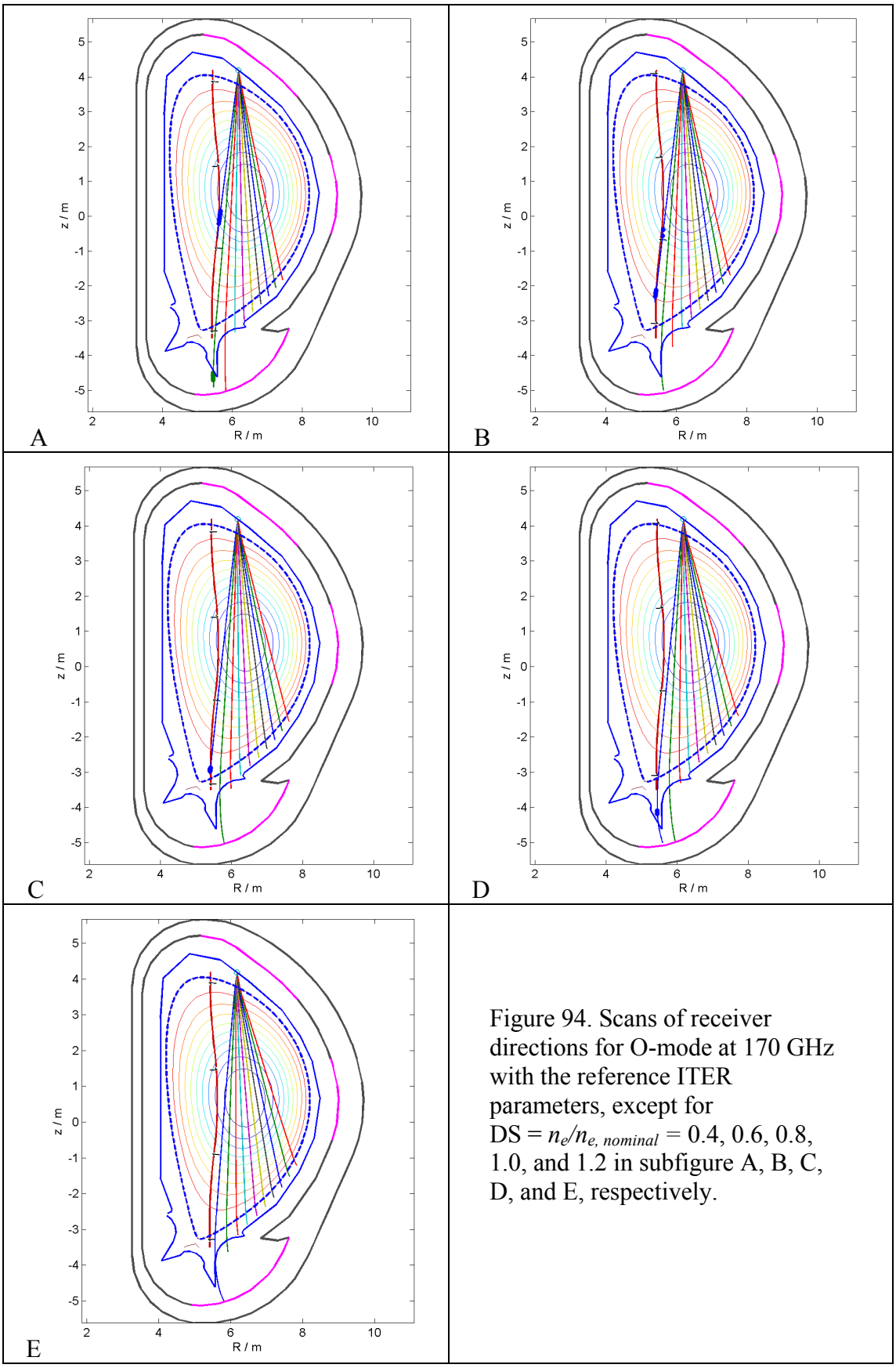

Figure 94. Scans of receiver directions for O-mode at 170 GHz with the reference ITER parameters, except for DS = $n_e/n_{e,\,nominal}$ = 0.4, 0.6, 0.8, 1.0, and 1.2 in subfigure A, B, C, D, and E, respectively.

4 Probe frequency above electron cyclotron spectrum (≈ 3 THz)

4.1 Introduction

Choosing the far infrared (FIR) region for CTS ion diagnostics has the obvious advantage of no or low ECE background noise since it is above the main electron cyclotron resonance spectrum. Furthermore, the refraction at the low THz frequencies is practically non-existent. Bremsstrahlung might have been a matter of concern, but a cautious estimate of the spectral density around 3 THz arrives at a noise level of 0.001 eV.

FIR CTS systems have been built before, and in [14] a 779 GHz system at the TCA tokamak in Switzerland is described.

The main drawback with the THz CTS option is that no appropriate sources are currently available. In order to give a picture of the future possibilities as exactly as possible, we have consulted a number of external experts, and the response we were able to get back from them forms part of the basis of the following, where we describe the possibilities of obtaining a ~3 THz CTS system for ITER.

One obvious possibility to pursue is to utilise a high power molecular gas laser such as the 111 μm line of a D_2O gas. At 111 μm (2.7 THz) the non-thermal tail of the electron distribution still radiates some ECE noise. There is some uncertainty in the calculation since small distortions to the high energy tail of the electron distribution function will affect the spectral power density of the high harmonic ECE that is relevant at these high frequencies. Assuming a thermal electron population, the calculated ECE spectral power density, T_{rad}, as a function of the central electron temperature (T_{e0} = 25 keV is the temperature of the nominal plasma) for a 2.7 THz beam going vertically through the centre of the plasma is presented in Figure 95 and Figure 96 for O-mode and X-mode, respectively. From the figures it is clear that one should choose O-mode, however, at these frequencies the beam will not lock to a certain mode in the plasma, and one cannot avoid a certain amount of X-mode in the received signal. This could amount to perhaps 10 %. At the nominal temperature of 25 keV one should thus expect at least 0.5 eV of ECE background noise. At 30 keV the O-mode contribution is 1 eV, while the total X-mode background noise is around 5 eV.

With a source at 3.5 THz, the picture is somewhat different since the ECE background in both O-mode and X-mode drops by roughly a factor of 10, as seen in Figure 97 and Figure 98.

As mentioned above, the uncertainty in these ECE noise temperature levels is significant. As a consequence, the ECE noise level has not been included in the assessment of the powers needed for the source. We should point out that according to equation (1.23) the required probe power scales linearly with the noise temperature, such that with an additional 1 eV of ECE background added to the 2 eV noise temperature of the receiver, would require a source with 50% higher power.

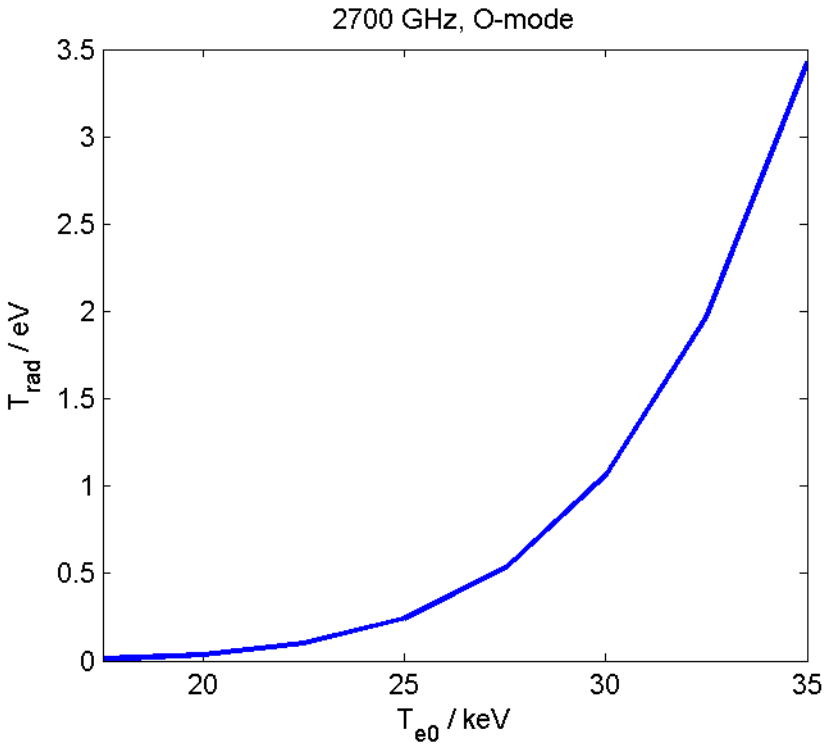

Figure 95. The background ECE noise temperature as a function of central electron temperature for O-mode at 2.7 THz.

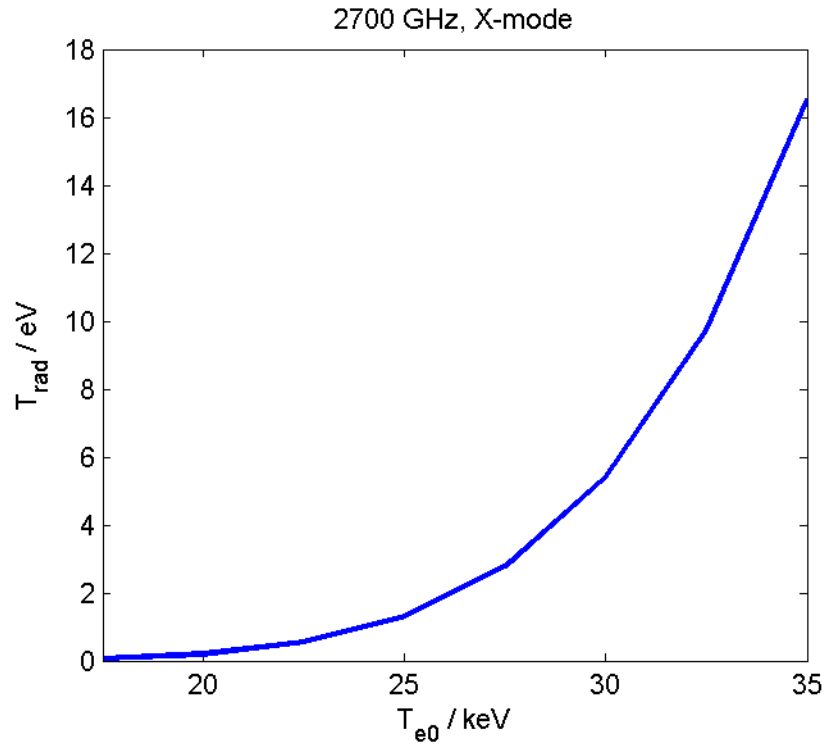

Figure 96. The background ECE noise temperature as a function of central electron temperature for X-mode at 2.7 THz.

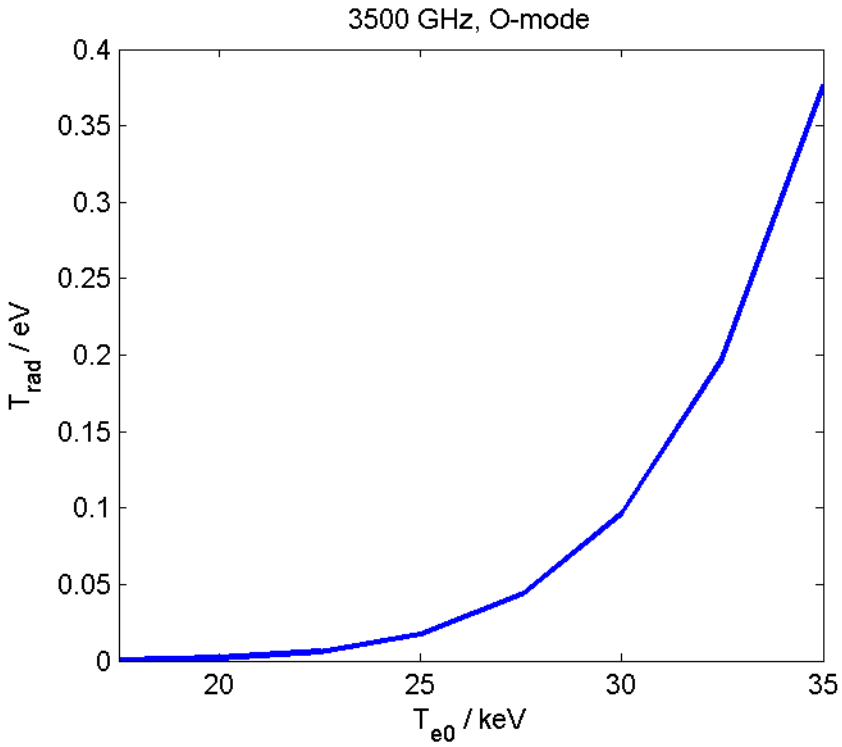

Figure 97. The background ECE noise temperature as a function of central electron temperature for O-mode at 3.5 THz.

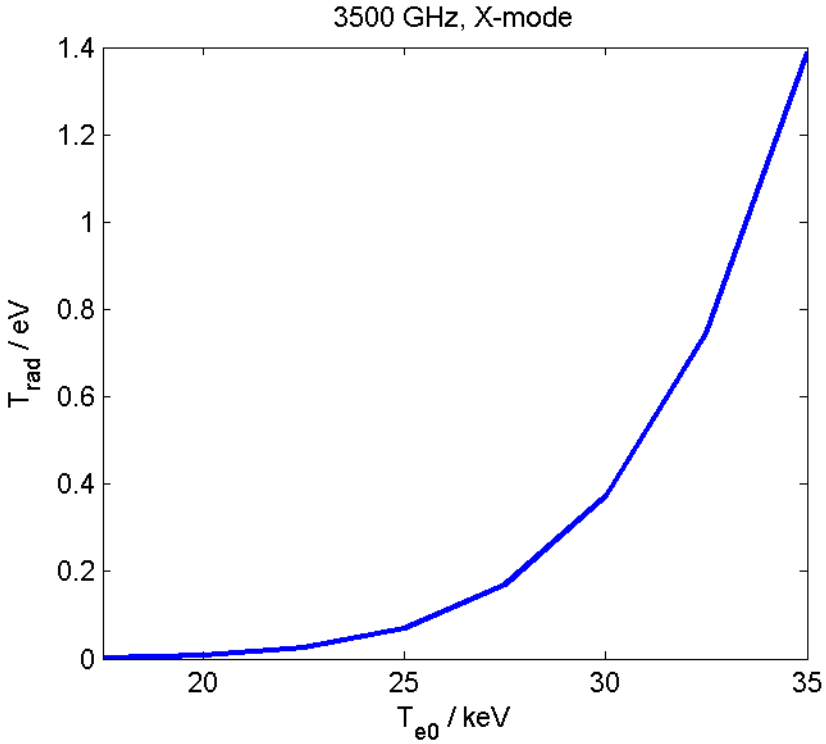

Figure 98. The background ECE noise temperature as a function of central electron temperature for X-mode at 3.5 THz.

4.2 Geometry

In order to do collective scattering and fulfil the Salpeter criteria, Equation (1.4), the scattering angle at 3 THz should be no greater than 5º, i.e., a far forward scattering geometry. This leaves two possibilities for a scattering geometry: one using two equatorial ports for the probe and the receiver, respectively, another using a top port and a port in the divertor area, for the probe and the receiver. The advantage of the latter system is that it leaves the option of getting both the perpendicular and parallel component of the scattered vector by using two receivers, one displaced radially and one displaced toroidally compared to the probing beam.

In Figure 99 we present a possible geometry of this system. Apertures for probe and receiver beams will be required both in the top and in the bottom ports, in order to dump the high power of the probe, to avoid stray light damaging the detectors and to reduce the ECE entering the receiver. The apertures should have diameters of approximately 50 mm. The distances between the beams at the ports are approximately 250 mm, if the scattering angle is 4º. At this frequency and scattering angle the length of the scattering volume is on the order of 0.5 m.

One may consider having several measuring volumes by having multiple receiving antennae displaced so that the respective scattering volumes are displaced vertically along the probing beam.

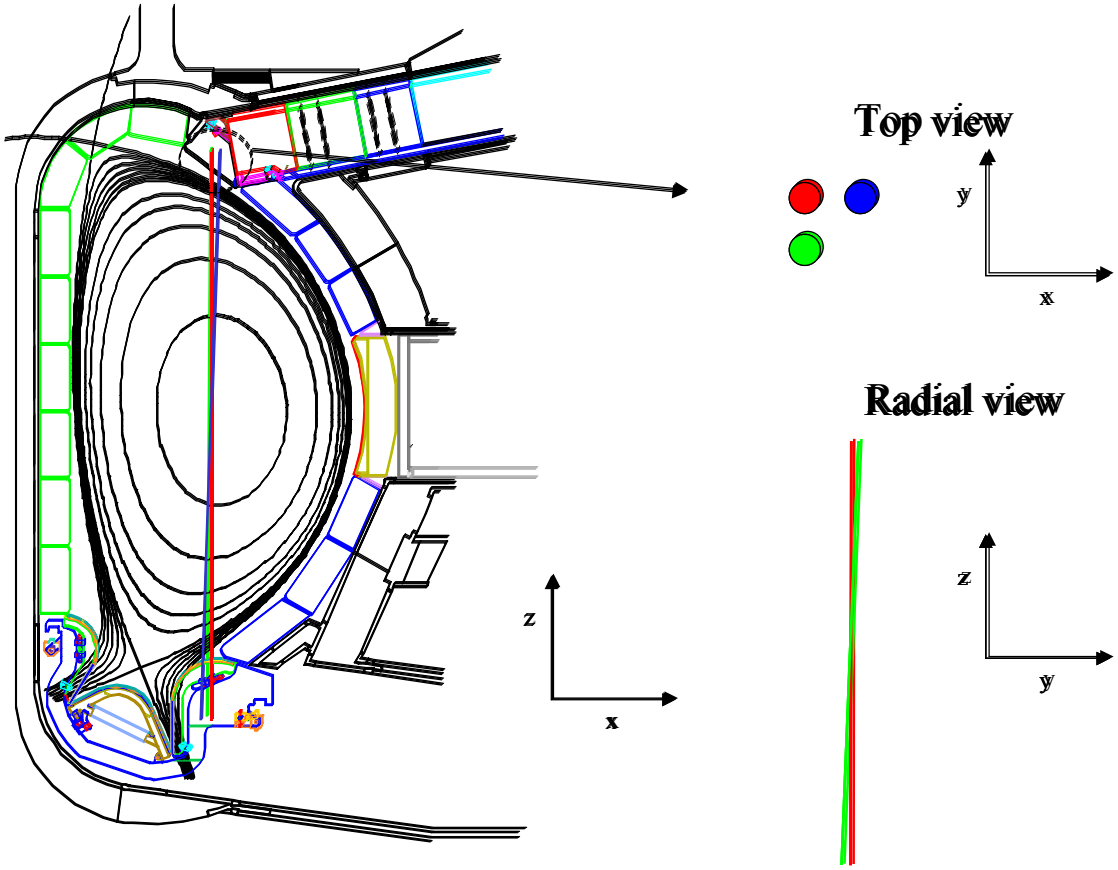

Figure 99. Sketch of the scattering geometry for a FIR CTS system. The true scattering angle is 4º. The geometry is presented in a poloidal cross-section, and for the top view and a radial view. The red beam is the probe, and the green and blue are the receivers displaced toroidally and radially, respectively. The beam diameter is 50 mm and the distances between the beams at the ports are approximately 250 mm.

4.3 Sources

The expression for the resolving power for a 3 THz source, given in equation (1.23), imposes certain specifications on a future source. Combined with other requirements we have drawn up a set of specifications:
A source working at 3 THz having a spectral purity of a few hundred MHz (ideally not more than 200 MHz), operating in pulses of a duration of 600 ns with a repetition rate of approximately 10 Hz with a pulse power of at least 10 MW.
Looking for laser lines in the region of 2.5 to 3.5 THz a D_2O gas seems to be a good option. At 111 μm there is a strong line corresponding to 2.7 THz. In order to approach the 3.5 THz that was found optimal with regard to ECE background noise in subsection 4.1, there is a D_2O line at 84.28 μm corresponding to 3.557 THz. The strength of this line has to be verified, though, before basing a system on it.
Below we describe a few source options.

4.3.1 Free-electron-laser (FEL)

The free electron laser is a well-established technology, but the pulse lengths are generally too short, and the spectral purity cannot live up to what is required to get a well resolved fluctuation spectrum. However, an FEL could be used as an amplifier in a composite source system, which would work by having a THz FEL amplifier using a narrow linewidth molecular gas laser such as the D_2O laser at 111 μm as the driver. A CO_2 laser would be used to optically pump the D_2O gas cell to convert the 10 μm CO_2 wavelength to the 111 μm D_2O wavelength. The output of the D_2O cell would then drive the FEL. The FEL amplifier would be a large device having an accelerator of 1 - 2 MeV and would require development to achieve the necessary average power for useful CTS signal to noise ratios [Private communication, Dr. Paul Woskov, MIT, 2003]. The main concern with a composite source, as described here, is the multiyear development time needed to develop such a source.

4.3.2 Optically pumped FIR laser

As discussed in subsection 1.8, the minimal requirement to the source is 10 MW in 600 ns pulses. This corresponds to an energy of 6 J, which might be obtained from a D_2O laser optically pumped by a CO_2 laser. The pulse energy of the CO_2 laser would need to be about 30 times that of the D_2O laser, i.e. approaching 200 Joules [Private communication, Dr. Paul Woskov, MIT, 2003]. With regard to the repetition rate of 10 Hz, this may pose one of the major technological challenges in this approach, since the CO_2 as well as the D_2O gas have to relax before a new pulse can be fired. One way of solving this may be to continuously flush the gasses.
The laser described here has not yet been developed, however Semet *et al*. [15] described in 1983 a similar FIR laser using a D_2O gas, pumped by a CO_2 laser. They used the 385 μm line of D_2O, as in [14]. This gives a frequency of 779 GHz. They achieved 2.5 J in 3 μs pulses with high spectral purity (line width smaller than 20 MHz). Assuming the same photon conversion efficiency this would extrapolate to about 8.5 J at 111 μm wavelength. The repetition rate was 0.1 Hz due to the CO_2 laser, but this might be improved with some development, by circulating the CO_2 gas

as described above. It might thus be possible to develop a source living up to the requirements of FIR CTS at ITER.

4.3.3 High harmonic gyrotron and other alternative sources

There may be alternative sources such as high harmonic gyrotrons or Cherenkov masers, but these have not yet been developed to the specified frequencies and powers, and would require several years of development.

4.4 Receivers

The number of existing suitable detectors in the THz range is very low, and when approaching 3 THz the Hot Electron Bolometric (HEB) (NbN) mixers may be the only ones suitable. The HEB detector is made of low-T_c superconducting components, thus a receiver using HEB detectors would require the entire receiver front end to be kept at liquid helium temperature (4.2K) including the first IF amplifier. This may be achievable, but one should remember the additional challenge in maintaining the detector at low temperatures, while the power loading by the stray light may be significant. The stray light will have to be dealt with by a gas box notch filter, which has to be very efficient, since the probe power is on the order of 10 MW, while the maximum power loading on a small signal device as the HEB[6] is typically less than 10 nW, i.e. 15 orders of magnitude lower. Although the pulse length of the probe is very short (600 ns) this is still approximately 400 times longer than the thermal time constant of the HEB detector system [Private communication, Dr. Piet de Korte, Space Research Organization Netherlands, 2003]. Though, it may still be possible to design larger devices, which will have higher power level abilities, one would still have to develop very efficient notch filters.

Before turning to the notch filters, we assess the amount of power that will hit the HEB detector in a FIR CTS system on ITER. It is possible to achieve an IF bandwidth of 10 GHz with a HEB mixer, which is exactly what is needed for a FIR CTS system. The power loading on the HEB device on the full bandwidth by the plasma ECE background will be 1.6 nW per eV spectral power density of the ECE. The other contribution is from the CTS radiation itself. From Figure 12 it is clear that the contribution from the bulk ions will be dominant. A rough integration of the bulk ion spectral power at 100 eV over a 2.5 GHz band gives a power of 40 nW. This estimate is 4 times the normal power tolerance of HEB devices, so it does need some development.

A notch filter at these frequencies would be a gas box absorption cell type, as described in [16] for a 385 μm line. In such a device one controls the line width of the notch by controlling the pressure of the gas, and the strength of the notch by the length of the cell (dB/m). A possible suitable gas has to be found, and some development has to be made before such a notch filter is a reality.

The noise temperature of a HEB detector is on the order of 2000 K to 2800 K at 3 THz. For the antenna noise temperature one should add approximately 10 dB of insertion loss for the front-end optics, which leads to a total noise temperature of 2-2.5 eV. The HEB detector is a technology in development and there is a great variation in the noise temperatures given from different teams. One trend seems certain, however; the noise temperature rises with increasing frequency. For example,

[6] HEB detectors are usually used in radio astronomy.

the temperature rises from 2000 K to approximately 3000 K when changing the frequency from 3 THz to 3.5 THz.

4.5 Conclusion

A FIR 2-3 THz CTS system for ITER would offer a number of nice features, such as low ECE background noise and basically no refraction. With a geometry as the one presented in Figure 99 one may be able to get both the perpendicular and the parallel components of the scattered light. However, no present-day sources live up to the required specifications, but some years of development could probably bring sources that would be suitable for a future CTS system.
Suitable detectors may be HEB mixers that are superconducting devices working at liquid helium temperatures. One issue on the detector system is whether it is possible to keep the input power on the HEB device lower than its threshold, and furthermore sufficiently low to utilise the dynamical range of the detector. The current maximum power threshold of HEB devices is exceeded by a factor of 4 by the spectral power of the bulk ions alone. Thus, further development of HEB devices has to be done to raise the power threshold.
An additional source of uncertainty for the low THz FIR range is the ECE background noise level that may augment the required power level of the probe, and may saturate the detectors.

5 CO_2 laser as probe (28 THz)

A CTS system using an infrared (IR) CO_2 laser as a probe benefits from negligible refraction and an absence of in band plasma emission. The power requirements for the probe are thus determined by the need to overcome the detector noise. Quantum well detectors are currently used as broad band detectors at 10.6 μm for the CO_2 laser based CTS at JT60U [17,18] resulting in an antenna noise temperature of just over 5 eV. In subsection 1.8 we found that this noise level led to a probe power requirement of 100 MW in pulses of 1 μs, corresponding to a pulse energy of 100 Joules, to achieve a resolving power of 4, which corresponds to meeting the required accuracy of 20 % in 8 velocity bins either side of zero at a fast ion density of $8\times10^{17}m^{-3}$. To increase the resolving power to 10 to reach the required accuracy at the lower fusion alpha density and to reach the resolving power achieved with the 60 GHz system, the pulse length would have to be increased to above 6 μs and the pulse energy to above 600 Joules.

Increasing resolving power implies an increase in the post integration signal to noise ration of the estimates of the signal spectral power densities recorded in the spectral channels of the diagnostic. For an integration time of τ, a noise power density of P_N and a signal power density of P^s the signal to noise ratio in a spectral channel with band width W is

$$\frac{S}{N}=\frac{P^s}{P_N+P^s}\sqrt{\tau W} \tag{5.1}$$

Noting that with a probe power of 100 MW the signal power density, P^s, is comparable to the noise power density, P_N, it follows from Equation (5.1) that the increased signal to noise ratio in the spectra cannot be achieved by increasing the probe power significantly above 100 MW. Thus improving the signal to noise ratio by a factor of 2.5 to increase the resolving power by almost the same factor requires an integration time, τ, increased by a factor 2.5^2, i.e. more than 6 μs.

To provide 100 ms temporal resolution of the fast ion dynamics the laser pulse rate should be 10 Hz, or 25 Hz to reach the 40 ms time resolution of the 60 GHz system. At this probe frequency the required scattering angle is on the order of 0.5 degrees or less, which makes the suppression of stray light an issue. Here the mode purity and stability is paramount. Ensuring mode purity at these power levels requires that each amplification stage is driven into saturation, which might be achieved with several amplification stages. It would probably also require a sophisticated automated tuning system. To pulse the laser at this power, maintaining mode purity would require gas circulation sufficiently fast to refresh the gas between pulses. Developing a 100 Joule, 10 Hz CO_2 laser with the required mode purity and stability is a challenge and would certainly require a significant engineering effort.

With the very small scattering angle the system alignment is sensitive to vessel movements during operation. A real time beam tracking and alignment system at the vessel may therefore have to be envisaged.

The small scattering angle makes it harder to satisfy both the requirements on spatial resolution and maintain a reasonable velocity space resolution. Reducing the widths of the probe and receiver beams reduces the size of the scattering volume (see Equations (C.13) in Appendix C), but increases the width of the distribution of the wave vectors of the resolved fluctuations (see Equation (C.14) in Appendix C) and consequently decreases the velocity space resolution and the number of independent

velocity points or velocity bins which can be measured (see Equation (1.12) and the discussion in subsection 1.5). Table 8 shows some numerical examples of relationships between beam widths and the resulting spatial resolution and velocity space resolution. From this table it follows that a Gaussian beam width of at least 1 cm is required to be able to resolve 8 independent velocity bins either side of zero, which we regard as a reasonable target for the velocity space resolution. This lead to an elongated scattering volume 5 metres in length, which would lead to poor spatial resolution if we used a vertical beam line resolution as evidenced by Table 8 and illustrated in Figure 100.

Gaussian width of probe and receiver beams in beam plane	10 mm	3 mm	2 mm	1.3 mm
Scattering angle	0.4°	0.5°	0.5°	0.5°
Length of scattering volume (Δz in Equation (C.13) in Appendix C	5 m	1.2 m	0.8 m	0.5 m
Relative resolution assuming vertical beam line	$a/0.6$	$a/2.5$	$a/3.8$	$a/6$
Number of resolved velocity bins either side of zero (Equation (1.12) in subsection 1.5).	8	3	2	1

Table 8. Relations between beam widths, spatial resolution and velocity space resolution, for a CTS with a probe frequency of 28.28 THz. The scattering angle is reduced to 0.4° for the widest beams to compensate the reduced beam overlap and hence signal with wider beams.

Even if we reduce requirement on velocity space resolution, we cannot achieve the required spatial resolution with a vertical beam line. Acceptable spatial resolution requires a geometry where the beam lines are near tangential to the toroidal direction as illustrated in Figure 101. With this geometry a spatial resolution of $a/4$ can be achieved while maintaining a velocity space resolution permitting 8 velocity bins to be resolved either side of zero.

To prevent the fast magneto-sonic wave entering the CTS spectral range (see discussions in subsection 1.4 and Appendix B) we would need to avoid a scattering geometry with $\phi = \angle(\mathbf{k}^{\delta}, \mathbf{B})$ near 90˚. This could be achieved by giving the beam lines a vertical component. This geometry would measure the perpendicular velocity distribution, while it does not permit measurements of the parallel velocity distribution.

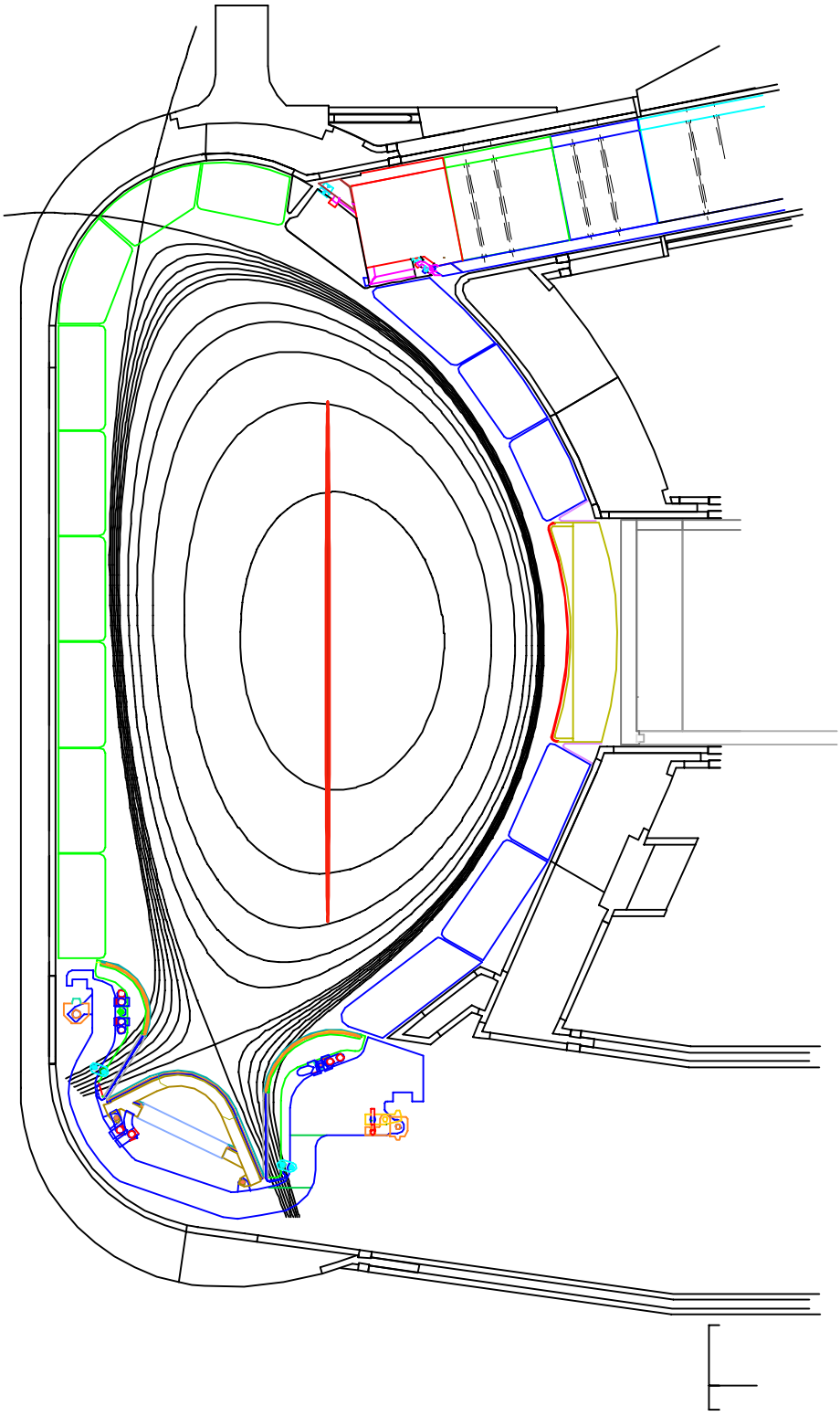

Figure 100. ITER poloidal cross section with the scattering volume of a CO_2 laser based CTS shown in red. Here the beam line is vertical.

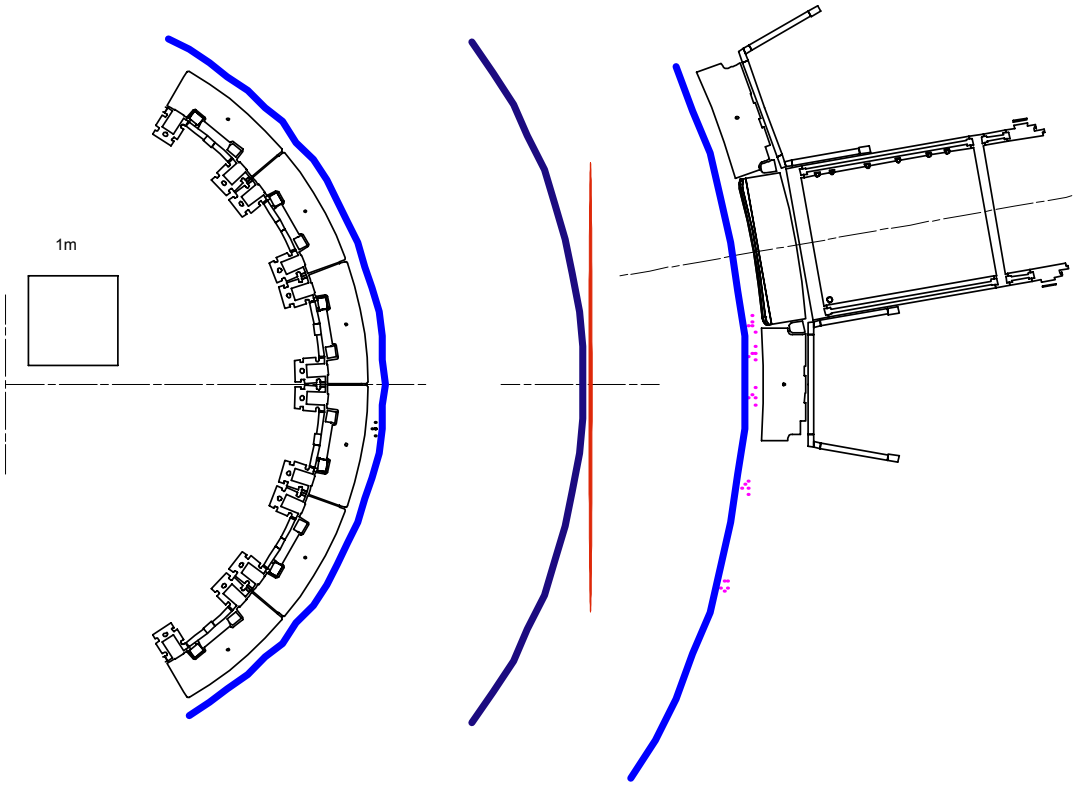

Figure 101. ITER toroidal cross section with the scattering volume of a CO_2 laser based CTS shown in red. Here the beam line is near horizontal. Access required from two midplane ports.

6 Summaries and comparisons

In Section 1 we identified which systems to consider as candidates for fast ion CTS diagnostics for ITER. We set out a number of topics and common tools for analysing the diagnostic capabilities of candidate systems, and conducted a preliminary study of the ability of each candidate to resolve the fast ion velocity distribution, depending in each case on design parameters of the candidate. In addition to an initial comparison of systems, this set out design targets for each candidate diagnostic. One element of this was formulated as estimates of the resolving power of each candidate diagnostic in terms of its design parameters. These included probe power, receiver noise temperature, antenna beam widths and scattering geometry. The resolving power was expressed by equations (1.20) to (1.24), valid for the plasma parameters of the reference ITER plasma described in Appendix A.

Important criteria include:

1. Resolving power (essentially the product of the number of resolved components of the fast ion contribution, and the accuracy with which the components are resolved).
2. Spatial and temporal resolution.
3. Operational ranges, in particular at which electron temperatures and densities the systems can operate.
4. Robustness of the systems to variations in plasma parameters.
5. Robustness of the systems to vessel movements, and to construction and operational inaccuracies.
6. Certainty in performance estimation and extrapolation.

7. Readiness of the technology.
8. Managable impact on other systems.

The first three criteria were essentially the basis of the initial investigations and comparisons in Section 1. In the subsequent sections, focussing on individual candidates, critical issues from all the criteria were discussed in further detail. Here we draw out the main points of the preceding discussions, and compare the candidates. A brief set of statements on potential performance and status of the candidate fast ion CTS systems is given in Table 9. The statements should serve only as reminders of the points made in the detailed discussions.

	55-60 GHz	170 GHz	2.7-3.5 THz	28 THz
Resolving power	Very good resolution of parallel and perpendicular velocity distributions across profile. $L > 10\times P^{i}/1\text{MW}$	Poor resolution of perpendicular velocity distribution in one radial location. No resolution of parallel distribution. $L < 1\times P^{i}/2\text{MW}$	Potentially good resolution of parallel and perpendicular distributions across profile. $L \approx 4\times E^{i}/6\text{J}$	Potentially good resolution of the perpendicular velocity distribution. $L \approx 4\times E^{i}/100\text{J}$
Spatial resolution	20 cm	5 cm	50 cm	500 cm
Operational ranges	$n_e < 1.3\times10^{20}\text{m}^{-3}$ for $T_e < 25$ keV $n_e < 1.0\times10^{20}\text{m}^{-3}$ for $T_e < 35$ keV	T_e limit N/A. No relevant n_e limit.	$T_e < 30$ keV (2.7 THz) $T_e < 35$ keV (3.5 THz) No relevant n_e limit.	No relevant T_e limit. No relevant n_e limit.
Robustness to plasma variations	Robust due to wide beam patterns orthogonal to the beam plane. No steering required.	Robust due to low refraction. Some trouble with receiver beam reflector. Requires steering.	Robust.	Robust.
Robustness to mechanical disturbance and misalignment	Robust.	Moderately sensitive.	Sensitive.	Very sensitive.
Certainty in performance estimation	Reliable.	Reliable, except for performance of specularly reflecting surface.	Uncertainty in ECE, in detector noise and in source performance.	Uncertainty in source performance, and stray-light handling.
Readiness of the technology	Essentially ready.	N/A.	Significant multi year development of source.	Significant multi year development of source.

Table 9. Brief statements on potential performance and status of the candidate fast ion CTS systems. The statements should serve as reminders of the points made in the detailed discussions.

6.1 Quality of the measurements

For the millimetre wave systems we can make performance predictions on the basis of the performance of existing or near term sources, while for the FIR and IR options we need to make assumptions about improved sources.

6.1.1 Resolving power and accuracies

With existing technologies, the predictions for the 60 GHz systems generally show resolving powers, L, well in excess of 10. This is achieved across the plasma cross section, for both the system measuring the parallel velocity distribution, one half of which is in the counter direction where beam ions are essentially absent, and for the system measuring the perpendicular distribution. This level of accuracy in the measurements comfortably satisfies our target of $L > 4$. It also satisfies our more stringent target of a resolving power above 8, for which the ITER measuring requirements on the accuracies of the measured distribution, resolved into 8 bins either side of zero are satisfied at an alpha density down to $4\times10^{17}\text{m}^{-3}$, and the

accuracy of the alpha density measurement is satisfied down to the required alpha density of $1\times10^{17}m^{-3}$.
With existing or near term sources in the 170 GHz range we find resolving powers well below 1, with optimistic estimates of the ECE noise background and the assumption of 2 MW sources. Assuming sources at higher power levels, which would bring the resolving power up to our target, is not realistic. Thus at 170 GHz we fall far short of the ITER measuring requirements.
In the FIR and IR range there is less certainty about the source performance that can be attained within a few years and with reasonable budgets. Since the present performances are inadequate, but development is realistic, we have chosen to select the source specifications which would meet our target in resolving power. These are microsecond pulse with energies in the range of 6 Joules for the FIR and 100 Joules for the IR systems, both with high spectral purity to attain a resolving power of 4. These pulses must be produced at a rate of 10 Hz to meet the ITER requirements on temporal resolution, or 25 Hz to reach the temporal resolution attained with the 60 GHz systems. There does not appear to be any fundamental obstacles to reaching these performances, but the engineering development required is considerable.
To meet the ITER requirements on accuracy and approach the accuracies attainable with the 60 GHz systems would require pulses in excess of 15 Joule in 600 ns for the FIR range and in excess of 600 Joule in 6 μs in the IR range.
To make it meaningful to include the 170 GHz system in the subsequent comparisons we have to relax the requirements on temporal resolution by a factor of 10 and increase the source power to 5 MW and assume machining of the first wall to perfectly reflect the receiver beam into the lowest part of the EC resonance.

6.1.2 Spatial resolution

The 60 GHz options could provide a radial resolution better than 20 cm, across the profile in the horizontal midplane, resulting in a relative resolution of $a/10$, thus satisfying the ITER requirements on spatial resolution.
The 170 GHz system would give one spatial measurement with a spatial resolution of down to 7.5 cm.
The FIR could provide measurements across the vertical profile with a vertical resolution of 50 cm, corresponding to a relative spatial resolution of $a/6$, thus approaching the ITER requirements on spatial resolution.
An IR system with a vertical beam line cannot simultaneously provide adequate velocity space resolution and spatial resolution. With a velocity space resolution permitting the 8 velocity bins to be measured independently either side of zero velocity, as required of the other systems, the IR system would have a spatial resolution of 5 metres in the vertical direction, exceeding the half height of 3 metres. Limiting the velocity space resolution to 3 bins would improve the spatial resolution for the IR system to $a/2.5$. At a spatial resolution of $a/6$, as attained with the FIR, the IR system would not resolve the fast ion distribution but only provide a weighted average over the distribution. Thus we conclude that the IR system cannot usefully be employed with a vertical beam line. With a horizontal beam line, tangential to the toroidal direction, the IR system can achieve a spatial resolution of $a/4$, somewhat short of the $a/10$ requirement, while retaining a velocity space resolution permitting 8 bins to be resolved either side of zero velocity.
The 60 GHz and FIR systems could provide spatial profiles with just one or two probe lines. The IR system would require a separate probe line for each spatial point. The 170 GHz system cannot provide a profile.

6.1.3 Directions in velocity space and the beam ions

The 60 GHz systems would be capable of resolving both the parallel and the perpendicular velocity distributions, as would the FIR option. The parallel distribution consists of the co direction (the direction of the current and the NBI injection) on one side of zero and the counter direction on the other side of zero. There are essentially no beam ions travelling in the counter direction so the fast ion distribution measured in that direction would be almost purely the fusion alphas. Thus the 60 GHz system and the FIR would be able to measure the fusion alphas in a direction where there is no addition of beam ions.
The 170 GHz system would resolve the perpendicular distribution, but not the parallel because of constraints on geometry.
To measure the parallel distribution with the IR system would require a vertical beam line, which as discussed above, is not compatible with achieving both reasonable velocity space resolution and spatial resolution. With a horizontal beam line tangential to the toroidal direction, the IR system can only resolve the perpendicular velocity distribution, not the parallel.

6.2 Robustness

The 60 GHz systems suffers most refraction, but the relatively high CTS signal strengths and consequent high resolving powers permit the robustness against refraction to be improved by widening the beam patterns in the direction orthogonal to the beam plane. The 60 GHz systems can meet the measurement requirements up to an electron density of $1.3\times10^{20}m^{-3}$ for the parallel measurements and $1.2\times10^{20}m^{-3}$ for the perpendicular measurements, both at an electron temperature of 25 keV. This is at the Greenwald limit for I_p = 15 MA. At 35 keV the density limits reduce to $1.0\times10^{20}m^{-3}$. This robustness is achieved without the need to introduce beam steering. The 60 GHz systems would also be robust against mechanical vibrations and other vessel movements.
At 170 GHz the fight to improve the resolving power leads to a strong focussing of the receiver and probe beams in the scattering region, widening the receiver beam at the reflecting mirror on the lower first wall. The need to hit the mirror and to ensure overlap in a slightly off perpendicular geometry, introduces the need to compensate refraction with beam steering. While a narrow band remote steering option is being developed for the ECRH/ECCD system at ITER, this system could not be use for the steering of the broadband receiver beam. A front-end steering system appears the only option for the broadband receiver, which is a more delicate and problematic system.
The FIR and IR systems would not suffer significant refraction, but to compensate mechanical movements these systems would need beam steering to ensure the beam overlap and scattering geometry. For IR this is augmented by the smaller scattering angle and the need to minimise the stray-light level. For the IR system real time monitoring of the beam trajectories may be necessary.

6.3 Readiness of the technology

The microwave options benefit from the successful operation of mm wave fast ion collective scattering on present machines. The 60 GHz system essentially assumes the use of existing technology and rugged plasma facing components. The most demanding development required is a 1 MW long pulse gyrotron at 60 GHz. Such gyrotrons already exist for the more challenging higher frequency of 140 GHz.

The 170 GHz system has to assume a very significant increase in gyrotron performance, and that a part of the first wall can be maintained as a mirror. Also it assumes broad band beam steering. The strategy of using the cold part of the EC resonance as a receiver viewing dump was tried without success at JET.
The FIR system assumes significant technological developments. Our calculations assume use of low noise detectors used in astrophysics. They are fragile and would need further development for use in an FIR CTS. Sources to deliver a probe pulse energy of 6 to 15 Joules in 600 ns at a repetition rate of 10 Hz (to meet the requirement on time resolution) are not currently available. While it may be possible to reach these specifications with a free electron laser run as an amplifier, this solution appears prohibitively expensive. An alternative route is an optically pumped molecular gas laser, such as a D_2O laser pumped by a CO_2 laser. Achieving 6 to 15 Joules from the molecular laser would require on the order of 200 to 500 Joules in the CO_2 laser, at 10 Hz. The line width requirements on the CO_2 laser would be the same as those required at the probe frequency. Designing such a source is a formidable engineering task.
The IR systems using CO_2 lasers directly as the sources of the probe radiation also assume significant technological development. Sources with pulse energies at 100 Joules, with high spectral purity and spatial mode purity at a repetition rate of 10 Hz are not currently available. Developing such a source is demanding. To meet the ITER requirements on accuracy at the lower alpha densities demands a source delivering 6 μs pulses with more than 600 Joules, spectrally pure and at 10 Hz. This is truly a formidable engineering challenge.

6.4 Impact on other sysems

The CTS systems will have impact in terms of accss requirements. This is discussed in detail for the 60 GHz system in the conceptual design study presented as Annex 2 of this study. The impacts of access requirements for the IR, FIR and 170 GHz CTS systems have not been assessed in this study. Straylight from the probes has the potential for impacting on other diagnostics. For the IR and FIR systems the probe is dumped outside the torus vessel. Attention needs to be paied to keeping straylight levels sufficiently low not to impact on other diagnostics in the optical range. For the 170 GHz system the probe is dumped on the electron cyclotron resonace in the plasma. The perturbation of the plasma will be modest and no influence on other diagnostics would be expected. For the 60 GHz system the probe would be absorbed by the first wall after multiple reflections. The average probe power density at the wall can be expected to be on the order of 7 kW/m^2, which is very small compared with the total electromagnetic power load on the walls. Nonetheless, with the power falling within a narrow spectral range microwave diagnostics working in the same range, notably reflectometers, will need filters for protection. ECE diagnostics will work at higher frequencies permitting effective high pass filters, e.g. a section of fundamental wave guide, to be used. Interference of CTS probe with bolometers has been reported from the FTU tokamak. This effect was not found with the CTS at JET where the probe wall power load was comparable to that expected in ITER. Further experimental verification of the compatibility of CTS probes with other diagnostics will be available from fast ion CTS diagnostics at ASDEX upgrade and TEXTOR. The former will present probe wall power loads far in excess of what would be expected for ITER.

6.5 Conclusion

In conclusion, the only system which can fully meet the ITER measurement requirements for confined fusion alphas is the 60 GHz system. This includes measuring the fusion alphas in the counter direction where there are essentially no beam ions. This is achievable with existing or near term technologies, the most demanding of which is the development of a 1 MW long pulse gyrotron at 60 GHz. Such gyrotrons already exist for the more challenging higher frequency of 140 GHz. The technologies have been tested successfully on current machines. The system can meet the measurement requirements up to the Greenwald density limit for the reference electron temperature of 25 keV. At higher temperatures the density limit is reduced so that the limit effectively is a beta limit which is close to the plasma operational beta limits. Thus it is not expected that this limit will be of practical consequence. The 60 GHz fast ion diagnostic can be combined with a fuel ratio diagnostic at 60 GHz which uses the same front ends as the 60 GHz fast ion diagnostic.

The only other system which is close to meeting all the ITER measurement requirements for confined fusion alphas is the 3 THz FIR system. This system does, however, require significant source and detector developments.

The IR CO_2 laser system cannot meet the ITER measurement requirements for confined fusion alphas. In particular, the system cannot measure the velocity distribution of the fusion alphas in the counter direction with the required spatial resolution. Resolving 8 velocity bins leads to no spatial resolution, while resolving 3 velocity bins leads to a resolution of a/2.5. The CO_2 laser based system can measure the perpendicular distribution with a spatial resolution of a/4. A CO_2 laser based CTS does require significant source developments.

A 170 GHz system cannot meet the ITER measurement requirements.

A ITER reference plasma

For the computations in this report we use the ITER Q = 10, H-mode reference plasma provided by Y. Gribov, ITER [*ftp://itergps.naka.jaeri.go.jp/PF_control/EQDSK_files/Scen2_burn_PET*].
The equilibrium has a vacuum toroidal field on axis of -5.3 Tesla and a toroidal current of -15 MA. The magnetic equilibrium is displayed in Figure 102 and electron density and temperature profiles in Figure 103.

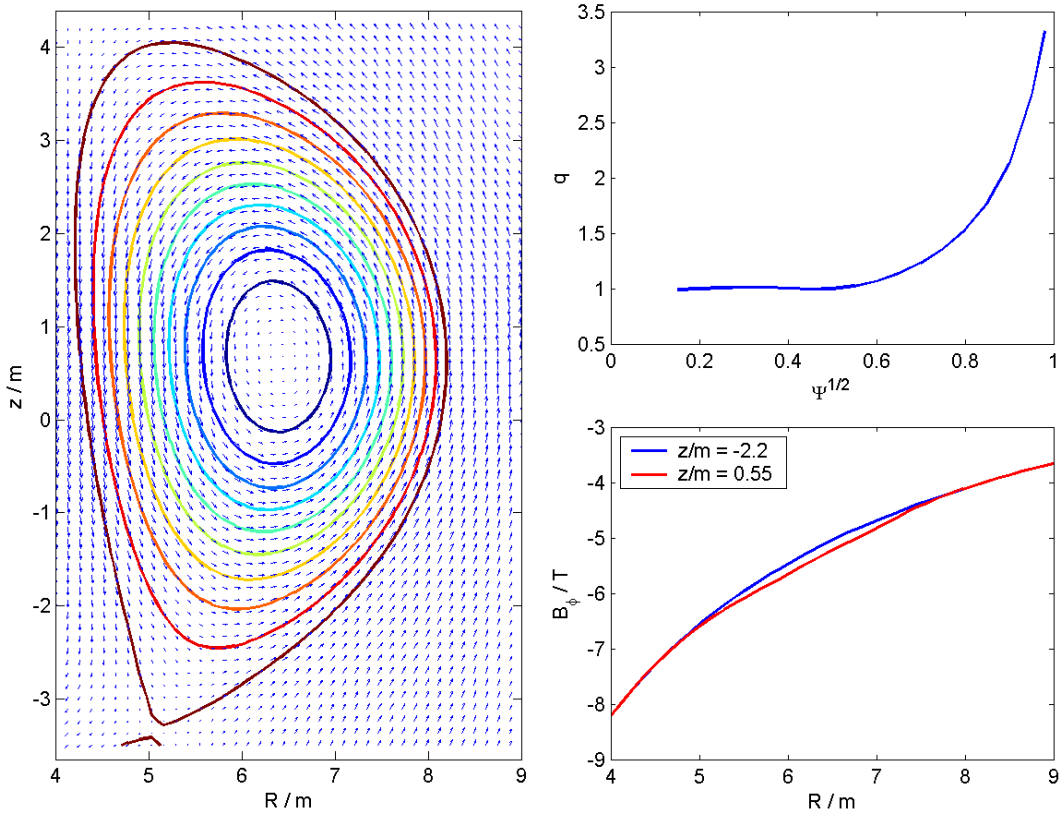

Figure 102. Reference ITER equilibrium. The left pane shows the poloidal field and poloidal flux surfaces as functions of major radius and height. The upper right plot shows the safety factor q as a function of the square root of the normalized poloidal flux. The lower right plot shows the toroidal magnetic field as a function of major radius at two heights.

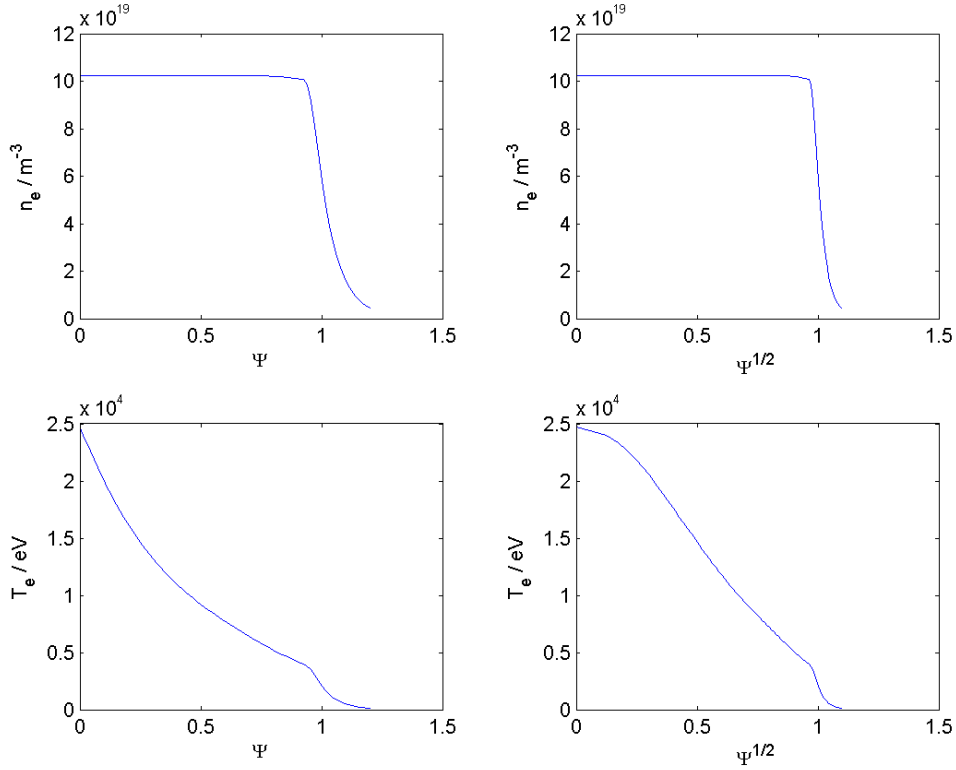

Figure 103. Electron density and temperature profiles as functions of normalized poloidal flux and the square root thereof.

From the following we get a rough estimate of the fusion alpha density in ITER, n_α, and the phase space density f_α.

$$
\begin{aligned}
P_{\text{fus}} &= 400\ \text{MW} \\
P_\alpha &= P_{\text{fus}} / 5 = 80\ \text{MW} \\
\partial N_\alpha / \partial t &= P_\alpha / E_{\alpha\,\text{birth}} = 1.4\times10^{20}\ / s \\
\tau_{\text{slowdown}} &= 1\ s \\
N_\alpha &= \partial N_\alpha / \partial t \times \tau_{\text{slowdown}} = 1.4\times10^{20} \\
V_{\text{core}} &= 250\ \text{m}^3 \\
V_{\text{full}} &= 840\ \text{m}^3 \\
n_\alpha &= N_\alpha / V_{\text{core}}\ \left(N_\alpha / V_{\text{full}}\right) = 5.6\times10^{17}\,\text{m}^{-3}\ \left(1.7\times10^{17}\,\text{m}^{-3}\right) \\
v_{\alpha\,\text{birth}} &= 12.9\times10^{6}\,\text{m/s} \\
f_\alpha &= \frac{n_\alpha}{2v_{\alpha\,\text{birth}}} = 2.2\times10^{10}\,\text{s/m}^4\ \left(6.6\times10^{9}\,\text{s/m}^4\right)
\end{aligned}
\qquad \text{(A.1)}
$$

B Scattering function

In the equation of transfer for a CTS system (see Section 1.3) the scattering function[4], Σ, accounts for the spectral variations in the microscopic fluctuations, which give rise to scattering, and the spectral variations in the coupling of the incident probe field, via the bilinear interaction with the fluctuations, into the received scattered field. The scattering function includes scattering due to fluctuations in electron density, electron flux, magnetic field and electric field, accounting for the relative phase between the scattered fields resulting from each of the types of fluctuations. In the figures below the scattering function is plotted as a function of the frequency of the resolved fluctuations, $\nu^{\delta} = \nu^{s} - \nu^{i}$, for a range of probing frequencies, ν^{i}, and scattering geometries characterised by the scattering angle $\theta = \angle\left(\mathbf{k}^{i}, \mathbf{k}^{s}\right)$ and the angle between the wave vector of the resolved fluctuations and the magnetic field, $\phi = \angle\left(\mathbf{k}^{\delta}, \mathbf{B}\right)$. The figures also show the contributions electrons, bulk ions and fast ions make to the scattering function. To make inference about the fast ions we generally require that the fast ion contribution, also referred to, as the *fast ion feature* must be significant compared to the electron feature. This is only marginally the case in Figure 107.

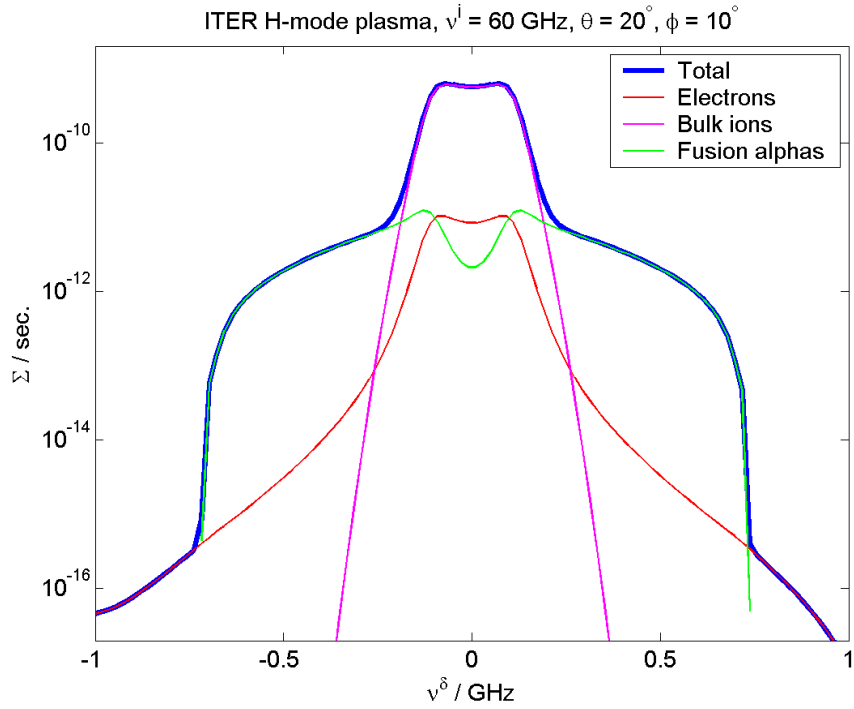

Figure 104. CTS scattering function, Σ, as a function of resolved fluctuation frequency, $\nu^{\delta} = \nu^{s} - \nu^{i}$. Here the probe frequency is $\nu^{i} = 60\,\text{GHz}$, $\theta = \angle\left(\mathbf{k}^{i}, \mathbf{k}^{s}\right) = 20°$, $\phi = \angle\left(\mathbf{k}^{\delta}, \mathbf{B}\right) = 10°$. The incident and received scattered radiations are both in X-mode. The plasma is a reference H-mode ITER equilibrium (see Appendix A) with, $B = 5.3\,\text{T}$, $n_e = 1\times10^{20}\,\text{m}^{-3}$ and $T_e = T_i = 25\,\text{keV}$. The fusion alpha density is $n_{\alpha} = 5\times10^{17}\,\text{m}^{-3}$. The fusion alphas are assumed to have a classical slowdown distribution. The figure shows the total form factor (fat blue curve), the electron contribution (thin red curve), bulk ion (thin magenta curve) and fusion alpha (thin green curve) contributions.

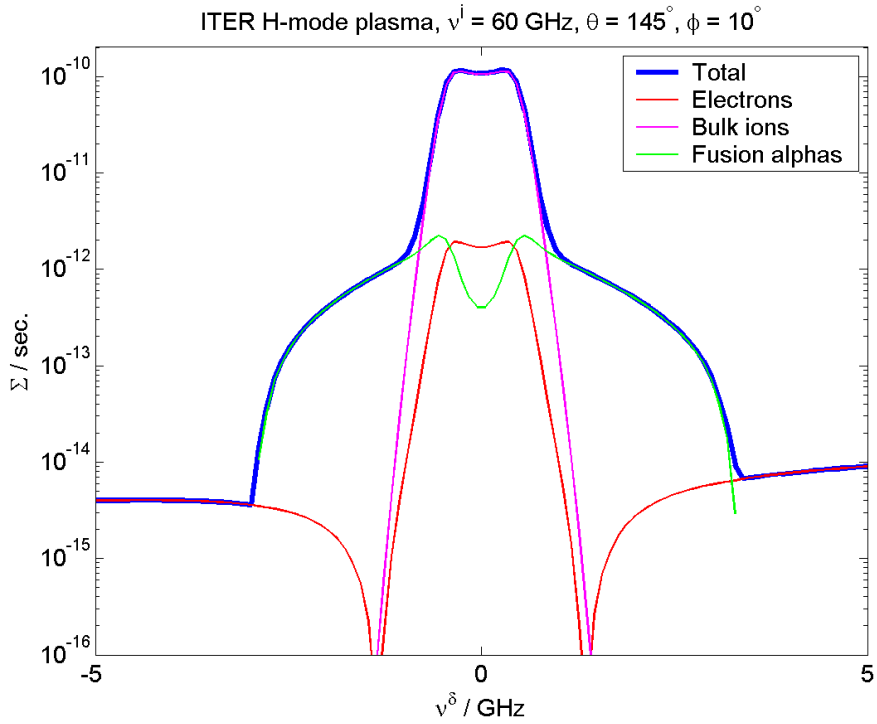

Figure 105. CTS scattering function for the same plasma as in Figure 104. Here the probe frequency is also $\nu^i = 60\,\mathrm{GHz}$, but $\theta = 145°$, $\phi = 10°$.

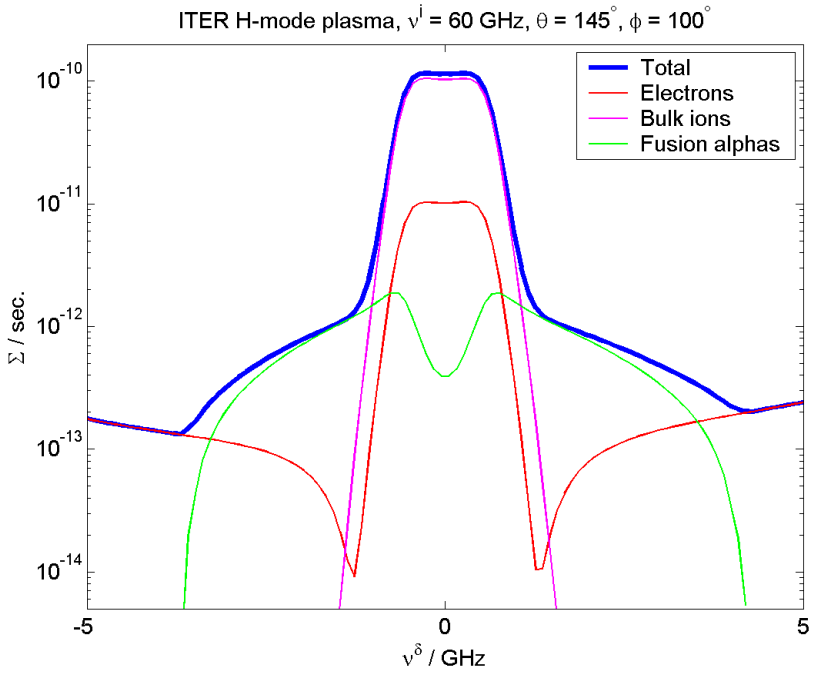

Figure 106. CTS scattering function for the same plasma as in Figure 104. Here the probe frequency is also $\nu^i = 60\,\mathrm{GHz}$, but $\theta = 145°$, $\phi = 100°$.

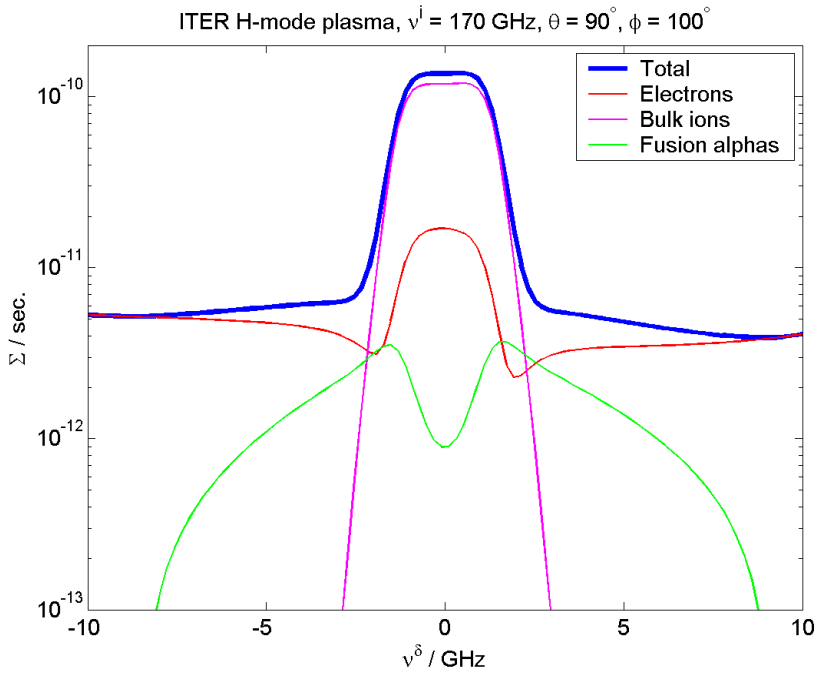

Figure 107. CTS scattering function for the same plasma as in Figure 104. Here the probe frequency is $\nu^i = 170$ GHz, $\theta = 90°$, $\phi = 100°$. The incident and received scattered radiations are both in O-mode.

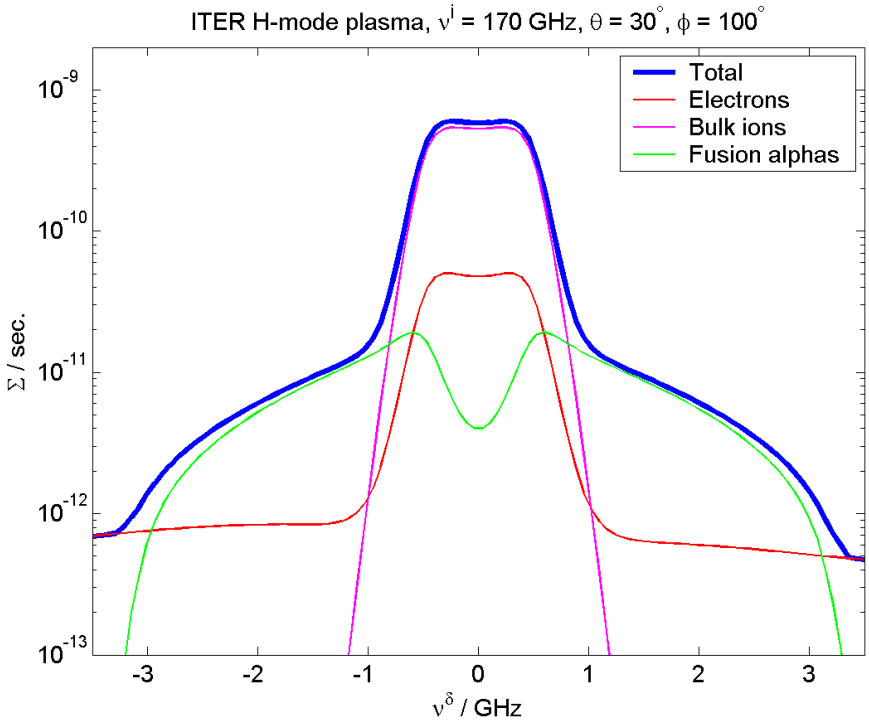

Figure 108. CTS scattering function for the same plasma as in Figure 104. Here the probe frequency is $\nu^i = 170$ GHz, $\theta = 30°$, $\phi = 100°$. The incident and received scattered radiations are both in O-mode.

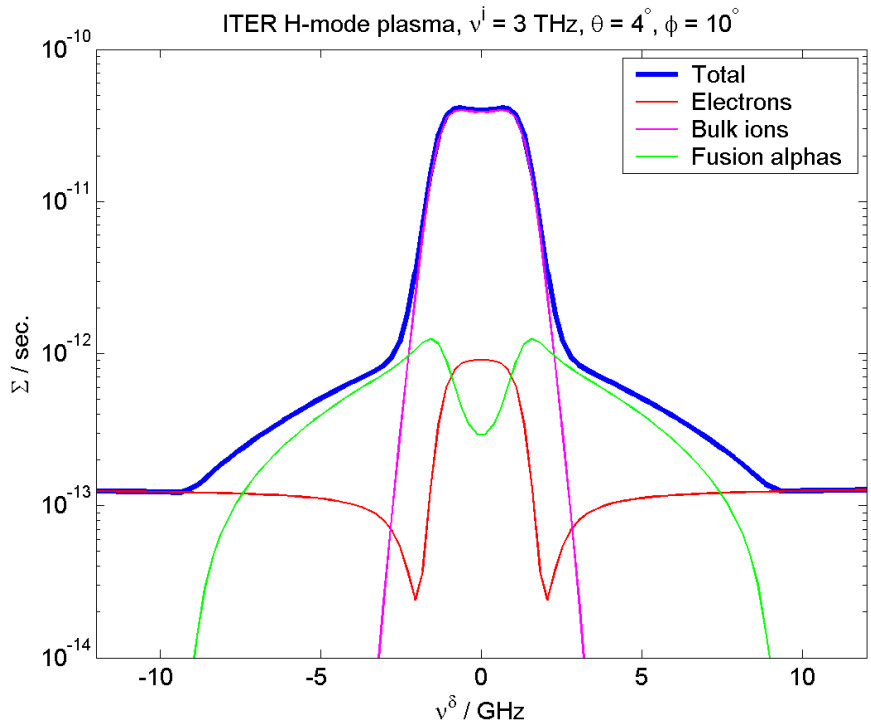

Figure 109. CTS scattering function for the same plasma as in Figure 104. Here the probe frequency is $\nu^i = 3\,\mathrm{THz}$, $\theta = 4°$, $\phi = 10°$. The incident and received scattered radiations are both in O-mode.

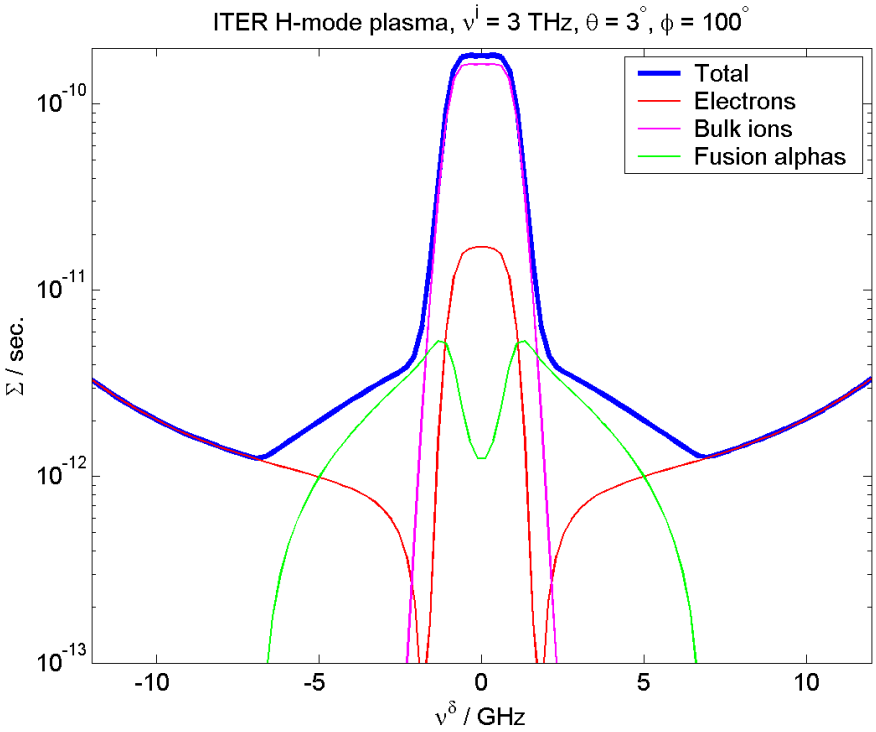

Figure 110. CTS scattering function for the same plasma as in Figure 104. Here the probe frequency is $\nu^i = 3\,\mathrm{THz}$, $\theta = 3°$, $\phi = 100°$. The incident and received scattered radiations are both in O-mode.

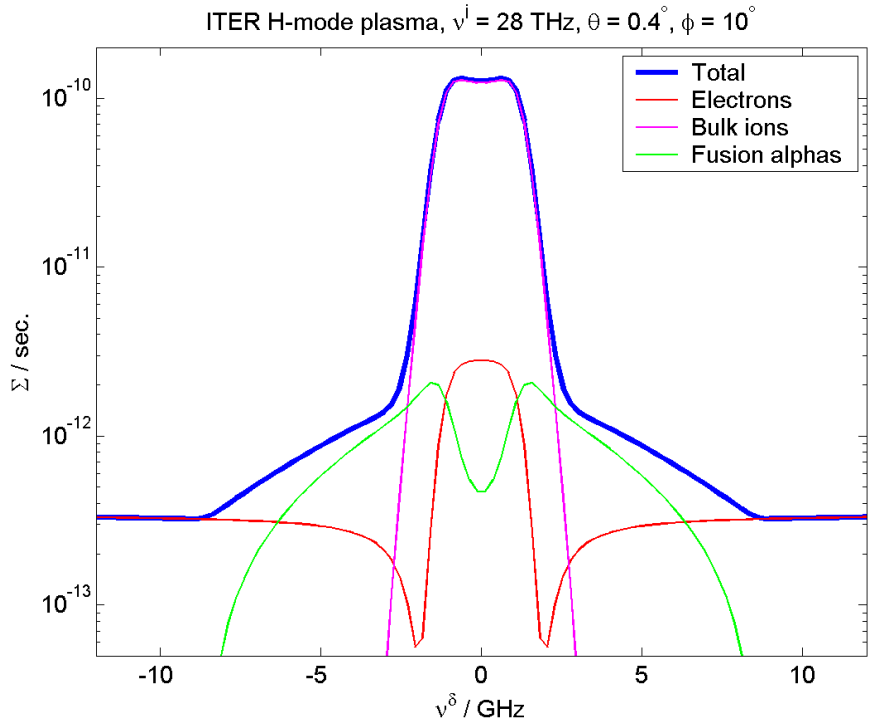

Figure 111. CTS scattering function for the same plasma as in Figure 104. Here the probe frequency is $\nu^i = 28.28\,\text{THz}$, $\theta = 0.4°$, $\phi = 10°$.

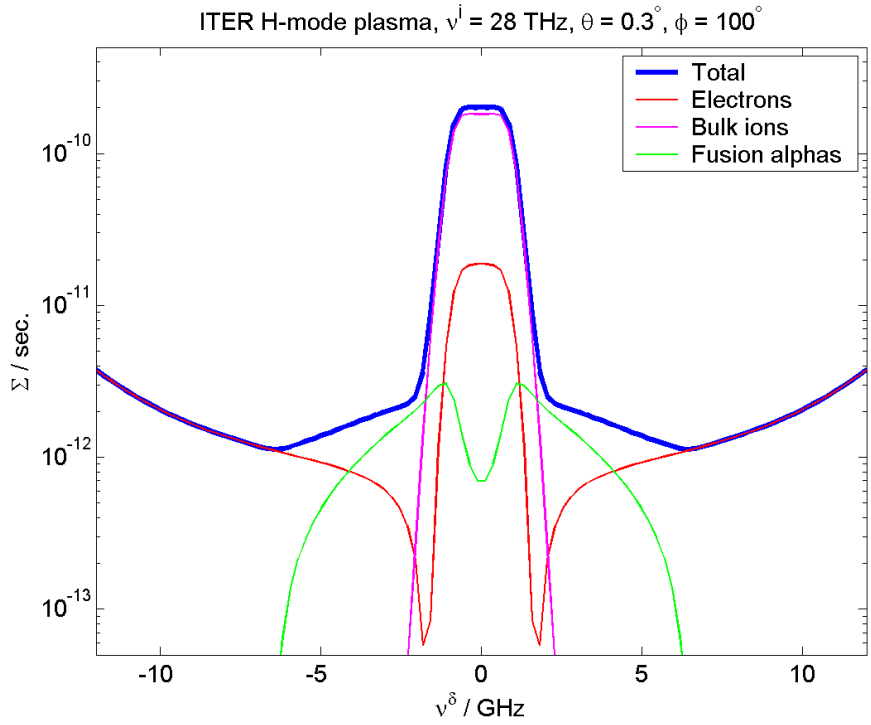

Figure 112. CTS scattering function for the same plasma as in Figure 104. Here the probe frequency is $\nu^i = 28.28\,\text{THz}$, $\theta = 0.3°$, $\phi = 100°$.

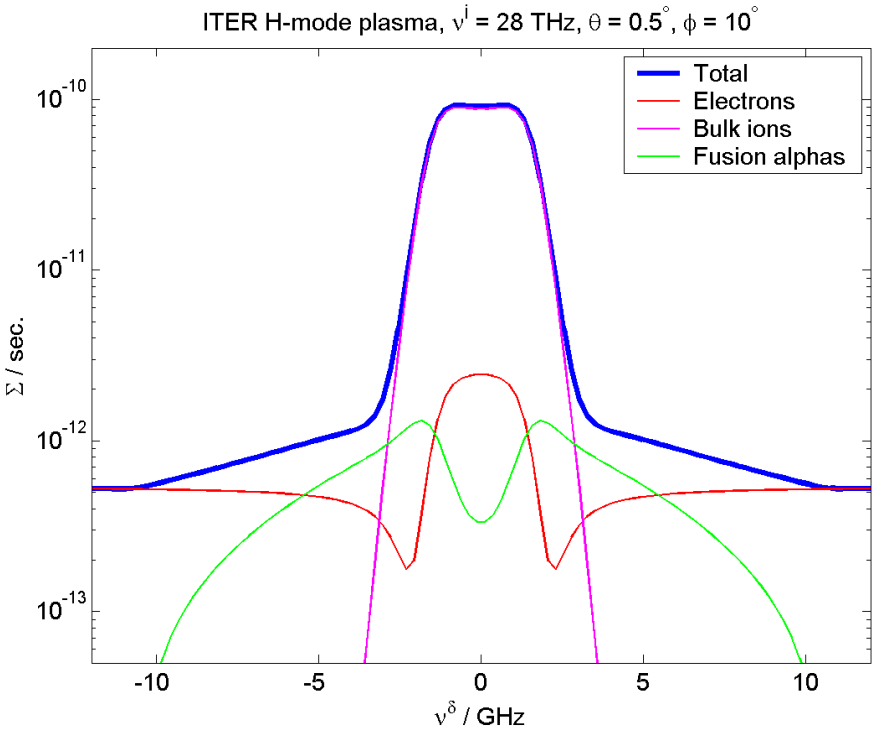

Figure 113. CTS scattering function for the same plasma as in Figure 104. Here the probe frequency is $\nu^i = 28.28\,\mathrm{THz}$, $\theta = 0.5°$, $\phi = 10°$.

Note that as the probe frequency increases the scattering angle must decrease to maintain a fast ion feature, which is larger than the electron feature. Also note that the electron feature is lower when resolving fluctuations with wave vectors more parallel to the magnetic field (Figure 105) as compared with fluctuations with wave vectors more perpendicular to the field (Figure 106). For the higher probing frequencies this leads to the need to decrease the scattering angle for perpendicular viewing (Figure 110 and Figure 112) as compared with parallel viewing (Figure 109 and Figure 111).

When the wave vector of the resolved fluctuations is close to perpendicular to the static magnetic field the fast magneto-sonic (FMS) wave enters the spectrum of fluctuations. This results in strong variations in the spectrum as a function of frequency and the fluctuation angle $\phi = \angle\left(\mathbf{k}^\delta, \mathbf{B}\right)$, as is brought out in the plots in Figure 114 and Figure 115.The signal is increased near the FMS but the large sensitivity to the magnitude of the component of $\mathbf{k}^\delta$ parallel to $\mathbf{B}$ makes this geometry unsuitable for diagnosing the fast ion velocity distribution.

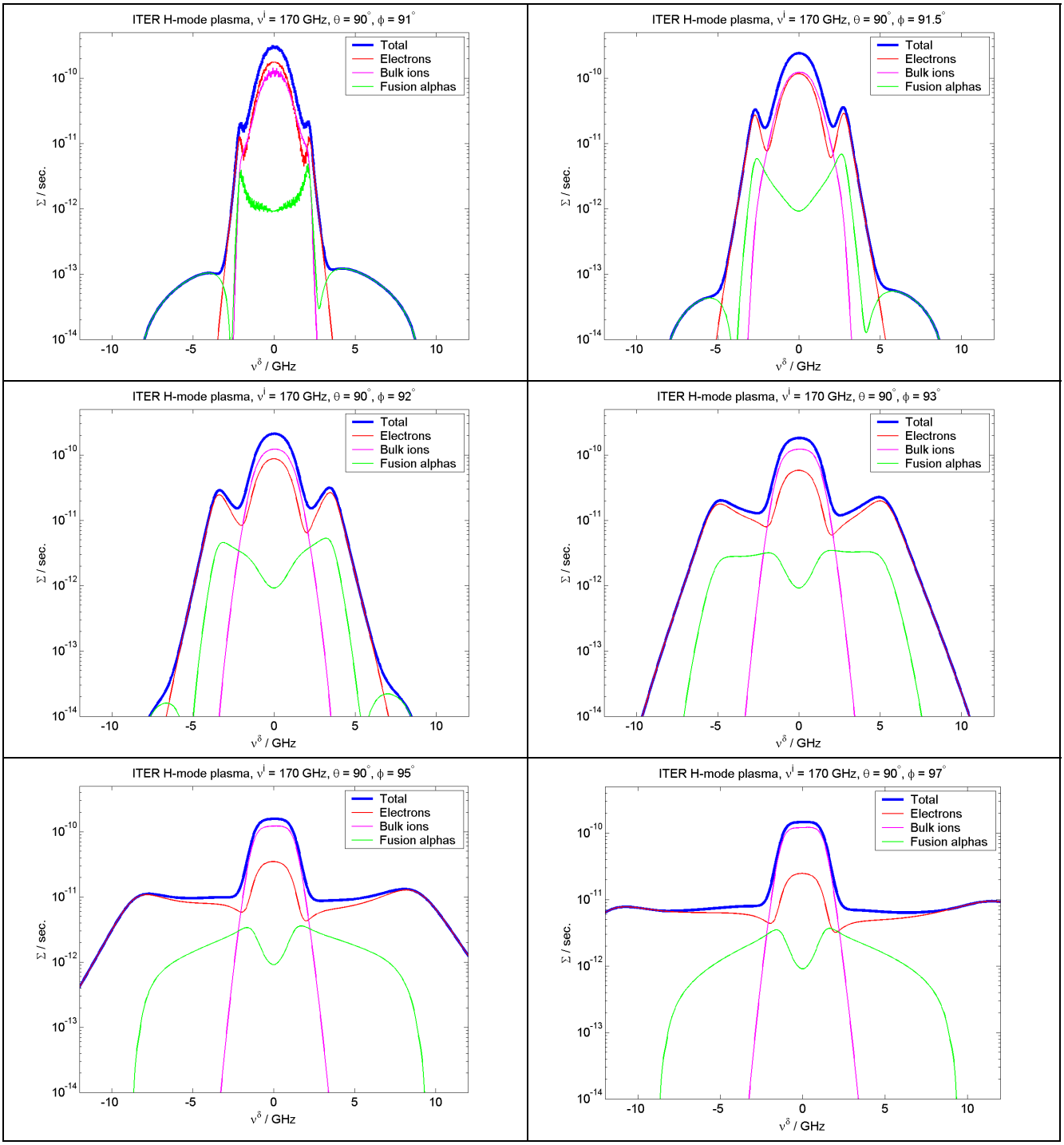

Figure 114. CTS scattering function for the same plasma as in Figure 104. Here the probe frequency is $\nu^i = 170$ GHz and $\theta = 90°$. Here the fluctuation angle $\phi = \angle\left(\mathbf{k}^\delta, \mathbf{B}\right)$ is varied in a narrow range around perpendicular. The spectrum is showing large variations because of the presence of the fast magneto-sonic wave in the spectrum of fluctuations. The incident and received scattered radiations are both in O-mode.

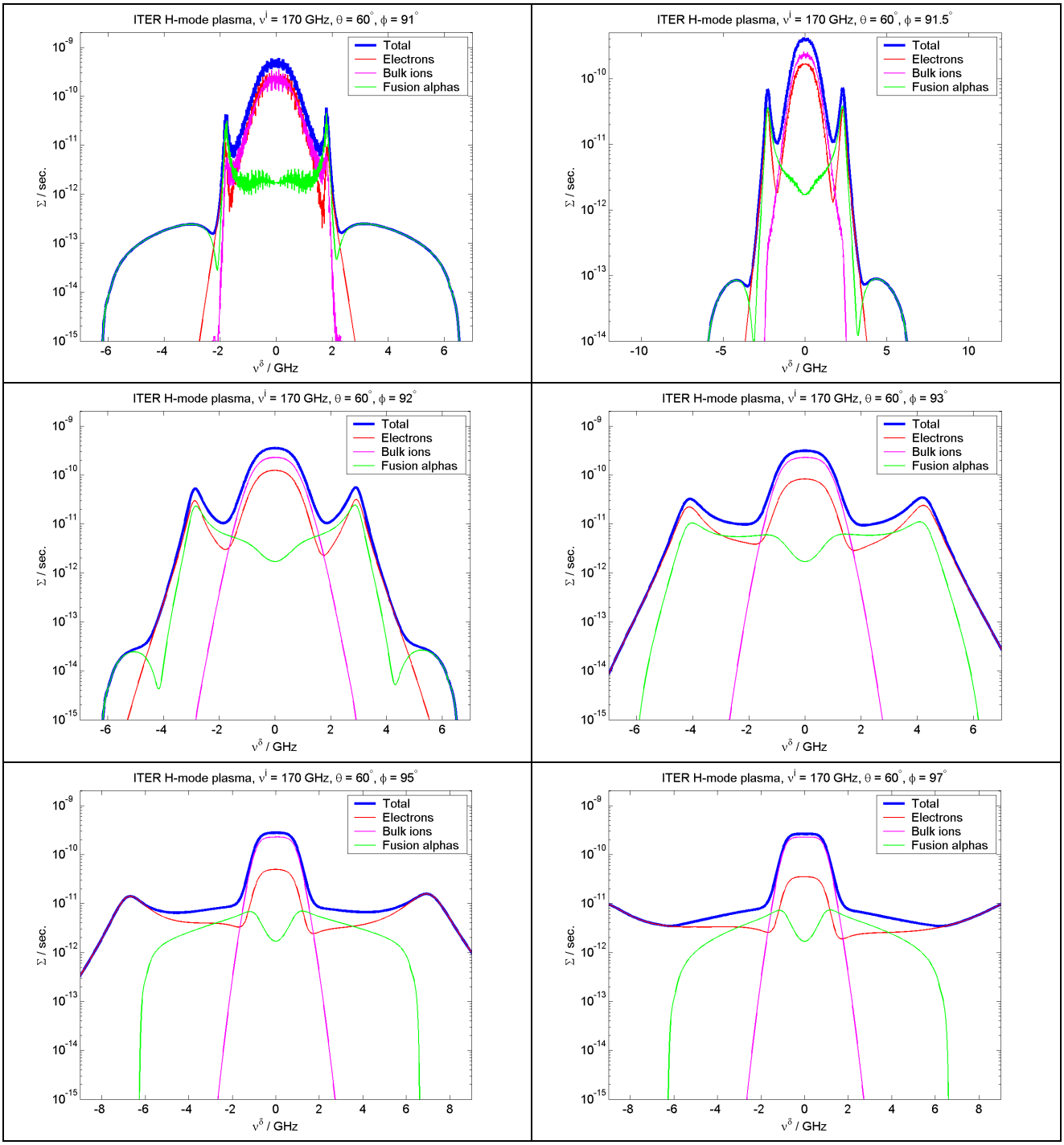

Figure 115. As Figure 114, only here for a reduced scattering angle of $\theta = 60°$ to increase the ratio of the fast ion feature to the electron feature.

C Gaussian beam intersection

Assume a straight uniform beam with bivariate normal intensity distribution in the plane orthogonal to the beam. Its normalized beam intensity can be written

$$I^{\mathrm{i}} = \frac{1}{2\pi\sqrt{|\alpha^{\mathrm{i}}|}} \exp\left(-\frac{(r_i - r_i^{\mathrm{i}})\alpha_{ij}^{\mathrm{i}}(r_j - r_j^{\mathrm{i}})}{2} \right), \tag{C.1}$$

with $\mathbf{r}^{\mathrm{i}}$ a point on the beam centroid and the inverse covariance matrix given by

$$\alpha^{\mathrm{i}} = \mathbf{U}^{\mathrm{i}} \operatorname{diag}\left(\frac{1}{\left(\sigma_1^{\mathrm{i}}\right)^2}, \frac{1}{\left(\sigma_2^{\mathrm{i}}\right)^2}, 0 \right) \mathbf{U}^{\mathrm{i}T}. \tag{C.2}$$

Here $\mathbf{U}^{\mathrm{i}}$ is an orthonormal matrix, the column vectors of which are the unit eigenvectors of α^{i}. The third column vector is in the direction of the beam, the first and second vectors are in the directions of the major axes of the ellipsoidal contours of constant normalized beam intensity, I^{i}. The Gaussian half widths, w_1^{i} and w_2^{i}, defined as the distances from the beam centre along the major axes to the points where the intensity has dropped to $1/e^2$ of the peak value, are relate to the eigenvalues of α^{i} as

$$w_{1,2}^{\mathrm{i}} = 2\sigma_{1,2}^{\mathrm{i}}. \tag{C.3}$$

A bivariate normal intensity distribution, or simply ellipsoidal Gaussian distribution, is illustrated in Figure 116 for the case of a beam with ellipsoidal cross section and Gaussian half widths of 1 and 2 length units.

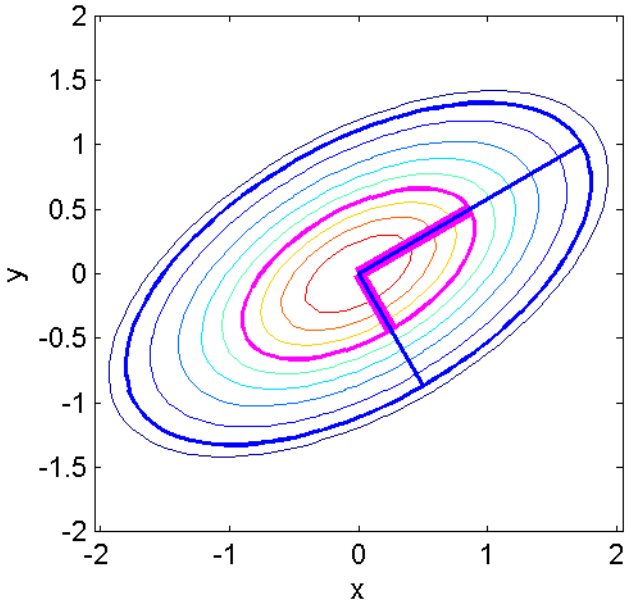

Figure 116. Normalized intensity, *I*, of beam propagating in the z direction. The fat straight magenta lines have the lengths σ_1^{i} and σ_2^{i} and are in the directions of the first and second column vectors in $\mathbf{U}^{\mathrm{i}}$. The straight blue lines have the

lengths w_1^{i} and w_2^{i}, which are the Gaussian half widths where the intensity has dropped to *1/e²* of the peak value.

Assume we now have a second beam identified by superscript s. Assume the first beam is the incident probe and the second the receiver beam pattern. Let the two ellipsoidal Gaussian beams propagate in different directions. The product of their normalized beam intensities, with which the CTS measurements are spatially weighted, takes the form

$$I^{\mathrm{i}}I^{\mathrm{s}} \propto \exp\left(-\frac{(r_i - r_i^{\delta})\alpha_{ij}(r_j - r_j^{\delta})}{2}\right), \tag{C.4}$$

where the inverse covariance entering here is the sum of the two beam inverse covariances

$$\alpha = \alpha^{\mathrm{i}} + \alpha^{\mathrm{s}}, \tag{C.5}$$

and $\mathbf{r}^{\delta}$ is the centre of the peak of the weighting function and hence the centre of the scattering volume. It is given by

$$\mathbf{r}^{\delta} = \alpha^{-1}\left(\alpha^{\mathrm{i}}\mathbf{r}^{\mathrm{i}} + \alpha^{\mathrm{s}}\mathbf{r}^{\mathrm{s}}\right). \tag{C.6}$$

In this mathematical approximation the weighting function extends to infinity. Thus to give a meaningful definition of scattering volume we define it as the smallest volume from which a certain fraction of the total CTS signal comes. With this definition the scattering volume is delimited by an iso-surface of the weighting function $I^{\mathrm{i}}I^{\mathrm{s}}$. We identify the iso-surfaces by the parameter *s* in the equation

$$r_i\alpha_{ij}r_j = 4s^2. \tag{C.7}$$

In the beam plane projection the iso-surface corresponding to $s = 1$ is tangent to the Gaussian half widths of each beam in the beam plane (see Figure 4). The fraction, $R(s)$, of the CTS signal coming from inside the iso-surface identified by *s* is given by

$$R(s) = \frac{16}{\sqrt{2\pi}}\int_0^s x^2 \exp\left(-2x^2\right)dx \tag{C.8}$$

and plotted in Figure 117.

The finite spatial extent of the weighting function results in a finite distribution of wave vectors of the resolved fluctuations. The distribution, $f_{\mathbf{k}}$, of wave vectors is the Fourier transform of the weighting function modulated by the difference in wave vectors of the incident probe and received scattered waves. The result is

$$f_{\mathbf{k}} \propto \exp\left(-\frac{(k_i - k_i^{\delta})\alpha_{ij}^{k}(k_j - k_j^{\delta})}{2}\right), \tag{C.9}$$

where

$$\alpha^{k} = \alpha^{-1}. \tag{C.10}$$

The CTS weighting functions, $I^{\mathrm{i}}I^{\mathrm{s}}$, and corresponding distributions of resolved wave vectors, $f_{\mathbf{k}}$, are plotted in Figure 4 for scattering angles of 90° and 30°. For narrow beams the resolution of the fluctuation wave vector can become a limiting factor.

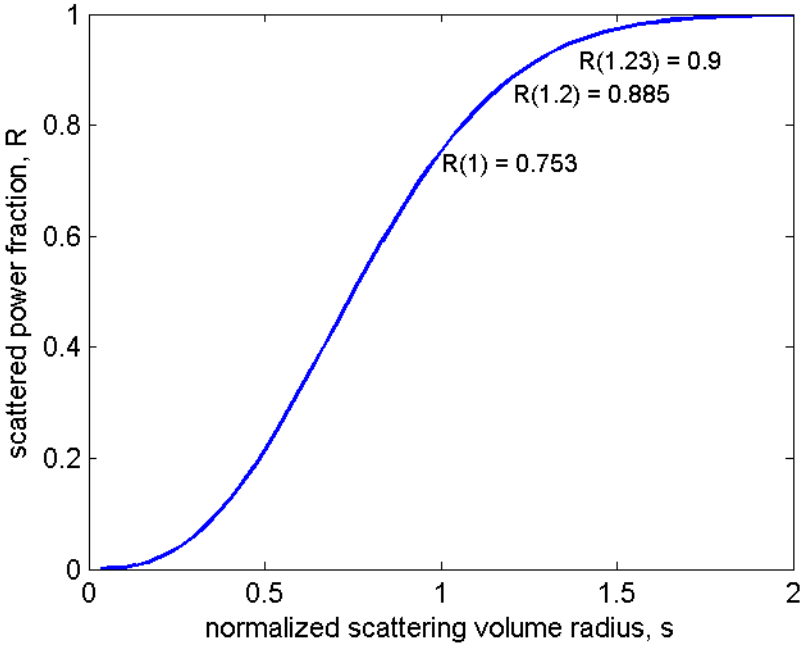

Figure 117. Fraction, $R(s)$, of the CTS signal coming from inside the iso-surface identified by s. Relation between iso-surface and s is given by equation (C.7). The expression for $R(s)$ is given in (C.8). At $s = 1.23$ we find R = 90 %

We now provide simplified expressions characterising the scattering geometry for the case where the principal axes of the cross sectional intensity distributions of both the probe and receiver beams are in and orthogonal to the beam plane. In this plane the Gaussian half widths of the beams are both w_B and orthogonal to the beam plane they are both equal to w_N. We further introduce a local Cartesian coordinate system with the z-axis orthogonal to the beam plane and the x and y axes in the beam plane and oriented such that the probe and receiver beams both make an angle of $\theta/2$ to the x-axis. The axes of this coordinate system are the principal axes of the weighting function $I^{\mathrm{i}}I^{\mathrm{s}}$ and the scattering volume. With these assumptions we find the following simplified expressions for the beam inverse covariances,

$$\alpha^{\mathrm{i}} = \begin{pmatrix} s_B^2 & -s_B c_B & 0 \\ -s_B c_B & c_B^2 & 0 \\ 0 & 0 & u_N^2 \end{pmatrix};\ \alpha^{\mathrm{s}} = \begin{pmatrix} s_B^2 & s_B c_B & 0 \\ s_B c_B & c_B^2 & 0 \\ 0 & 0 & u_N^2 \end{pmatrix}; \qquad \text{(C.11)}$$

$$s_B = \frac{2\sin(\theta/2)}{w_B};\ c_B = \frac{2\cos(\theta/2)}{w_B};\ u_N = \frac{2}{w_N}$$

resulting in weighting function inverse covariance and covariance

$$\alpha = 2\begin{pmatrix} s_B^2 & 0 & 0 \\ 0 & c_B^2 & 0 \\ 0 & 0 & u_N^2 \end{pmatrix};\ \mathbf{C} = \alpha^{-1} = \frac{1}{2}\begin{pmatrix} s_B^{-2} & 0 & 0 \\ 0 & c_B^{-2} & 0 \\ 0 & 0 & u_N^{-2} \end{pmatrix}, \qquad \text{(C.12)}$$

from which follow the full linear extents of the ellipsoidal scattering volume along its principal axes

$$\Delta x = \frac{s\sqrt{2}\, w_B}{\sin(\theta/2)};\ \Delta y = \frac{s\sqrt{2}\, w_B}{\cos(\theta/2)};\ \Delta z = s\sqrt{2}\, w_N, \tag{C.13}$$

where s is the parameter introduced in Equation (C.7) to identify the scattering volume. The standard deviations of the distribution of resolved wave vectors along principal axes also follow from (C.12) and take to form

$$\sigma_x^k = \frac{2\sqrt{2}\sin(\theta/2)}{w_B};\ \sigma_y^k = \frac{2\sqrt{2}\cos(\theta/2)}{w_B};\ \sigma_z^k = \frac{2\sqrt{2}}{w_N}. \tag{C.14}$$

The linear extents of the scattering volume and the standard deviations of the distribution of resolved wave vectors, both along principal axes, are given in Table 10 for a range of scattering geometries.

ν^{i} / THz	0.06	0.06	0.17	0.17	3	28
w_B /cm	8	8	3	6	1	1
w_N /cm	15	15	3	6	1	1
θ / 1°	25	145	90	90	4	0.4
O_b / m^{-1}	8.9	6.6	19	9.4	809	8082
Δx /cm	64	14.6	7.4	14.8	50	498
Δy /cm	14	46	7.4	14.8	1.7	1.7
Δz /cm	26	26	5.2	10.4	1.7	1.7
σ_x^k /m^{-1}	7.7	34	67	33	9.9	0.99
σ_y^k /m^{-1}	35	11	67	33	283	283
σ_z^k /m^{-1}	19	19	94	47	283	283
$k^{\delta}/2\sigma_y^k$ *	7.9	113	37.8	75.6	7.8	7.3

Table 10. Set of scattering geometries and associated linear extents of the scattering volume and standard deviations of the distribution of resolved wave vectors. It is assumed that the principal components of the beam cross sectional distributions are in and orthogonal to the beam plane, and that the beam widths are the same in and orthogonal the beam plane. * The fluctuation wave vector is computed here as $k^{\delta} = 2\sin(\theta/2)k^{\mathrm{i}}$.

D Supporting material for the 60 GHz LFS investigations

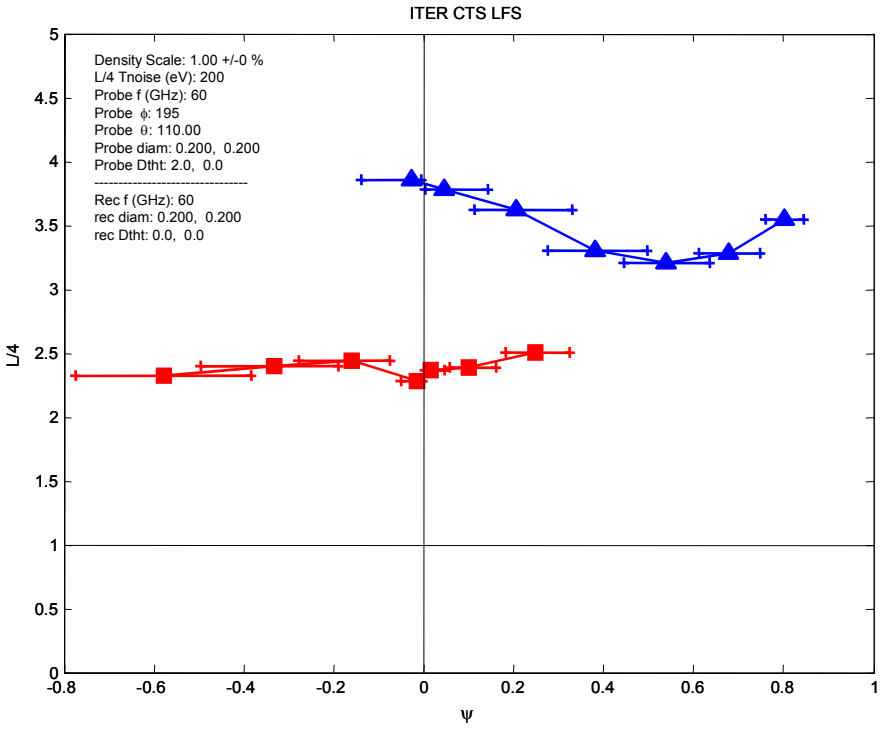

Figure 118. L / 4 of the two receivers for the angles shown in Figure 32 versus the magnetic surfaces where the centroid of the scattered volume is located. DS = 1.0, $D_{b\theta}^{\,i} = D_{b\kappa}^{\,i} = D_{b\theta}^{\,s} = D_{b\kappa}^{\,s} = 200$ mm, $\Omega_{\kappa}^{\,s} = \Omega_{\theta}^{\,s} = 0$ for the receivers and $\Omega_{\kappa}^{\,i} = 2°$, $\Omega_{\theta}^{\,i} = 0$, $\kappa^{i} = 10°$ for the probe.

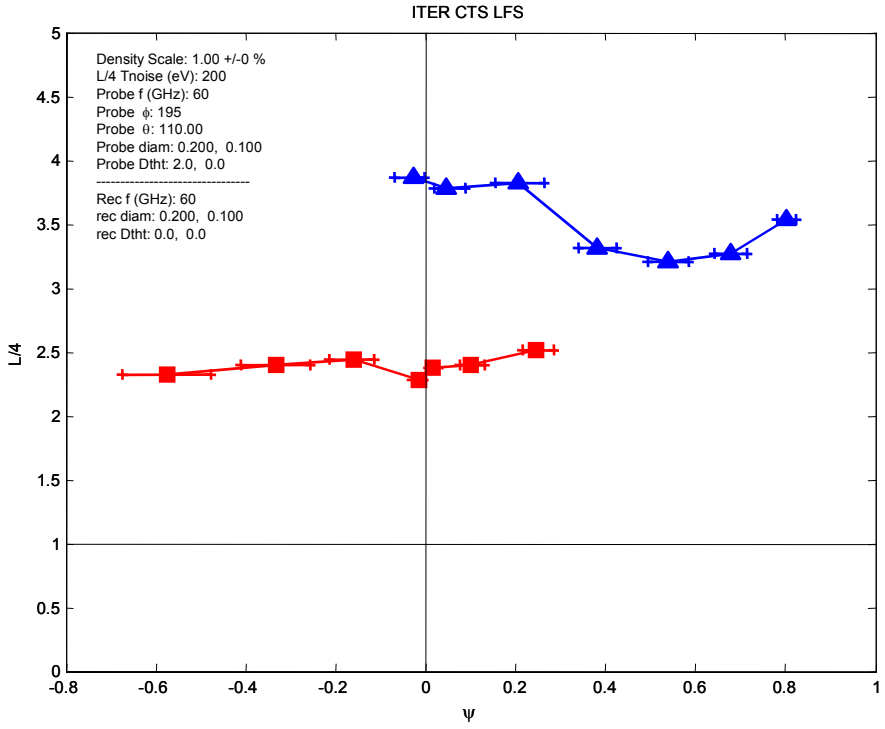

Figure 119. L / 4 for the same beam configuration except for $D_{b\theta}^{\,i} = D_{b\theta}^{\,s} = 10$ mm

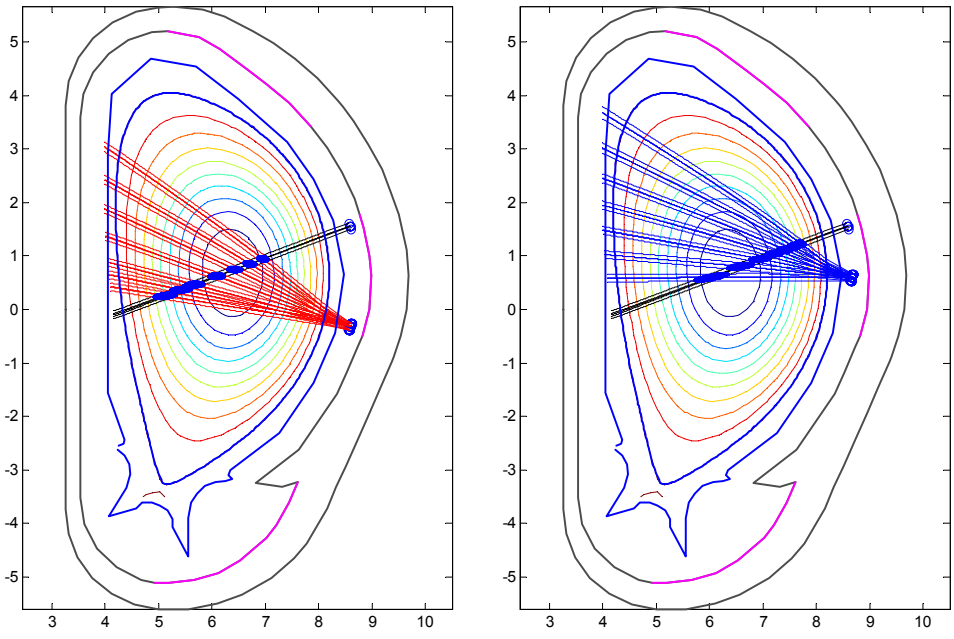

Figure 120. Ray trace for DS = 0.7 for the two receiver positions.

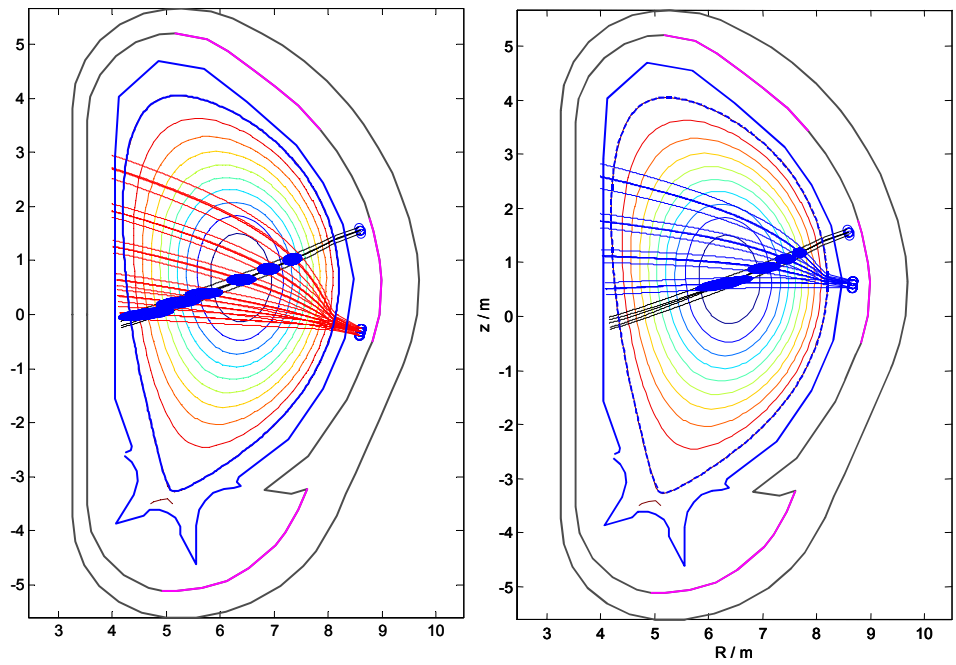

Figure 121. Ray trace for DS = 1.1 for the two receiver positions.

E Supporting material for the 60 GHz HFS investigations

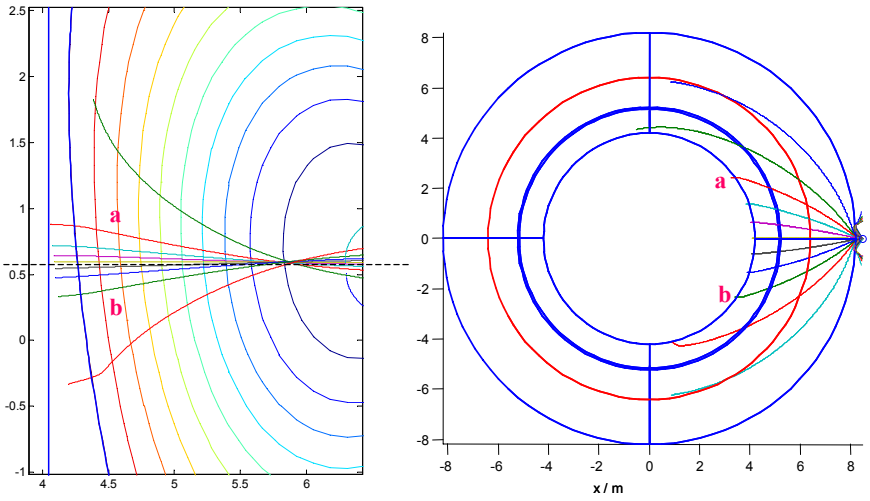

Figure 122. Ray traces for a scan of toroidal launch angle, κ, in the reference plasma. Left a poloidal map, right a top view. To enter the plasma the toroidal launch angle must be less than 25º from the poloidal plane for a plasma with the reference density (DS = 1). Vertical refraction is lower for rays launched in the co direction. For ray 'a': vertical refraction on last flux surface is about 24.5 cm. For ray'b': -21.8 cm. The asymmetry increases with density.

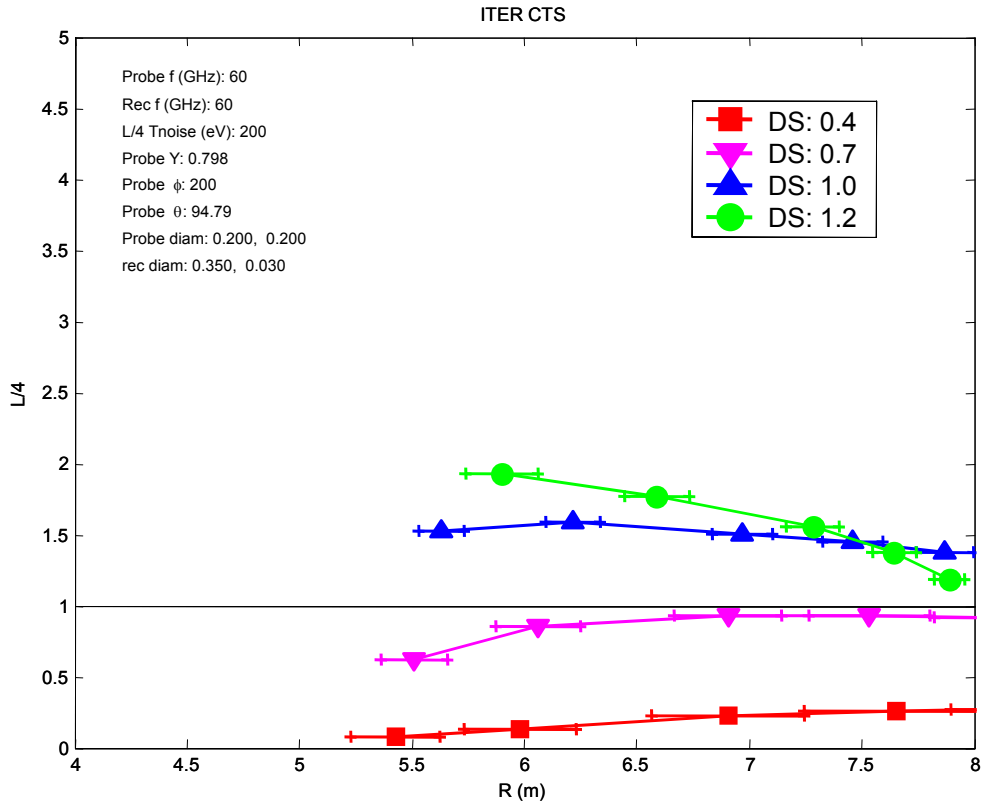

Figure 123. Mirror 2, probe position "b", $\kappa^i = 15^o$:

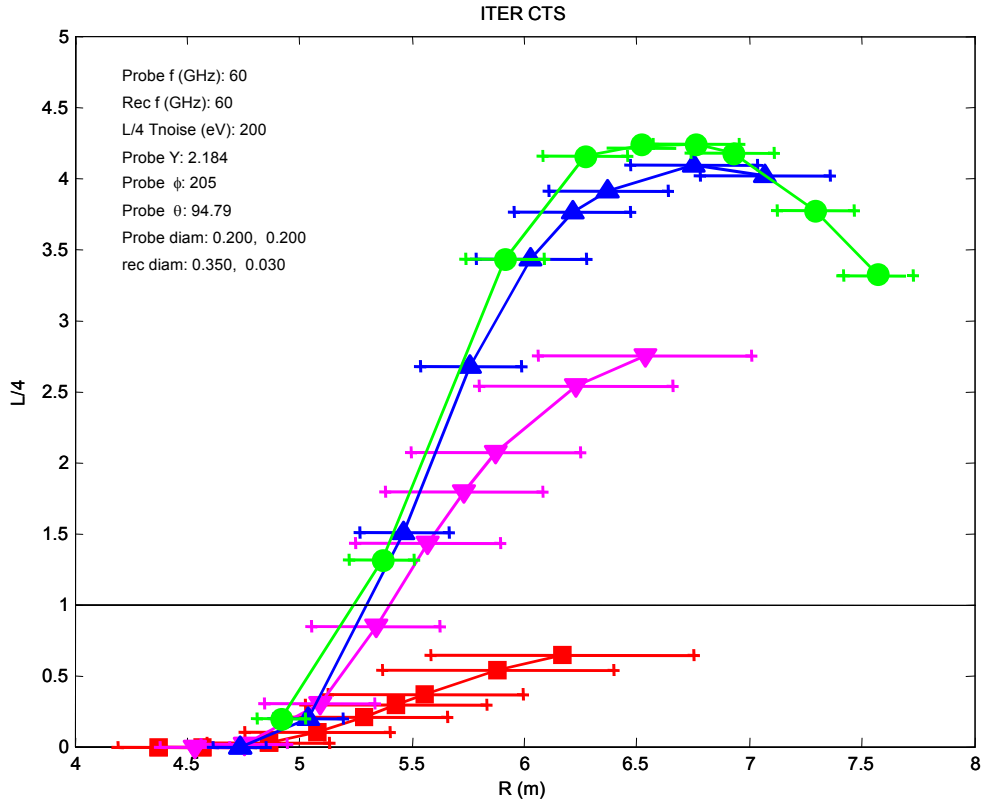

Figure 124. Mirror 2, probe position "*a*", $\kappa^j = 10^o$:

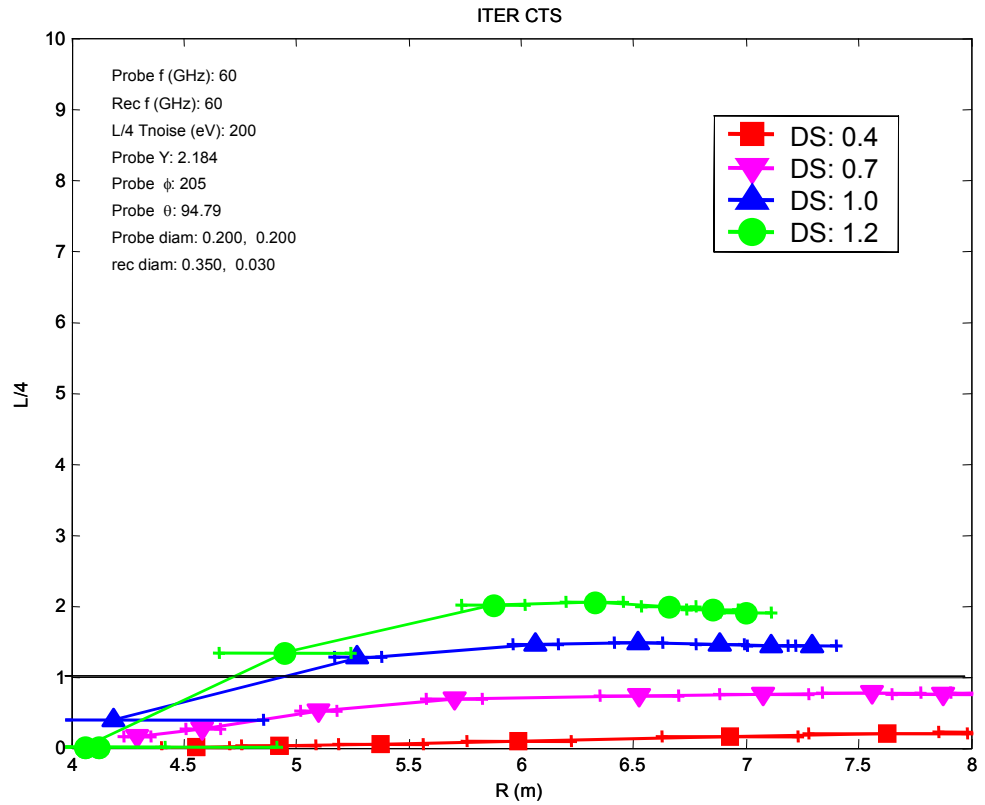

Figure 125. Mirror 1, probe position "*a*", $\kappa^j = 10^o$:

F Supporting material for the 170 GHz investigations

F.1 Additional material for Section 3.2.2 Beam tracing - Figure 74

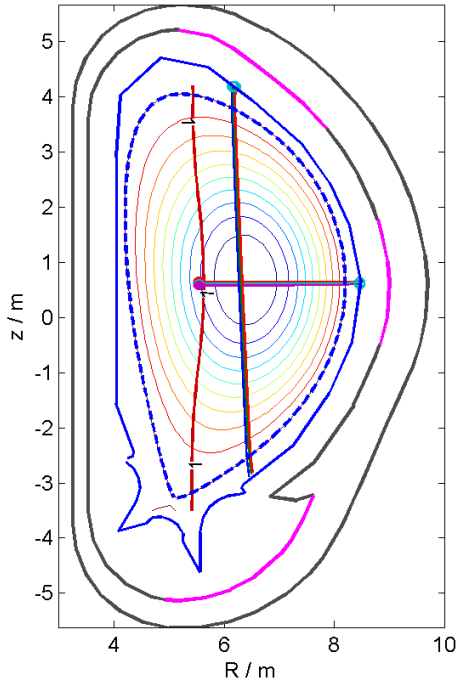

Figure 74 (repeated) Beam traces for the 170 GHz scattering geometry with the probe in the horizontal plane (nominal ITER2 parameters). The parameters used for the beams are presented below.

The parameters for the gyrotron are:
f = 170 GHz, mode = 'O', launch position = [-8.46, 0.0, 0.62], launch angle (θ,φ) = (90°, 0°).

The parameters for the receiver are:
f = 170 GHz, mode = 'O', receiving position = [-6.17, 0.00, 4.19],
receiving angle (θ,φ) = (179°, 0°).

The calculated output parameters are:
Beam Overlap, O_b = 16 m^{-1}, Scattering angle = 87.5°, $\angle(k^{\delta}, B)$ = 90.8°.
Scattering volume centre (x, y, z) = (-6.2977, 0.0076, 0.6197)
Distance between beam centroids, D = -0.012 m
Unit vectors in directions of major axes of the scattering volume ellipsoid:
Axis 1 (x, y, z) = (0.1030, 0.9938, 0.0414)
Axis 2 (x, y, z) = (-0.3288, -0.0052, 0.9444)
Axis 3 (x, y, z) = (0.9388, -0.1108, 0.3262)

Diameters of scattering volume along its major axes: d0 = (0.0516, 0.0769, 0.0833)

F.2 Appendix to Section 3.2.2 Beam tracing – 178.75 GHz

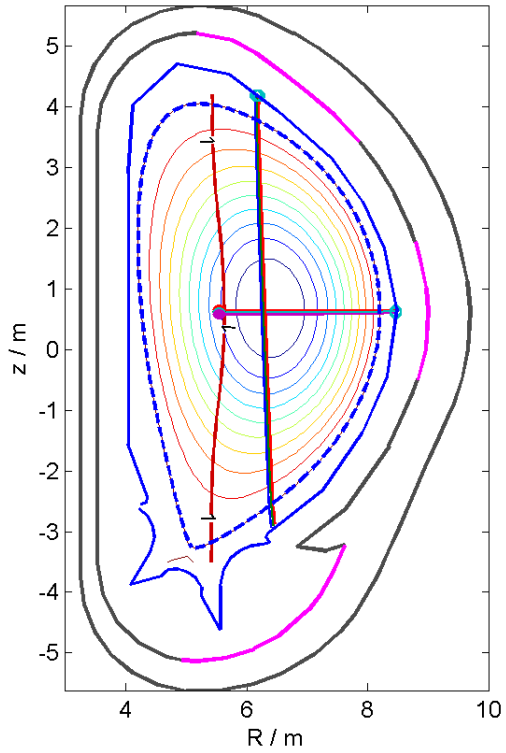

Figure Beam traces for the 170 GHz scattering geometry with the probe in the horizontal plane (nominal ITER2 parameters). The frequency of the receiver is 178.75 GHz. The parameters used for the beams are presented below.

The parameters for the gyrotron are:
f = 170 GHz, mode = 'O', launch position = [-8.46, 0.0, 0.62], launch angle (θ,φ) = (90°, 0°).

The parameters for the receiver are:
f = 178.75 GHz, mode = 'O', receiving position = [-6.17, 0.00, 4.19],
receiving angle (θ,φ) = (179°, 0°).

The calculated output parameters are:
Beam Overlap, O_b = 17.5 m^{-1}, Scattering angle = 87.9°, $\angle(k^{\delta}, B)$ = 91°.
Scattering volume centre (x, y, z) = (-6.2751, 0.0058, 0.6197)
Distance between beam centroids, D = -0.00822 m
Unit vectors in directions of major axes of the scattering volume ellipsoid:
Axis 1 (x, y, z) = (0.0944, 0.9946, 0.0428)
Axis 2 (x, y, z) = (-0.3488, -0.0072, 0.9372)
Axis 3 (x, y, z) = (0.9324, -0.1034, 0.3463)

Diameters of scattering volume along its major axes: d0 = (0.0515, 0.0770, 0.0822)

F.3 Appendix to Section 3.2.2 Beam tracing – 161.25 GHz

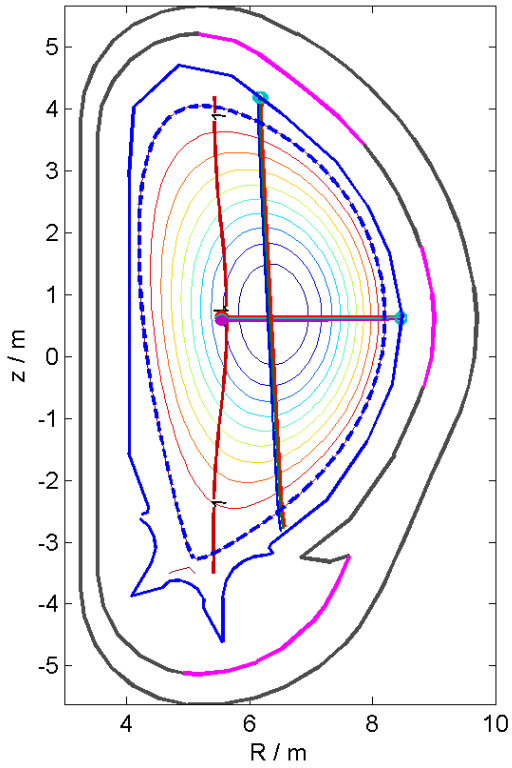

Figure Beam traces for the 170 GHz scattering geometry with the probe in the horizontal plane (nominal ITER2 parameters). The frequency of the receiver is 161.25 GHz. The parameters used for the beams are presented below.

The parameters for the gyrotron are:
f = 170 GHz, mode = 'O', launch position = [-8.46, 0.0, 0.62], launch angle (θ,φ) = (90°, 0°).

The parameters for the receiver are:
f = 161.25 GHz, mode = 'O', receiving position = [-6.17, 0.00, 4.19],
receiving angle (θ,φ) = (179°, 0°).

The calculated output parameters are:
Beam Overlap, O_b = 13.6 m^{-1}, Scattering angle = 87°, $\angle(k^{\delta}, B)$ = 90.5°.
Scattering volume centre (x, y, z) = (-6.3254, 0.0095, 0.6197)
Distance between beam centroids, D = -0.0171 m
Unit vectors in directions of major axes of the scattering volume ellipsoid:
Axis 1 (x, y, z) = (0.1125, 0.9929, 0.0397)
Axis 2 (x, y, z) = (-0.3113, -0.0027, 0.9503)
Axis 3 (x, y, z) = (0.9436, -0.1193, 0.3088)

Diameters of scattering volume along its major axes: d0 = (0.0517, 0.0768, 0.0847)

F.4 Appendix to Section 3.3.1 Beam tracing - Figure 81

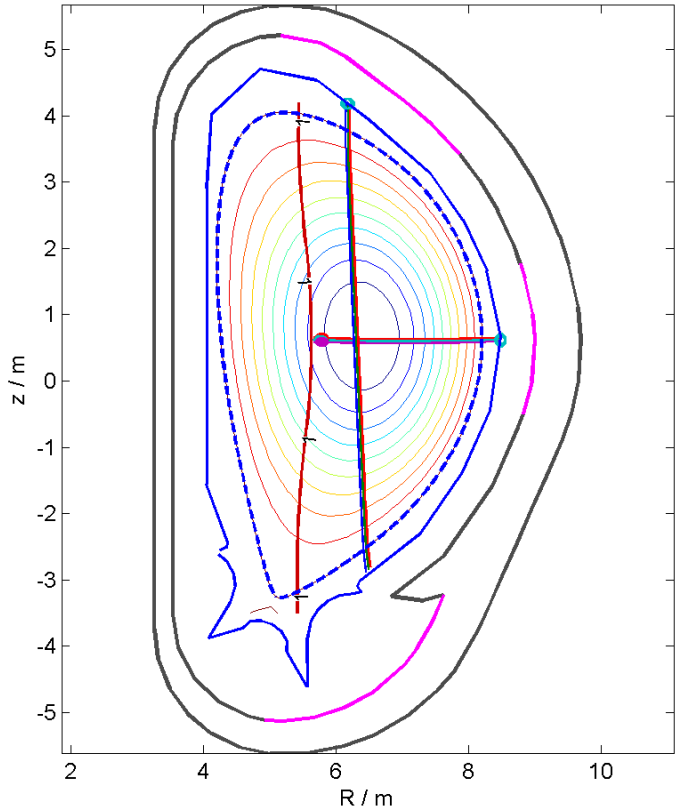

Figure 81 (repeated) Beam traces for the optimised 170 GHz scattering geometry with the probe displaced in the horizontal plane (nominal ITER2 parameters). The parameters used for the beams are presented below.

The parameters for the gyrotron are:
f = 170 GHz, mode = 'O', launch position = [-8.46, -0.55, 0.62], launch angle (θ,φ) = (90°, 16°).

The parameters for the receiver are:
f = 170 GHz, mode = 'O', receiving position = [-6.17, 0.00, 4.19],
receiving angle (θ,φ) = (179°, 0°).

The calculated output parameters are:
Beam Overlap, O_b = 18 m^{-1}, Scattering angle = 86.8°, $\angle(k^{\delta}, B)$ = 104°.
Scattering volume centre (x, y, z) = (-6.2978, 0.0139, 0.6109)
Distance between beam centroids, D = -0.000773 m
Unit vectors in directions of major axes of the scattering volume ellipsoid:
Axis 1 (x, y, z) = (0.1092, -0.9935, -0.0307)
Axis 2 (x, y, z) = (0.5895, 0.0896, -0.8028)
Axis 3 (x, y, z) = (0.8003, 0.0696, 0.5955)

Diameters of scattering volume along its major axes: d0 = (0.0538, 0.0761, 0.0815)

F.5 Appendix to Section 3.3.1 Beam tracing – sawtooth robustness

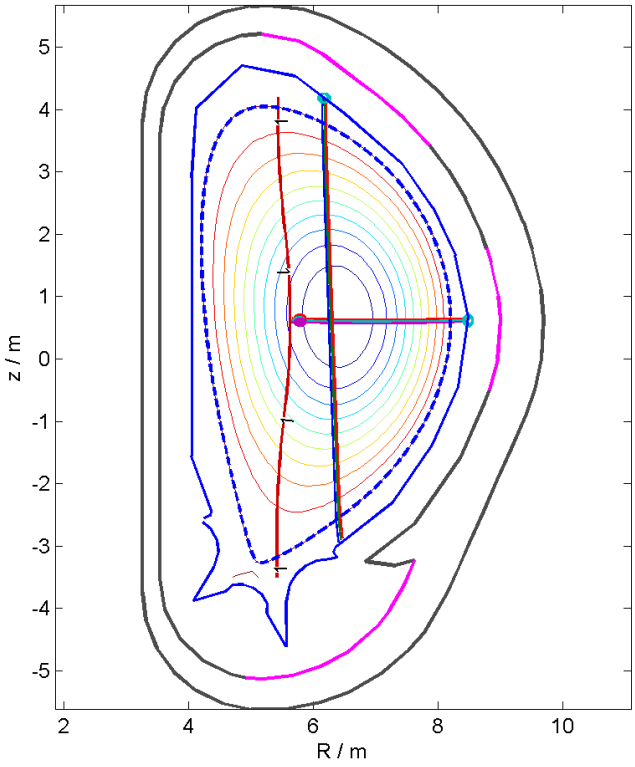

Figure Beam traces for the optimised 170 GHz scattering geometry with the probe displaced in the horizontal plane. Nominal ITER parameters are used except for the density being scaled down by 10% simulating a sawtooth crash. The parameters used for the beams are presented below.

The parameters for the gyrotron are:
f = 170 GHz, mode = 'O', launch position = [-8.46, -0.55, 0.62], launch angle (θ,φ) = (90°, 16°).

The parameters for the receiver are:
f = 170 GHz, mode = 'O', receiving position = [-6.17, 0.00, 4.19],
receiving angle (θ,φ) = (179°, 0°).

The calculated output parameters are:
Beam Overlap, O_b = 13.8 m^{-1}, Scattering angle = 87.3°, $\angle(k^{\delta}, B)$ = 104°.
Scattering volume centre (x, y, z) = (-6.2775, 0.0178, 0.6125)
Distance between beam centroids, D = 0.0163 m
Unit vectors in directions of major axes of the scattering volume ellipsoid:
Axis 1 (x, y, z) = (0.1248, -0.9918, -0.0273)
Axis 2 (x, y, z) = (-0.5927, -0.0965, 0.7996)
Axis 3 (x, y, z) = (-0.7957, -0.0836, -0.5999)

Diameters of scattering volume along its major axes: d0 = (0.0536, 0.0759, 0.0804)

F.6 Appendix to Section 3.3.1 Beam tracing – 161.25 GHz and 178.75 GHz

For a frequency of 161.25 GHz:

The calculated output parameters are:
Beam Overlap, O_b = 15.8 m^{-1}, Scattering angle = 86.3°, $\angle(k^{\delta}, B)$ = 104°.
Scattering volume centre (x, y, z) = (-6.3228, 0.0131, 0.6103)
Distance between beam centroids, D = -0.0112 m
Unit vectors in directions of major axes of the scattering volume ellipsoid:
Axis 1 (x, y, z) = (0.0950, -0.9950, -0.0298)
Axis 2 (x, y, z) = (0.5449, 0.0770, -0.8350)
Axis 3 (x, y, z) = (0.8331, 0.0630, 0.5495)

Diameters of scattering volume along its major axes: d0 = (0.0539, 0.0760, 0.0824)

For a frequency of 178.75 GHz:

The calculated output parameters are:
Beam Overlap, O_b = 16.3 m^{-1}, Scattering angle = 87.2°, $\angle(k^{\delta}, B)$ = 104°.
Scattering volume centre (x, y, z) = (-6.2771, 0.0148, 0.6114)
Distance between beam centroids, D = -0.01 m
Unit vectors in directions of major axes of the scattering volume ellipsoid:
Axis 1 (x, y, z) = (0.1219, -0.9920, -0.0313)
Axis 2 (x, y, z) = (-0.6352, -0.1022, 0.7655)
Axis 3 (x, y, z) = (-0.7626, -0.0734, -0.6426)

Diameters of scattering volume along its major axes: d0 = (0.0536, 0.0761, 0.0808)

References

1. G A0 GDRD 2 01-07-13 R 1.0, ITER Final Design Report, Design Requirements and Guidelines Level 1 (DRG1), 2001.

2. V. S. Mukhovatov, R. Bartiromo, D. Boucher, and A. E. Costley, in *Diagnostics for Experimental Thermonuclear Fusion Reactors 2*, Edited by P. E. Stott, G. Gorini, P. Prandoni, and E. Sidoni (Plenum Press, New York, 1998).

3. H. Bindslev, *Recent developments in theory of wave scattering in plasmas*, 1996, Edited by A. G. Litvak 1 (Russian Academy of Sciences, Institute of Applied Physics, Nizhny Novgorod, 1996), p. 109-128.

4. H. Bindslev, Journal of Atmospheric and Terrestrial Physics **58,** 983 (1996).

5. H. Bindslev, Plasma Physics and Controlled Fusion **33,** 1775 (1991).

6. E. Holzhauer and J. H. MASSIG, Plasma Physics and Controlled Fusion **20,** 867 (1978).

7. H. Bindslev and F. R. Hansen, JET-IR(91)02, Numerical Investigations of the Propagation of Electromagnetic Millimetre Waves in a Fluctuating Plasma - Impact of Density Fluctuations on JET Alpha Particle Diagnostic, 1991.

8. H. Bindslev, *Collective Thomson scattering for diagnosis of fast ions*, 1997, Edited by T. Donne 1997), p. 265-276.

9. H. Bindslev, JET Joint Undertaking JET-R(97)12, Assessing and optimising measuring capabilities of complex diagnostic systems, 1997.

10. C. A. Balanis, in *Antenna Theory Analysis and Design*, (Harper & Row, New York, 2003), Chap. 11.

11. ITER Report S 55 RE2 97-01-24 F1. 1998.

12. U. Tartari *et al.*. Intermediate Report on:"Initial feasibility study of the possibility of diagnosing the confined energetic particle populations in ITER by CTS". 2002. Istituto di Fisica del Plasma, EURATOM-ENEA-CNR, Milano.

13. H. Bindslev *et al.*. Collective Thomson scattering of millimetre waves in JET. Proceedings of the Russian boat Workshop on Strong Microwaves in Plasmas 1996 , 142. 1996.

14. R. Behn *et al.*, Physical Review Letters **62,** 2833 (1989).

15. A. Semet, L. C. Johnson, and D. K. Mansfield, International Journal of Infrared and Millimeter Waves **4,** 231 (1983).

16. P. Woskoboinikow, W. J. Mulligan, and R. Erickson, IEEE Journal of Quantum Electronics **19,** 4 (1983).

17. T. Kondoh *et al.*, Review of Scientific Instruments **74,** 1642 (2003).

18. R. K. Richards *et al.*, Review of Scientific Instruments **74,** 1646 (2003).

Acknowledgements

The authors would like to thank colleagues in the field for helpful comments, in particular Drs Alan Costley, Christian Ingesson and Umberto Tartari.